Experimental and numerical analysis of the failure modes induced in ceramic materials under dynamic loading

Marielle Dargaud

THÈSE

Pour obtenir le grade de

DOCTEUR DE L'UNIVERSITE GRENOBLE ALPES

Spécialité : 2MGE : **Matériaux, Mécanique, Génie civil, Electrochimie**

Arrêté ministériel : 25 mai 2016

Présentée par

Marielle DARGAUD

Thèse dirigée par **Pascal FORQUIN**, Professeur des Universités, Université Grenoble Alpes

préparée au sein du **Laboratoire Sols, Solides, Structures et Risques** dans **l'École Doctorale I-MEP2 - Ingénierie - Matériaux, Mécanique, Environnement, Energétique, Procédés, Production**

Analyse expérimentale et numérique des modes d'endommagement induits dans des matériaux céramiques sous chargement dynamique

Experimental and numerical analysis of the failure modes induced in ceramic materials under dynamic loading

Thèse soutenue publiquement le **23 avril 2021**,
devant le jury composé de :

Yannick CHAMPION
Directeur de recherche CNRS, Laboratoire SIMaP – **Président**

Stéphane ROUX
Directeur de recherche CNRS, ENS Paris Saclay – **Rapporteur**

Michel ARRIGONI
Professeur des Universités, ENSTA Bretagne – **Rapporteur**

Daniel EAKINS
Maître de conférences, Université d'Oxford – **Examinateur**

Eric BUZAUD
Docteur - ingénieur, CEA CESTA – **Examinateur**

Pascal FORQUIN
Professeur des Universités, UGA – **Directeur de thèse, Examinateur**

Jérôme BRULIN
Docteur - ingénieur, Saint-Gobain Research Provence – **Co-encadrant, Invité**

Alexane MARGOSSIAN
Docteur - ingénieur, Saint-Gobain Research Provence – **Co-encadrant, Invité**

François BARTHELEMY
Docteur - ingénieur, DGA Techniques Terrestres – **Invité**

SIGILLUM UNIVERSITATIS GRATIANOPOLITANE
VERI TAS
LIBE RABIT
1339

Abstract

Due to their high resistance to extreme loading conditions, ceramic materials have been extensively investigated to be part of vehicle and body armour protections. Combined to a ductile backing, ceramics are very interesting for lightweight bulletproof systems. The link between damage mechanisms occurring in the ceramic upon impact and its microstructural properties is still not well understood. For this reason, a *make-and-shot* iterative approach is the common way followed to develop this type of material. However, such an optimisation process is very expensive, time consuming and hardly leads to any conclusions on the link between microstructural features and ballistic performance. The first goal of this PhD is to bring insight on the connection between microstructural properties of the ceramic armour and its failure mechanisms under dynamic loading. The natural second step consists in using these results to improve a modelling, which is representative of ceramic brittle damage under tensile loading on a large range of strain rates.

Ceramics are highly sensitive to the presence of inherent defects. Under low loading rate, they have a stochastic strength linked to the size of the most critical defect in the loaded volume. The common approach consists in using quasi-static tests to identify the defects responsible for failure (Weibull approach) and assumes that the same ones are causing failure at high loading rates. Such an assumption is questioned in the present work. Under high strain rate, numerous cracks are triggered simultaneously from multiple defects, causing an intense and deterministic fragmentation. Six ceramic materials, presenting different microstructural features, are analysed and tested under dynamic conditions in this project. Highly instrumented edge-on impact, normal impact and tandem impact dynamic tests, combined with a micro-tomography analysis of damage patterns, provided a better understanding of the fragmentation properties of the different grades of ceramics. A shockless experimental spalling technique was developed to evaluate the intrinsic tensile strength sensitivity to strain-rate of ceramic materials. To do so, the plate-impact configuration was adapted, using specific flyer-plate geometries designed to generate a tailored loading in the sample. From a hybrid approach mixing numerical simulations and experimental results, the spall-strength of the tested ceramic can be related to a well-controlled loading rate.

A new methodology is proposed to model the multiple fragmentation process induced in ceramics under high strain rate. This method is built on the identification of material defects (mainly pores) from micro-tomography analysis. This realistic description of the defect distribution is explicitly implemented in the Denoual-Forquin-Hild (DFH) damage model to predict the dynamic failure behaviour of ceramics under tensile loading, through so-called continuous and discrete approaches. A comparison with experimental results of fragmentation and spalling tests provided a validation of the approach. Predictions of this micro-mechanical model were compared for a Weibullian distribution of critical defects and a description based on micro-tomography analyses. Comparisons on a large range of strain rates showed that, for materials presenting multiple flaw populations, the Weibull-based solution is highly invalid. In this case, the use of a proper flaw description, obtained via micro-tomography, is much more relevant. These results highlight the importance of considering microstructural features to properly model the failure behaviour of ceramics at high loading rate, and therefore move toward a design of the next generation of ceramic-based armour protections.

Keywords: Ceramics, Brittle materials, Microstructural defects, X-ray Computed Tomography, Dynamic fragmentation, Spalling, Strain rate sensitivity, Damage model

Résumé

De par leur aptitude à résister à des chargements mécaniques extrêmes, les céramiques sont utilisées comme matériaux constitutifs de blindages. Couplées à une face arrière ductile, elles permettent un gain de poids considérable. Le lien entre les mécanismes d'endommagement générés au sein de la céramique lors de l'impact, et ses propriétés microstructurales n'est pas encore bien compris. L'approche classique adoptée pour leur développement consiste ainsi à itérer entre la fabrication de nouveaux matériaux et l'évaluation de leurs performances via des essais balistiques. Cependant, ce type d'optimisation est coûteux et ne permet que très rarement de tirer des conclusions sur ce lien entre propriétés microstructurales et performances balistiques. Le premier objectif de cette thèse est d'améliorer la compréhension du lien entre microstructure et mécanismes d'endommagement engendrés sous chargement dynamique. Ces résultats visent à enrichir une modélisation, représentative du comportement fragile des matériaux céramiques sous chargement de traction dynamique, et sur une large gamme de vitesses de déformations.

Les matériaux céramiques sont hautement sensibles à la présence de défauts. A faible vitesse de déformation, ils présentent une résistance stochastique reliée à la taille du défaut le plus critique du volume sollicité. L'approche classique consiste à utiliser des essais quasi-statiques pour identifier les défauts responsables de la rupture (approche de Weibull) et supposer qu'ils sont aussi à l'origine du processus de rupture sous chargement dynamique. Ce travail remet en question cette hypothèse. A haute vitesse de déformation, de nombreuses fissures s'amorcent simultanément sur de multiples défauts et conduisent à une fragmentation intense et déterministe. Six matériaux céramiques de propriétés microstructurales différentes sont analysés et testés sous chargement dynamique. Des essais dynamiques, hautement instrumentés, de type impact sur tranche, normal et tandem, combinés à une analyse par micro-tomographie des faciès d'endommagement, ont permis de mieux comprendre leurs propriétés de fragmentation. Une technique d'écaillage par impact de plaques sans choc a été développée pour évaluer la sensibilité à la vitesse de déformation de la résistance intrinsèque en traction de matériaux céramiques. La conception de plaques impactrices ondulées a permis de transmettre un chargement contrôlé à l'échantillon testé. Une approche hybride, combinant des simulations numériques et des résultats expérimentaux, a mis en évidence le lien entre leur résistance à l'écaillage et la vitesse de déformation.

Une nouvelle méthodologie est proposée pour modéliser le processus de fragmentation induit dans les céramiques à haute vitesse de chargement. Cette approche s'appuie sur l'identification des défauts (essentiellement des porosités) à partir d'analyses micro-tomographiques. Cette description réaliste de la distribution de défauts est implémentée dans le modèle d'endommagement Denoual-Forquin-Hild (DFH) de façon explicite, via des approches dites discrète et continue, pour prédire le comportement sous chargement de traction dynamique. Une confrontation aux résultats d'essais de fragmentation et d'écaillage, a permis une validation de l'approche. Les prédictions de ce modèle micromécanique sont comparées pour une population de défauts déterminée via l'approche de Weibull et à partir d'analyses micro-tomographiques. Cette étude a montré que, pour des matériaux présentant plusieurs populations de défauts, l'approche de Weibull n'est plus correcte à haute vitesse de déformation, et l'utilisation d'une population de défauts identifiée via micro-tomographie est grandement pertinente. Ces résultats soulignent l'importance de considérer les propriétés microstructurales pour réussir à correctement modéliser le comportement de matériaux céramiques à haute vitesse, et ainsi progresser vers l'optimisation des prochaines solutions de blindage céramique.

Mots clés : Céramiques, Matériaux fragiles, Défauts microstructuraux, Micro-tomographie, Fragmentation dynamique, Ecaillage, Sensibilité à la vitesse de déformation, Modèle d'endommagement

Acknowledgements

First, I am grateful to my director, Prof. Pascal Forquin, for his dedication, guidance and trust regarding this project. His immense knowledge and experience have encouraged me though this academic and *dynamic* journey. I deeply thank Prof. Michel Arrigoni and DR. Stéphane Roux for accepting to review my work and providing constructive suggestions. My full gratitude also goes to my committee members, Dr. Daniel Eakins, Dr. Eric Buzaud and DR. Yannick Champion, for their highly stimulating discussions during my defence. The few experts in this field makes this sharing moment very rewarding.

I am deeply thankful to my co-supervisors from Saint-Gobain. Dr. Jerôme Brulin, who initiated this adventure by welcoming me in his team at Saint-Gobain Research Provence about four year ago. Thank you for your invaluable mentoring and support. My sincere gratitude also goes to Dr. Alexane Margossian and Dr. Matthieu Graveleau for their insightful contributions. Keeping an industrial interest was an absolute source of motivation and I appreciate that you made it possible for me to openly share my results.

This work would not have been possible without the technical support of J. Sant for the manufacturing of RBBC ceramics, Dr. Edward Andò, Pascal Charrier and Dr. Nicolas Lenoir for the X-Ray tomography analyses and Wojtek Kaczmarek and Emile Pollier for the dynamic experiments. It was a great pleasure to share your expertise and enthusiasm. I am also grateful to Dr. Jean-Luc Zinszner, who paved the way through his PhD, and provided helpful clarifications regarding the interferometry system and data post-processing.

Special thanks go to my beloved co-workers and friends: Ritesh Gupta, David Georges, Yannick Duplan, Maria Blasone and Antoine Mertz. It was a pleasure to share with you the ups and downs which are so specific to the PhD adventure. Many people contributed to the friendly atmosphere in the lab, they will recognize themselves, thank you to all of you.

I am extremely grateful to my parents, twin sisters and grandparents for their unwavering support and belief in me. My strongest source of motivation was probably to make you proud. Lastly, I thank you Bruno; for patiently dealing with my *confined* writing period and being so supportive all along this journey.

Contents

1 | Introduction

Contents

1.1 Context

1.1.1 Ceramic materials for ballistic protection

In the last decade, the development of lightweight armour systems for personal, vehicle and helicopter protection was intensively studied. Initially made of metallic plates, mostly hard steel, the bulletproof systems have evolved to answer the challenge of weight reduction. During the 60's, ceramic-based protective systems started to be developed for aircrews, where the weight is a major issue with, for instance, hot pressed B_4C on Kevlar29 for helicopter ballistic seats (1969) [1]. With a density of more than 50 % less than metals, advanced ceramics partially replaced metallic armour plates. High hardness, high compressive strength and high elastic modulus are often used as arguments to include ceramic materials in armour solutions. However, no direct link has been established between these mechanical properties and the ballistic performance. Moreover, the high brittleness of ceramics leads to their intense fracture under a ballistic impact. For this reason, ceramics are not used stand-alone in armour applications, but are bonded to a ductile backing such as a soft metallic layer (aluminum alloy) or a laminate made of high tensile strength fibres (aramid fabric or ultra-high-molecular-weight polyethylene fibres). The ceramic front plate is usually covered by a ballistic nylon, which provides a better integrity of the system. Several examples of applications including a ceramic armour are presented in Figure 1.1.

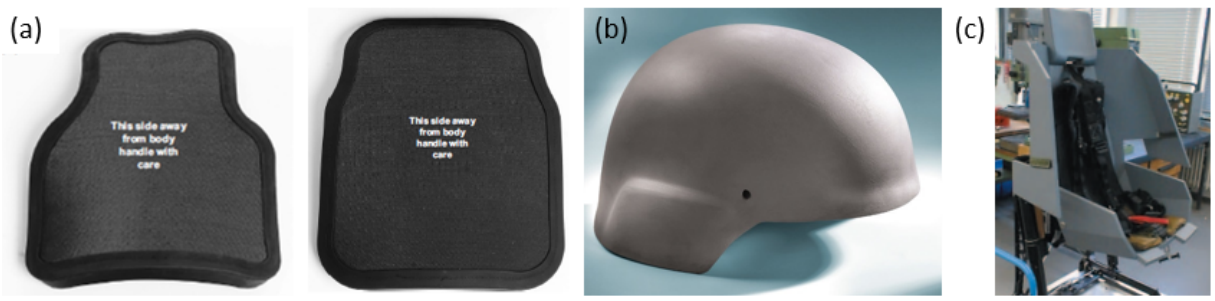

Figure 1.1. Examples of ceramic-based armour systems. (a) Osprey body armour, ceramic/composite front and back plates (MOD Crown Copyright 2015) [2]. (b) Silicon carbide armour helmet (Credit: Saint-Gobain). (c) European Tiger Helicopter Seat, Cercom Inc.

A large range of ceramics is used as armour materials. Oxide armour ceramics are mostly alumina-based materials Al_2O_3. Non-oxide armour ceramics correspond to borides, carbides, nitrides, such

as materials based on boron carbide B_4C, silicon carbide SiC, silicon aluminium oxynitride SiAlON, aluminum nitride AlN, titanium diboride TiB_2 and others. Al_2O_3 is the most economical material but has a high density (3.90 g/cm^3). Boron carbide is a valuable candidate for lightweight armour due to its lower density (2.52 g/cm^3) combined with its elevated Vickers hardness ($>$ 30 GPa). In Table 1.1, the main mechanical characteristics of these materials are presented. It has to be kept in mind that these properties highly depend on the manufacturing process. For silicon and boron carbides, properties of materials obtained by reaction bonding (RB) are presented (detailed in section 3.1.3). These materials correspond to ceramic-metal composites, with a predominant ceramic phase of SiC (RBSiC) or B_4C (RBBC). They present very interesting properties for lightweight ballistic protection [3] [4].

Table 1.1. Main mechanical properties and relative cost of ceramics for armour application [5]

Property	Al_2O_3	SiC	RBSiC	B_4C	RBBC	TiB_2
Density (g/cm^3)	3.90	3.21	3.10	2.52	2.58	4.52
Bending strength (MPa)	310-370	300-400	300-350	350-410	319-415	500-750
Young's modulus (GPa)	300-370	410-480	300-400	400-460	300-350	560
Hardness (GPa)	14-15	24-27	18-20*	30-32	20-22*	26-28
Fracture toughness (MPa$\sqrt{m}$)	3.5-4.5	2.5-4.5	2.5-4.5	2.5-3.5	5.5-7.9	6.8-7.5
Cost comparison	1	5.3	2	8	4.6	10

* informative values because hardness measurement is not adapted to RB heterogeneous microstructures

1.1.2 Complex mechanisms involved in a ballistic impact

Metal and ceramic-based armours present completely different failure mechanisms to dissipate the projectile energy. While metals dissipate energy through plastic deformation mechanisms, hard ceramic materials use some mechanisms of micro-plasticity and friction between fragments to defeat the projectile, through a complex succession of events. A ballistic event can be decomposed into three main chronological steps, during which the role played by the ceramic evolves.

- The first step corresponds to the few microseconds after the contact between the steel core and the ceramic (1-2 μs). During this first interaction, the ceramic is subject to a compression loading, which corresponds to very high pressure levels (hydrostatic pressures exceeding 5 GPa [6]). At this stage, the ceramic zone directly beneath the projectile nose undergoes some local micro-plasticity, such as amorphisation and shear localization [7]. This damaged zone, called the Mescall zone (MZ), is highly comminuted and compacted under the compressive action of the projectile [8]. As for the steel core, its nose starts to erode and dwell on the ceramic surface without any penetration, thanks to the high hardness of the ceramic.

- Then, spherical compressive waves generated upon impact lead to hoop tensile stresses in the material. But as the tensile strength of ceramics is relatively low, about three to fifteen times lower than their compressive resistance [9], this step causes the intense cracking of the ceramic, called *multiple-fragmentation*. It is commonly accepted that the nucleation of micro-cracks under tensile loading happens on the inherent microstructural defects such as pores, inclusions, sintering flaws at grain boundaries and heterogeneities [10] [11]. After about 6-7 μs, the ceramic tile is fully fragmented.

- Finally, the last step is the penetration of the remaining core part and debris through the fragmented ceramic. The penetration can only happen once the ceramic material has failed underneath the projectile and can be pushed away from its path. During this stage, the finely fragmented material is mainly subject to friction, flow and abrasive properties [12]. The residual kinetic energy is finally absorbed by the plastic deformation of the backing, thus stopping the core and ceramic debris (about 50 μs after impact).

In Figure 1.2, a sequence of flash X-ray radiographs were taken during the impact of a 7.62 mm APM2 steel core on a boron carbide based target [13]. These radiographs illustrate the different steps of a ballistic event and the corresponding degradation stages of the steel core and ceramic. The proportions of the projectile energy dissipation were estimated to be approximately 35 % for its dwell under compression and 50 % for its erosion, both failure mechanisms induced by the hard ceramic strike-face, and the last 15 % are dissipated by the ductile backing [14]. The post-mortem X-ray radiograph of a ceramic-based torso plate, impacted by a 7.62 mm APM2 steel core, permits the visualisation of damage patterns in Figure 1.2 (b). The white circular zone around the projectile hole corresponds to a through-thickness conoidal fracture, commonly called Hertzian cone cracks [15]. This conical cracking spreads the impact loading on a larger area of the backing, about 3 to 5 times larger than the projectile dimension according to the ceramic thickness. This highly damaged zone results from the high compressive loading (first step), whereas the radial cracks propagating to the edge of the plate are triggered from the induced hoop tensile stresses (second step). The interactions between the compression spherical waves and the waves reflected at the free edges of the plate lead to the formation of circumferential cracks (tension). It has been demonstrated that the amount of energy dissipated by the creation of new surfaces via the trigger of cracks is negligible [16]. Finally, the absence of fragments in the central part is due to the displacement and ejection of the ceramic material from the projectile penetration in the fragmented media.

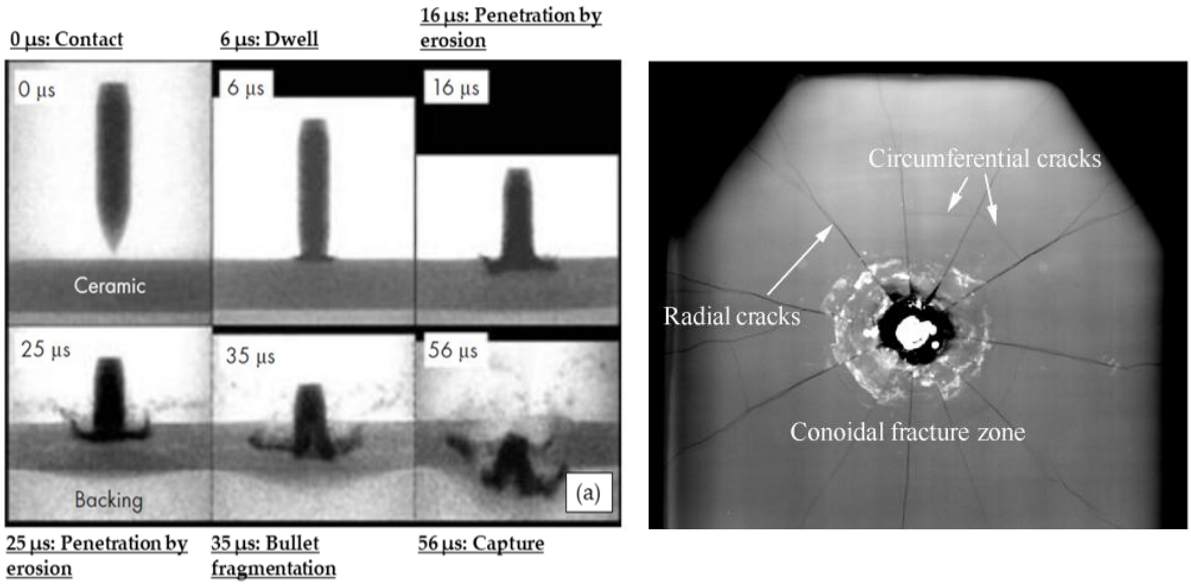

Figure 1.2. (a) Sequence of flash X-ray radiographs taken during the impact of a 7.62 mm APM2 steel core and a boron carbide based target [13]. (b) X-ray radiograph of an impacted hard armour torso plate showing damage from a 7.62 mm APM2 round [17]

Krell and Strassburger showed from their study on transparent armour ceramics (Al_2O_3 and spinel) that the top priority factor driving armour ballistic performance is the ceramic fragmentation [18]. This is justified by the fact that the ceramic fragmentation behaviour has an effect on all the three main steps described previously. A lower ceramic fragmentation increases the dwell (flow) time of the projectile on the ceramic surface before its penetration (step 1) and coarse ceramic debris provide a better abrasive efficiency (step 3). Moreover, they underlined that the fragmentation behaviour of armour ceramics is essentially governed by the ceramic microstructural features and the dynamic stiffness of the backing.

1.1.3 Toward an improvement of the ceramic material

Extensive studies were devoted to the development of ceramic-based protective systems. To evaluate their ballistic performance, the ceramic plate can be tested alone or integrated to a specific configuration, such as bonded to a ductile metal or composite backing. In most cases, the goal is to compare the ballistic efficiency of several ceramic plates, according to their composition (ceramic material, type of

backing, etc.) and configuration (thicknesses, number of composite layers, etc.). From this, solutions can be ranked with respect to their areal density [19]. Three main experimental techniques provide an evaluation of the ballistic efficiency of an armour solution. The first one consists in impacting the tested system above its velocity of penetration and measuring the projectile (or core debris) residual velocity, using a high speed camera [20]. The second way, called Depth Of Penetration (DOP), consists in comparing the projectile depth of penetration in a semi-infinite backing (usually made of metal or polycarbonate), with and without a ceramic front tile [21]. In the third test used to rank armour solutions, a target is impacted at different velocities to determinate the minimum velocity necessary to penetrate the target with a probability of 50 %. This technique, called Ballistic Limit Velocity V_{50}, requires testing a sufficiently large number of targets (about 10) to be statistical and to provide conclusions on the ballistic performance of an armour system. One limitation of these ballistic techniques is that they need to perforate the target, so the thickness of the tested system is limited by the projectile velocity.

So far, damage mechanisms occurring in a ceramic armour, when subject to an impact loading, are still not well understood. For this reason, a *make-and-shot* iterative approach is the common way followed to develop this type of materials. But such an optimisation process is expensive, time consuming and hardly leads to any conclusions on the link between microstructural properties and ballistic performances. Instead, they are replaced by some mechanical characterisations, which are supposed to help forecasting the ceramic ballistic performance. In the literature, most studies on armour ceramic development relate the effect of some of their microstructural features on their mechanical properties (such as hardness, fracture toughness, Young's modulus, quasi-static compressive strength, etc.). However, because of the different mechanisms involved in an impact event, the direct correlation between mechanical performance and ballistic performance is not trivial [22] [3]. Moreover, ceramics present a complex behaviour, involving several different failure modes and a strain rate dependent strength. This makes the optimisation of their composition/microstructure very difficult, according to the application. Therefore, it becomes essential to better understand the link between the microstructural parameters and the failure modes induced upon impact. From this, numerical tools, based on models reliably describing the failure behaviour of ceramics, should provide relevant predictions for the design of the next-generation of ceramic armour. Models predicting the behaviour of brittle materials under impact loading can be used to forecast ceramic failure modes under impact and to help dimensioning dynamic experimental tests. Available simulations in the literature rely on continuum damage models [23] [24] [25], from which it is difficult to extract general physical concepts to predict material behaviour, or on models with some incorporated subscale physics accounting for microstructure and fragmentation micro-mechanisms [26] [27].

1.2 Problematic and methodology

The goal of the present work is to better understand the link between microstructural features and the dynamic behaviour, according to the loading rate. To do so, six ceramic materials of various microstructures are analysed and tested under dynamic conditions. Two homogeneous dense SiC materials are studied as the reference to develop a modelling work. The effect of the pores size distribution is the main parameter studied for this modelling work, which aims at better understanding the fragmentation behaviour and tensile strength sensitivity to the strain rate. Two other types of materials, presenting more complex microstructures, were also included. The goal is to investigate the effect of microstructural heterogeneities (large grains, gradient of porosity) or mixed compositions (ceramic-metal composite) on the fragmentation properties.

The choice was made to focus on the tensile behaviour as it was found, in the literature, to be the most damaging loading upon impact [18]. In order to properly identify the defects causing failure, ceramic materials were analysed with X-ray tomography. The realistic flaw description obtained by this method was implemented in the Denoual-Forquin-Hild (DFH) micro-mechanical model, which accounts for crack

initiation, propagation and interaction mechanisms involved in the dynamic tensile fracture and the strain rate sensitivity of brittle materials. Such an approach, based on a real description of the defects distribution from micro-tomography, was developed as part of the Brittle CODEX Chair framework, launched and developed at the Laboratoire 3SR. This research program aims at investigating the role played by the microstructure on the strain-rate sensitivity of brittle materials, in order to improve their modelling at high loading rates [28].

1.3 Outline

The **first Chapter** presents the context of the study, the main challenge of ceramic armour development and the way it is addressed in the present work. Armour systems made of a hard ceramic as front face and a fibre-resin composite as backing present suitable properties for lightweight bulletproof personal and vehicle protections. However, ceramic materials present complex failure behaviour (different failure modes and strain rate sensitive), which complicate their microstructural optimisation. For this reason, it is crucial to bring insight on the link between their microstructural features and dynamic failure behaviour. To do so, experimental techniques need to be developed to capture the intrinsic properties of the material. Resulting parameters can be used to supply models accounting for mechanisms specific to the behaviour of brittle ceramic materials.

In the **second Chapter**, a brief review presents the main specificities of ceramic brittle materials. The focus is given on the pre-existing defects and how critical they are, according to the loading rate. Several experimental techniques, available in the literature, to investigate the fragmentation and tensile failure of ceramic are presented. Finally, this chapter presents an overview of different types of models, developed to characterize the dynamic failure of ceramics under tensile loading.

In the **third Chapter**, the six materials studied in this work are analysed. First, their microstructural properties are investigated via scanning electron microscopy and X-ray tomography. This study is completed by some mechanical and ballistic characterisations to apprehend the complexity of making a link between microstructural features, mechanical properties and ballistic efficiency.

In the **fourth Chapter**, dynamic laboratory tests are performed to evaluate the link between the microstructure and the fragmentation process of the materials. These tests provide some quantitative data on the damage chronology and fragmentation intensity. The use of X-ray tomography is investigated as a way to obtain valuable information on the fragmented post-mortem samples. Finally, a possible correlation between fragments size and their residual strength is explored.

The literature review showed a lack of experimental configurations to evaluate the intrinsic tensile strength sensitivity to strain rate of ceramic materials, based on the plate-impact technique. For this reason, the **fifth Chapter** focuses on the development of an innovative experimental solution. The flyer-plate geometry was adapted, compared to a classical planar-impact configuration, to generate a tailored loading in the sample. From a hybrid approach mixing numerical simulations and experimental results, the spall-strength can be related to a controlled loading rate.

In the **sixth and last Chapter**, a micro-mechanical modelling (DFH) is developed to describe the dynamic failure behaviour of ceramic materials under tensile loading over a large range of strain rates. A flaw description, obtained from X-ray tomography in **Chapter 3**, is used as an input to account for the real population of defects. This modelling work focused on two SiC materials, with a homogeneous microstructure and different size distributions of porosity (main defect). Finally, results in terms of cracking density and strength sensitivity to the loading rate, obtained in **Chapters 4 and 5**, are compared to the model predictions to validate the approach.

2 | State of the art

Contents

2.1 The brittle nature of ceramic materials

2.1.1 High sensitivity to the presence of pre-existing flaws

Type and origin of defects in ceramic materials

Microstructural pre-existing flaws can be of different nature in ceramics. A flaw can be defined by a microstructural heterogeneity which can lead to a stress concentration, eventually causing failure. This includes cavities (voids, pores), micro-cracks, large grains, stress or chemical heterogeneities (inclusions) [29] [30]. Mechanisms leading to bulk-defect formation are generally related to the manufacturing process. The primary type of defects is pores which can result from the manufacturing of the green body, such as irregularities of pressing or extrusion, or trapped bubbles in the ceramic slurry for slip casting. But they can also be caused by the removal of organic binders used for the shaping of granulated powder for pressing or as dispersing agent to improve the slip casting of a ceramic slurry. Finally, a lack of sintering can lead to residual porosity at the grain boundaries. Another type of common defect is the presence of inclusions in the final product. They correspond to an embedded phase in the host material and can result from impurities in the raw powders, contamination or an excess of sintering additives. The higher the mismatch between the inclusion and the host-material properties (such as thermal expansion), the more detrimental/critical the defect. Bakas et al. performed ballistic tests (V_{50} with a 30 caliber AP) on hot pressed SiC [31]. They found the presence of very large inclusions on the fragments (carbonaceous and aluminum-iron-oxide phases of average size 10-40 μm and 100 μm, respectively). From the comparison of two materials with different distributions of inclusions, they suggested that such a type of defect should not be neglected, as they might have influenced the crack formation. Some examples of microstructural defects leading to stress heterogeneities are illustrated in Figure 2.1.

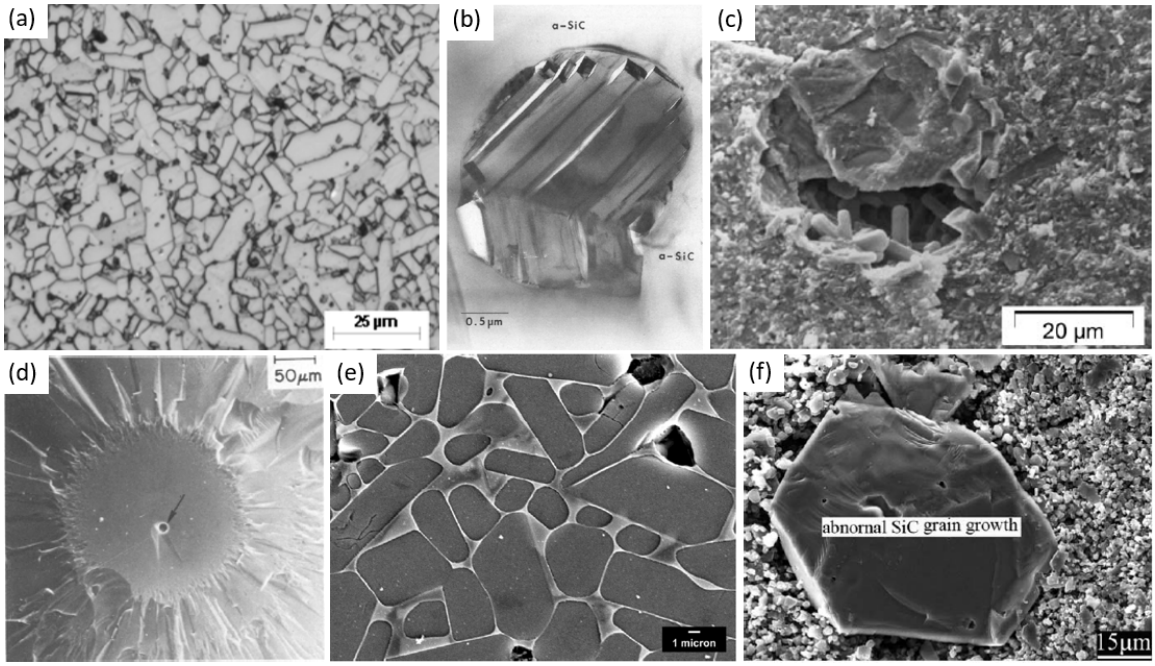

Figure 2.1. Non exhaustive examples of ceramic bulk defects. (a) Pore at the grain boundaries (Hexoloy SA®) [32]. (b) Graphite-rich inclusion in a (C+B)-doped α-SiC [33]. (c) Agglomerate related to a pore at the origin of a tensile brittle fracture in a silicon nitride valve [34]. (d) Brittle failure of a flame-polished SiO_2 rod from an internal bubble [35]. (e) Pores in LPS SiC with some micro-cracks on some grains [36]. (f) Abnormal SiC grain growth in RBSiC material, containing some residual pores [37].

To reduce the size of inter-granular inherent defects present in ceramic materials (mainly pores), several options are available, according to the firing process. First, a high temperature and an external force, such as pressure (Hot Pressed sintering) and possibly combined with an electrical current (Spark Plasma Sintering SPS), can be applied during the sintering step. A less expensive solution consists in preforming a pressureless sintering. When performed in solid state, the addition of some sintering aids (such as Al_2O_3, MgO, boron, carbon, etc.) can ease the consolidation of the powdery structure and considerably reduce the level of porosity [38] [39]. Otherwise, the pressureless sintering can be enhanced thanks to a liquid phase (LPS) (such as Y_2O_3 [40] or YAG [41]), which induces a rearrangement of the particles and facilitates their densification via some mechanisms of dissolution and precipitation. The presence of residual sintering additives or an inter-granular glassy phase (LPS) in the final product can affect the material properties [42]. In all these cases, starting from very small and uniform particles provides a better diffusion during the sintering process. These above-mentioned firing processes involve a phenomenon of shrinkage of the part. A different method than sintering, adopted to densify the material body without shrinkage, is the reaction-bonding (RB) process. It consists in filling the inter-granular pores with one or several new phases generated in situ. Two main RB processes can be distinguished. In the first type of RB process, the synthesis of this in situ phase can happen from a solid-gas chemical reaction, between particles present in the green body and a specific gas atmosphere used during the process (such as nitrogen, hydrogen, helium) [43]. In the second type of RB process, the in situ phase (or phases) results from a solid-liquid chemical reaction between the elements of the green body (such as free carbon) and a wetting liquid (such as molten silicon Si [44]), introduced by capillary infiltration through the channels of the porous green body. In the end, the mechanical properties of the composite materials (ceramic/ceramic or ceramic/metal), resulting from reaction bonding, depend on the properties of each different phase present, their proportions and their interface properties.

For a long time, large spherical pores were assumed not to be part of failure-causing flaws because of the relatively low stress concentration induced by their blunt/smooth shape [29]. However, Rice underlined that, in polycrystalline materials, microcracks are very likely to exist along the grain

boundaries in direct contact with the pore (about one-half grain deep into the matrix) [29]. So, due to their interaction with the surrounding grains, large spherical pores must be considered as sharp defects. Fractography analysis is the common way to identify the defects responsible for failure. Rice's study on glass materials confirms that spherical pores act as fracture origin [35]. Moreover, some authors acknowledged that most of these large pores present circumferential or semi-circumferential (event more critical) cracks [45] [46], as shown in Figure 2.2 (b). A further demonstration of the need to consider large pores as integral part of flaws was given by Matthews et al. showing that the Weibull distribution of large pores in SiC bodies is consistent with the Weibull strength distribution [47]. The possible interaction between defects is another parameter which needs to be addressed. Rice gave a threshold distance below which pore interactions are no longer negligible [48]. This criterion is that the centre-to-centre distance between two pores has to be lower than about two times their diameter, for the two pores to interact. This corresponds to a porous volume higher than about 5-7 vol. %. This defect distance/density is important as it is expected to influence the fragmentation of ceramic materials.

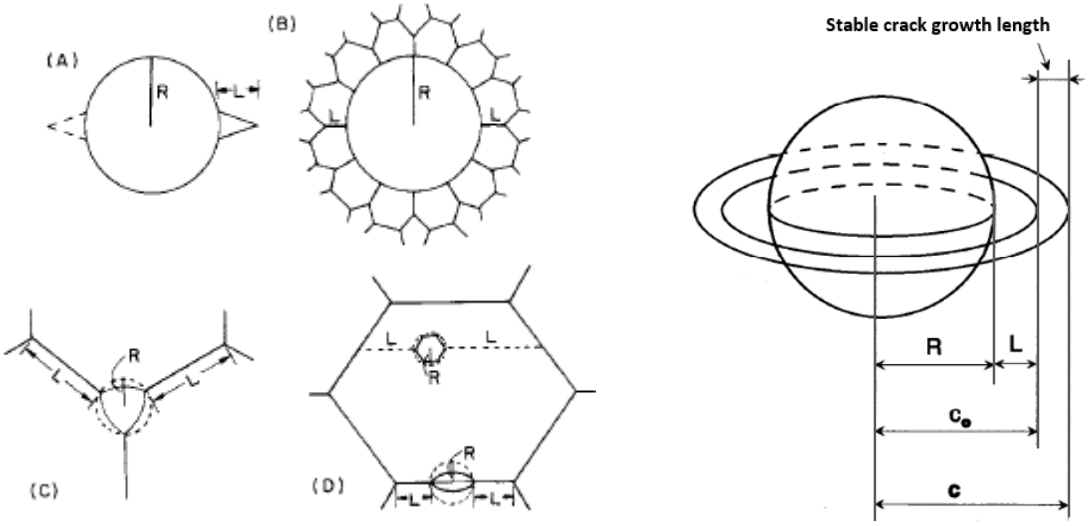

Figure 2.2. (a) Pores of different sizes (radius R, compared to the grain size) and locations (triple points, grain boundaries or within grains) with a radiating crack of length L [29]. (b) Pore with a circumferential crack of length L (c_0 is the initial crack length and c the crack length after a stable crack growth) [45]

Fracture and strength of brittle materials

Contrary to metals and alloys, ceramic materials hardly present any plastic deformation. Indeed, the stricter bonding conditions (ionic or covalent) limit the formation of dislocations, which are moreover immobile at room temperature [49]. Due to this lack of plasticity, ceramic materials have a brittle behaviour and are highly sensitive to the presence of porosity and cracks. When subject to a uni-axial and uniform tensile stress σ_0, the presence of a pore or micro-crack leads to high stress concentrations at the defect edges or crack tip. The magnified stress σ_{max} can be expressed as:

$$\frac{\sigma_{max}}{\sigma_0} = 2\sqrt{\frac{a}{R}} \tag{2.1}$$

where a is the half-crack length and R is the radius of curvature of the crack tip, which reflects the sharpness of the defect [50]. Whereas plastic deformation in metals would reduce the stress intensification by increasing the crack tip radius of curvature, brittle materials have no possible stress relaxation from plastic deformation. So, the presence of pores in ceramics is much more critical under tensile loading and triggered cracks are more likely to propagate. Such a behaviour implies that the strength of the materials is directly related to the flaw with the lowest failure strength, through the Weibull (1939) weakest-link theory [51] (further detailed in the next section). Therefore, it is necessary to identify the most critical defects to understand the failure strength of ceramic materials.

The Linear Elastic Fracture Mechanics (LEFM) allows expressing the macroscopic critical stress required to trigger an unstable crack of half-size a, as follows:

$$\sigma_c = \frac{K_{IC}}{Y\sqrt{\pi a}} \tag{2.2}$$

where K_{IC} is the critical stress intensity factor (fracture toughness) under mode-I (tensile) loading and Y is a dimensionless correction factor, related to the geometry of the crack. For a straight crack of length $2a$, perpendicular to the direction of an uniaxial tensile loading, the factor Y is equal to 1. Sack (1946) extended this stress failure criterion to 3-dimensional flaws and showed that a value of $2/\pi$ for Y can be considered for an internal circular flaw, equivalent to a semi-circular surface flaw of radius a [52]. This relationship between the critical stress for crack propagation and flaw size, relies on the assumption that flaws are independent and do not interact [53]. So, for defects of size ($2a \sim D_{eq}$), very small compared to the specimen dimension, this theory provides an approximation of the critical stress required to trigger a crack from it [27].

A way to indirectly limit the high brittleness of ceramic materials is to slow down the crack propagation. To do so, the addition of particles, fibres or an inter-granular phase in the ceramic matrix can increase the required energy to propagate the crack, by forcing its deflection around obstacles (cracks bend toward the phase presenting the higher elastic modulus). Large grains in the microstructure can also impede the crack propagation, as they act as bridges across the crack, preventing its further opening. Several authors reported the slow crack growth in heterogeneous ceramic microstructures, containing weak and strong interfaces [54] [55] [56]. Thus, the inhibition of the crack propagation leads to an increase of the material fracture toughness and critical stress for failure. For these multiple reasons, it is complicated to give a single guideline for the design of ceramic material.

2.1.2 Statistical approach to the quasi-static failure strength of ceramics

Probability of brittle failure - the Weibull model

Because of the high defect-sensitivity of ceramic materials, the statistical scatter in the quasi-static fracture data is directly correlated to the scatter in the defect size [57]. Therefore, unlike metals or polymers, which strength is given by a single failure load, for ceramics it has to be described with a statistical approach, through a probability of failure. This approach relies on two assumptions. First, the fracture starts at flaws, which are randomly distributed in the specimen. And then, once the local stress exceeds the critical stress of one defect, a crack nucleates from the flaw and propagates perpendicularly to the loading direction, causing the whole material to fail (weakest-link theory). So, under quasi-static loading, the fragmentation regime corresponds to a single fragmentation [58]. From this, Weibull gave a probabilistic expression to describe the distribution of failure strengths for a volume V, when subject to a uniform tensile stress σ [51]:

$$P_f(\sigma) = 1 - \exp(-V\lambda_{flaw}(\sigma)) \tag{2.3}$$

where λ_{flaw} is the density of critical flaws in the material. This probability of failure depends on the specimen volume. The bigger the tested volume, the more likely it is to contain a critical flaw. A common approach consists in considering a Weibull distribution of the flaw population in brittle materials. The flaw density of a Weibullian distribution can be expressed as a power law of the positive principal local stress σ [51]:

$$\lambda^W_{flaw}(\sigma) = \lambda_0 \left(\frac{\sigma - \sigma_u}{\sigma_0}\right)^m \tag{2.4}$$

where m is the Weibull modulus and $\lambda_0\sigma_0^{-m}$ is the Weibull scale parameter. A high value for the parameter m traduces a narrow scatter in failure stresses. σ_u corresponds to a threshold stress below which no failure can be observed. A simplified expression with only two parameters ($\sigma_u = 0$) can be considered [59] [60].

This distribution function has been widely used to characterize and model the fracture strength of various brittle materials, such as ceramics [61], rocks [62], concrete [63] and polycristallin ice [64]. The probability of failure for material presenting a Weibullian flaw population becomes:

$$P_f(\sigma) = 1 - \exp\left(-V\lambda_0\left(\frac{\sigma}{\sigma_0}\right)^m\right) \tag{2.5}$$

It is possible from the dispersion of the failure stresses obtained by quasi-static bending tests to graphically determinate the Weibull parameters. To do so, the experimental flexural strengths are ranked from the lowest to the highest and are assigned to an index i. A failure probability is attributed to each of them as follows [65]:

$$P_f = \frac{i - 0.5}{N} \tag{2.6}$$

where N is to the total number of bending tests performed on a material (the standard suggests at least 30 samples for reliability). In order to take into account the stress heterogeneity in the loaded volume, according to the bending configuration, an effective volume V_{eff} is defined. This volume corresponds to the theoretical volume for the stress to be uniform in the structure with the same average failure stress [66]. Equation 2.5 can be rewritten as follows:

$$\ln(-\ln(1 - P_f)) = m\ln(\sigma) + \ln(V_{eff}\lambda_0\sigma_0^{-m}) \tag{2.7}$$

By plotting the Weibull diagram, which corresponds to $ln(-ln(1 - P_f))$ as a function of $ln(\sigma)$, the Weibull parameter m can be deduced as it is the slope of the curve. This parameter depends on the flexural strength scattering, therefore it is related to the flaw dispersion. When considering a Weibullian flaw distribution, the average bending stress and its standard deviation are given by:

$$\sigma_w = \sigma_u + \sigma_0(V_{eff}\lambda_0)^{-\frac{1}{m}}\Gamma\left(\frac{m+1}{m}\right) \tag{2.8}$$

$$\sigma_{sd}^2 = \sigma_0^2(V_{eff}\lambda_0)^{-\frac{2}{m}}\Gamma\left(\frac{m+2}{m}\right) - (\sigma_w - \sigma_u)^2 \tag{2.9}$$

where Γ is the incomplete gamma function.

Limitations of the Weibull approach for the description of critical defects

It has to be underlined that the Weibull modulus determined by quasi-static bending tests does not describe the full flaw distribution. Indeed, it is limited to the defects causing the flexural failure (according to the effective volume and loading rate). Some early studies on surface and edge flaw populations in SiC ceramics, showed that concurrent flaw populations can lead to misinterpretations on the evaluation of material strength, having consequences on the reliability of their large scale design [67]. Moreover, some studies showed that from quasi-static bending tests, even performed at several scales, it is hardly possible to reach a complete description of the flaw distribution and verify whether a Weibull-type of distribution is really relevant for the material or not [68]. Danzer et al. presented numerous reasons why a brittle material would not have a Weibullian stress distribution. Among them, a bi- or multi-modal flaw distribution, the combination of surface and volume defects and the presence of internal residual stress fields are mentioned [59]. Peterlik gave an exhaustive list of the different attempts made to extend this Weibullian approach to bi-modal flaw populations [69], by using a multiplicative or additive bi-modal Weibull model for two *concurrent* (four Weibull parameters) [67] or *non-concurrent* (five Weibull parameters) [70] [71] flaw populations, respectively. Nevertheless, finding an accurate experimental way to evaluate the Weibull parameters of each flaw population remains a clear limitation, especially since the captured flaw population during bending tests depends on the specimen size (would require multiple tests at different scales). Danzer discussed the limitation of the Weibull theory for the description of very small defects, because specimens of effective volume smaller than 10^{-3} mm^3 have not yet been reached experimentally [72].

Moreover, describing a flaw population only from quasi-static tests becomes even more problematic

when the application involves dynamic loadings. Indeed, several authors reported that the flaw population responsible for failure highly depends on the loading rate [73]. For instance, the early stage study of Katz et al. on the fractographic analysis of ballistically loaded boron carbide showed that the defects, responsible for failure close to the impact zone, are much more difficult to identify than the ones at about 10-15 mm, which are similar to the defects responsible for quasi-static failure [74].

2.1.3 Strain rate sensitive behaviour at high loading rates

Deterministic behaviour of ceramics at high strain rate

It has been advanced in previous works that microstructural defects take part in the formation and development of the fracture network under dynamic loading. However, it is still not understood which flaw population is responsible for dynamic failure. As a result, so far, the link between microstructural defects and armour ceramic performance remains undefined. Whereas in quasi-static fracture a single (or few) crack nucleates and propagates, for a dynamic loading numerous cracks nucleate at different sites and propagate independently [75]. Ramesh et al. illustrated how the loading rate is expected to influence the type of defects activated through the schematic in Figure 2.4 (a) [73]. The top right plot-section shows the probability of finding a defect according to its size in the material. The bottom right presents the stress level required to trigger a defect according to its size (based on equation (6.14)). From this, at a low loading rate only few large defects are expected to be triggered, whereas at a high loading rate a large number of small defects should be responsible for the material failure. Forquin et al. performed dynamic tests on a pressureless sintered SiC ceramic (Edge-On-Impact test, further detailed in section 2.2.1) and showed from the fragments sieving that the resulting fragment size distribution is reproducible [76]. This result demonstrates that the dynamic fragmentation process of ceramic materials is deterministic. At high loading rate, even if the material behaviour remains discrete and the strength stays stochastic at the scale of one crack (highly depends on the geometry of the defect), it becomes deterministic at the whole volume scale due to the multiple fragmentation.

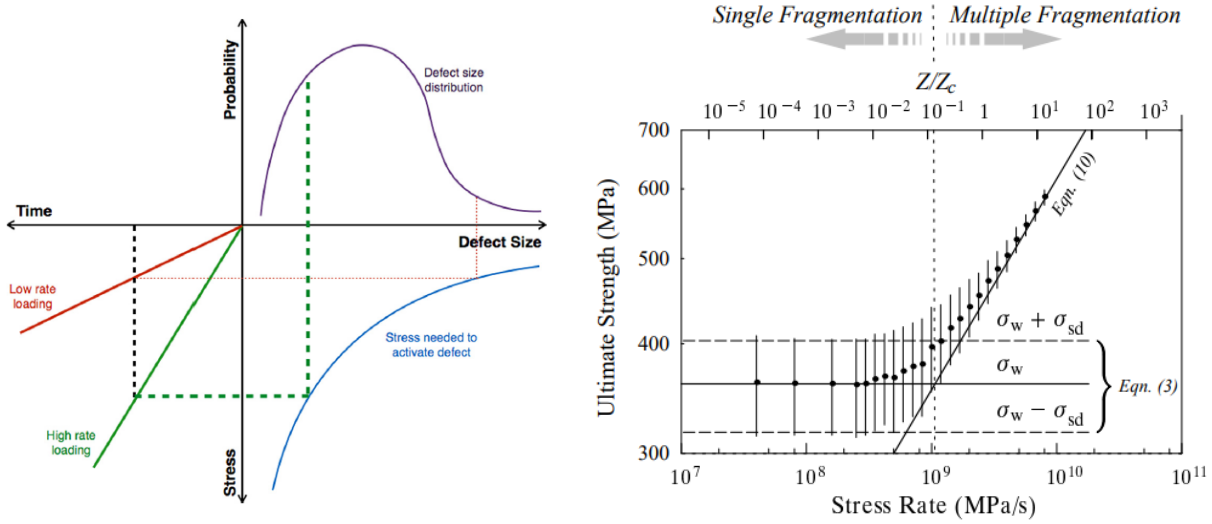

Figure 2.3. (a) Multipart schematic showing the influence of the loading rate on the activation of defects in a material containing a distribution of defects [73]. (b) Probabilistic–deterministic transition involved in a fragmentation process of SiC-100 ceramic from Monte-Carlo simulations [58]

From micro-mechanical modelling, Hild, Denoual and Forquin studied the strength sensitivity to strain rate of different types of brittle materials [58] [77]. To do so, they performed Monte-Carlo simulations on a volume having the mechanical properties of a SiC-100 ceramic and containing randomly distributed defects following a Weibull distribution, given in equation (2.4). The phenomenology

implemented in this damage model is further detailed in section 2.3.2, but it includes mechanisms of cracks initiation, propagation and interaction. For each point of the plot presented in Figure 2.4, they carried out 500 tensile numerical tests at a constant stress rate (or strain rate) on this volume. The results show a high sensitivity of the ultimate strength to the loading rate. They explained this rate-hardening behaviour by the transition from a single probabilistic fragmentation to a multiple deterministic fragmentation process, according to the applied loading rate. Below a strain-rate transition value of about 2500 s^{-1} (stress rate of 10^9 MPa/s), the whole volume is damaged by a single crack (single fragmentation), so a high scatter of strength is obtained, traducing the size-scatter of the most critical defect included in the considered volume. Above this threshold value, a large number of cracks are simultaneously triggered in the whole volume (multiple fragmentation), so the strength-scatter is highly reduced. They related the strain-rate threshold value between single and multiple fragmentation to the material Weibull modulus, the velocity of crack propagation and the size of the considered volume [77] [78].

Experimental demonstrations of the strength sensitivity to strain rate in brittle materials

Experimental quantification of the strain rate sensitivity of brittle material strength has been widely addressed during the last twenty years. However, it is far from being simple because it requires for experimental techniques to reach relatively high strain rates (according to the tested material) with a constant and controlled strain rate in the failure zone. Ramesh et al. related the difficult comparison of experimental fragmentation results found in the literature to the approximate estimation of the loading rate [73]. For some brittle materials, such as concrete, micro-concrete and ultra-high performance concrete, it has been experimentally shown that their tensile strength is strain rate sensitive, above a threshold value of about 10 s^{-1}, as shown in Figure 2.4 (a). This was demonstrated by making some adaptations of the Split Hopkinson Pressure Bars (SHPB) technique to reach strain-rates ranges from 30 to 150 s^{-1} [79] [80] [81] [82]. But such adaptations are not sufficient for ceramic materials mainly due to their higher strain rate transition, above which their tensile strength is sensitive to the applied strain-rate (further detailed in section 2.2.2). In most experimental studies on ceramics, available in the literature, dynamic strength is not correlated to strain rate in the failure area, but only to the impact loading [83]. To our knowledge, Zinszner et al. provided the only reliable studies experimentally demonstrating the strain rate sensitivity of the tensile behaviour of ceramic materials (alumina [84] and silicon carbide [85] ceramics). For this, they generated a shockless loading in the material by using an electromagnetic device (high-pulsed power technology GEPI [86]), to properly control the strain rate in the loaded specimen (further detailed in section 2.2.2). Their main results on two SiC ceramics are shown in Figure 2.4 (b).

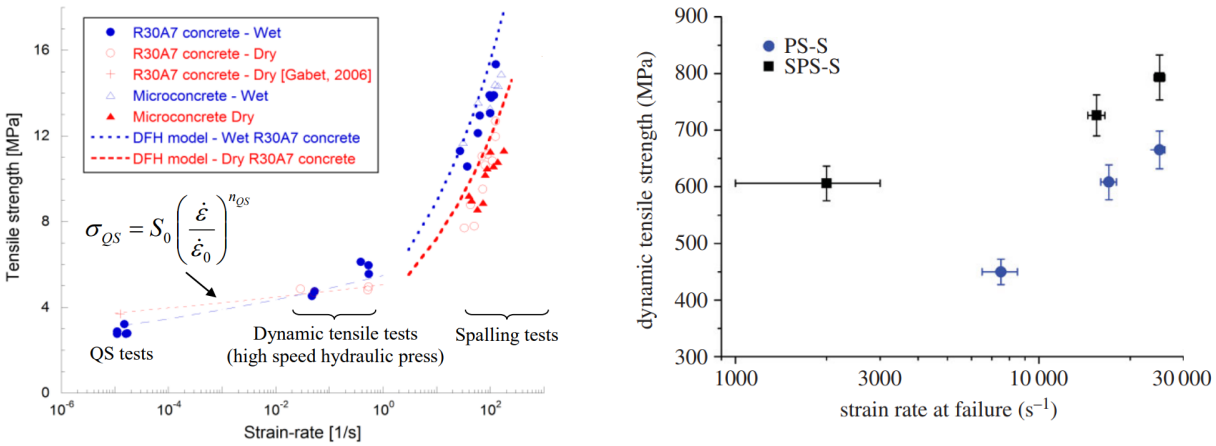

Figure 2.4. Tensile strength as a function of the strain rate at failure for (a) dry and wet microconcrete and common concrete [87] [88] and (b) two SiC grades (solid state pressureless (PS-S) and spark plasma (SPS-S) sintering) [85]

Because of the high complexity of the ballistic event, no clear determination of the involved strain-rate levels has been reported in the literature. Mentioned value are around 10^5 s^{-1} [89], and up to 10^8 s^{-1} [90]. This large range accounts for the differences between strain rates involved in compressive and tensile states and variations within the sample. Very high strain rates are rather involved in the early stages of the event (compressive loading), whereas relatively lower loading rates are responsible for the ceramic fragmentation further from the impact point.

2.2 Experimental techniques to evaluate the dynamic behaviour of ceramic materials

A ballistic event includes various stages, involving different failure mechanisms: confined compression, dynamic fragmentation and the projectile penetration in the damaged ceramic. As mentioned in section 1.1.2, the fragmentation process of ceramics is fundamental for two main reasons. First, it occurs very early in the failure process, due to the low tensile strength compared to compressive strength. Secondly, it controls the state of the damaged ceramic, responsible for the projectile erosion [12] [18]. In the present work, the choice was made to focus on the dynamic fragmentation of ceramic materials under tensile loading and the residual strength of fragmented media. Nevertheless, it has to be kept in mind that the behaviour under confined compression (triaxial) needs to be characterized in order to have a complete understanding of a ceramic behaviour under impact. Experimental techniques used to determine the compressive resistance of ceramic materials are triaxial compression tests, pyrotechnic spherical expansion and plate-impact tests. In the plate-impact testing configuration, a gas gun is used to launch a planar flyer plate at relatively high velocity toward a flat sample of the studied material. Therefore, it leads to a uniaxial loading (strain rates 10^5-10^7 s^{-1}) [91]. This method allows the shock response of ceramic materials to be studied at pressure levels above their transition point from elastic to inelastic behaviour, called Hugoniot Elastic Limit (HEL). For instance, classical HEL values for dense SiC ceramics are about 12-15 GPa, depending on the manufacturing process [92] [32] [93].

2.2.1 Characterisation of the fragmentation under impact

During a ballistic impact, it is possible to visualise the projectile/ceramic interaction thanks to techniques such as flash X-ray radiographs, as presented in section 1.1.2 Figure 1.2. However, such a configuration is not suitable to capture the damage evolution in the ceramic during and after impact. Laboratory tests were developed to investigate the failure modes induced in the ceramic and quantify its fragmentation intensity for further comparison with analytical modelling or numerical simulations.

Investigation of damage processes in a ceramic target

To gain insight on failure mechanisms induced in a ceramic target upon impact, the Edge-On-Impact (EOI) technique was developed at the Fraunhofer Institute [94] and at the Arcueil Research and Study Center [95]. This experiment consists in impacting a relatively thin ceramic tile on its edge with a rigid projectile (commonly a sphere, cylinder or Split Hopkinson Pressure Bar). This EOI configuration provides a visualisation of the fragmentation process on the sample surface (2D), usually non-visible as it occurs in a cone localized in the bulk of the material, as illustrated in Figure 2.9. The use of an ultra-high speed camera allows the chronology of the fragmentation process to be captured [96]. Tensile failure mechanisms generated during a ballistic impact and an EOI test are supposed to be relatively similar, for comparable loading conditions [97]. To date, a large variety of glasses, transparent [96] and opaque [95] ceramics, ultra-high-strength concrete [98] and rock [62] materials have been analysed using this technique. For transparent specimens, an observation in transmission is possible and the use of crossed polarizers provides further information on the stress waves propagation [99]. Whereas for opaque materials, the sample needs a mirror polishing for the damage process to be observed from light reflection on the surface.

The EOI configuration reveals the anisotropy of the fragmentation process, developing only few microseconds after impact (2-3 μs) in ceramic materials. A large number of radial cracks nucleate in ceramic targets upon impact, even before any wave reflection. It has been demonstrated from elastic numerical simulations that hoop tensile stresses are generated by the radial displacement of material, in the wake of the compressive wave [95]. Such a tensile state leads to the nucleation of numerous oriented micro-cracks (normal to the tensile loading direction) on the defects present in the material, as shown on transparent ceramics in Figure 2.6.

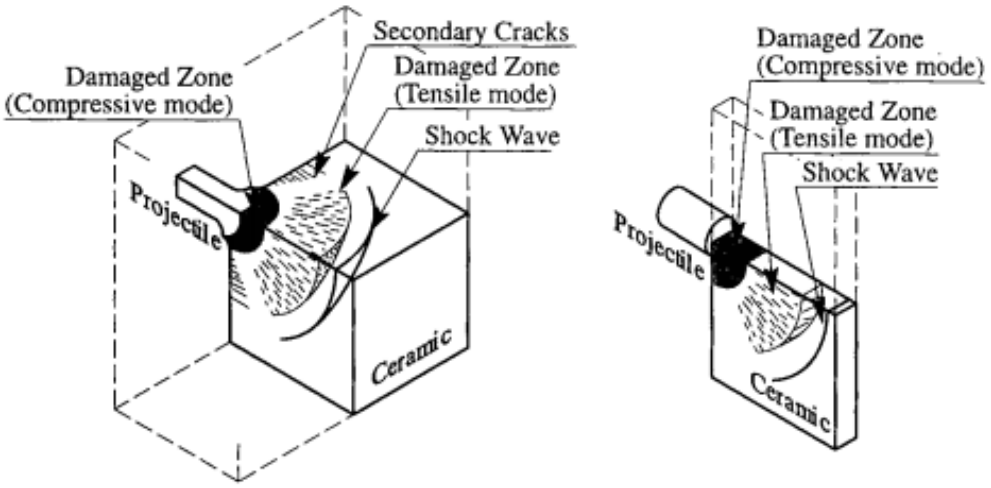

Figure 2.5. Representation of the damage during a ballistic impact test (a) and and Edge-On-Impact test (b) [96]

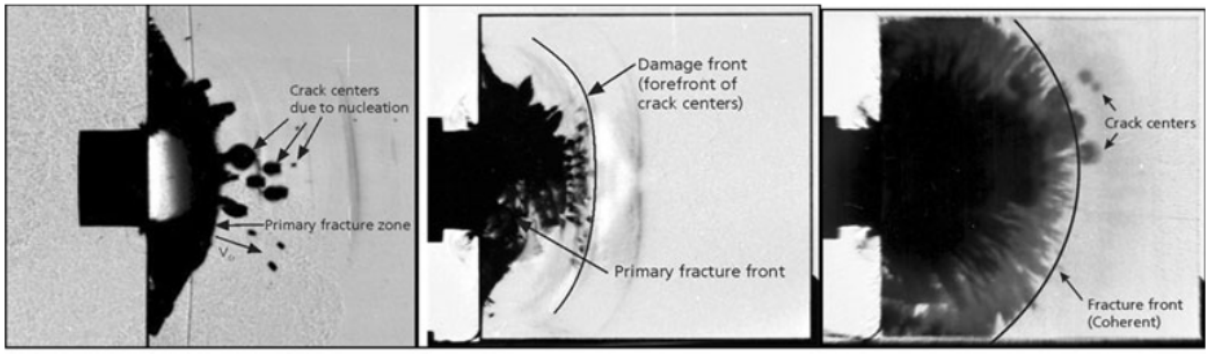

Figure 2.6. Damage patterns obtained using the regular transmitted light technique without crossed polarizers. Typical damage pattern in (a) float glass at $\sim$ 200 m/s, (b) Starphire glass at $\sim$ 400 m/s and (c) AlON at $\sim$ 400 m/s. Visible nucleation of cracks ahead of the damage front, probably from bulk defects [99]

The identification of sites for cracks nucleation is very limited for opaque specimens, compared to transparent materials. The reason is that defects are mainly in the bulk material, and finding crack origins from fragments post-mortem analysis is very delicate. To overcome these limitations, Parab et al. showed the potential of using high-speed synchrotron X-ray imaging (recording speed of 75 frames per second) to observe in situ fracture processes in a reactive powder concrete (Cor-Tuf), a high-strength concrete (HSC) and Indiana limestone [100]. They used a modified configuration of the Kolsky bar apparatus to generate dynamic cracks. Recently, Forquin et al. managed to reproduce this type of in-situ observation via ultra-high speed X-ray imaging with synchrotron radiation. Thus, they investigated the dynamic fragmentation process in ceramics when impacted by a steel cylindrical projectile (recording speed of about 1 Mfps) [101].

Post-mortem analysis of the fragmentation properties

The most common way to obtain quantitative information on the fragmentation intensity is to perform sieve or image analysis on the recovered fragments [102] [103]. Some authors focused on identifying the defect populations involved in dynamic fracture from fractography. For instance, Hohan et al. analysed the fragmentation generated by the impact of a spherical projectile (mainly made of tungsten carbide) at various velocities (275-930 m/s) on a hot-pressed boron carbide ballistic ceramic [104]. The ceramic contained large carbonaceous disks (up to about 40 μm), oriented normally with respect to the impact direction. From fractography and image analysis, they suggested a correlation between the size of the fragments recovered from high speed impacts and the spacing between carbon defects, as shown in Figure 2.7. They introduced the idea of a *microstructural-controlled* fragmentation and formulated the possibility of adapting the defect spacing to control the fragments size to, in the end, improve their ability to erode the projectile (further discussed in the next section).

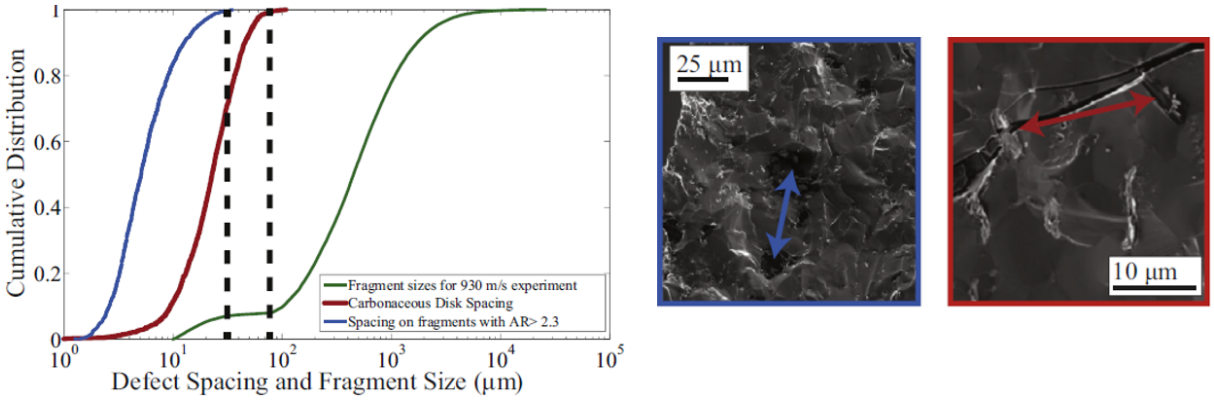

Figure 2.7. Cumulative distribution of fragments compared to the spacing distribution between the graphitic disks in the elongated ballistic fragments (blue SEM image) and the spacing in the in-plane direction (red SEM image). Possible correlation between the inflexion point at about 30 μm for the fragment size distribution and the defect spacing [104]

Denoual managed to perform EOI tests in a metallic casing to keep the fragments close to their initial position [105]. An infiltration of the fragmented tile was performed with a fluid transparent resin to recover a post-mortem sample, which was polished for further inspection of surface fragmentation patterns. The different steps of this sarcophagus configuration and post-processing are illustrated in Figure 2.8. By using such a technique, Forquin et al. compared the damage patterns of a porous R-SiC ceramic, presenting about 17 % of porosity, and the same ceramic for which the porosity was almost fully filled by the infiltration of an aluminum metal R-SiC-Al (about 2.5 % of residual porosity) [106]. They found that the presence of the metal phase changes the Weibull parameters of the material (higher average bending strength) and therefore consequently reduces the number of cracks induced by an EOI impact (200 m/s). In another study, Forquin et al. used EOI tests (cylindrical projectile, 175 m/s) to compare the effect of the manufacturing process of SiC ceramics on their fragmentation properties [76]. Even though the damage chronology was found to be relatively similar between the different SiC materials, they observed a more intense fragmentation for SiC ceramics resulting from liquid phase sintering compared to solid state sintering.

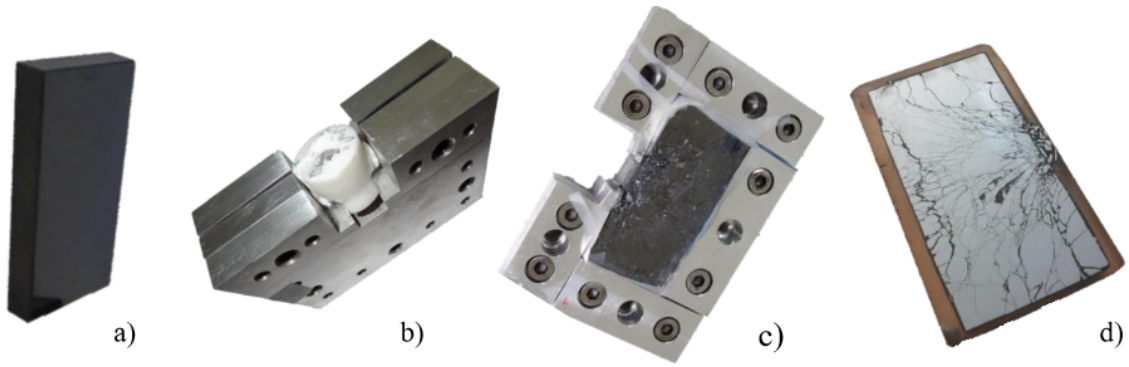

Figure 2.8. Successive steps of an EOI experiment performed in a sarcophagus configuration. a) Intact ceramic tile 60 x 60 x 8 mm^3. b) Fragmented ceramic in the metal casing. c) Most-mortem ceramic visible once the sarcophagus open. d) Damaged sample after resin infiltration and surface mirror-polishing [76]

Several authors suggested the use of X-ray tomography as a non-destructive technique to analyse the damage patterns induced in armour ceramics upon impact. However, only few studies provide proper quantitative information on the fragmentation [107] [19] [90]. Wells provided an overview of the possibilities offered by this non-invasive technique to diagnose the damage of armour systems, detect the projectile fragments and observe the composite backing delamination [107]. Forquin and Ando used X-ray micro-tomography applied on post-mortem specimens recovered from an EOI sarcophagus configuration. Tomography analyses allowed fragmentation patterns to be observed in the material bulk. Fragment size distribution could be obtained from a post-processing segmentation algorithm, applied to the 3D-reconstructed image [103]. The 3D-image of a post-mortem sample after fragments identification is presented in Figure 2.9 (a). They demonstrated the accuracy of their approach by comparing the fragment size distribution obtained from tomography post-processing and sieve analysis for two SiC materials. Results are shown in Figure 2.9 (b) for SiC ceramics made from solid-phase spark plasma sintering (SPS-S) and liquid-phase assisted spark plasma sintering (SPS-L). As mentioned before, the high repeatability illustrates the fact that the fragmentation behaviour of ceramic materials is deterministic at high strain rate. Moreover, these fragmentation tests bring quantitative results on fragmentation chronology and crack density (fragment size), which are indispensable to help the development and validation of existing models used in computer codes to simulate the impact performance of ceramic armour materials [108] [76] [109]. Nevertheless, these experiments do not provide any quantification of the tensile strength of the ceramic material, according to the strain rate.

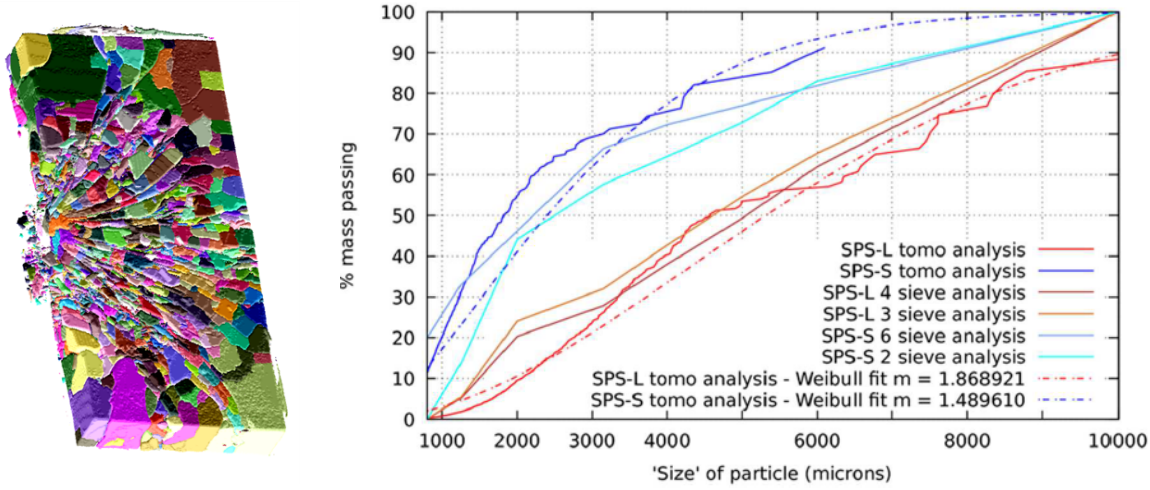

Figure 2.9. (a) 3D rendering of a fragmented ceramic, obtained from X-ray tomography. (b) Comparison of particle size distributions obtained from sieving [40] and tomography analysis [103] on SiC ceramics made from SPS-L and SPS-S manufacturing processes, impacted in an EOI configuration

2.2.2 Characterisation of the dynamic tensile strength

The damage evolution under dynamic loading is directly related to the nucleation of micro-cracks on the microstructural defects under tensile loading. Therefore, the inherent performance of a ceramic-based armour system relies in part on the ceramic tensile strength, which is about three to fifteen times lower than its compressive resistance [9]. For this reason, it is necessary to properly evaluate the ceramic tensile strength and its sensitivity to the loading rate.

Limitations of the classical techniques

Several classical experimental techniques, such as the Brazilian test [110] [111] or the split Hopkinson (Kolsky) pressure bar (SHPB) [112] [113], can be used to determine the resistance of brittle materials having a relatively low dynamic spall strength (concrete, rock, ice, etc.). However, to draw any conclusions from SHPB experiments, the sample needs to be in a static equilibrium during the test. This means that the loading time (related to the strain rate) has to be well above the round-trip time of the one-dimensional wave in the specimen. Thus, the strain rate is limited by the equation [114]:

$$\frac{\epsilon_{failure}}{\dot{\epsilon}} >> \frac{2L}{C_{1D\ wave}} \tag{2.10}$$

Classical values for ceramic materials are about 10^{-3} for the tensile failure strain $\epsilon_{failure}$ (the ceramic tensile strength being about one thousandth of their Young's modulus) [115] and 8500-14000 m/s for the wave speed $C_{1D\ wave}$, according to the material (alumina - boron carbide, Table 1.1). Therefore, considering five round-trips of the wave in the specimen of length L (about 20-30 mm) [114], to prevent any wave dispersion, the use of the Hopkinson pressure bar technique for ceramic tensile characterisation would be limited to very low strain rates of about 30-70 s^{-1}, according to the material. Above this threshold, the specimen is in an unbalanced state, leading to possible misinterpretation of the experimental data. Moreover, this technique hardly allows reaching an homogeneous stress in the cylindrical specimen due to the influence of lateral edges, as the loading time is relatively long (about 20-30 μs) with respect to the small size of the sample.

Plate impact technique for spalling

A more suitable technique to investigate the tensile behaviour of ceramic materials at higher strain rate is the plate-impact experiment. The planar impact is most commonly used to evaluate the dynamic compressive strength of ceramics. To be used for tensile characterisation, this technique needs to be performed at relatively low impact velocities and without any window material at the rear face of the target, to prevent any compression-induced damage to interfere with the tensile response of the material [116]. The flyer plate is placed in a sabot during the launching and generates a shock loading upon impact with the studied specimen. Such an impact configuration is illustrated in Figure 2.10 (a).

A Lagrangian x-t diagram is presented in Figure 2.10 (b) to illustrate the waves transfer and interaction in the flyer and target upon impact. The X-axis indicates position, with zero defined as the interface between the flyer and target. The Y-axis indicates time, with zero defined at the moment of impact between the flyer and target. Two compression stress-waves are generated at the contact between the flyer-plate and the target. They propagate in opposite directions through both materials at their longitudinal wave speeds (C_f and C_t) and are reflected at the free surfaces. The overlap of the corresponding release waves brings the material into a state of tensile stress. If the tensile stress exceeds a critical strength value for the material, the sample undergoes a tensile damage. Moreover, if the loading duration is long enough, cracks propagate in the material and coalesce, thus leading to the spall fracturing [117]. The duration of the compressive pulse and the location of the spall plane can be adjusted by playing on the flyer material properties and the relative thicknesses of the flyer plate and target (L_f and L_t). Ideally the failure should happen in the mid-plane of the tested ceramic tile.

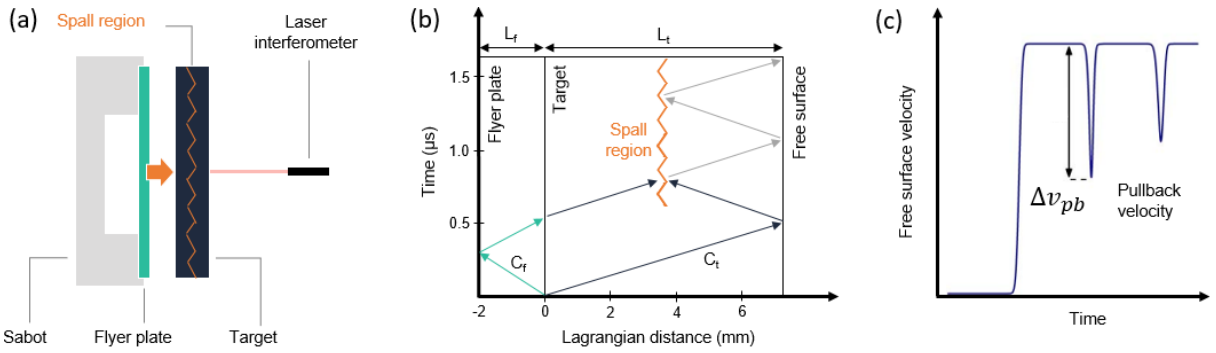

Figure 2.10. (a) Scheme of the plate-impact technique for spalling. (b) Lagrangian diagram x-t of a spalling test via plate-impact. (c) Classical velocity profile of the target free-surface. The pullback velocity is determined from the velocity rebound

The spall failure of the sample can be detected by a VISAR probe pointing at the ceramic backface during the test. The classical plot for the velocity history of the target free-surface (further detailed in section 5.2.2) is shown in Figure 2.10 (c). The first rebound on the velocity profile indicates the spalling failure in the ceramic target. This velocity rebound is related to the wave reflection on the spall plane (new free surface) toward the ceramic rear face. The difference between the maximum velocity and the minimum rebound velocity, called pullback velocity Δv_{pb}, is used to calculate the material spall strength, assuming a linear elastic behaviour for the material before reaching the tensile ultimate strength [118]:

$$\sigma_{spall} = \frac{1}{2}\rho_t C_t \Delta v_{pb} \tag{2.11}$$

where $\rho_t C_t$ is the acoustic impedance of the ceramic, defined as the product of the target density and longitudinal wave speed.

The spall strength of SiC materials, sintered and hot pressed, is found to increase with the impact loading, up to a threshold stress-loading, above which the spall strength decreases. For instance, Bartkowshi et al. conducted spalling experiments, via planar plate-impact, on a sintered SiC material and found that the spall strength increases with the impact velocity for an impact stress below 3.7 GPa, and decreases above this threshold value [119]. Martin performed the same type of experiments on the dense pressureless sintering SiC studied in the present work, named Hexoloy SA, at stress levels below and above the HEL of 13.8 GPa [32]. He observed the same trend for the spall strength evolution according to the impact stress, with a stress threshold around 5-7 GPa. Some authors explain such a behaviour by a prior damage generated under compression loading, due to plastic deformation, resulting in a lower resistance of the material under tensile loading [120]. Grady does not relate this phenomenon to a prior damage under compression, but under decompression. Therefore, responsible for a reverse shear yield before reaching the tensile axial stress, the material decompression would be at the origin of a material loss of cohesion above a certain impact level [121].

As presented in section 2.1.3, brittle materials present a strain-rate hardening behaviour. Based on thermodynamic energy conditions, Grady gave a criterion to traduce the spall strength increase of brittle solids with strain rate $\dot{\epsilon}$ [122] [121]:

$$\sigma_{spall} = (3\rho C_0 K_c^2 \dot{\epsilon})^{\frac{1}{3}} \tag{2.12}$$

where ρ is the density, K_c the critical intensity factor and C_0 the bulk velocity ($C_0 = \sqrt{B_0/\rho}$ with B_0 the bulk modulus). The material is considered to follow the relation given in equation (2.12) above a certain strain rate threshold and the Griffith criterion below this value. However, in most of the spalling experimental studies, no information is given on the strain rate level reached in the spall plane [119]. The main reason for this is the difficulty of imposing the strain rate during a plate-impact experiment, as it requires to smooth the loading pulse [123]. A solution to overcome this experimental complexity is to

design a test in which the stain rate is tailored and maintained constant in the specimen during its spall failure. However, during a planar impact experiment, the shock loading (rectangular compressive pulse) induces a discontinuity of pressure, which leads to extreme and uncontrolled strain rate levels in the spall region, in the order of 10^5-10^7 s^{-1} [124]. To avoid this issue, the specimen needs to be slowly loaded by a ramp pulse [123]. To do this, the planar impact experimental method can be adapted to achieve a constant strain rate loading as well as uniform tensile stress state in the spall area. Few studies already investigated shockless plate-impact by using graded-density flyer plates, with a mixed composition (Al-Cu, Mg-Cu for instance) manufactured via 3D printing, tape casting or plasma spray [125] [126]. But this solution presents the limitations of manufacturing cost and quality (uniformity, stability, reproducibility of the complex layered microstructure) and a difficult design via numerical simulations. Moreover, in most of the cases, even if a linearly ramping loading is achieved, the initial pressure shock is not avoided [127]. Early-stage studies have been playing on the flyer surface shape to transfer a smoothed tailored ramp to the ceramic target upon plate-impact [128], as shown in Figure 2.11. The works found in the literature always include a complex flyer-geometry and expensive manufacturing processes and are not performed on ceramic materials.

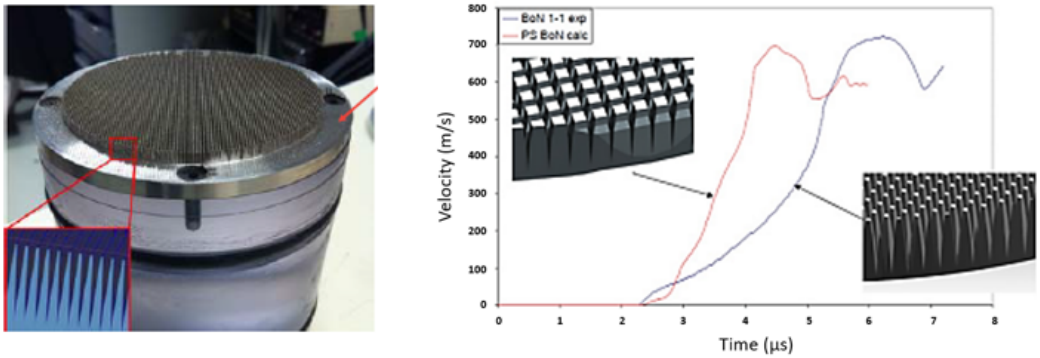

Figure 2.11. Steel flyer-plate made from additive manufacturing consisting in an array of tapered spikes. Resulting tailored velocity profiles for impacts at about 900 m/s on tantalum targets [128]

GEPI testing technique for shockless spalling

An experimental technique, which allows the specimen to be slowly loaded by a ramp pulse and thus provide a controlled strain rate at failure, is the high-pulsed power generator (GEPI) equipment [129]. The installation based at CEA Gramat is presented in Figure 2.12 (a). As mentioned before, this type of experiment was used in recent studies to perform spall tests on alumina [86] [130] and SiC ceramics [85] at controlled strain rates, therefore providing a valuable insight of their dynamic tensile behaviour. The GEPI technique consists in transferring an intense pulsed current to a loop-shaped conductive electrode to generate a tailored ramp pressure via the Laplace effect. This pressure is transferred to the ceramic sample put in between two electrodes. A schematic illustrates the configuration in Figure 2.12 (b). Therefore, rising time of about 0.2-0.5 μs can be reached and the strain rates levels in the specimen are in the order of 10^4-10^5 s^{-1}. Tailored velocity profiles of the ceramic free-surface are presented in Figure 2.12 (c) for three different strain rates (7500, 17000 and 25000 s^{-1}). This technique presents the interest of possible recovering of post-mortem samples for further studies, such as fractography, whereas in plate-impact experiments, the specimen is fully pulverized if no specific adaptations are made. Nevertheless, this technique presents the main drawbacks of having a rising time limited by the electrodes size (the larger the electrode, the lower the magnetic pressure), requiring an adaptation of the set up to reach different loading rates and being relatively expensive. Finally, this literature review showed a lack of experimental techniques, based on the plate impact technique, providing a reliable measurement of ceramic tensile strength at controlled loading rate. In Chapter 5, this issue is addressed and a new experimental technique, based on an adaptation of the classical plate-impact test, is developed to evaluate the strain rate sensitivity of ceramic spall strength.

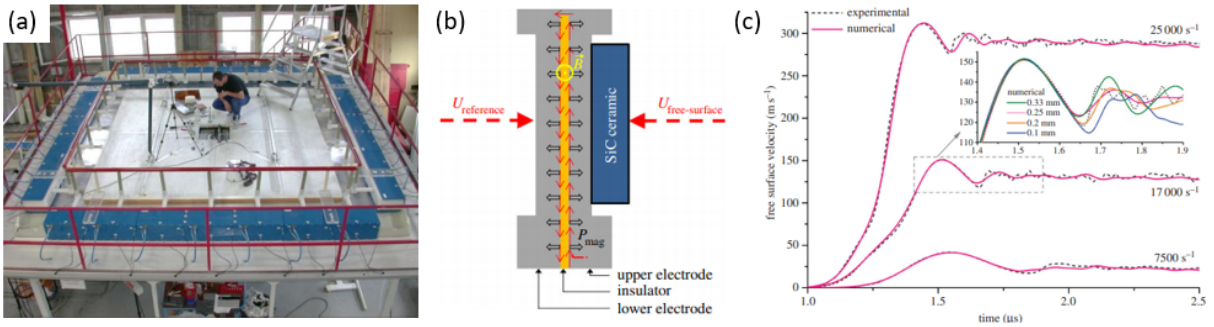

Figure 2.12. (a) GEPI installation based at CEA Gramat [131]. (b) Overview of the GEPI experimental configuration for spalling experiments [85]. (c) Velocity profiles of SiC samples during spall tests at 7500, 17000 and 25000 s^{-1} via the GEPI technique, showing smooth rising times of about 0.2-0.5 μs [85]

2.2.3 Characterisation of the residual strength of the pre-fragmented ceramic

The residual strength of failed material is of paramount importance in the ceramic ballistic response [132]. Indeed, the behaviour of the fragmented ceramic beneath the projectile is related to the armour ability to limit the projectile penetration (longest phase of the ballistic event of about $\sim$ 50 μs) [12]. However, it is complex to evaluate the behaviour of the comminuted ceramic as it is correlated to its pre-damage state, which is itself linked to the ceramic microstructure, the involved compressive and fragmentation failure mechanisms, loading conditions and the full system configuration (radial confinement, covering sheet [133]). The comminuted zone is supposed to be formed through a series of dynamic cracking events, however, the process of ceramic shattering under a high pressure at high loading rates is still not well understood.

Experimental tests to evaluate the behaviour of the pre-damaged ceramics

The ceramic intense fragmentation beneath the projectile results from compressive and tensile damages, prior the projectile penetration. The first way to investigate the residual strength of the comminuted ceramic consists in assuming it can be assimilated to a ceramic powder. Under this assumption, several authors studied the flow behaviour of ceramic powder under static (friction coefficient), dynamic or ballistic solicitations. From the constitutive laws characterising the granular flow properties, the behaviour of the fragmented media can be incorporated to the post-fragmentation events. Thus, Cil et al. (2019) found that taking into account such a flow behaviour is key, as it influences the erosion of the projectile [134]. Appleby-Thomas et al. (2017) studied the ballistic response of powder compacts to a 7.62 x 51 mm AP FFV projectiles in DOP configuration. They compared the residual strength of cold-pressed alumina particles of different shapes (spherical and angular) and demonstrated that the particles morphology had a strong influence on the nature of compact collapse [135]. So, the shape of the fragments plays a role on the residual strength of the pre-fragmented ceramic.

Considering ceramic powders, with shapes close to spherical, often leads to an under-estimation of the ability of the media to limit the penetration process. For example, Horsfall et al. (2010) compared the ballistic performance of comminuted Al_20_3 ceramic (shattered by the shock wave from an explosive loading) and pressed Al_20_3 powder (spherical particles of 50-150 μm, shaping-pressure 40 MPa, 30 % of residual porosity). A confinement rig was used during the DOP tests with a 7.62 x 51 mm AP FFV ammunition [136]. Tests were performed with different tiles thicknesses to obtain similar areal densities between samples. They obtained a ballistic performance drop of approximately 30% for the pre-fragmented ceramic and 40% for the pressed powder, compared to the intact ceramic tile. Such a difference was attributed to the difference in terms of initial particle morphologies, which were supposed

to dominate the inter-particular friction and flow resistance. Nanda et al. (2011) performed the same type of DOP tests (same projectile and radial confinement) on alumina and SiC ceramics pre-damaged from an explosive loading [137]. From the similar ballistic performance obtained between pre-damaged alumina and SiC liquid phase sintering ceramics, presenting similar initial fragment size distributions, they concluded that the controlling parameter for enhanced ballistic performance of a damaged ceramic is rather the fragment morphology than the intact material strength.

Toward a modelling of the behaviour of the fragmented ceramic

Anderson et al. (2009) studied the effect of the degree of damage on the residual strength of SiC-N ceramics against the ballistic penetration of high-speed long gold rods (1-3 km/s). They compared damaged levels induced by a thermal shock with and without additional mechanical loading cycles, and compared both results to compacted SiC powder [138]. As underlined by the authors, the pre-damage state is only supposed to be comparable to a comminuted ceramic, with a Mescall zone, but with no demonstration. They used the Drucker-Prager model to simulate the constitutive response of the comminuted ceramic [139]. Numerical simulations were used to determine the three constitutive constants of the model to best fit the experimental ballistic response of the failed material. However, they found that more than one single set of parameters were suitable, possibly leading to a limitation of this model description of the comminuted media. They opened the discussion toward the use of a Mohr-Coulomb plasticity model.

Forquin developed a *Tandem impact* configuration to evaluate the residual strength of a ceramic with a pre-damage closer to ballistic conditions [140]. The first step, consists in generating an intense fragmentation in the ceramic via a *Normal impact*. Zinszner et al. used numerical simulations to first develop this configuration for the dynamic impact of a cylindrical steel projectile at about 175 m/s on a SiC ceramic target (Hexoloy SA®) [141]. A ductile aluminum backing (60 x 60 x 6 mm^3) was placed behind the ceramic target (60 x 60 x 8 mm^3) to provide a configuration close to a ballistic impact and avoid debris ejection. A thin layer of steel (same material properties as the projectile) was used as a frontal confinement to avoid the fragments ejection and ensure a homogeneous fragmentation of the ceramic along the loading axis. This *sandwich configuration* is confined in a metallic casing having circular openings: one in its front centre to allow the projectile impact and a second one in its rear centre for the aluminum backing to deform upon impact. An initial gap of 0.1 mm was imposed between the ceramic and the aluminium backing to ensure an impedance discontinuity and increase the damage in the ceramic tile [141]. To do so, small pieces of steel sheet 0.1 mm were placed between the ceramic and the aluminum backing. The configuration is presented in Figure 2.13 (a). To evaluate the residual strength of the pre-damaged ceramic, a second impact was performed with a perforating projectile (conical nose) on the fragmented media resulting from the Normal impact. A schematic in Figure 2.13 (b) shows this second Tandem impact on the pre-fragmented ceramic, recovered from the Normal impact test. They used high-speed imaging to record the Tandem impact (inter-frame time of 8 μs). Some images of the interaction between the pre-damaged ceramic and the perforating projectile are presented in Figure 2.13 (c), and show the ejection of the fragments located close to the projectile nose upon impact. In addition, the interaction (contact force) between the projectile and the fragmented ceramic was captured from the velocity profile of the backing backface, recorded via laser interferometry. This experimental measurement can be used to calibrate constitutive models, such as the Drucker–Prager [139], Rajendran-Grove [142] or Johnson-Holmquist [143] models, via inverse approach to reach a description of the dynamic behaviour of the fragmented ceramic [93] [144].

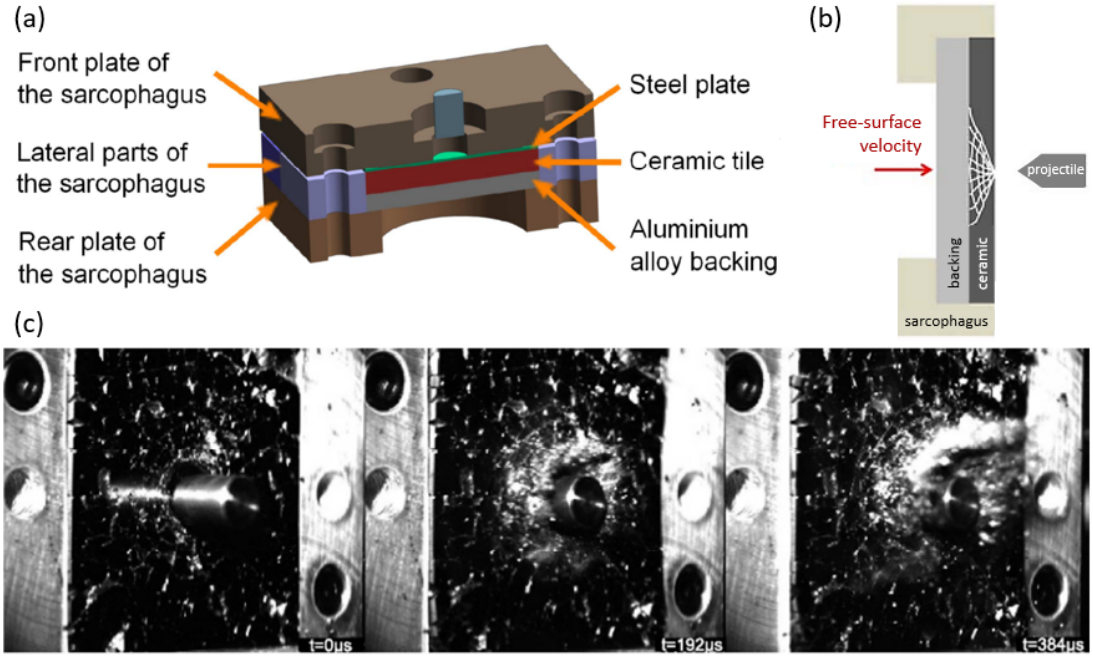

Figure 2.13. (a) Sarcophagus configuration used during the Normal impact, with a steel front plate, a ceramic tile and an aluminium backing [93]. (b) Schematic of the target during the Tandem impact, illustration adapted from [93]. (c) High-speed images of the second impact on the pre-damaged ceramic with a perforating projectile (conic-nose) at an impact speed of 175 m/s [93]

2.3 Existing models representative of the fragmentation behaviour of ceramic materials

Computational models are of paramount importance to consequently decrease the time and cost for armour material development. To design materials for improved performance, it is necessary to properly capture the failure mechanisms induced upon dynamic impact. But the combination of the high complexity of ceramic behaviour (various failure modes and strain rate sensitivity) and the several damage mechanisms involved in a ballistic event (compression, fragmentation, shearing, granular flow of the fragmented media, plasticity, phases transformation, etc.) make this modelling work not a trivial issue. As mentioned before, during a ballistic impact, the main loading conditions underwent by the ceramic target correspond to confined compression (triaxial compression) and dynamic traction.

The Johnson–Holmquist damage model (JH-2) is the most widely used model to simulate the behaviour of ceramic armour materials over a large range of strain rates [143]. This model describes the behaviour of brittle materials under confinement and takes into account the strength increase when the material is subject to hydrostatic pressure, and its decrease once the material is damaged. One specificity of the JH-2 model is the incorporation of a progressive damage evolution with an increased deformation, traducing the effect of the growth of microcracks. However, no physically-based principles and no information on the defect distribution are included in the phenomenology of this continuum damage model, the material is considered homogeneous. Moreover, this model does not describe damage induced anisotropy. Another limitation is that the damage under tensile loading is not considered, so this model cannot be used to study the fragmentation process of ceramics upon impact. Finally, no sensitivity of the tensile strength to the loading rate is considered, even though is has been experimentally demonstrated to be a key parameter [85].

In this section, the focus is on the tensile-driven fragmentation models. This section does not have the pretension of giving an exhaustive view of the modelling work available on ceramic dynamic failure but presents the main types of models, by introducing some key works. During the last decades, the scientific

community has developed a large range of models based on theoretical, energetic or phenomenological (micro-mechanisms) approaches.

2.3.1 Energy balanced principles and geometric statistics-based models

Due to the extremely high-velocities involved during an impact event, the very first models developed for the behaviour of brittle materials focused on the final stage of the fragmentation process, for which experimental data could provide a validation. These models, called *end-state* models, were based on energy balanced principles or geometrical statistics. In such models, the main concern is on the accurate prediction of the average fragment size and fragment size distribution.

Models based on energy-balance arguments

Grady (1982) proposed a fragmentation model based on energy balanced arguments [23]. By assuming that the kinetic energy is fully converted into fracture energy, he gave predictions on the fragments average size at high strain rate. Later, Glenn and Chudnovsky (1986) added the contribution of elastic potential energy to improve the model on a larger range of strain rates (dominant for lower strain rate values) [24]. Comparisons to numerical simulation and experiments showed that energy-based models overestimate the fragmentation intensity (asymptotic distribution [145]). This is justified by the time-dependency of the fragmentation process and the implication of other mechanisms in the energy dissipation process than the creation of fractured surfaces. Even though these pioneer models rely on some strong simplifications, because the material flaw distribution and wave interactions are not included, they still constitute a reference framework for energy-based fracture models. Very recently, Dascalu (2020) used the average fragment size expression given by the Grady-Glenn-Chudnovsky model to determine a characteristic microstructural length (depending on local strain rate and the material parameters, such as density, Young's modulus and fracture energy) to be implemented in a damage law of a two-scale model [146]. In this work, he managed to account for the strain-rate sensitivity of the tensile strength for brittle concrete and alumina ceramics. The main limitation of this approach is that the fragment size and stress-strain laws used to compute the damage problem solution require calibration from quasi-static and low-dynamic experimental tests. Moreover, a single fragment-size expression (locally periodic distribution of microcracks) is considered, thus limiting the scope of such a modelling.

From geometric statistics-based models to micro-mechanical models

Mott and Linfoot (1943) introduced the theoretical modelling of fragmentation. They studied the instantaneous partitioning of two and three-dimensional bodies into random geometric shapes [147]. Initially based on statistical fragmentation, Mott's work evolved towards more physically-based mechanisms considering the activation of fracture sites and the propagation of stress released waves in a rapidly expanding ring (1D) or shell (2D) [26]. An illustration of Mott's approach [148] is presented in Figure 2.14. This work provided the foundation of a large number of fragmentation analyses. From the apparent need to consider process-driven failure mechanisms, Shenon and Kim (2003) incorporated key features of micro-mechanics. They considered the combination of elastic wave propagation and a cohesive failure process (intrinsic time scale) for the fragmentation modelling of a 1D-bar of a brittle material [149]. Based on this approach but considering a ceramic ring, Zhou et al. (2005) analysed the effect of loading conditions [150], strain rate and internal defects distribution [151] on the resulting average fragment size and fragment size distribution. This work is partially illustrated in Figure 2.15, where the influence of the spacing between uniform defects (a) on the average fragment size (b) is presented. Levy and Molinari (2010) enriched this approach by considering an heterogeneous ceramic ring [145]. They studied the role of initial defects on average fragment size as a function of strain rate, by considering various distributions of defects (Gauss, Weibull and Uniform, with different parameters). Based on Hild and al (2003) work [58], they introduced an interaction factor between micro-crack sites, which is function of the number of defects and the loading rate. This communication parameter traduces the need to account for the stress

waves propagation and interaction subsequent to failure, because they can prevent damage nucleation at other defects. The number of large defects and the rate required to initiate cracks were found to consequently affect the stress release waves, and therefore the average fragment size [145]. Finally, both geometric statistics-based models and energy balanced principles converged toward a reduction of the fragment size with an increase of the loading rate.

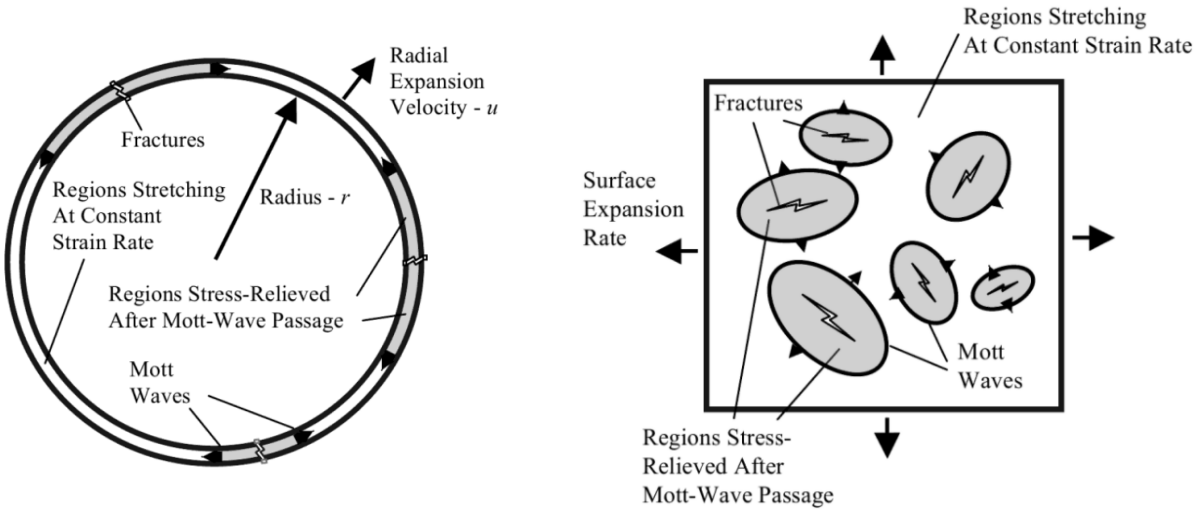

Figure 2.14. Illustrations from Grady [148] of the activation of fracture sites and the subsequent propagation of stress release in the dynamic expansion of (a) the Mott ring (1D, circumferential) and (b) biaxially expanding sheet (2D)

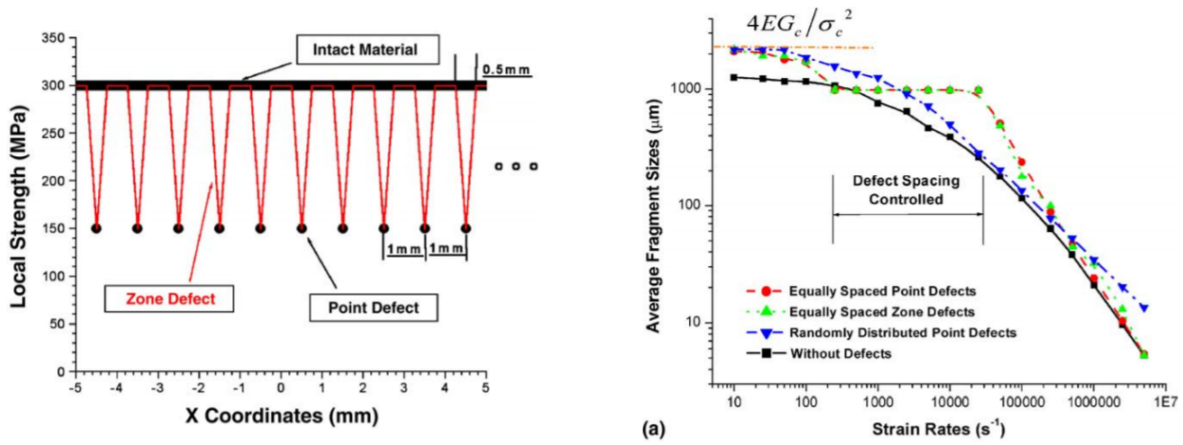

Figure 2.15. (a) Local strength distribution along the bar with no defects, equally-spaced point defects, and equally-spaced zone defects. (b) Average fragment size vs strain rate obtained from fragmentation simulations [151]

Advantages of these types of models is that, by considering highly simplified geometries (bar, ring, shell), the prohibitive calculation cost related to the multiple crack fractures is limited, while providing some reliable general tendencies on the fragmentation properties. However, such simplifications also limit their accuracy and scope of validity. Initially based on few physics-based parameters (interfacial strength, fracture energy and crack opening), this type of modelling was progressively enriched by process-driven mechanisms such as stress wave propagation and interaction between damaged sites. The integration of several initial defect distributions demonstrated the importance of such parameters on the rate-dependant fragmentation process [145]. Nevertheless, the role played by microstructural features is often neglected.

2.3.2 Denoual-Forquin-Hild (DFH) micro-mechanical damage model

Micro-mechanical models consists in incorporating physical mechanisms observed during failure at the micro-scale (crack nucleation, propagation, interaction, etc.) to predict the macro-scale response of the material. The main focus is to make connections between the failure mechanisms triggered under external loads and the effective strength of the material (not only fragmentation properties). The implementation of fundamental physics in such a modelling approach was found to provide more representative outcomes [73]. Most micro-mechanical models available in the literature focus on the uniaxial compressive failure through the so-called *sliding* or *wing crack* models. However, such a loading (if it occurs) is not the predominating cause of failure during an impact. The Denoual-Forquin-Hild (DFH) damage model focuses on the micro-mechanisms causing failure in brittle materials under dynamic tensile loading [27] [58] [77].

Phenomenology of crack initiation on critical defects and crack propagation

Under a slow loading rate, once the tensile stress exceeds the critical stress of the weakest defect, it causes the failure of the whole loaded volume. The consequence of this dominant crack growth is that other potential sites for crack nucleation are unloaded, thus leading to a single fragmentation. As defects are discrete and randomly distributed in ceramic materials, the failure probability given by Weibull and introduced in section 2.1.2 equation (2.3) [51], is considered in the DFH model:

$$P_f = 1 - \exp(-\lambda_{flaw} Z) \tag{2.13}$$

as a reminder, λ_{flaw} is the density of critical defects, for which the microscopic stress overcomes their stress of activation. In the *original* DFH model, the density of critical defects is supposed to be the two parameters expression, given in the Weibull model [51]:

$$\lambda^W_{flaw}(\sigma) = \lambda_0 \left(\frac{\sigma}{\sigma_0} \right)^m \tag{2.14}$$

therefore, the maximum principal stress is supposed to drive the fragmentation process.

In the case of high rate of deformations, the hypothesis of the weakest flaw is not applicable anymore at the whole volume scale and the local-weakest link hypothesis applies [77]. Indeed, as the information travels at a finite velocity, local stress keeps increasing outside the obscuration zone, where unload is occurring. Therefore, multiple cracks can be triggered simultaneously in the loaded volume. It can be assumed that the stress-release waves are controlled by the crack propagation. Several authors showed that once the crack length reaches a value significantly higher than its initial size, the velocity of crack propagation is limited by the material fracture toughness (in mode I) [152]. So, the crack velocity can be considered constant and proportional to the longitudinal wave speed of the material, C:

$$v_{crack} = kC \tag{2.15}$$

Based on an energetic approach, Broek (1982) found that the ratio coefficient k, traducing the crack velocity attenuation, can be taken equal to 0.38 [153]. Several experimental studies showed that this ratio can be relatively higher for ceramic materials. For example, Strassburger et al. used edge-on-impact tests to experimentally evaluate the crack velocity of SiC materials. They found that it reaches a terminal crack velocity of about $0.5C_r$, with C_r the Rayleigh wave speed [94]. Duplan et al. managed to propagate a single crack under dynamic conditions thanks to a *Rockspall* testing technique and measured a crack tip velocity from the analysis of displacement fields [154]. From the testing of an alumina and a Forceram® ceramics, they confirmed that the crack velocity of ceramic materials is expected to be slightly greater than $0.38C$. However, this value of 0.38 remains a good first approximation that will be kept for the present work.

Thus, the dynamic fragmentation process in brittle materials is first based on the initiation of multiple cracks, from defaults randomly distributed in the specimen, and then on the propagation of these cracks perpendicularly to the loading direction at a constant velocity. As a first approximation,

defects triggered under a dynamic loading can be considered the same as defects initiated under quasi-static loading, defined by the Weibull flaw density given in equation (2.14) [58] [77]. The modelling work, presented in Chapter 6, aims at questioning the relevance of this assumption.

Cracks interaction and obscuration mechanism

The propagation of a crack from a critical defect induces a local release of stress in the volume surrounding the crack rim. This local stress relaxation prevents any neighbour critical defects from being activated [78]. To describe this mechanism, Denoual introduced the concept of obscuration volume [155]. The size of this volume is supposed to be controlled by the triggered crack. Therefore, as the stress keeps increasing at a constant rate in the loaded volume, the crack keeps propagating and the obscuration volume keeps spreading by homothety. In order to model this fragmentation behaviour, the growth velocity of the obscuration zone Z_0 can be supposed constant and proportional to the crack velocity. Based on this phenomenological approach, the fragmentation process can be illustrated by the schematic in Figure 2.16. Defects (red dots) are randomly distributed along the spatial scale (horizontal axis) and their stress of activation is observed in the time/stress scale (vertical axis), for a stress increasing linearly with time. As the first crack is triggered on the most critical defect (lowest stress of activation), an obscuration zone centered on the defect starts to grow (represented by a conical domain). No defect situated in the obscuration cone can be activated. Therefore, the condition for a point M to be in an undamaged zone (not obscurated) at a time T corresponds to the probability of having no prior activation of surrounding defects (in its horizon represented by a dash line). So, the time-evolution of an obscured volume, growing from the initiation of a crack at time t, can be expressed as:

$$Z_0(T-t) = S(kC(T-t))^n \tag{2.16}$$

where T is the current time, n corresponds to the considered spatial dimension (n=3 for 3D) and S a shape parameter for the obscuration zone, estimated at 3.74 for an almost spherical zone in 3D dimension ($S = 4\pi/3$ if considered spherical). Finally, the fragmentation process of brittle materials can be described as a competition between the growth of obscuration volumes around triggered cracks and the nucleation of new cracks out of these damaged volumes. It can be noticed that a lower crack velocity (larger obscuration cones) or a higher stress rate (defects closer to each other in the vertical direction) are acting in favour of a higher number of nucleated cracks (higher crack density).

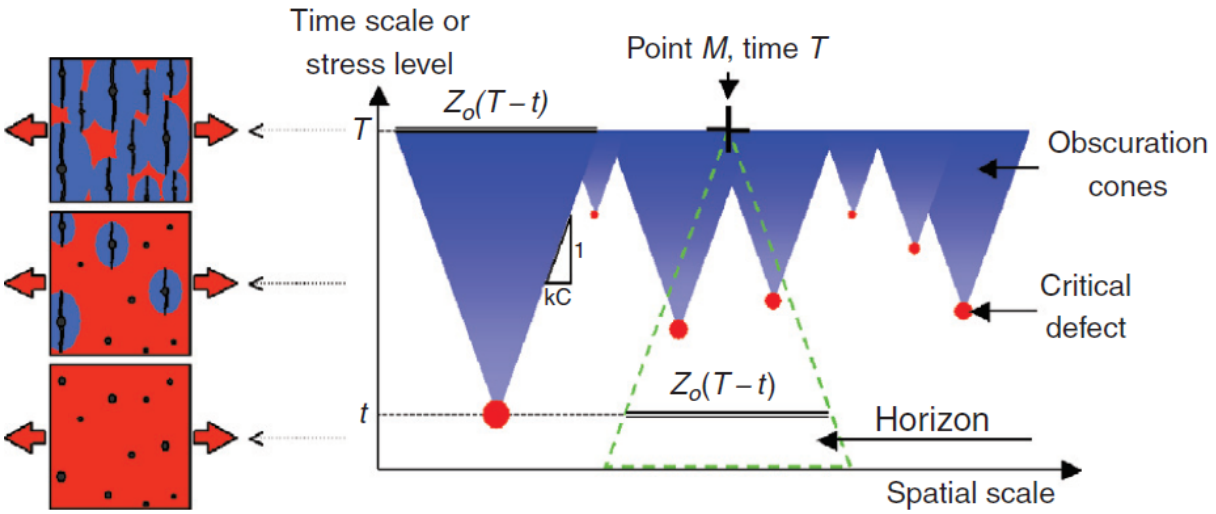

Figure 2.16. (a) Schematic of a discrete fragmentation process and obscuration phenomena [77]

Based on the obscuration mechanism, the weakest-flaw probabilistic theory becomes valid, but only at a local scale [77]. Thus, the failure probability of any point in the loaded volume corresponds to the probability that this point is not obscurated by the prior activation of a neighbouring fault in its horizon.

This probability of non-obscuration $P_{no}(M,T)$ of a point M at a time T can be expressed by the product of the elementary non-obscuration probabilities of all the spacio-temporal elementary sub-volumes $dVdt$ in its horizon [78]:

$$P_{no}(M,T) = \prod_{horizon\ (M,T)} P^i_{\not\in}(x,t) \tag{2.17}$$

where the elementary non-obscuration probabilities can be expressed by [156]:

$$P^i_{\not\in}(x,t) = exp\left(-\frac{\partial \lambda_{flaw}(x,t)}{\partial t} dZdt\right) \tag{2.18}$$

Locally, the density of critical defects and the applied stress are considered homogeneous (independent of the spatial variable x). In the specific case of a uniform stress field, Forquin and Hild gave the following expression for the obscuration probability [77]:

$$P_o(T) = 1 - \underbrace{exp\left(-Z\int_{t=0}^{t_z} \frac{d\lambda_t(t)}{dt}dt\right)}_{Single\ fragmentation} * \underbrace{exp\left(-\int_{t=t_z}^{T} \frac{d\lambda_{flaw}(\sigma(t))}{dt} Z_0(T-t)dt\right)}_{Multiple\ fragmentation} \tag{2.19}$$

where the density of critical defects $\lambda_{flaw}(\sigma(T))$ can be described by a Weibull power law λ^W_{flaw} or any continuous function. The horizon domain of a point (M, T) reaches the size Z of the whole structure at the time t_z. From this definition of t_z, the obscuration probability can be split into two terms, related to the single and multiple fragmentation process respectively. At low loading rate, t_z tends towards the current time T. In this case, a single fragmentation occurs and the obscuration probability, defined in equation (6.2), approaches the definition given by Weibull for the failure probability (equation (2.13)) [51]. At high loading rate, t_z is equal 0 (no interaction with the domain boundaries), so multiple cracks are triggered and the obscuration probability converges towards the damage evolution given by Denoual and Hild for a multiple fragmentation [78]. In the end, the microstructural parameters are introduced in the DFH model as an explicit law of critical defects λ_{flaw} and parameters related to cracks propagation (S, kC). The main advantage of incorporating sub-scale physics, accounting for microstructure and fragmentation micro-mechanisms, is that it can lead to general physical guidelines to improve the material from its behaviour predictions, for a reasonable computational cost. The main limitation of this micro-mechanical model is that, so far, it is restricted to homogeneous material, for which the internal meso-structure (grain size, phases, etc.) does not consequently influence the fragmentation process.

2.3.3 Meso-scale finite elements models

A possible solution to numerically simulate the behaviour of polycrystalline materials at the grain-scale consists in using meso-scale modelling via finite elements. To do so, a real ceramic microstructure can be digitized from micrographs [157] or X-ray Computed Tomography [158]. Such an approach provides a direct and accurate representation of material internal structures. Another way consists in numerically generating different randomly shaped microstructures from Voronoi tessellation [157]. Grains are often represented by polygonal morphologies and meshed using Delaunay triangulation. A representative volume element needs to be identified and can be periodically repeated. Schematics from Espinosa (2003), in Figure 2.17, present a 2D-digitalization (from micrographs) and mesh of a ceramic microstructure [157]. Interface elements were added along the grain facets. On the first hand, the damage initiation can be based on a stress failure criterion (independently of the interface elements). For instance, Camacho and Ortiz (1996) considered a critical value of tensile stress T_{max}, above which interfaces at grains boundaries open [159]. Once the microcrack initiated, additional nodes are introduced along the failed interface (microcrack propagation). The second way consists in implementing a fracture criterion in the cohesive interface elements [160].

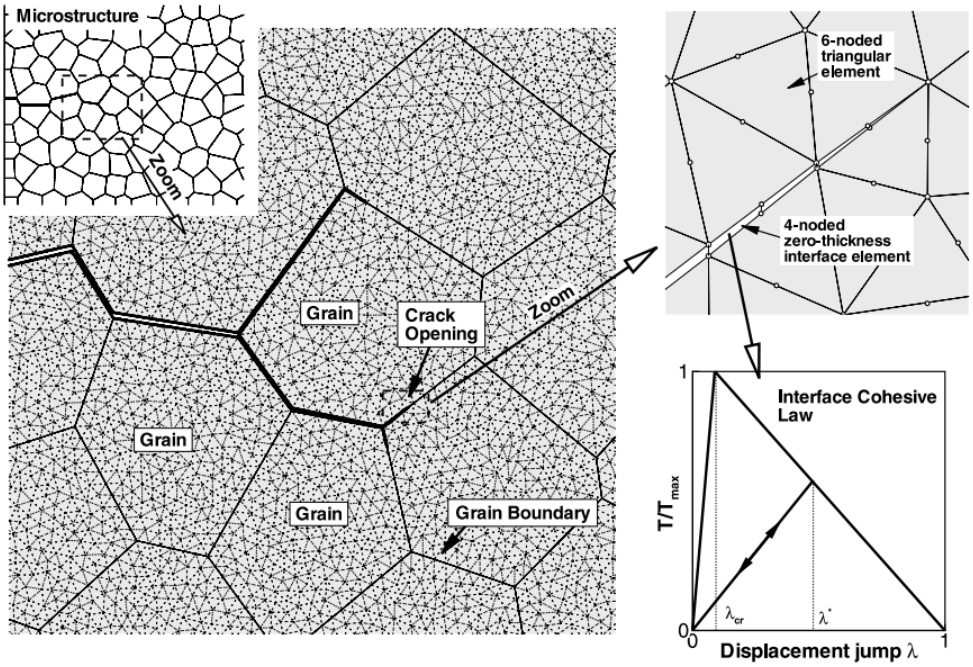

Figure 2.17. Schematics of 2D micro-cracking at grain boundaries using an irreversible interface cohesive law [157]. The tensile stress evolution at the interface is function of the crack opening

The main advantages of this type of model is that the grain size distribution, morphology, anisotropy, chemical phases, and presence and location of initial defects can be considered [157]. From these realistic microstructures, damage and failure mode can be investigated, according to the loading rate. Zavattieri et al. (2001) used 2D meso-scale simulations to evaluate the influence of the grains size, morphology and anisotropy on the cracking density under multi-axial dynamic loading [161]. They observed that introducing grain elastic anisotropy leads to an increase of microfractures. Moreover, the crack density, strongly sensitive to the grains morphology, was found to decrease with the grain size. In order to take into account the possible presence of second phases, impurities and defects, stochasticity can be introduced in the microfracture process [161].

Such a meso-scale modelling approach presents several limitations. First, it requires a proper choice of model parameters, because the cohesive failure law is phenomenological in nature. Parametric studies showed that the accuracy of the results highly rely on the implemented interface properties. For instance, Zavattieri et al. found that the fracture toughness and maximum traction T_{max} parameters strongly influence the damage intensity and patterns [161]. In addition, the main drawback of such meso-scale models is the calculation cost, especially at high loading rate because each individual crack is considered. Due to the prohibitive calculation time, such techniques are often restricted to 2D FE models. However, considering a 3-D case is expected to reduce the crack density because the coalescence of crack is stronger in a 2D calculation. Another limitation is the difficult experimental validation of this type of approach under dynamic loading. Nevertheless, meso-scale simulations are expected to provide valuable information on the complex fracture processes occurring in heterogeneous multi-phase media.

Conclusion of the chapter

This bibliographic chapter was organised in the same way as the rest of the manuscript in order to provide an overview of previous studies related to each key point addressed in the present work. Therefore, the focus was first given on the identification of critical defects causing failure and the behaviour sensitivity of ceramic materials. Then, several experimental techniques were presented to evaluate ceramic behaviours

and their damage modes under tensile dynamic loading. Finally, some modelling works were presented. This review highlighted the need for any model to achieve the correct balance between accurate representations of the physical phenomenon, while maintaining some degree of computational efficiency. The main points resulting from this bibliography are summarized as follows:

- Ceramics correspond to brittle materials. They are highly sensitive to the presence of pre-existing defects leading to a stochastic fracture at low loading rate. In this case, the failure strength is related to the most critical defect in the loaded volume (weakest-link theory). On the other hand, at high strain rate, the behaviour of brittle materials becomes deterministic. This is mainly due to the simultaneous nucleation of numerous micro-cracks in the volume, leading to a multiple-fragmentation. This overview allowed a better understanding of the type of defects present in ceramic materials and responsible for failure. This will be used in **Chapter 3** to analyse the microstructural features of the studied ceramics. The aim will be to reach an accurate description of the complete flaw distribution and overcome the limitation of considering a Weibull flaw distribution, identified from quasi-static tests.

- Several techniques are available in the literature to, first, observe the failure modes induced in ceramics upon impact, then, evaluate the fragmentation patterns and intensity and, finally, apprehend the residual strength of the fragmented ceramic. Edge-on-impact, normal impact and tandem impact tests introduced in this literature review are conducted in **Chapter 4** to analyse the fragmentation properties of the studied ceramics. This literature review showed a lack of experimental techniques, based on the plate-impact technique, to properly characterise ceramics high-strength sensitivity to strain rate. For this reason, a new experimental technique is developed in **Chapter 5**, within the framework of the Brittle CODEX Chair [28], to measure the spall strength of ceramic materials at controlled loading rate. Experimental results provided in the literature, using a GEPI technique, will be used as a valuable reference to verify the developed methodology.

- Finally, a brief review of the models available to study the fragmentation behaviour of ceramic materials is given. This overview showed the necessity to account for a proper description of the flaw population and more physics-based processes. The phenomenology of the micro-mechanical DFH model was introduced. This model includes a realistic representation of failure mechanisms at high strain rates, while taking into account microstructural features (defects). One main interest of such models is that the distribution of defects, from which cracks may be activated, can be directly implemented as an explicit law to give valuable predictions for the controlled design of engineering brittle materials. This damage model will be used in **Chapter 6** and adapted to question the limitations of considering a Weibull flaw distribution on a large range of loading rates.

3 | Microstructural, mechanical and ballistic characterisation of the ceramics

Contents

Ceramic materials, used in combination with a ductile backing, are shown to be of major interest for armour protection. However, so far, the behaviour complexity of a ceramic material (several different failure modes and a strain rate dependent strength) makes the optimisation of its composition/microstructure very difficult, according to the application. To better understand which are the main microstructural parameters driving the failure under a dynamic impact, several armour ceramics are studied in this project. The goal of this chapter is to have a description of these ceramic materials, first in terms of microstructure (type of defects and their quantification, proportion of each phase, heterogeneities, etc.) and then in terms of performance (mechanical properties and ballistic limit velocity). To do so, the first part of this chapter corresponds to a brief description of the different studied ceramics through their manufacturing process to understand what could be the cause of defects in the resulting material. The manufacturing process descriptions of the commercial ceramics are voluntarily less detailed for confidential reasons. The microstructure of each material was analysed via scanning electron microscopy and X-ray computed tomography to identify and quantify the defects (mainly pores and inclusions). Then, bending tests and fractography analysis provide a description of the flaw population responsible for failure under quasi-static loading, according to the Weibull approach. Finally, a comparison of materials ballistic performance (ballistic limit velocity of perforation) is presented.

3.1 Presentation of the families of studied materials

In order to consider the effect of different microstructural parameters on the dynamic behaviour of ceramics, six different ceramic materials are studied in this thesis. They can be paired to form three families of materials. In each family, the two materials have almost the same microstructure with, ideally, only one main microstructural difference. Thus, the goal is to allow a better understanding of the effect of this microstructural feature on the material quasi-static and dynamic failure mechanisms.

3.1.1 Dense SiC with and without size-controlled spherical pores: Hexoloy grades

Hexoloy SA®

The first material is a dense silicon carbide ceramic, corresponding to a commercial product of Saint-Gobain, named Hexoloy SA®. Examples of torso plates and tiles, made of this material, are presented in Figure 3.1 (a). To manufacture this material, submicron SiC alpha powders are raised into suspension with some additives such as dispersing agents, binders and sintering additives (carbon and boron carbide [162] [40]). This step ensures a correct mixing of all the raw materials to guarantee a good homogeneity of the final product. Then, an operation of granulation leads to the shaping of a powder which is uniaxially pressed to obtain a relatively dense green body. The full densification of the green part is ensured by a final step of solid state pressureless sintering at temperatures higher than 2000 °C. The resulting material is a dense ceramic, 3.15 g/cm^3, made of fine SiC grains sized in the range 4-10 μm [163] and some few minor defects typical from solid-state sintered SiC materials, as shown in Figure 3.1 (b) [32].

Hexoloy SA with Controlled Porosity: Hexoloy SA-CP

The second material is a grade of Hexoloy SA® with size-controlled porosity, called Hexoloy SA-CP (CP for Controlled Porosity) in this work. These pores are discrete and non-interconnected. They are homogeneously distributed in the material and represent less than 2 vol. %. The resulting material has a density of about 3.11 g/cm^3. In the present work, the focus is on the effect of these large size-controlled pores on the dynamic fragmentation process of the ceramic. Indeed, these large pores are supposed to act as fuse flaws during a dynamic tensile loading, preventing the crack initiation on smaller (and more numerous) pores and, thus, limiting a very intense multi-fragmentation.

Finally, the microstructure of both Hexoloy grades is relatively homogeneous, with small and uniform grain sizes of the same composition (SiC). Between the two materials, the only changing microstructural parameter is the distribution of porosity, which is characterized in the next section. Being partially controlled in size and volume proportion, the porosity remains homogeneously distributed in the material bulk. It must be underlined that the main work of this thesis relies on the study of these two materials. Indeed, their relatively *simple* microstructure helps understanding how pores can affect the ceramic fragmentation properties through a modelling work.

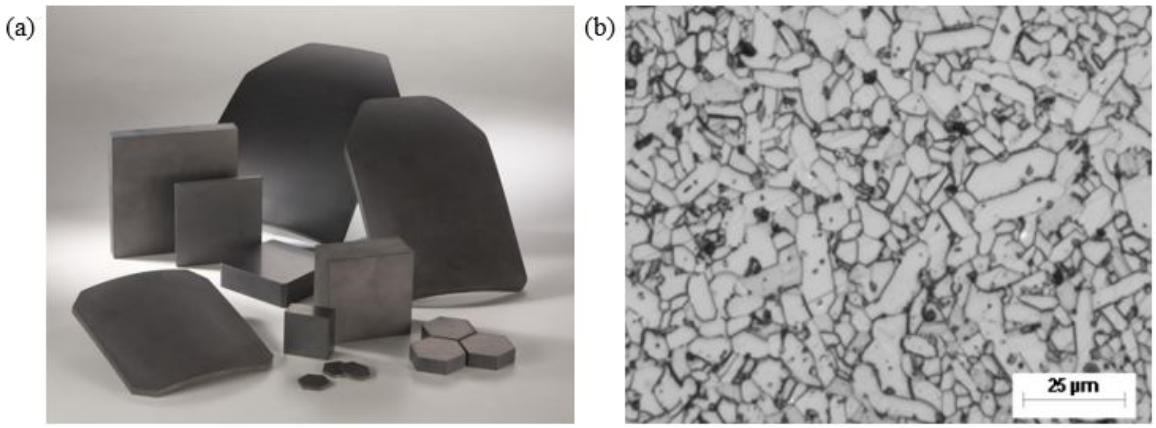

Figure 3.1. (a) Saint-Gobain products in Hexoloy SA® [164]. (b) SEM image of Hexoloy SA® microstructure with homogeneous grain sizes and some pores at the grain boundaries [32]

3.1.2 Reaction-bonding SiC-based ceramic composites: Forceram grades (ceramic binder-phase)

Forceram®

The Forceram® material is one of the commercial products of Saint-Gobain armour portfolio. This material is mainly made of a matrix of ceramic binder-phase, small and large silicon carbide grains (about 68 vol. % [165]) and a porous volume of a least 10 %. The ceramic binder-phase is generated in situ by a solid-gas reaction-bonding process under specific thermal and chemical conditions. This phase takes the form of relatively small grains in between the large SiC grains, therefore providing a densification of the final product. A specificity of this material is the presence of a median plane in the thickness of the material, characterized by different microstructural properties, mainly a higher porous volume. The thickness of this median plane can reach a value of about 1 mm, according to the tile thickness. This median plane is visible on the cross section of a 7 mm thick tile, as shown in Figure 3.2 (b). A SEM image in Figure 3.2 (a) provides an overview of the meso-structure of this material. Such a composition leads to a hard and lightweight material, with a density of 2.8 g/cm^3 [165].

Improved Forceram

The second material of this type, called Improved Forceram, is made of the same SiC-based composition. However, it presents a reduced open porosity of about 9 % compared to the Forceram ceramic. The bulk density is slightly increased, reaching about 2.82 g/cm^3. Moreover, the median plane with a different porous volume is also present, but has a thickness more variable than in the Forceram® (further detailed in the next section).

Finally, both Forceram materials contains a large proportion of SiC grains, but present a much more complex microstructure compared to Hexoloy grades. Made from a reactive-bonding process, they contain large SiC grains (meso-structure), a secondary ceramic phase (smaller grains) and a porous network. Moreover, they present an gradient of porosity in the bulk of the material. So, the only difference between the two Forceram materials is the distribution of porosity, in terms of volume proportion as well as local distribution.

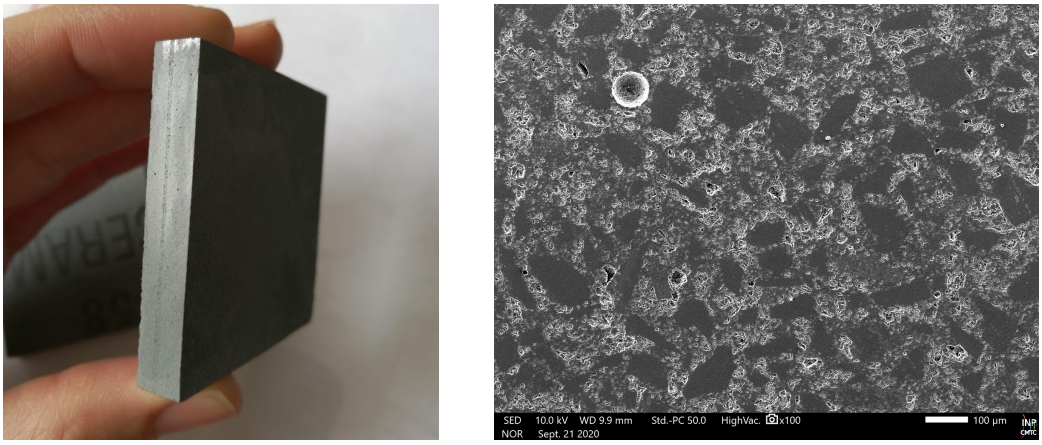

Figure 3.2. (a) Picture of a Forceram® tile cross-section, showing a gradient of microstructural properties (mainly porosity) in the thickness (7 mm). (b) SEM image (secondary electrons) of the Forceram® microstructure with large SiC grains, a ceramic binder-phase and a porous network

3.1.3 Reaction-bonding ceramic-metal composites: RBBC (metallic binder-phase)

In the endless search for armour weight reduction, boron carbide (B_4C) has been found to be a relevant candidate. Indeed, B_4C is the widely commercially available hardest ceramic and has a lower density than SiC (2.52 g/cm^3 against 3.21 g/cm^3 for SiC). Pure boron carbide is a difficult material to densify by pressureless sintering as it occurs at very high temperature. Typically, the use of sintering aid (such as carbon and zirconium dioxide ZrO_2) can lead to final relative densities of 90-96 %, for a pressureless sintering performed at 2000-2300 °C [166]. To reach higher densities for B_4C ceramics, hot pressing is usually used. This process can densify parts by using a lower temperature (1950-2050 °C), under a pressure of several MPa (typically 30-40 MPa), but is limited to produce complex shapes at reasonable cost [167]. An alternative to B_4C bulk processing technique is the reaction-bonding, which forms a Reaction-Bonded Boron Carbide (RBBC) material [4].

The manufacturing process of RBBC material consists in infiltrating by capillarity a green body, made of packed B_4C particles, with molten silicon. This green part can be shaped by the slip casting of a highly-loaded stable suspension containing multi-modal B_4C powder mixture, or by the cold pressing of B_4C granules. The initial porosity of this preform is crucial because it directly influences the composition of the final material [4] [3]. During the preform infiltration, at relatively low temperature (1450-1700 °C), some chemical reactions allow the consolidation of the particles via the formation of a new SiC phase. The in-situ formation of this beta-SiC phase comes from the reaction of silicon melt with any source of carbon in the green body (addition of carbon black or carbon impurities of the raw powders), following equation 3.1 [4]:

$$Si_{liq} + C_{sol} \longrightarrow SiC_{sol} \tag{3.1}$$

$$3B_4C_{sol} + Si_{liq} \longrightarrow SiC_{sol} + B_{12}(B,C,Si)_3 \tag{3.2}$$

A second possible reaction, given in equation 3.2, is responsible for the consumption of B_4C by the silicon and the formation of a ternary phase containing bore [168] [44]. Both reactions bond the original pre-existing boron carbide particles to produce a dense composite material. In the end, four different phases are present in the RBBC composite, as shown in Figure 3.3: the initial B_4C grains core, some unreacted residual silicon, the in-situ formed SiC also called β-SiC and the B_{12}(B, C, Si)$_3$ phase surrounding B_4C particles [44] [169]. The density of RBBC materials is close to 2.5 g/cm^3. One particularity of this material is the absence of porosity, as it has nearly been fully filled with silicon.

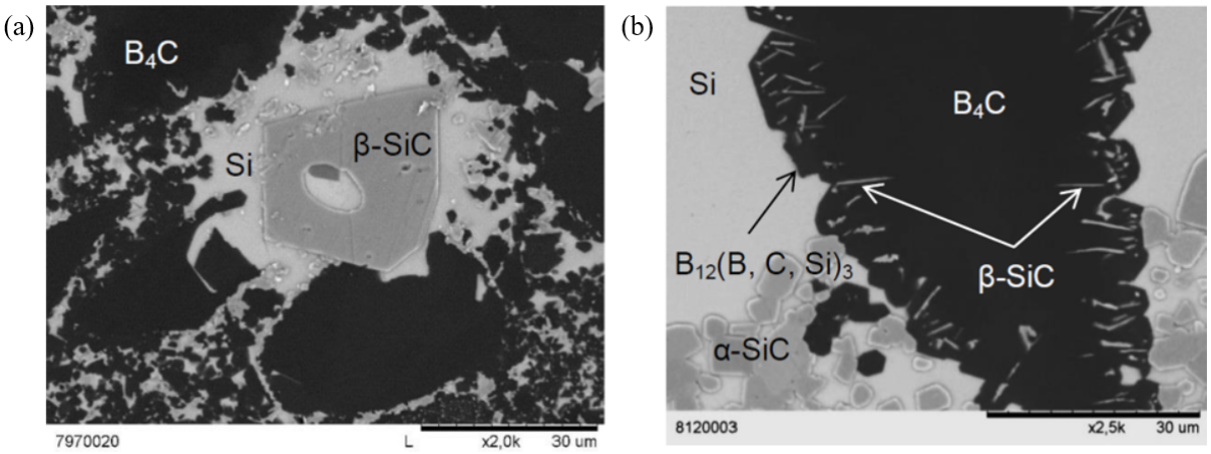

Figure 3.3. (a) Typical RBBC microstructure with (a) a polygonal beta-SiC grain resulting from the consumption of free carbon and (b) plate-like beta-SiC particles resulting from the B_4C consumption

To better understand the dynamic behaviour of such composite materials, this thesis work includes the development of several RBBC materials at Saint-Gobain Research Provence, presenting different microstructural features. Their ballistic performance was evaluated from the determination of their ballistic limit velocity of perforation (detailed in section 3.3.2). For the sake of concision and clarity of this thesis report, the details of the manufacturing optimisation (rheology of the ceramic slurry, powder packing, conditions of the silicon infiltration, etc.) are not presented. However, this work led to a communication in the Workshop LWAG 2019 (Light-Weight Armour for Defence & Security) [170]. Two RBBC ceramics, named RB2 and RB3, with different microstructures and good ballistic performances were selected for their dynamic behaviour to be further studied at the Laboratoire 3SR. Both ceramics were made from the same process ; starting from bi-modal (fine/coarse) B_4C particles, with no addition of free carbon, but with different B_4C particle size distributions. Their infiltration with liquid silicon was performed at 1500 °C during 1 h under vacuum. Their microstructure and phases proportions are studied in the next section.

3.2 Microstructural analysis via SEM and X-ray tomography

Whatever the manufacturing process, the resulting ceramic is never fully densified and always includes some inherent defects (detailed in section 2.1.1), acting as stress concentrators. The goal of this section is to analyse the microstructural features of the studied materials and evaluate what type of defect could be responsible for failure.

3.2.1 Defaults identification via Scanning Electron Microscopy analysis

All the materials were studied under Scanning Electron Microscopy (SEM Hitachi TM-1000 and JEOL IT500HR). The samples for microstructural characterisation were prepared using a standard metallographic procedure that includes a polishing step. In order to check the sample homogeneity in its thickness, SEM observations were conducted on tiles cross sections. Both Backscattered-Electron (BSE) and Secondary electrons (SE) imaging were performed to have a complete visibility on the nature of the defects. Indeed, BSE and SE are respectively beneficial for the inspection of chemical contrast and surface topography. Due to the topography effect, voids and cavities appear to be surrounded by a uniformly white glow on the SE images, therefore making possible to distinguish pores from inclusions.

Hexoloy grades

The SEM images of Hexoloy SA and Hexoloy SA-CP are presented in Figure 3.4 (1) and (2) at four different magnitudes, with BSE (a) and SE (b) imaging. First, it can be noticed that the Hexoloy SA ceramic is very dense, with only few pores exceeding a size of 10 μm in the SiC matrix (grey). As the samples were not highly polished, it is hardly possible to distinguish the different SiC grains. However, according to the literature and the manufacturer, the grain size are of about 4-10 μm and most of the flaws are pores situated at the boundaries of grains [32] [163]. Pore shapes are variable and can be very complex. The presence of dark phases, not corresponding to pores according to the SE images, demonstrates the presence of chemical inclusions having a low atomic number (appear black on the SEM images), which can be confused with the cavities without SE complementary imaging. These inclusions correspond to carbon and boron carbide residual sintering additives used for the densification of Hexoloy SA [162] [171]. It is reported, in the literature, that the carbon inclusions are mostly free graphite. The boron carbide grains can reach up to a few μm and smaller boron-containing precipitates (10-20 nm) can be observed at the grain boundaries [162] [172]. The B_4C grains seem to be well embedded in the SiC matrix, whereas carbon inclusion are more difficult to distinguish as they tend to be sheet structures surrounded by pores.

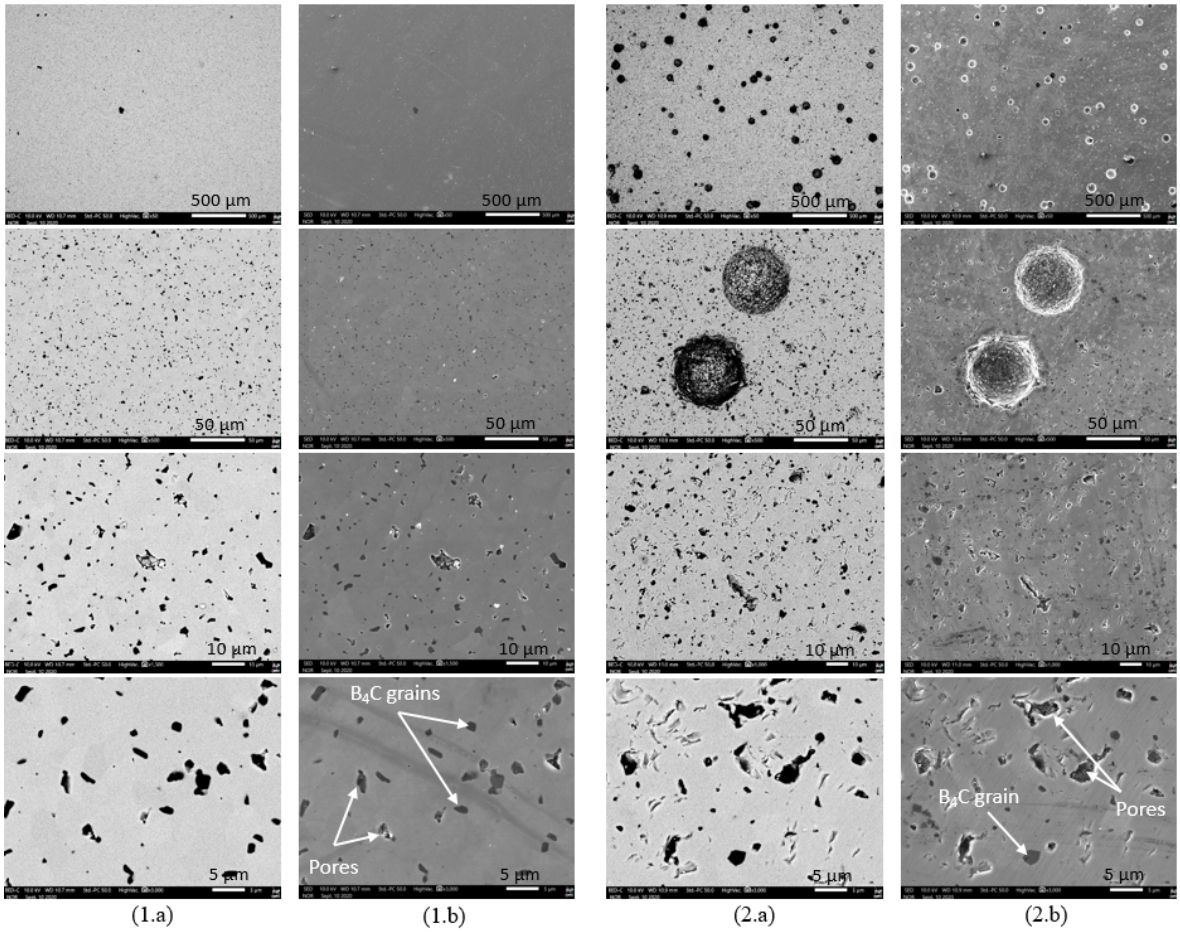

Figure 3.4. SEM images of Hexoloy SA (1) and Hexoloy SA-CP (2) at four different magnitudes, with BSE (a) and SE (b) imaging to distinguish chemical and topography contrasts

The Hexoloy SA-CP also presents these small sintering defects, which seem more numerous. It is easy to distinguish the large size-controlled pores, homogeneously distributed in the SiC matrix. Their shape is very spherical, except for the largest ones which correspond to merged (2-3) spherical pores. A 2D image analysis on about 5 images (with magnitudes of x50 and x250), using ImageJ, provided a first approximation of the porosity proportion in both materials. The estimation of porosity amounts are presented in Table 3.3 for Hexoloy SA and Hexoloy SA-CP. The value obtained for the Hexoloy SA is consistent with the pore area of 3.5 % measured by Martin from the same method of micrographs analysis [32]. For comparison, Saint-Gobain Research Provence provided a measurement of the level of closed porosity for both Hexoloy grades, obtained from the pycno-helium technique. Results are given in Table 3.3. It can be noticed that the 2D SEM image analysis over-estimates the porous volume compared to the pycno-helium technique. This can be explained by the fact that carbon and boron carbide inclusions are confused with porosity on the BSE images used for quantification.

Forceram materials

The SEM images of the Forceram and Improved Forceram materials are presented in Figure 3.5 (1) and (2), respectively, at four different magnitudes. Compared to the Hexoloy grades, the microstructure is more heterogeneous in the Forceram grades, with an apparent meso-structure. First, at a large scale, a median plane with a higher porous volume is visible on a tile cross-section of both materials. On the SEM images, the thickness of this median plane seems lower in the Improved Forceram (about 500 μm) compared to the Forceram material (about 1 mm), for 7 mm thick tiles. Then, the microstructure is also more heterogeneous in terms of particle sizes distribution.

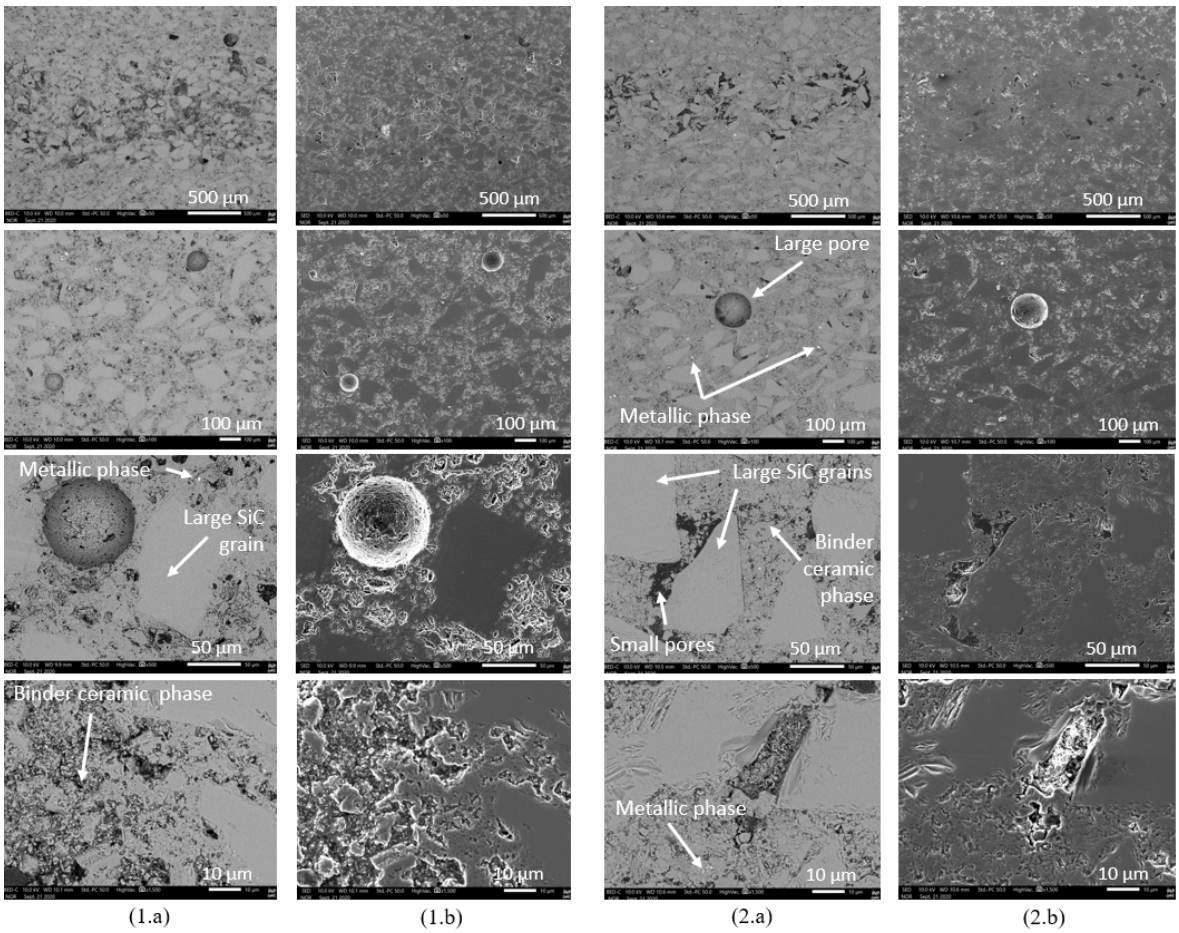

Figure 3.5. Cross-section SEM images of Forceram (1) and Improved Forceram (2) at four different magnitudes with BSE (a) and SE (b) imaging to distinguish chemical and topography contrasts

Large grains (light grey) of about 50-150 μm and with angular shapes correspond to initial SiC grains forming the green body. Smaller grains are made of some SiC grains and the binder ceramic-phase, which is generated in-situ and provides a cohesion and densification between the large SiC grains. This binder phase seems to be more present in the median plane, where a larger inter-grain space allowed its greater formation. This in situ ceramic phase does not allow the full densification of the final microstructure, and a porous network (interconnected pores) remains between the large grains and even within grains of the ceramic binder-phase. The shape of these interconnected voids is very complex. Moreover, some large spherical pores with sizes of few dozen or few hundreds of microns are present in both materials. Unlike the inter-phases small interconnected pores, these pores have a size comparable, or higher, than the large SiC grains. Finally, the presence of small inclusions of a metallic phase is visible on the SEM images (white phase). These scattered residual metallic areas seem to be well embedded in the other phases. Their proportion and size distribution are further analysed in the next section.

RBBC materials

The SEM images (BSE) of the RBBC materials RB2 and RB3 are presented in Figure 3.6 (a) and (b), respectively, at three different magnitudes. Four different phases can be observed: the initial B_4C grain core (dark), some unreacted residual silicon (white), the in-situ formed SiC (grey) also called β-SiC, and a B_{12}(B, C, Si)$_3$ phase surrounding B_4C particles (dark grey) due to the partial reaction of B_4C and Si [169]. In accordance with the initial fine (< 40 μm) and coarse (> 40 μm) proportions of B_4C particles used to shape the green body, given in Table 3.1, the RB2 material presents a higher concentration of large (> 40 μm) B_4C grains in the final product than RB3. For both materials, the green part porosity

was fully filled by the liquid silicon as no residual pores could be observed on the SEM images, except some few close pores in few large boron carbide grains (unreachable) visible in Figure 3.7. The resulting materials RB2 and RB3 present densities of about 2.55 and 2.50 g/cm^3, respectively. In the literature, the shape of β-SiC particles (polygonal or plate-like) is shown to be directly related to the type of carbon reacting with the silicon (respectively free carbon and carbon from B_4C) [168]. Surprisingly, the β-SiC predominant shape in both RBBC materials is polygonal, even if B_4C is expected to be the only source of reactive carbon. Therefore, these large polygonal grains can witness the presence of free carbon impurities on the surface of raw B_4C particles. Moreover, it can be noticed that most of the large polygonal SiC grains ($\sim$ 50-100 μm) are surrounded by areas of residual silicon.

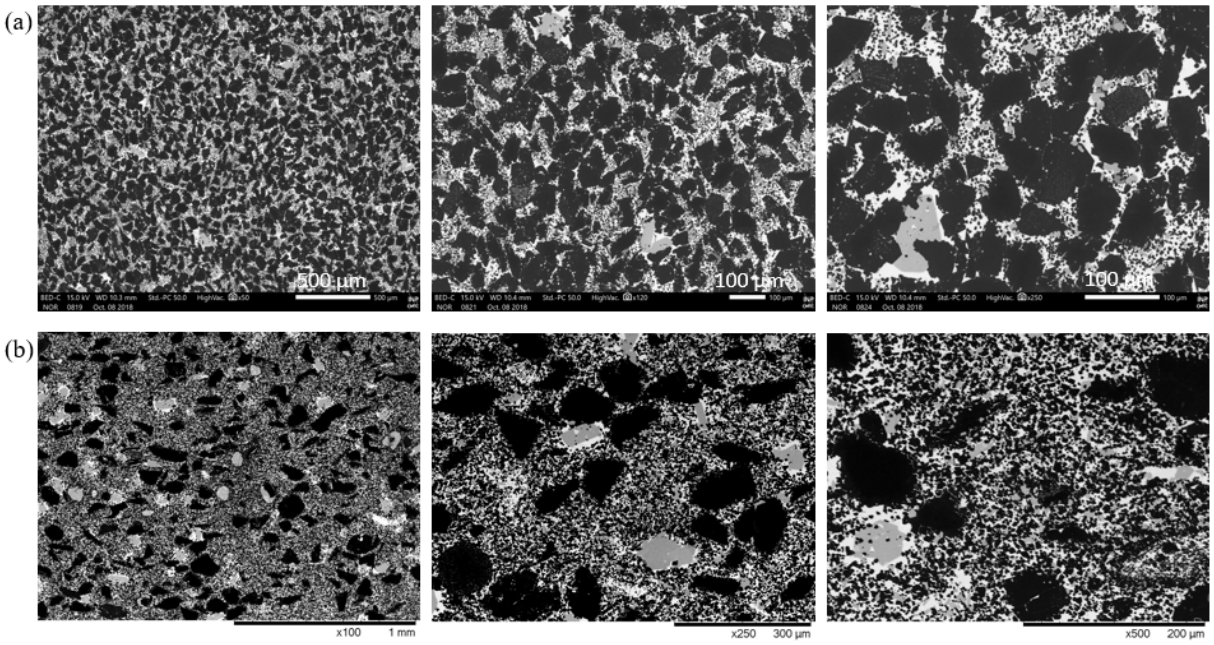

Figure 3.6. SEM images (BSE) of the RBBC materials (a) RB2 and (b) RB3 at three different magnitudes, with B_4C (dark), residual Si (white), β-SiC (grey) and $B_{12}(B, C, Si)_3$ (dark grey) phases

A further exploration was performed to better distinguish boron-based phases ($B_{12}(B, C, Si)_3$ and B_4C) and the Si-based phases (Si, β-SiC and $B_{12}(B, C, Si)_3$). To do so, the chemical contrast of these phases was enhanced by playing on the SEM operating conditions (probe current and accelerating voltage). In Figure 3.7, two images of a same zone in different observation conditions are presented. SEM pictures were post-processed from grey-level thresholding, using the Image J software, to estimate the ratio of each phase on 7 images at two different magnitudes. Results are presented in Table 3.1. Finally, both RBBC materials present the same proportion of boron-containing (B_4C and ($B_{12}(B, C, Si)_3$), β-SiC and Si phases, of about 76, 12 and 12 vol. %, respectively. Due to their high specific surface, small B_4C particles seem to highly react with silicon melt and form the ternary boron phase. Whereas large boron carbide particles were not highly consumed by the reaction with silicon-melt. The initial green porosities of RB2 and RB3 materials, before infiltration, was of 25.3 and 30 vol. %, respectively. Finally, the relatively high porosity of RB3 initial green part, initially risking to lead to a high amount of residual silicon, was offset by the major production of large β-SiC grains and $B_{12}(B, C, Si)_3$. Therefore, despite the difference of initial compositions and green porosities, both microstructures present an amount of residual Si of about 12 vol.%, compatible with good ballistic performance [4] [3]. In the end, the difference between both developed RBBC materials is essentially the size distribution of B_4C and β-SiC grains, mentioned in Table 3.1.

Table 3.1. Microstructural characteristic of the RBBC materials

		RBBC RB2	RBBC RB3
Proportion of B_4C initial powder (wt. %)	Fine (< 40 μm)	45	65
	Coarse (> 40 μm)	55	35
Size of the phase β-SiC (μm)		5-60	5-100
RBBC phases proportions (vol. %)	B_4C	10 ± 3	15 ± 3
	$B_{12}(B, C, Si)_3$	66 ± 2	61 ± 3
	β-SiC	12 ± 2	13 ± 1
	Si	12 ± 1	11 ± 1
	Porosity	< 1	< 1

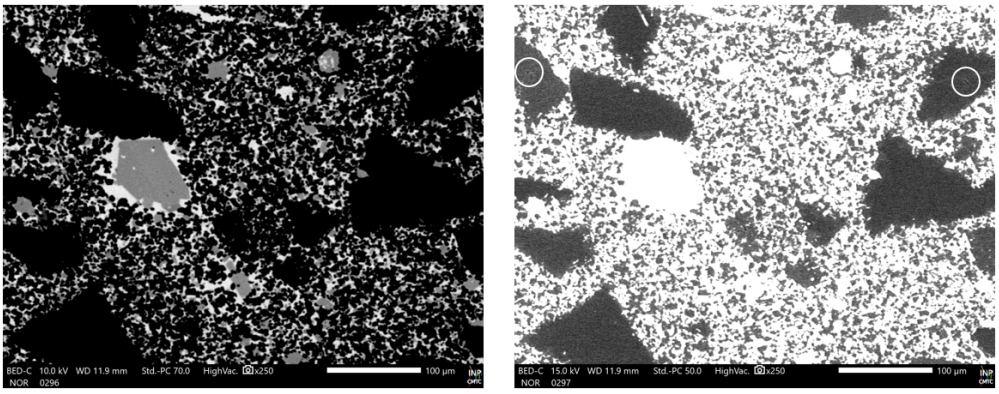

Figure 3.7. SEM images of RB3 with two different observation conditions. Some pores in large B_4C grains are surrounded

3.2.2 Defects characterisation via micro-tomography analysis

The X-ray scanner EASYTOM XL Nanofoyer in the Laboratoire SIMaP was used to reach a high resolution for the tomography scans of all the materials. The principle of X-ray Computed Tomography (CT) consists in measuring the attenuation coefficient of an X-ray beam passing through a sample. This X-ray attenuation level, being linked to the atomic number of the scanned material, the grey levels of the resulting 3D reconstructed image are directly linked to the material gradient of density. Therefore, this technique hardly allows the detection of the different grains of the SiC-based microstructure. However, it is adapted to detect heterogeneities, such as pores or inclusions (with a density sufficiently different from the host-material). Parallelepiped samples of section 1.5 x 1.5 mm^2 and variable thicknesses (7-20 mm) were considered to capture the small sintering defects (few μm) and include a volume large enough to properly describe the microstructures (scan duration about 4-6 hours). Additional scans, performed in the X-ray scanner in Laboratoire 3SR, were made on larger specimens to capture potential heterogeneities at larger scales (scan duration about 1-2 hours). The list of scans performed is detailed in Table 3.2 with the corresponding voxel sizes.

The spatial resolution (voxel size) depends on the resolution of the detector panel and distances between the electron source, the scanned sample and the detector. Therefore, the voxel size is conditioned by the size of the scanned specimen. The detector used is composed of 2084 $\times$ 2084 pixels with a physical pixel size of 24 μm. The second parameters assessing the good quality of an X-ray tomography scan is the level of noise in the 3D reconstructed image. This parameter mainly depends on the current and voltage of the poly-chromatic conical beam (source size of 3.5 μm) and the number of projections acquired during one full rotation of the specimen around the vertical axis. In the present work, the current and voltage of the source were respectively set to 26 μA and 100 kV and the scans reconstruction was made from 1856 projections. Some scans were made from the stack of 2 or 3 scans in order to access a larger zone of the specimen.

Table 3.2. Characteristics of the CT micro-tomography scans

Material	Specimen size (mm^3)	Type of scan	Geometry	Analysed volume (Z, Y, X) (vx^3)	Voxel size (μm)
Hexoloy SA	20 × 1.5 × 1.5	Stack (3 turns)	Cylindrical	800 × 1120 × 1120	1.1
	10 × 5 × 5	Stack (2 turns)	Rectangular	804 × 1067 × 708	3.0
Hexoloy SA-CP	7 × 1.5 × 1.5	Classic (1 turn)	Cylindrical	610 × 1350 × 1350	0.7
	20 × 1.5 × 1.5	Classic (1 turn)	Cylindrical	1100 × 1060 × 1060	1.33
	20 × 3 × 4	Stack (3 turns)	Rectangular	800 × 1560 × 1100	3.0
Forceram	9 × 1.5 × 1.5	Stack (2 turns)	Cylindrical	1000 × 1050 × 1050	0.9
	7 × 30 × 60	Stack (4 turns)	Rectangular	310 × 2700 × 1480	20.0
Improved Forceram	9 × 1.5 × 1.5	Classic (1 turn)	Cylindrical	1074 × 304 × 304	2.8
	7 × 30 x 60	Stack (4 turns)	Rectangular	330 × 2900 × 1460	20.0
RBBC RB2	9 × 1.5 × 1.5	Stack (2 turns)	Cylindrical	1550 × 1470 × 1470	1.0
	7 × 30 x 60	Stack (4 turns)	Rectangular	320. × 1460 × 2960	20.0
RBBC RB3	9 × 1.5 × 1.5	Stack (3 turns)	Cylindrical	1850 × 1450 × 1450	1.0

A grey-level threshold was applied to the 3D reconstructed images in order to distinguish the ceramic phase from pores (black due to the low density) or inclusions (if possible, depending on their composition). The threshold value was chosen by visually comparing the microstructural defects between the original 3D image and the binary image resulting from threshold. This step was found to influence on the resulting proportions of flaws, so the resulting porous volume obtained from tomography post-processing (ratio of pore voxels to total voxels) is compared to results from mercury porosimetry (open porosity, for Forceram grades) and pycno-helium (closed porosity, for Hexoloy grades and Forceram grades) in the next section. Mercury porosimetry and pycno-helium data were provided by Saint-Gobain Research Provence. From this, the pores or inclusions could be individually-labelled using the ITK watershed tool [173] and their size were approximated to be the equivalent diameter of a sphere of the same volume. To avoid any confusion between the smallest pores and the scan noise, pores with an equivalent diameter lower than 5 pixels were removed. This cut-off criterion is compatible with other studies found in the literature (diameter 4 pixels [174] and containing 2×2×2(8) voxels [175]).

Porosity characterisation and quantification in Hexoloy grades

For the Hexoloy grades, which were more deeply analysed for the modelling study in Chapter 6, scans at different scales and spatial resolutions were acquired, in order to properly describe the population of small and large pores. For the post-processing of scans with a low pixel size, the 3D reconstructed image as cropped into a cylindrical shape (axis Z) to avoid artefacts in the corners of a rectangular reconstructed volume. Slices extracted from the 3D images are presented in Figure 3.8 (1.a) and (2.a) for Hexoloy SA and Hexoloy SA-CP. Corresponding binary images are shown in Figure 3.8 (1.b) and (2.b). A 3D visualisation of the pores is given in Figures 3.8 (1.c) and (2.c) for a cubic box of size 500 μm, extracted from the post-processed 3D-image. As with the SEM analysis, carbon-containing inclusions (C and B_4C) could not be distinguished from pores by the tomography analysis as their absorption is very low.

The procedure was applied similarly to both materials, and the levels of porous volume before and after applying a size cut-off are compared in Table 3.3. The proportion of pores attributed to the large size-controlled pores in Hexoloy SA-CP (15-100 μs) were estimated to about 1.3 % from the scan at 3 μm/px. It can be noticed that the total porous volume estimated from micro-tomography is lower than the one expected from pycno-helium. This is mainly due to the limitation in resolution of the tomography technique, due to the minimal voxel size and the noise in the data. To overcome this

limitation, several scans need to be performed at different scales. Thus, a trade-off between a high resolution (small sample) and sampling statistics (large sample) can be reached to obtain data on the whole spectrum of the pore sizes. Nevertheless, in the present work, the hypothesis is made that the smallest pores ($D_{eq} < 5$ px) not captured by the X-ray tomography technique do not have a major effect on the fragmentation properties in the range of loading rates of interest for ballistic application. This hypothesis will be validated from the modelling predictions, based on X-ray tomography, given in Chapter 6.

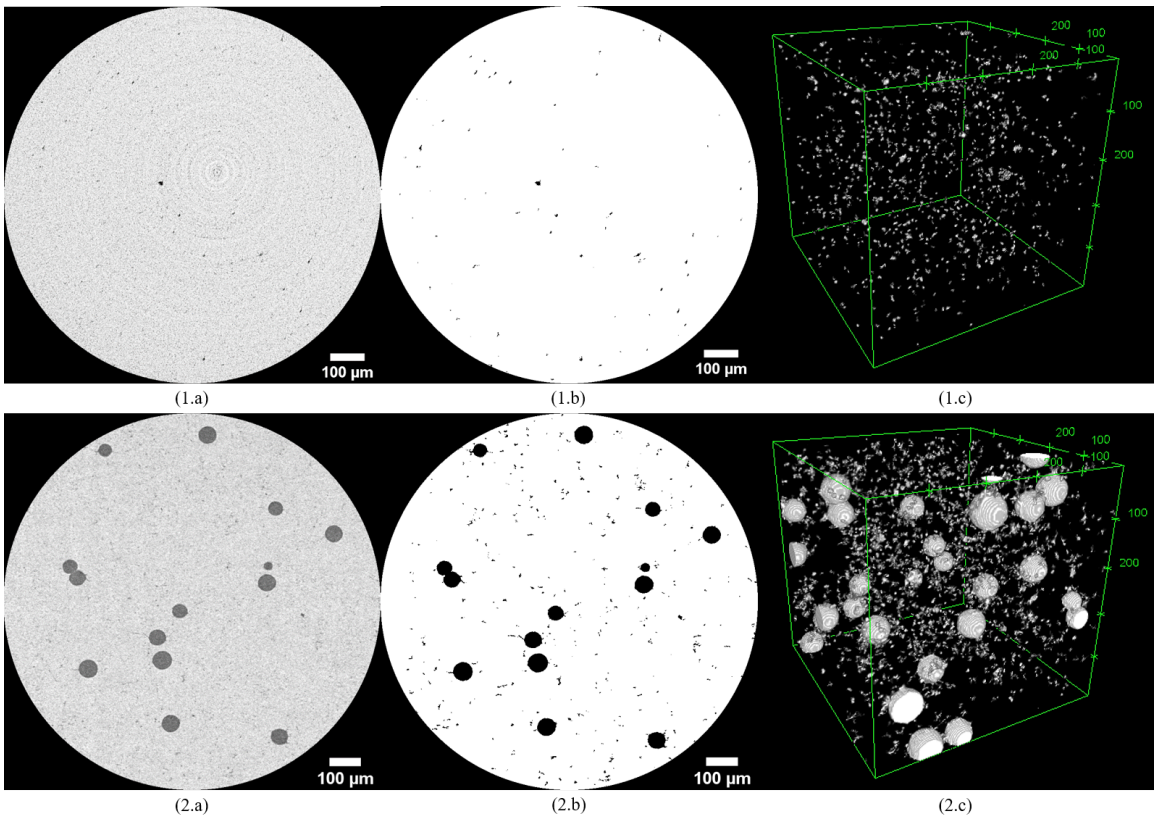

Figure 3.8. Slices of the 3D-images reconstructed from the tomography scans (a), corresponding binary images after the grey-level threshold and applying the label-size cut-off (b) and 3D view of the extracted pores (box size 500 μm) (c), for Hexoloy SA (1) and Hexoloy SA-CP (2) (scans 1.1 - 1.33 μm/px)

Table 3.3. Comparison of the porous volume measured from SEM, tomography and pycno-helium for the Hexoloy grades

Technique for porosity measurement (vol. %)		Hexoloy SA scans (1.1 / 3) μm/px	Hexoloy SA-CP (0.7 / 1.33 / 3) μm/px
Pycno-helium (close porosity)		1.48*	3.07*
SEM image analysis		3.4 ± 0.9	6.4 ± 1.6
X-ray tomography	No denoising	0.24 / 0.02	2.92 / 2.3 / 1.43
	Cut-off ($D_{eq} < 5$ px)	0.09 / < 0.01	1.81 / 1.42 / 1.3

* data provided by Saint-Gobain Research Provence

The python package SPAM [176] was used to plot an histogram of the pores size and evaluate the pores sphericity for both materials, as shown in Figure 3.9. The presence of size-controlled pores in the material Hexoloy SA-CP is clearly visible on the histogram in Figure 3.9 (a), where two flaw populations can be identified with a transition around 20-40 μm. Whereas the Hexoloy SA only shows the presence of the small pores, mainly associated to sintering defects. This histogram also shows which scan size/resolution provides a good description of each flaw population. The pore morphology was characterized using a fitted ellipsoid, centered on the pore centre of mass and enveloping the whole pore contour. The ratio of

the maximal to minimal principal axis lengths provides information on the shape of the flaw. The factor of sphericity was computed from the volume V_e and surface S_e of the fitted ellipsoid as follows:

$$\phi = \frac{\pi^{1/3}(6V_e)^{2/3}}{A_e} \tag{3.3}$$

A value close to 0 is reached for a pore presenting a needle-like shape, whereas a value of 1 is related to a perfectly spherical flaw. It has to be noticed that this type of study could be performed because the analysed defects are convex pores, which can reasonably be represented by ellipsoid (unlike defects such as dislocations, closed cracks, etc.). This morphology analysis illustrated in Figure 3.9 (b) shows that the small sintering defects of both materials have quite irregular shapes, whereas the large size-controlled pores in the porous SiC ($D_{eq} > 30$ μm) are highly spherical (ϕ close to 1). All the pores of size 80-100 μm and some smaller pores (60-80 μm) are non-spherical in the Hexoloy SA-CP. They result from the merge of several spherical-pores. Some of those few merged-pores are visible in the large-scale SEM images and tomography slice presented in Figure 3.4 (2.b) and Figure 3.8 (2.b), respectively.

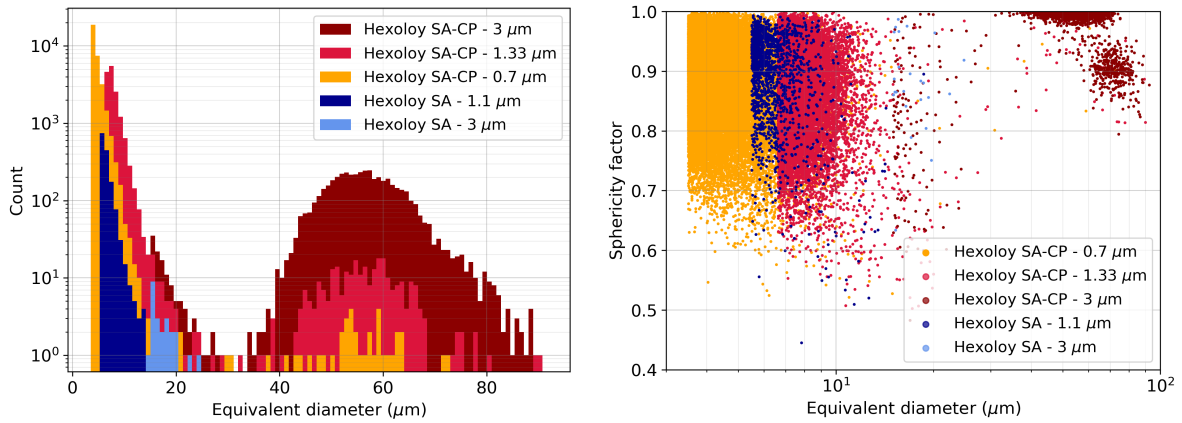

Figure 3.9. Comparison of the pore size histogram (a) and sphericity factors (b) of Hexoloy SA (2 different pixel sizes) and Hexoloy SA-CP (3 different pixel sizes)

The spatial distribution of pores was studied by investigating the spacing between nearest neighbour flaws. This analysis is motivated by the role of inter-defect spacing on their potential interaction during the fragmentation process. The histogram given in Figure 3.10 presents the minimal centre-to-centre distance between the size-controlled spherical pores in Hexoloy SA-CP. The nearest neighbour distance was found to be relatively well represented by a normal distribution with a mean spacing of 100 μm, and 170 μm when considering an average minimal distance between the six closest pores. This result shows that, except from few merged-pores, the large size-controlled pores are regularly distributed in the volume. Then, it can be noticed that this centre-to-centre distance (100 - 170 μm) is very close to two times the pores average diameter (about 100 μm), so from Rice criteria given in the section 2.1.1, the large pores in the Hexoloy SA-CP might interact during the fragmentation process.

In addition, by ranking pores for an increasing equivalent diameter, the density of pores according to their size can be determined. This flaw density function is plot in Figure 3.11 and emphasises the quasi-absence of porosity for the Hexoloy SA-CP between 20-40 μm, with a large plateau at 100 pores/mm^3. Flaw density curves of the Hexoloy SA-CP for different scan resolutions are found to perfectly overlap. This result shows the good homogeneity of the microstructure and the accuracy of the post-processing technique (high resolution versus sampling statistics). It can be noticed that the Hexoloy SA-CP presents a larger number of small pores compared to the Hexoloy SA, with almost ten times more pores smaller than 10 μm. The modelling work on the dynamic fragmentation process in both Hexoloy grades, presented in Chapter 6, relies on these flaw density curves, extracted from X-ray tomography analyses.

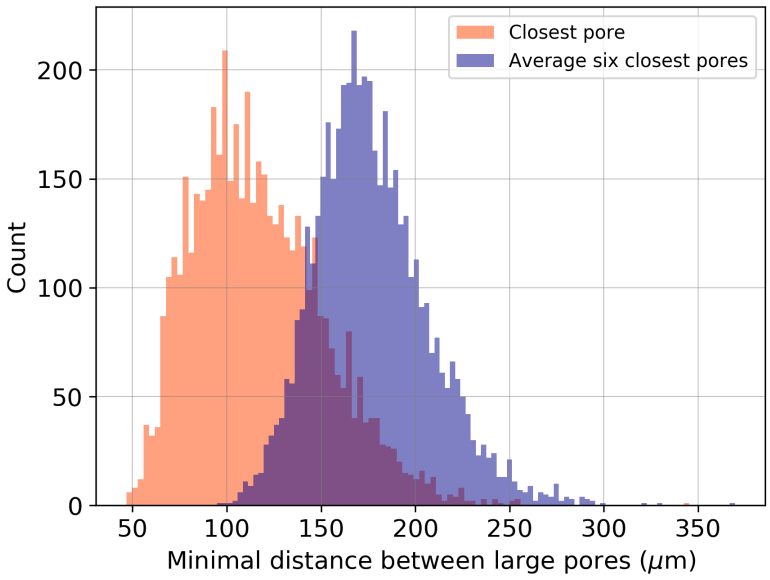

Figure 3.10. Histogram of the minimal distance between the size-controlled pores in the Hexoloy SA-CP (scans 3 μm/px), considering the closest pore and an average value for the six closest pores

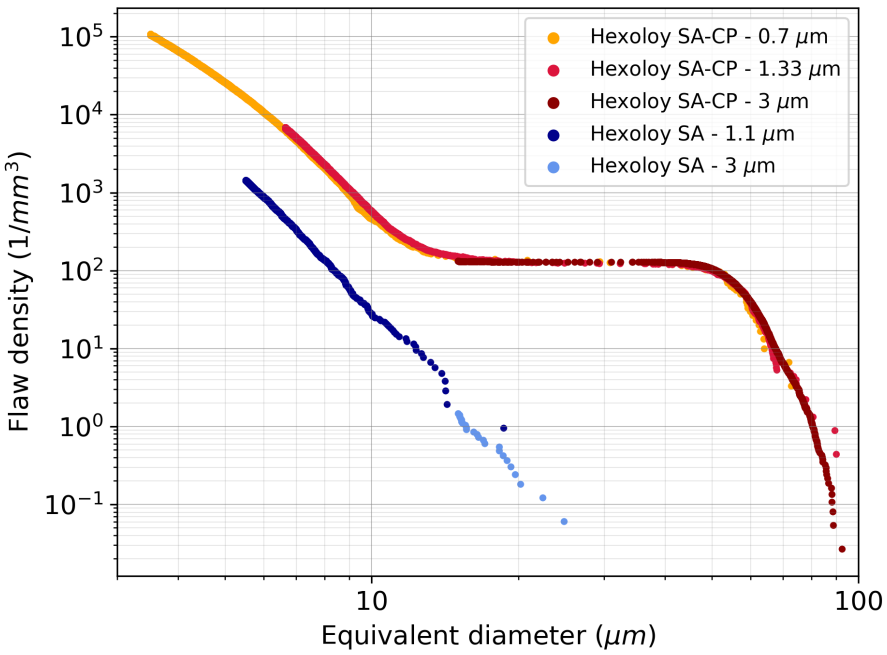

Figure 3.11. Comparison of the cumulative flaw density as a function of the flaw equivalent diameter for Hexoloy SA and Hexoloy SA-CP, from tomography scans of different pixel sizes

Porosity and inclusions quantification for the Forceram grades

Tomography scans of Forceram grades at large scales provided a visualisation of porosity gradient in the tile cross-section and the presence of the large spherical pores, in both materials. Slices of the 3D reconstructed volumes (7 x 30 x 60 mm^3) of Forceram (a) and Improved Forceram (b) are shown in Figure 3.12. The median plane is slightly off centre and with some thickness variability in the Improved Forceram (about 1 mm in zone 1 and 0.5 mm in zone 2, in Figure 3.12 (b)), unlike the Forceram (about 1 mm in Figure 3.12 (a)). Moreover, it can be noticed that the large spherical pores are much larger than in the Hexoloy SA-CP material, reaching up to about 400-500 μm in Forceram grades. The density of large pores ($>$ 100 μm) outside of the median plane, was quantified from the post-processing of scans of spatial resolution 20 μm/px. To do so, the areas of both side of the median plane were extracted, referred

as zones A_1 and A_2. It can be observed in Figure 3.13 that the density of large pores in both sides of the median plane are similar. In addition, the Forceram material presents a higher number of large pores compared to the Improved Forceram, up to about 7-10 times more for the largest pores (200-400 μm). A quantification of the volume occupied by these large pores is given in Table 3.4, corresponding to about 0.23 vol. % and 0.07 vol. % for the Forceram and Improved Forceram, respectively.

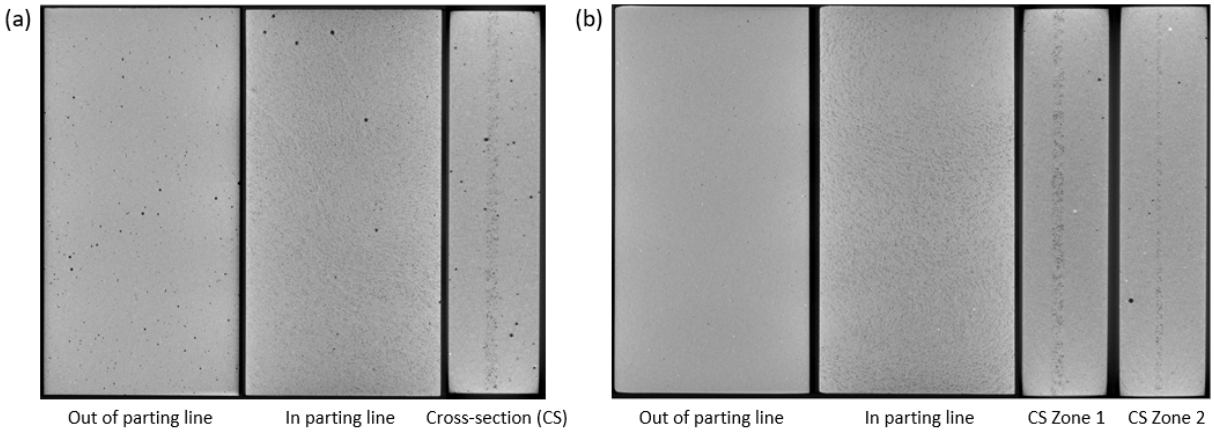

Figure 3.12. In-plane (30 x 60 mm^2) and cross-section (7 x 30 mm^2) slices of the 3D reconstructed images for Forceram (a) and Improved Forceram (b) (voxel size 20 μm)

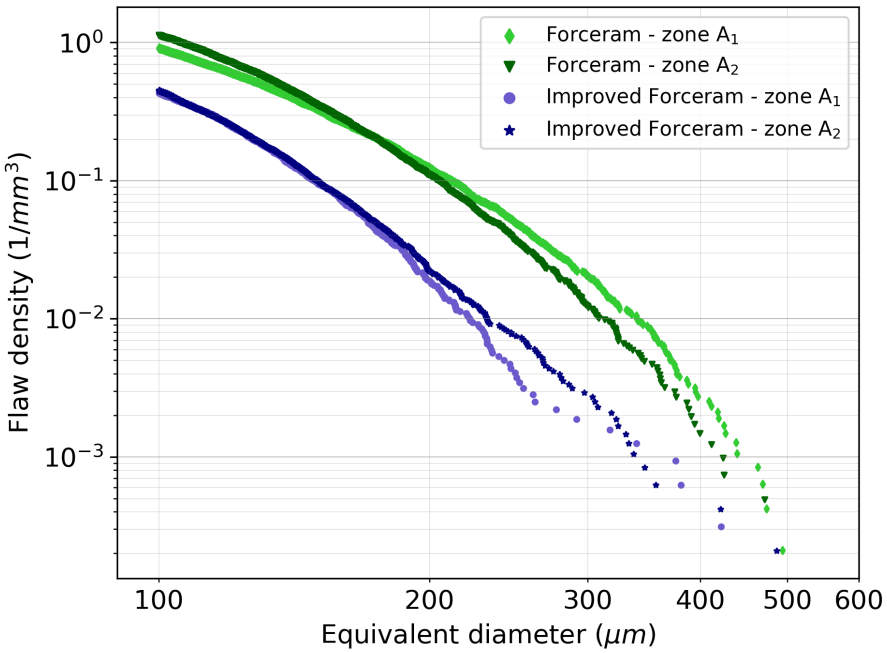

Figure 3.13. Size distribution of the large pores ($>$ 100 μm) out of the median plane, for the Forceram and Improved Forceram materials. Zones A_1 and A_2 correspond to area on both sides of the median plane (scans of voxel size 20 μm/px)

From scans with a lower voxel size, the main four different phases can be identified: pores (black), metal inclusions (white), silicon carbide (light grey) and the ceramic binder-phase (grey). They are shown in slices of the 3D reconstructed image given in Figure 3.14. Compared to Hexoloy grades, Forceram grades present a higher porous volume, which is non homogeneously distributed in the material bulk. At a close scale, this porosity mainly includes interconnected pores of complex shapes. The tile cross-section can be divided into three different zones, where the pore density is different. Named B, A and C, these zones correspond to increasing level of porosity, as shown in Figure 3.14 (zone C is the median plane). Pores and metal inclusions were extracted from a binary threshold and are shown in

Figure 3.14 (in white). The metal phase seems to be homogeneously distributed in the volume. The quantification of phases, resulting from grey-value threshold, is given in Table 3.4. The large margin of error given for both ceramic phases (SiC and binder) is due to their very close grey value. The porous volume obtained from X-ray tomography analysis is in good agreement with the sum of close and open porosity volumes, specified in Table 3.4 and obtained from pycno-helium and mercury porosimetry, respectively. The maximal size of metal inclusions is found to be consequently lower than the size of spherical pores for both Forceram grades (Table 3.4, calculated from scans of different volume and voxel size). Therefore, the presence of the metal inclusions are expected to be a less critical defect that the porosity.

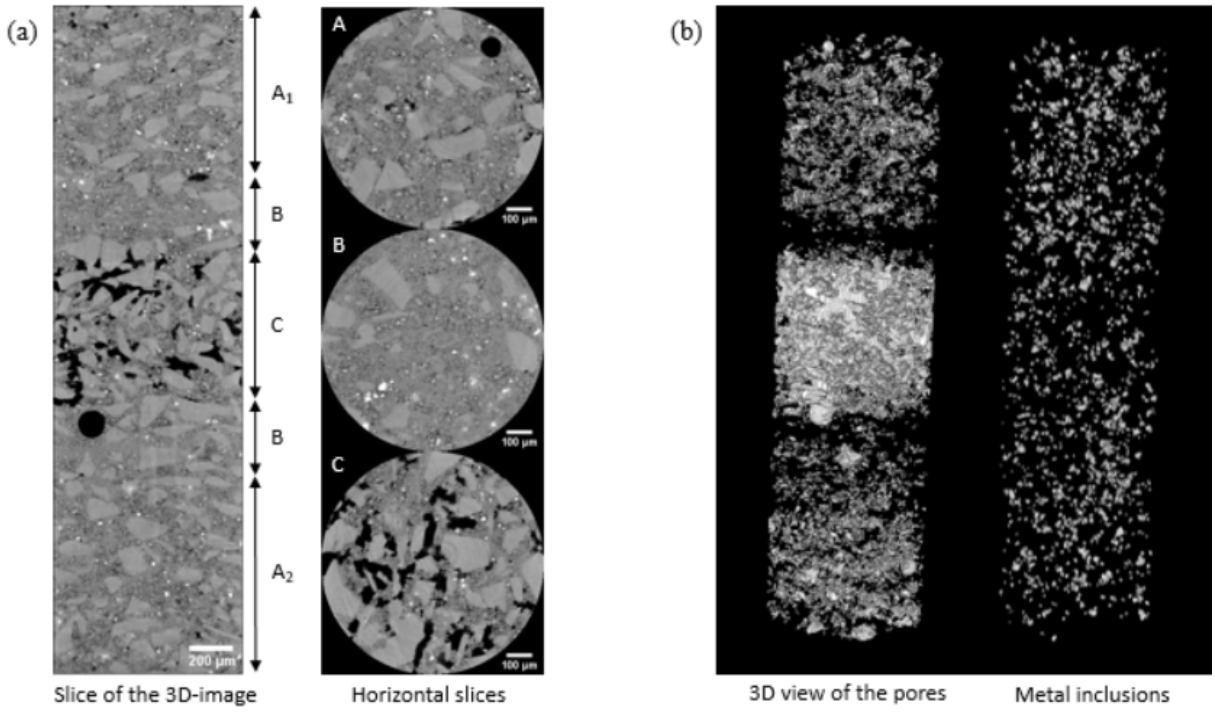

Figure 3.14. (a) Slices of the 3D-image obtained from tomography scan of the Improved Forceram. Three zones along the tile cross-section (A, B and C) present different pore densities. (b) 3D view of the extracted pores and metal inclusions (cylindrical shape of about 3 mm height and 0.85 mm diameter)

Table 3.4. Microstructural characteristic of the Forceram and Improved Forceram materials

		Forceram	Improved Forceram
Close porosity (pycno-helium) (vol. %)		1.45*	2.63*
Open porosity (mercury porosimetry) (vol. %)		11.20*	9.33*
Phases proportions from X-ray tomography (vol. %)	SiC	67.7 ± 3	68.8 ± 2
	In situ binder phase	19.8 ± 3	20.7 ± 2
	Metal inclusions	0.5 ± 0.2	0.8 ± 0.2
	Porosity	12 ± 1	9.7 ± 1
Large pores (> 100 μm) out of the median plane (vol. %)		0.23 ± 0.05	0.07 ± 0.05
Equivalent diameter of the largest metal inclusion (μm)		31	47
Size range of large SiC grains (μm)		50-150	50-150

* data provided by Saint-Gobain Research Provence

Identification of potential sources of heterogeneities in RBBC materials

The RBBC complex microstructure makes the identification of defects more difficult. Two horizontal slices of the 3D-images of scanned samples (a) RB2 and (b) RB3 are presented in Figure 3.15. First, pores of few microns are visible in some large B_4C grains, mainly in RB3 containing larger B_4C particles. Such pores are only located in some very few specific porous grains. Most of this porosity is closed and cannot be filled by the silicon during the infiltration. Another potential source of heterogeneity could be the relatively large areas of residual silicon (10-50 μm) surrounding the large polygonal β-SiC grains in RB3 or embedded in small SiC particles in RB2. Moreover, the presence of elongated B_4C grains, mainly present in RB3, could also be a source of stress concentration. Another type of flaw, probably the most critical type of defect, is the lack of infiltration [177]. An un-reacted area could be identified, in the RB3 sample, as a blurry and black zone without the sharp edges of a B_4C grain.

An additional scan was performed on a large sample of RB2 (7 x 30 x 60 mm^3) to detect some large scale defects. Some spherical air-pores filled with silicon of size up to 400 μm are visible in Figure 3.15 (c). Moreover, an irregular zone, filled with silicon, is visible on the cross-section slice. This zone is called *parting line* and result from the slip casting process, used for the shaping of the green part. A vertical slice taken in the parting line shows some irregular Si-rich wrinkle zones. This type of large defects were previously observed by several authors on this type of materials [178] [177]. Moreover, some authors highlighted the risk of interfacial crack formation between B_4C and SiC grains during cooling (residual stresses), due to their thermal expansion mismatch (CTE of 5.73.10$^{\check{}}$6 K^{-1} and 3.07.10$^{\check{}}$6 K^{-1}, respectively) [179]. However, this type of defects was not observed in both studied RBBC materials, possibly due to their absence or a lack of resolution.

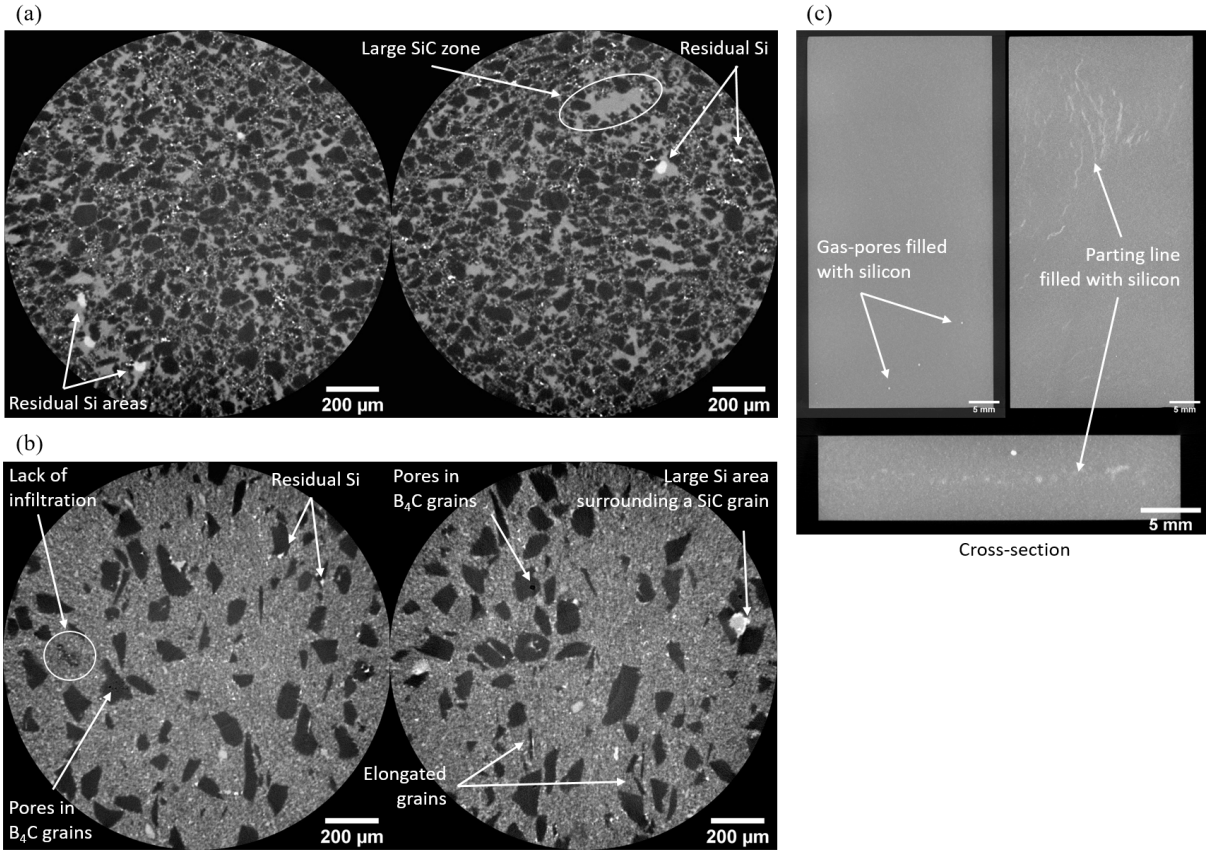

Figure 3.15. Identification of possible sources of microstructural heterogeneities in (a) RB2 and (b) RB3 materials, from slices of the 3D image (1 μm/px). (c) In-plane (30 x 60 mm^2) and cross-section (7 x 30 mm^2) slices of 3D images of RB2, showing Si-rich areas at large scale (20 μm/px)

3.2.3 Meso-structure characterisation via micro-tomography analysis

To evaluate the meso-structure in the Forceram grades, several processing steps were required. To accurately distinguish the large SiC grains from the matrix, the procedure developed by Stamati et al. for concrete materials containing a matrix, pores and large aggregates was followed [158]. The main steps are illustrated in Figure 3.16. Pores and metal inclusions could be identified from a simple threshold but the large SiC grains required the use of a variance filter for their contours to be revealed, as shown in Figure 3.16 (b). A threshold of the variance 3D image allows grains identification. A morphological dilation (x2) was required to recover the original size and shape of the grains. Finally, the representative horizontal slice in Figure 3.16 (c) contains the four identified phases. The image is strictly composed of four sets of pixels having the same (chosen) value: the metal inclusions (white), the ceramic binder-phase (light grey), the SiC grains (grey) and pores (black). From this segmentation procedure, the particle size distribution of the labelled SiC grains was determinated, with an equivalent diameter corresponding to the diameter of a sphere of same volume. Finally, from this post-processing, the size range of the large SiC particles was evaluated to 50-150 μm for both Forceram grades, as given in Table 3.4.

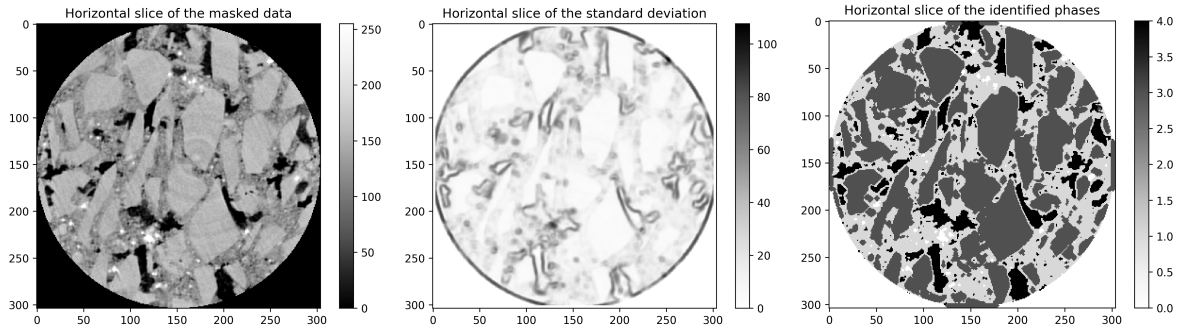

Figure 3.16. Identification of the different phases in the Improved Forceram X-ray scan, based on Stamati et al. procedure [158]. (a) Initial tomography horizontal slice. (b) Variance map based on a specific structuring element, to identify the SiC grains. (c) Resulting identification: metal inclusions (white), ceramic binder-phase (light grey), SiC grains (grey) and pores (black)

3.3 Mechanical and ballistic characterisation

3.3.1 Mechanical properties

Brittle materials present a stochastic strength at low strain rate, related to the presence of critical defects in the loaded specimen. As detailed in section 2.1.2, a statistical approach based on the Weibull model can be used to describe their quasi-static failure behaviour under tensile loading. In this section the Weibull parameters of the Hexoloy grades are presented for the purpose of the modelling work presented in Chapter 6. Concerning the Forceram and RBBC grades of materials, few bending tests were performed to observe fracture surfaces and identify the failure modes generated under quasi-static loading, but not enough samples were tested to evaluate accurate Weibull parameters. A characterisation of the elastic properties of the Hexoloy and Forceram grade is given to be used for the numerical simulations work developed in Chapter 4.

Quasi-static tensile strength from bending tests - Weibull parameters

Results of quasi-static bending tests performed on the Hexoloy grades were provided by Saint-Gobain Research Provence. The dimensions of the tested specimens were 3 x 4 x 45 mm^3 (height x width x length). The support and loading (for 4-points bending configuration) spans were of 40 and 20 mm, respectively. As brittle materials are susceptible to crack nucleation at external and internal flaws, each surface of the specimens was polished and the corners chamfered. The main characteristics of the tests

are summarized in Table 3.5. The failure strength σ_f is calculated from the maximal force reached before failure F_{max}, expressed as follows for 4-points bending test (l=0 for 3-points bending configuration):

$$\sigma_f = \frac{3F_{max}(L-l)}{2bh^2} \tag{3.4}$$

where b, h are the width and height of the samples and l, L are the loading and support span dimensions. The average flexural strength σ_w is given in Table 3.5. To take into account the non uniformity of the loading in the specimen during bending tests, an effective volume is calculated. This volume is related to the testing configuration and the flexural strength scattering, via the Weibull modulus m. It can be expressed as follows, for three and four point bending tests [66]:

$$V_{eff-3pts} = \frac{V}{2(m+1)^2} \tag{3.5}$$

$$V_{eff-4pts} = \frac{bhl}{2(m+1)} + \frac{bh(L-l)}{2(m+1)^2} \tag{3.6}$$

where V is the sample total volume. The Weibull parameters were determined graphically from the linear regression in the log-log Weibull diagram, as described in section 2.1.2.

Table 3.5. Parameters of the bending tests and obtained Weibull parameters for the Hexoloy grades

	Hexoloy SA*	Hexoloy SA-CP**
Configuration	4 pts	3 pts
height x width x length (mm)	3 x 4 x 45	3 x 4 x 45
Loading span (mm)	20	-
Support span (mm)	40	40
Number of samples	160	24
Effective volume V_{eff} (mm^3)	8.52	0.836
Average bending strength σ_w (MPa)	406 ± 34	300 ± 22
Weibull modulus	14.05	16.04

* data provided by Saint-Gobain Research North America (NRDC)
** data provided by Saint-Gobain Research Provence

First, the high Weibull modulus (narrow strength distribution) obtained for the Hexoloy SA-CP material (16) is consistent with the good size-homogeneity of the large size-controlled pores, which are the ones causing the failure during the bending tests according to the weakest-link theory [51]. In addition, the presence of large pores led to a reduction of the flexural strength of the material compared to the Hexoloy SA, which is consistent with the lower macroscopic critical stress of large defects, introduced in section 2.1.1.

Not enough samples from both types of RBBC materials could be tested to provide an accurate measurement of the Weibull modulus, however, about 10 tests allowed to estimate the average bending strength. Values of 266 ± 32 MPa and 238 ± 13 MPa were obtained for RB2 and RB3, respectively. It can be noticed that these flexural strengths are close to value of commercial products for RBBC composites presenting relatively large B_4C particles. Hayun et al. obtained similar flexural strength properties for their RBBC material (named RBM) presenting a microstructure close to RB2 and RB3, in terms of density (2.54 g/cm^3), B_4C particle size (multi-modal 1/70/106 μm) and amount of residual silicon (10 vol. %) [180]. They obtained a Weibull modulus of 13.3 and a flexural strength of 273 ± 23 MPa from 20 experimental values of the flexural strength.

Fractography analysis: critical defects and failure mode identification

For each material, fractography analyses were performed via SEM imaging on the fracture surfaces (except for the Hexoloy SA, which flexural data were provided by the factory quality control of

Saint-Gobain NRDC). Corresponding BSE and SE images are shown for two different magnifications in Figure 3.17. The orientation of the samples during the bending test (height and width dimensions) is shown on the large scale image, in Figure 3.17 (1). The goal of this analysis is to try to understand the causes of failures. The images taken at high magnitude are a close-up visualisation of a possible defect responsible for the specimen tensile failure. It must be underlined that for the Forceram ceramic, specimens were manufactured to have the median plane through all the height and placed in the width-centre of the specimen, as shown in Figure 3.17 (2a). As for the Improved Forceram material, the bending tests were performed on specimens extracted out of the median plane. The position (or absence) of the median plane is expected to have consequences on the resulting strength and Weibull modulus, as the flaw population in the loaded volume differs. The identification of a critical defect was not possible for all the materials. For the Forceram grades, the presence of abnormally large air-pores (about 200 μm) made the identification relatively simple, whereas for the Hexoloy SA-CP several potential critical defect-zones could be identified, one of them is shown in Figure 3.17 (1). From the fracture surface examination of the RBBC materials, no clear features could clue the fracture origin. Close-up images highlight some large areas of residual silicon, however, there is no evidence that they are responsible for the failure. The presence of a parting line, fully filled with silicon, was noticed on some RB3 samples, visible in Figure 3.17 (3b).

Moreover, observations of the fracture surfaces also provide information on the failure modes. First, the Hexoloy SA-CP presents a brittle fracture mainly exhibiting transgranular failure mechanisms with a typical *river pattern* fracture. Some authors observed the same type of fracture mode in Hexoloy SA under quasi-static failure [181] [93]. Such a fracture behaviour can be related to fine grains microstructure and to the solid state sintering, which ensures a good cohesion of the grains. Few slip traces are visible on the fracture facets. The Forceram grades mainly show intergranular failure. Indeed, the large SiC grains present cleavage step patterns which are a consequence of the crack propagation through neighbouring grains with highly twisted boundaries. Most crack paths seem to follow the low-carbide density planes adjacent to the SiC grain boundaries, therefore leading to intergranular fracture. Several zones of interface decohesion between the matrix and large SiC grains could be observed. Concerning the RBBC materials, the three phases (boron carbide, silicon carbide and silicon) showed different fracture characteristics. First, the large boron-carbide grains mainly display a transgranular cleavage fracture mode (cleavage planes), whereas small B_4C particles allow crack deflection and crack bridging. Then, the transgranular fracture of the SiC phase seemed to provide more irregular fracture patterns (twisted, cleavage steps) than the coarse B_4C grains. And finally, some semi-ductile deformation occurred in the residual silicon phase. These multi-failure modes in RBBC composite materials are in balance with observations made by other authors from fractography performed on quasi-static bending [179] [182] and ballistic fragments [183].

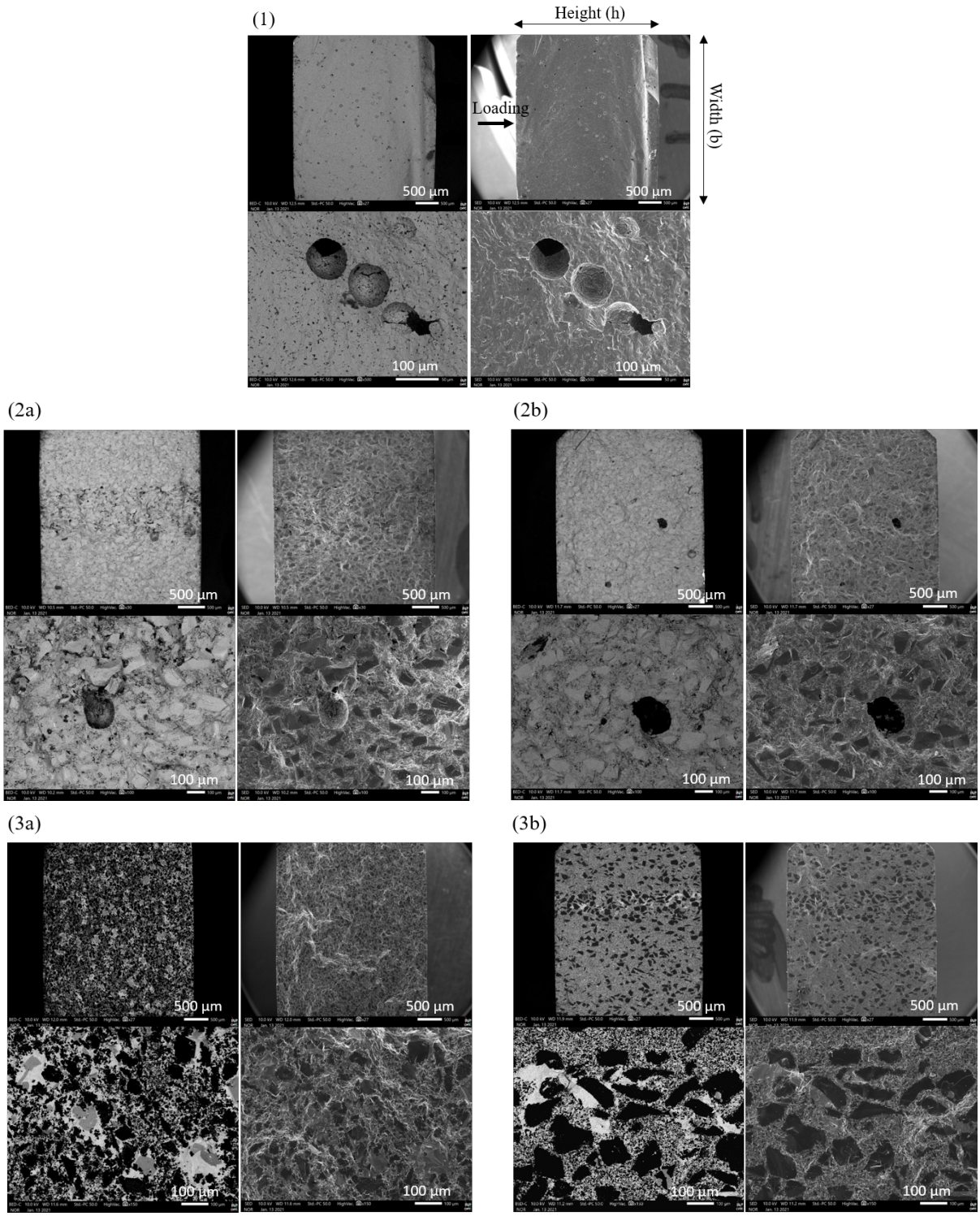

Figure 3.17. Fractography via SEM BSE (left) and SE (right) imaging of the failure surface obtained from quasi-static bending tests at two different magnifications. (1) Hexoloy SA-CP, (2a) Forceram, (2b) Improved Forceram, (3a) RBBC RB2 and (3b) RBBC RB2

Complementary mechanical properties

Due to their high cost, it is not often that ballistic tests are performed on ceramic materials to drive their optimisation. Instead, they are replaced by some mechanical characterisations, which are supposed to help forecasting the ceramic ballistic performance. Indeed, in the literature, most of the studies on armour ceramic development relate the effect of some of their microstructural features on their mechanical properties. However, because of the impact event complexity, the direct correlation between mechanical and ballistic performance is not trivial. Nevertheless, some mechanical parameters have been demonstrated to be relevant indicators for ballistic performance, at least for one stage of the ballistic event. By isolating the physical processes involved in a ballistic event, it is possible to apprehend which quasi-static and dynamic mechanical parameters might be indicators of good performance. The main mechanical properties referred to in the literature as beneficial to limit the projectile penetration and ensure its erosion are the ceramic compressive strength and hardness [12], even though the friction-flow property of ceramic fragments, related to their size [97] [114], is also expected to play a major role. However, some authors underlined that the compressive strength of ceramic, determined from quasi-static tests, might not reflect the ceramic strength when subjected to the high strain rate levels involved in a ballistic impact [184]. For this reason, the Hugoniot Elastic Limit (HEL) is presented as a more relevant material parameter. High elastic properties, such as Young's modulus, are also presented as important factors to ensure a high ballistic efficiency, as they are correlated to the speed of shock waves [3]. Finally, the fracture toughness (also called critical stress intensity factor) is often studied for armour ceramic development, as it is related to the material ability to resist crack propagation. Therefore, a high value is expected to limit the intense micro-fragmentation of the brittle ceramic [16]. These mechanical parameters seem to be involved in the various failure mechanisms induced during a ballistic impact, though they cannot definitively rank armour materials.

Some of the above-mentioned mechanical properties were provided by Saint-Gobain Research Provence for the Hexoloy and Forceram grades of ceramics and are summarize in Table 3.6. Young's modulus (E_{dyn}) and shear modulus (G) were determined using resonance flexural and torsion modes of vibration, respectively, according to the following standards [185]. The resonant frequencies, dimensions and mass of the specimen are used to compute both modulus and the Poisson ratio (ν) could be deduced from them. The one-dimensional wave velocity is calculated from the density and Young's modulus ($C_{1D\ wave}=\sqrt{E/\rho}$). The static fracture toughness was determined from Single Edge Notched Beam (SENB), according to the standards on specimens of dimensions 40 x 4 x 3 mm^3 via four point bending tests [186]. Elastic properties (ρ, E_{dyn} and ν) were used as input material properties for the elasto-plastic numerical simulations performed on Hexoloy and Forceram grades of materials in Chapters 4 and 5 and the numerical simulations with the DFH model on both Hexoloy grades in Chapter 6.

Table 3.6. Main mechanical properties of Hexoloy and Forceram grades of materials

	Hexoloy SA	Hexoloy SA-CP	Forceram	Improved Forceram
ρ (g/cm^3)	3.15	3.11	2.77*	2.82*
E_{dyn} (GPa)	430 [163]	390*	232*	246*
ν	0.14 [163]	0.12*	0.14*	-
$C_{1D\ wave}$ (m/s)	11680	11200	9150	9340
K_{IC} (MPa.$\sqrt{m}$)	3.0 [40]	2.9*	3.6 [165]	-

* data provided by Saint-Gobain Research Provence

The presence of size controlled large pores in the Hexoloy SA-CP grade slightly reduced the density of the material, compared to the Hexoloy SA. However, the presence of a higher porous volume lead to a decrease of the elastic properties (E_{dyn} = 390 GPa) compared to the dense Hexoloy SA (E_{dyn} = 430 GPa [163]). It can be noticed that this difference of pore size distribution has no clear effect on

fracture toughness. The presence of a porous network of about 10 % in Forceram grades reduces the material density, down to 2.77-2.82 g/cm^3. This low density makes this type of ceramics interesting for lightweight armour. The presence of a porous network seems to have reduced the elastic properties of the Forceram grades compared to Hexoloy grades. In addition, the higher fracture toughness of the Forceram material (3.6 MPa.$\sqrt{m}$ [165]), compared to the Hexoloy grades ($\sim$ 3 MPa.$\sqrt{m}$ [40]), might be related to the apparent meso-structure of the Forceram, with large grains acting as obstacles deflecting the crack path or bridging the crack to limit its opening [187].

Concerning the RBBC composite materials RB2 and RB3, they keep a dynamic Young's modulus of about 387 and 356 GPa, comparable to the Hexoloy SA-CP, despite the presence of the metallic phase. In the literature, the proportion of residual silicon phase and the size of ceramic grains are shown to directly affect the mechanical properties of the RBBC materials. Chhilar et al. showed that an increase of residual silicon in RBBC decreases its hardness, flexural strength and Young's modulus, but increases its toughness (RBBC $\sim$ 5 MPa.$\sqrt{m}$ compared to monolithic B_4C $\sim$ 3 MPa.$\sqrt{m}$) [188] [189]. A large range of fracture toughness, between 3 and 5.3 MPa.$\sqrt{m}$, can be found in the literature for RBBC materials, depending on the composition [182] [188] [189]. High values of the RBBC fracture toughness, are supposed to be linked to the large grains [179] and a relatively large proportion of metallic phase [188], which should absorb energy by crack deflection and bridging. Thus, the presence of a ductile phase, in limited proportions, is suspected to influence the crack propagation (ceramic toughness). Nevertheless, Hayun recommended a minimum proportion of silicon of about 12 vol. % to achieve good fabrication yields and limit cracks propagation [3]. Finally, the high fracture toughness obtained for the RBBC materials (in the literature $\sim$ 5 MPa.$\sqrt{m}$ for large B_4C grains [189] [179]) and Forceram grades are consistent with the privileged inter-granular failure mode observed, in the previous section, on the fracture surfaces of samples recovered from bending tests. Concerning the hardness, Aghajanian et al. noticed that the RBBC composite hardness is proportional to the volume fraction of hard phases (SiC and B_4C) [190] [4]. Yet, the silicon phase is considerably softer than the B_4C and SiC phases (Vickers hardness $\sim$ 11-12 GPa, E $\sim$ 160 GPa) [190]. However, Hayun highlights the fact that, for this type of composite material, the hardness refers to an average hardness of the multi-phase material [3].

3.3.2 Ballistic limit velocity of perforation

To evaluate the material potential for armour application and to compare different ceramic solutions, ceramic tile of each material were stuck on a 5 mm thick aluminum backing. This assembly was shot with a steel-core 7.62*51 mm P80 projectile at various speeds, ranged from 650 to 900 m/s. At least four samples of each material were impacted at different striking velocities to determine the minimal velocity at which the projectile perforate the system. This system does not fully translate the real conditions of the ballistic plate use, however, this set up easily allows an evaluation of the material potential for armour application and to compare different ceramic solutions. A picture of the shooting room is presented in Figure 3.18 (a), with the cannon in the foreground and the target in the background. Ballistic limit velocities of the commercial grades are voluntarily kept confidential, but a relative comparison of the grade of the same type of materials are given. In this specific testing configuration, the modified grades resulted in higher performance than their equivalent commercial products, as follows:

- for the same weight, the Hexoloy SA-CP material presents 5 % of ballistic limit velocity increase compared to the Hexoloy SA®

- the Improved Forceram presents 10 % of weight reduction compared to Forceram® for a same ballistic performance

Focus on the ballistic performance of RBBC materials

The ballistic limit velocity obtained for both RBBC materials, developed in the framework of the PhD thesis, is compared to two alumina ceramics in Figure 3.18 (b), with respect to their areal densities. A dotted line was plotted for RB2, tested with tiles of different thicknesses. Despite their differences of particle size (B_4C and β-SiC), both RBBC metal-ceramic composites presented almost similar ballistic performances, with values around 750 and 890 m/s for areal densities of 20 and 25 kg/m^2, respectively. In the literature, the size distribution of the ceramic grains are found to have an effect on the mechanical properties (fracture toughness, bending strength, hardness), as detailed in the previous section. However, concerning the ballistic properties, no distinction could be made between the two materials, made of different B_4C and β-SiC particle size distributions. In the tested configuration, RBBC materials allowed reaching a weight decrease of 20% and 13% compared to alumina ceramics of 98 and 99.7% purity, respectively, while keeping the same ballistic performance. This result is in line with observations made by Cafri et al. They demonstrated that RBBC materials present a ballistic efficiency twice higher than alumina-based light armours through depth of penetration tests [191].

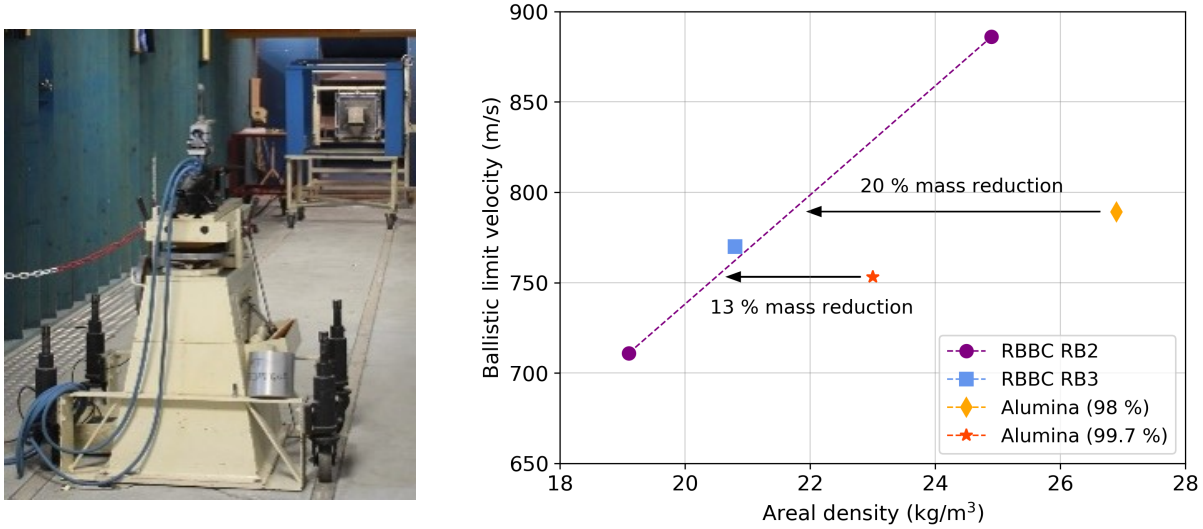

Figure 3.18. (a) Set up for ballistic characterisation. (b) Ballistic limit velocity vs ceramic areal density

Conclusion of the chapter

This chapter focused on the presentation and characterisation of the studied ceramic materials. To have a relatively complete picture of the link between microstructural features and the dynamic performance, six materials were included in this work. These materials can be paired in three families in which the two materials present very similar properties:

- The first pair of materials, named Hexoloy grades, includes dense silicon carbides presenting an homogeneous microstructure, with small and uniform grain sizes of the same composition (SiC). They present some few defects such as pores (voids, sintering defects at the grain boundaries) and residual sintering agents. Between the two materials, the only changing microstructural parameter is the size distribution of porosity, as spherical pores of controlled size are homogeneously distributed in the Hexoloy SA-CP material.

- The second pair of materials, named Forceram grades, is also made of SiC, but only partially as it is densified via reaction-bonding. The two materials of this type present large SiC grains ($\sim$ 50-150 μm) and a small-grains of SiC and a binder ceramic-phase generated in situ. Such a composition results in an apparent meso-structure. A porous network is present in the two materials and only differs in terms of volume proportion and local distribution.

- The last pair of materials studied presents the main particularity of having almost no pores. Called RBBC (Reaction Bonded Boron Carbide), these materials are made from the reactive infiltration of a liquid silicon metal in a boron carbide green part. The resulting microstructure is multi-phase, with ceramic grains of variable sizes (1-150 μm) and an inter-granular metallic phase. The main difference between the two materials of this type is the size distribution of initial B_4C grains and β-SiC particles, generated in-situ during the reaction-bonding process.

Pre-existing flaws in ceramic materials are mainly process-induced defects. Therefore, this chapter included a brief description of the manufacturing processes involved in the shaping of the studied ceramics. Scanning electron microscopy and X-ray computed tomography were used as complementary techniques to identify the microstructural defects in each material. The type of defects (pores, inclusions, heterogeneities) and their main characteristics (size, morphology, spatial distribution) could be clarified from analyses performed at different scales. The X-ray tomography technique had the key advantage of offering a sampling description of the defects in the material bulk. Several quantitative data could be extracted from micro-tomography post-processing to describe the pores, inclusions and meso-structure. Except for the RBBC materials, the porosity seems to be the most critical type of defect present in the studied materials, compared to inclusions, in terms of amount (volume proportion) and size. Cumulative density of pores could be extracted from X-ray tomography analyses. This information is of major interest to improve the modelling of ceramics fragmentation behaviour under tensile loading, as this failure mechanism relies on the presence of pre-existing critical defects in the material. Such a realistic microstructural description (flaw population) will be integrated into the micro-mechanical modelling developed in Chapter 6. From complementary quasi-static tests, it was possible to evaluate the variability of the material flexural strength, from the determination of the Weibull parameters in both Hexoloy grades. These Weibull parameters are directly related to the homogeneity of the defects, responsible for failure under quasi-static loading. They will be used as inputs in the modelling work. Fractographies provided a better understanding on the weak elements of the microstructure and some correlation between the fracture path and microstructural features.

In addition, the mechanical properties of ceramics have proven to be variable in between the different families of materials. The Hexoloy SA shows high elastic properties ($E_{dyn} = 430$ GPa) thanks to its small grain size and high homogeneity, whereas the Forceram grades take advantage of their heterogeneous microstructures (meso-structure) to reach relatively high fracture toughness ($K_{IC} = 3.6$ MPa.$\sqrt{m}$). As for RBBC materials, they seem to be a balanced material thanks to the near absence of porosity, which allows good elastic properties to be achieved ($E_{dyn} \sim 370$ GPa), and the combination of coarse grains and a soft metallic phase, which could slow down the propagation of cracks, according to the literature ($K_{IC} \sim 5\ \sqrt{m}$ when containing large grains). The determination of their ballistic limit velocity of perforation in the same configuration shows that, despite their very different microstructural features and mechanical properties, they all present good ballistic performance. Both RBBC materials, developed in the present work, show promising performance for lightweight amour, when compared to alumina products. These preliminary ballistic tests highlighted some improved ballistic performance, between the two materials of the same type, presenting different porosity distributions. So far, these gains in terms of ballistic performance are not properly understood, but they motivated the present work to better understand the link between the microstructural properties of a ceramic armour and its response to an impact. In order to further clarify the role of microstructural features on the ballistic performance, it is required to perform well controlled dynamic tests, with controlled stress states and strain rates, inducing failure mechanisms similar to those activated during a ballistic impact. The next Chapter 4 focuses on the fragmentation behaviour of these six grades of armour ceramics under relatively high loading-rates, through dynamic laboratory tests.

4 | Dynamic fragmentation and residual strength of the fragmented ceramic

Contents

Upon impact, the propagation of a spherical compressive wave generates hoop tensile stresses in the ceramic target. When the tensile state exceeds the activation stress of any pre-existing flaw in the material, multiple cracks, oriented perpendicular to the tensile loading direction, are nucleated (radial cracks). In addition, the literature review in section 2.2.3 showed that the size and morphology of the generated fragments, below the projectile nose, are expected to influence its penetration in the fragmented target, mainly due to the fragments abrasiveness and flow properties. In this chapter, the dynamic fragmentation and residual strength of the fragmented media (2^{nd} and 3^{rd} phases of a ballistic event) are investigated for the six ceramic materials, via three laboratory tests. These dynamic impact configurations correspond to the Edge-On-Impact (EOI), Normal and Tandem impact tests, introduced in section 2.2.1.

The EOI experiment consists in impacting a ceramic tile on its edge with a rigid projectile. In such a configuration, it becomes possible to visualize the fragmentation process on the sample surface (2D), usually inaccessible as it occurs in a cone localized in the bulk of the material [96] [192]. This test was first performed in an open configuration to visualize the fragmentation process (chronology and crack patterns). Then, EOI and Normal impact were performed in a sarcophagus configuration. The use of a casing allows the fragments to remain close to their initial position, for their further study via X-ray tomography. The Normal impact provides a configuration closer to a ballistic impact, as the sample is loaded in the same direction and is subject to a 3D-like expansion upon impact. This is especially important for materials with an anisotropic microstructure, like the Forceram materials presenting a gradient of porosity in the tile thickness. A comparison of the fragmentation behaviour of the different materials is expected to give further insight on the ability of the microstructures to withstand cracks opening and propagation. The experimental results in terms of cracking density are related to the

local strain rate responsible for failure, estimated from elastic numerical simulations. In addition, the potential of each microstructure to prevent the projectile penetration in the fragmented system is evaluated through a Tandem impact. This test was developed in the framework of Rossiquet [40] and Zinszner [93] PhD theses. It involves a perforating impact on a pre-fragmented ceramic, to evaluate the residual strength of the fragmented media.

4.1 Fragmentation behaviour under edge-on-impact test

4.1.1 Experimental configurations: open and sarcophagus

EOI tests were performed on the six grades of ceramics in the exact same configuration to evaluate the effect of microstructural features on the fragmentation patterns and intensity. The nominal dimension of the ceramic tiles is 60 x 30 x 7 mm^3. The same cylindrical projectiles (Ø10 mm and 15 mm-height), made of a high elastic limit steel (1350 MPa), as Zinszner [93], were in the present work. The projectile was placed in Teflon sabots to be properly positioned in the gas launching tube. The projectile nominal speed was set to 180 m/s in order to simply generate an intense fragmentation of the ceramic. Few additional tests were performed at lower velocity around 100 m/s for both Forceram grades to observe the effect on the generated failure modes. A confinement tank was used to collect the fragments ejected from the impact, for further analysis. As the fragmentation process lasts only a few microseconds, it is required to use a high-speed recording device to capture the damage growth on the sample surface. In this work, a Kirana camera was used with a recording speed of 2 or 5 millions of frames per second (resolution 924 × 768 pixels). Main challenges associated with high-speed imaging are the lighting level throughout the duration of the test and the precise triggering for the event to be properly captured in the time allotted for recording. To do so, a flashlight with a 2 ms duration and an inter-frame time of 200 ns were used. Three speed gates, made of optical fibres spaced by 25 mm and were placed in the launcher tube to record the projectile velocity and trigger the flashlight. In parallel, a laser pointing at the rear face of the target recorded the material free-surface velocity and triggered the camera. In order to reach a clear contrast visualisation of the fragmentation process, the observed surface of the ceramic tile was mirror polished and the camera was placed along the reflection axis of the light, as shown in Figure 4.1 and 4.2 (a).

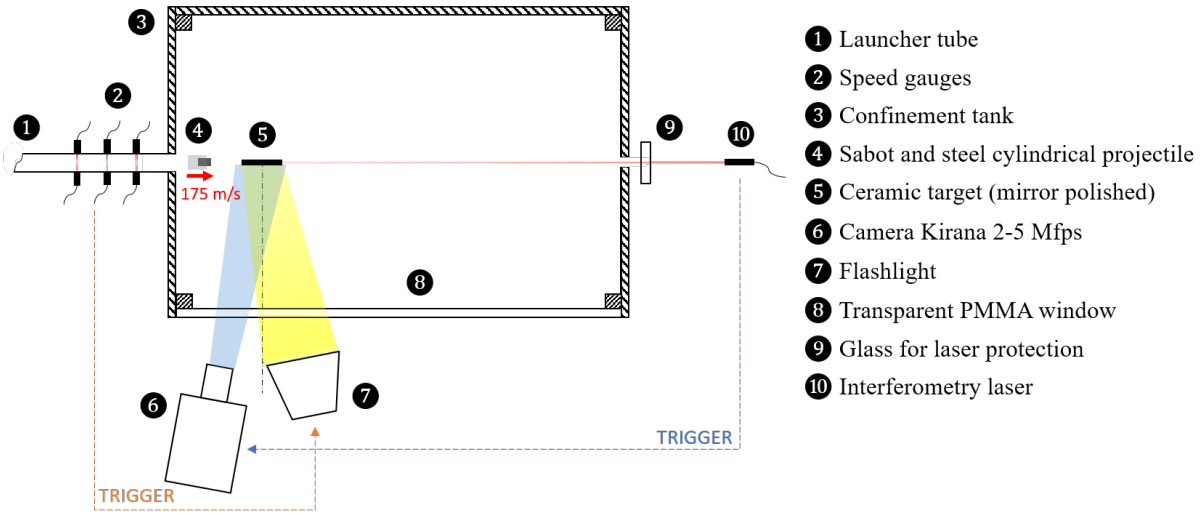

Figure 4.1. Top view of the Edge-On Impact test configuration

Further tests were performed on ceramics placed in a polycarbonate sarcophagus, as shown in Figure 4.2 (b). In order to limit the influence of the sarcophagus on the fragmentation process, an impedance discontinuity was allowed by placing 0.1 to 0.2 mm thick layers of scotch tape between the edges and

corners of the ceramic tile and the PC sarcophagus. In order to prevent the sarcophagus from being damaged upon impact, it was scaled so that the ceramic edge is the first element to be in contact with the projectile. Two small metallic shims in a *U-shape* were stuck on the sarcophagus to act as a stop-sabot. Such a polycarbonate casing combined the transparency and resistance required to capture the fragmentation growth and perform post-mortem analyses on the fragmented tile via tomography examination. Tomographic scans of sarcophagus are performed in the X-ray scanner in Laboratoire 3SR (scan duration of about 1h30-2h hours). A pixel size of 20 μm/pixel was yield while keeping the entire target in the camera field of view. All the EOI tests are summarized in Table 4.1 with the main characteristics.

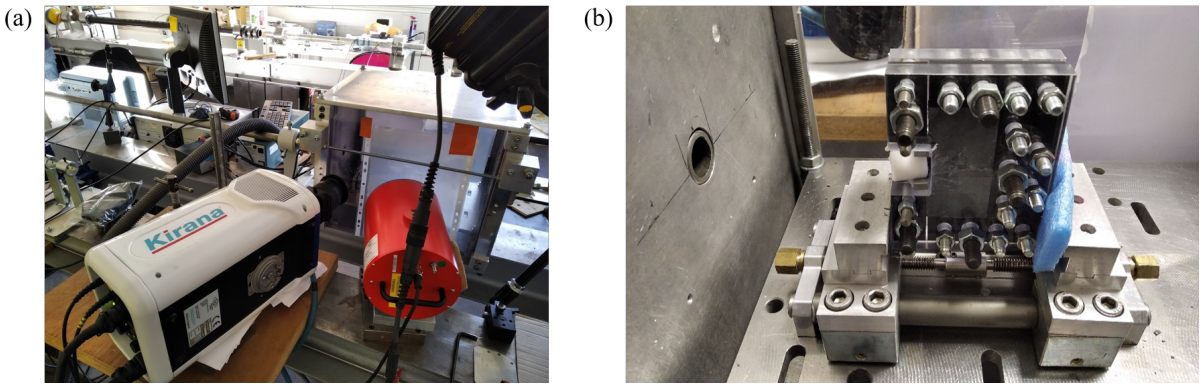

Figure 4.2. (a) Picture of the Edge-On Impact setup with recording and light devices. (b) View of an impacted polycarbonate sarcophagus at the exit of the launcher tube

Table 4.1. List of edge-on impact tests and characteristics

Material (sample reference)	Configuration	Impact velocity (m/s)	Camera frame rate (Mfps)
Hexoloy SA (2)	open	182.3	-
Hexoloy SA (3)	open	181.0	5
Hexoloy SA (1)	sarcophagus	182.1	-
Hexoloy SA-CP (3)	open	184.5	5
Forceram (4)	open	178.4	2
Forceram (6)	open	98.6	2
Forceram (7)	sarcophagus	182.3	5
Improved Forceram (3)	open	183.7	2
Improved Forceram (4)	open	98.9	2
RBBC RB2 (3)	open	175.66	2
RBBC RB2 (4)	sarcophagus	184.8	2
RBBC RB3 (2)	open	187.3	5
RBBC RB3 (1)	sarcophagus	183.7	2

4.1.2 Fragmentation chronology and intensity from ultra-high speed images

First, the use of ultra-fast imaging enabled to verify that the projectile correctly impacted the tile-edge, without tilt. Then, edge-on impact tests, combined to a ultra-high speed camera, allowed observing the 2D damage evolution in the ceramic tiles. A comparison of the fragmentation chronology between Hexoloy SA and Hexoloy SA-CP is presented in Figures 4.3. Pictures were selected between 2 μs and 12 μs after the projectile and ceramic-edge contact. This time range covers the fragmentation from its initiation till the end of cracks propagation. The black areas on the fragmented ceramic correspond to the loss of light reflection due to the inclination of the surface of certain fragments. Both materials

present Hertzian cone cracks formed by the compressive stress beneath the projectile nose and the induced tensile stress outside of the contact area. This conical area delimits a zone of high crack density. From 2D fragmentation patterns, the angle of Hertzian cone cracks seem to be lower for the Hexoloy SA (about 25-30°), corresponding to a larger damaged zone, than the Hexoloy SA-CP (about 35-40°). Moreover, the fragmentation chronology between both Hexoloy grades is very similar, with a fragmentation initiation and complete fragmentation reached around 3 μs and 7 μs respectively after contact, respectively. Both materials underwent an intense fragmentation, which will be quantified in the next section. It can be noticed that, during the 5-6 first microseconds, only radial cracks are visible. It is only after this elapsed time that the compressive wave and the released waves from the free surfaces (30 mm from the impact point) interact to create ortho-radial spalling cracks (circular shape). From these images, the Hexoloy SA-CP seems to present more spalling cracks at 12 μs, close to the rear face, than the Hexoloy SA.

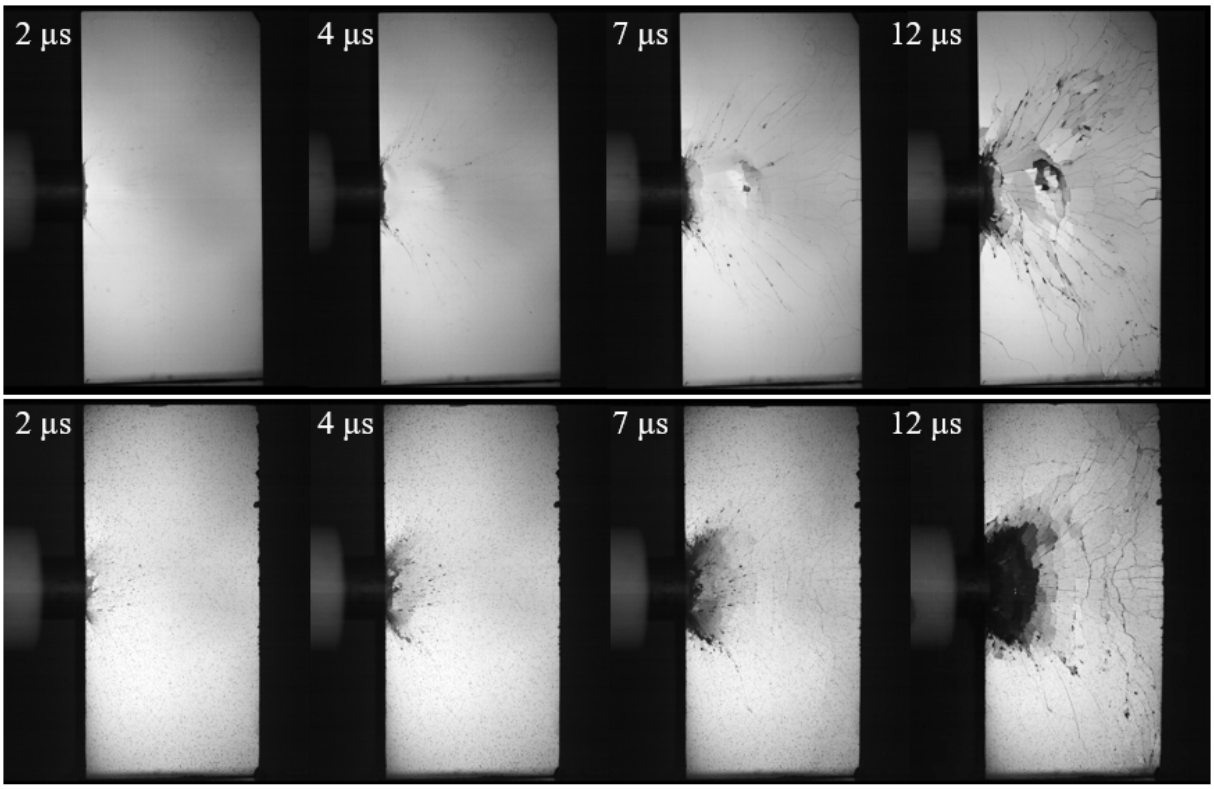

Figure 4.3. Fragmentation process of Hexoloy SA (top) and Hexoloy SA-CP (bottom) upon edge-on impact test at 181 and 182 m/s, respectively. Ultra-high speed camera frame rate: 5 Mfps

The fragmentation chronology captured for Forceram and Improved Forceram materials is presented in Figure 4.4. The presence of a higher level of porosity, compared to the Hexoloy grades, is visible from the lower amount of light reflected by the mirror polished surface. It has to be kept in mind that, in this EOI configuration, the median plane in the tile thickness of Forceram grades is along the loading axis. Thanks to the use of an ultra-high-speed camera, a clear difference of failure behaviours can be observed between the Hexoloy and Forceram types of materials. Whereas the impulsive load leads to the development of an intense fragmentation only 3 μs after impact for the Hexoloy grades, the fragmentation observed in the porous Forceram grades is delayed (10 μs) and attenuated, with remaining large fragments, which will be quantified in the next section. A possible explanation could be that this low fragmentation results from the collapse of porosity under the compression wave prior to the tensile loading. Indeed, the crushing of the porous network in Forceram grades could be responsible for some energy dissipation, preventing the intense fragmentation from developing. This type of pore collapse behaviour was previously observed for by Forquin et al. for the R-SiC ceramic (Saint-Gobain commercial product, named Crystar®) also presenting a porous volume of 17 %, when subject to EOI impact [106].

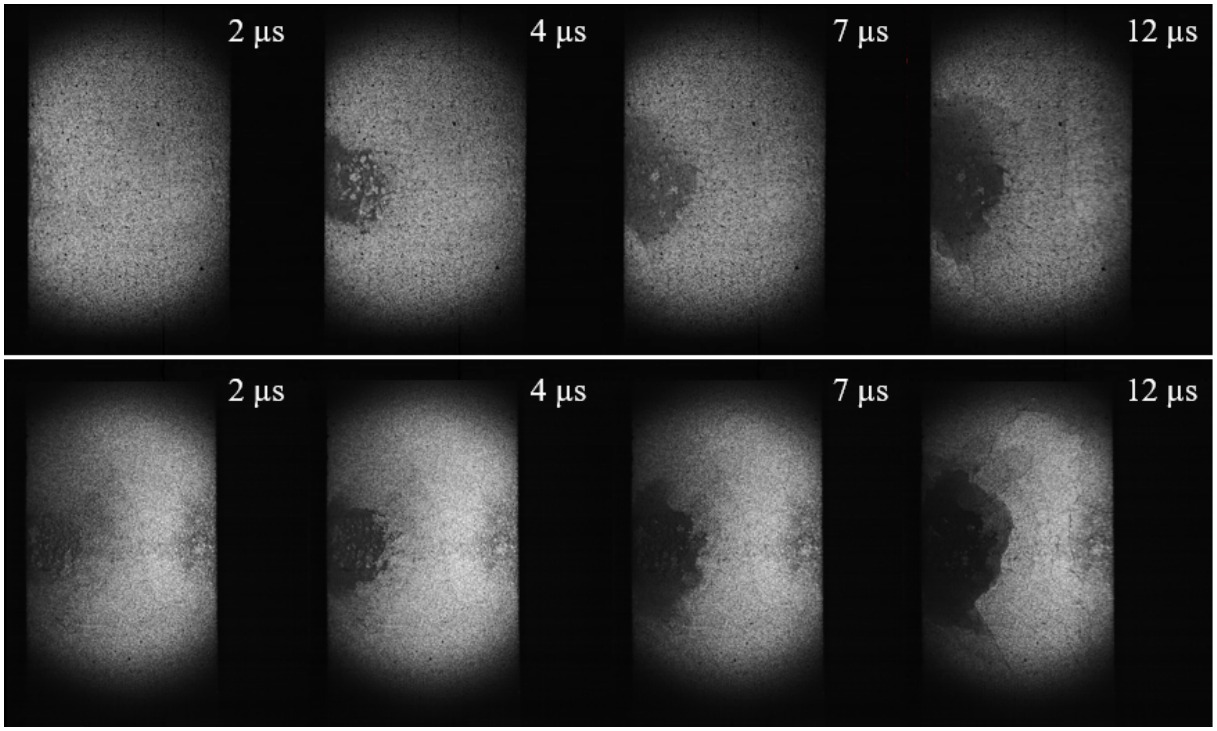

Figure 4.4. Fragmentation process of Forceram (top) and Improved Forceram (bottom) upon edge-on impact test at 178 and 184 m/s, respectively. Ultra-high speed camera frame rate: 2 Mfps

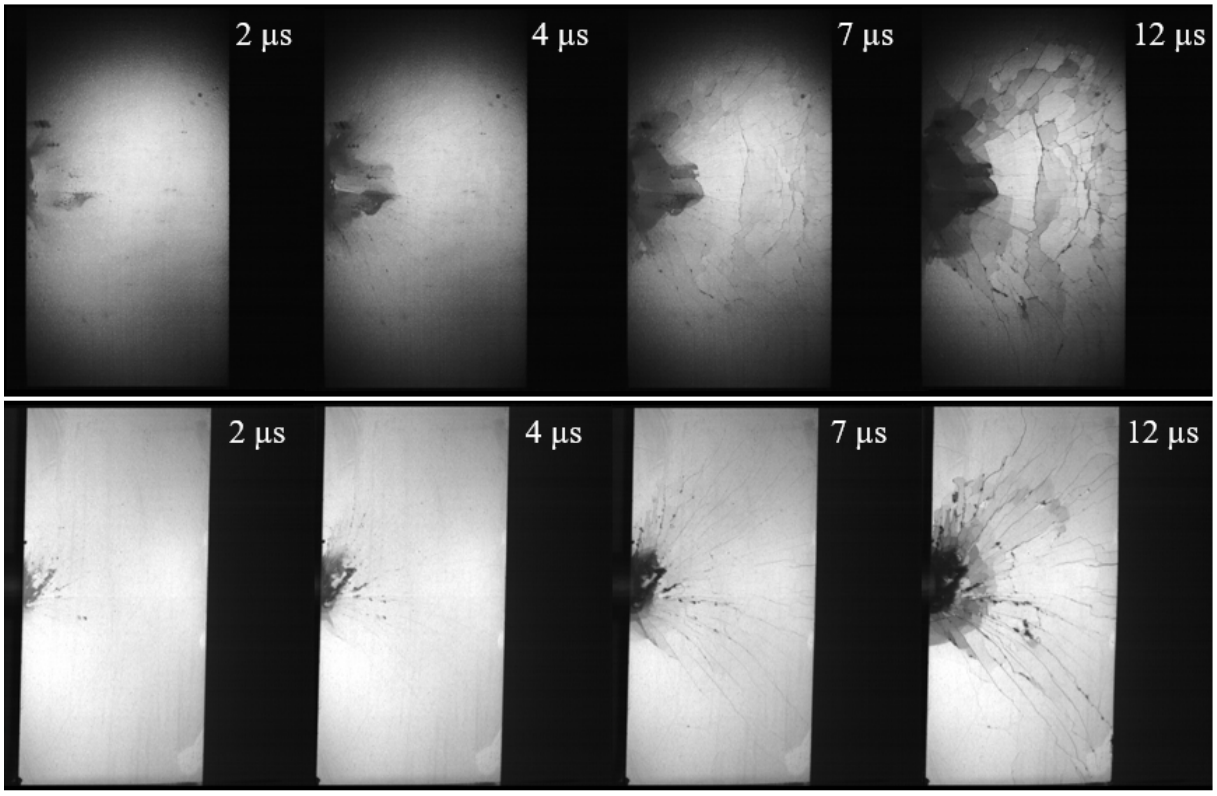

Figure 4.5. Fragmentation process of RBBC RB2 (top) and RB3 (bottom) upon edge-on impact test at 176 and 187 m/s, respectively. Ultra-high speed camera frame rate: 2 and 5 Mfps, respectively

As for RBBC materials, the high-speed camera images are presented in Figure 4.5. The fragmentation intensity seems to be intermediate between the two previous families of materials. The full fragmentation is reached about 5-7 μs after impact. Finally, no notable difference in terms of fragmentation chronology and failure mode induced upon EOI impact could be identified between the two materials of each type of materials from high-speed imaging. This can be explained by the fact that the damage chronology of brittle materials is highly related to their density and elastic properties. Therefore, differences in terms of fragmentation chronology are observed between the different families of materials presenting very different properties, but the 0.5 g/cm^3 or 40 GPa of density and Young's modulus difference between the ceramics of the same type was not enough to considerably affect the damage chronology.

4.1.3 Quantification of the fragmentation from sieve and micro-tomography analysis

In order to quantify the fragmentation intensity induced by EOI tests, ceramic fragments were collected after each test performed in an open configuration and were analysed using the ANALYETTE 28 ImageSizer [193]. This instrument consists in capturing photographs for a rate-controlled flow of particles (fragment here) passing in front of a large scale LED flash. This Dynamic Image Analysis (with up to 75 images per second) allows capturing both particle size and morphology. The telecentric lens enlargement (0.35x) used had an approximate depth of field of 5 mm, allowing the proper detection of powders and bulk solids of a size ranged from 40 μm to 9 mm. In order to have a reliable estimation of the fragments size distribution, the fragments collected from each test have been analysed three times. A cumulative size distribution was extracted for each test, as presented in Figure 4.6, with its dispersion due to the post-processing technique.

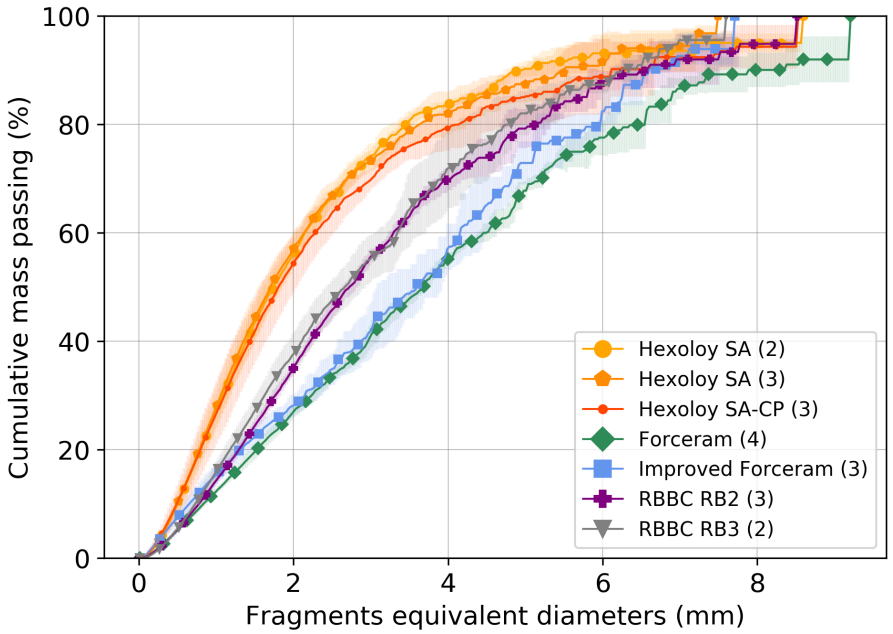

Figure 4.6. Fragment size distributions of all the ceramics from Dynamic Image Analysis, after EOI impact in the open configuration at about 180 m/s

EOI test in an open configuration was performed twice on Hexoloy SA (samples Hexoloy SA (2) and (3)). Both resulting fragment size distribution curves overlap in Figure 4.6, which confirms the good reproducibility of the test, but also the deterministic fragmentation behaviour of ceramic materials. The cumulative size distributions are in good agreement with the fragmentation tendency observed from the ultra-high speed images for the three families of materials. The fragmentation of the Hexoloy grades is the most intense with a large amount of small fragments, with about 55-60 wt. % of fragments smaller

than 2 mm. From the fragment size analysis, the Hexoloy SA-CP material seems to present a slightly less intense fragmentation compared to the Hexoloy SA material, with some large fragments reaching up to 8.5 mm (about 7.5 mm for the Hexoloy SA). The difference, in terms of particle size distribution, is clearly more pronounce when compared to Forceram materials. Forceram grades presented a larger amount of coarse fragments. Slightly coarser fragments were recovered from the impact of Forceram compared to Improved Forceram, with about 10 wt. % of fragments larger than 8 mm and none for the Improved Forceram. Both RBBC materials were found to have a similar fragmentation intensity with a level of fragmentation intensity intermediate compared to the Hexoloy and Forceram grades. Indeed, the weight proportions of fragments smaller than 2 mm corresponds to the ranges 55-60, 35-40 and 25-30 wt. % for Hexoloy, RBBC and Forceram grades, respectively. Moreover, no clear tendency in terms of fragments shape could be identified between the materials from the fragments morphological analysis.

Low speed impacts performed on the Forceram grades (100 m/s) did not show a consequent increase of the fragment size compared to impacts performed at 180 m/s, as shown on the fragment size distributions obtained from sieve analyses, in Figure 4.7. Models presented in the literature review in section 2.3 all converge toward an increase of the cracking density (decrease of the fragment size) for an increase of the applied dynamic tensile loading. Therefore, this result questions the type of failure mechanisms involved in Forceram grades. It supports the hypothesis of a failure under compressive loading, which could smooth the differences between the two compressive initial loadings, generated by impacts at 100 and 180 m/s. Thus, a collapse of porosity under the compressive loading could lead to an energy dissipation, prior to the tensile fragmentation.

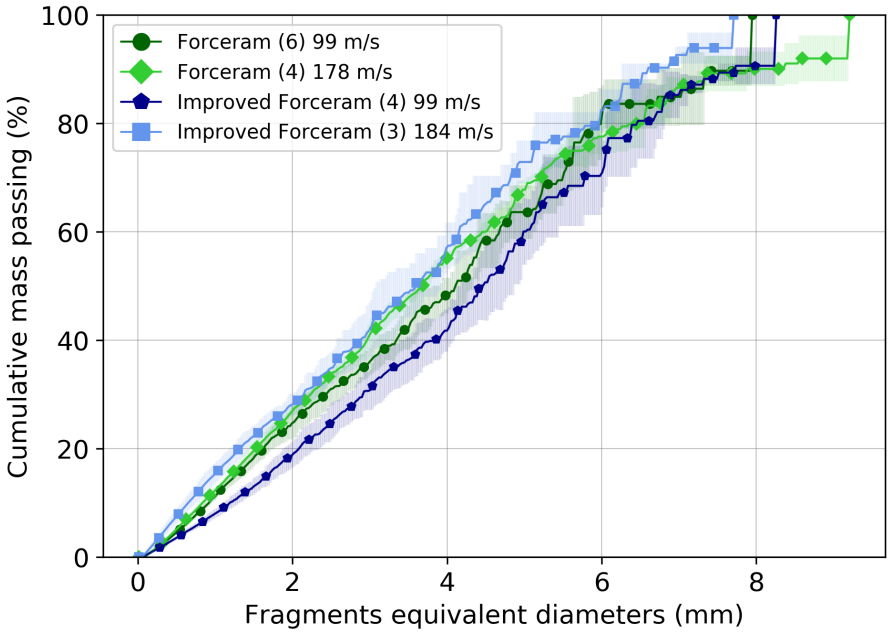

Figure 4.7. Fragment size distributions of the Forceram and Improved Forceram materials impacted at nominal speeds of 100 and 180 m/s

Finally, this first series of EOI tests, in an *open* configuration, showed an effect of microstructural properties on the size of the generated fragments, but only up to a certain extent. The differences of fragmentation were clear between materials of different families but more limited for materials of the same grade. In this section, the fragmentation quantification was compared for a given impact configuration (same projectile and impact velocity). The next section focuses on a way to evaluate the fragmentation intensity (cracking) in a given zone of the target, with respect to the local level of loading rate generated by the impact.

4.1.4 Strain rate and crack density estimation at a given distance from the impact

Determination of the strain rate from elastic numerical simulations

Elastic numerical simulations were conducted using the commercial Abaqus-Explicit Finite Element code to investigate the stress fields generated upon impact and leading to the ceramic fragmentation. On the basis of these calculations, the strain rate level was estimated at a given distance to the impact point. Elastic properties used for the ceramic are summarized in Table 4.2 and correspond to values presented in section 3.3. The behaviour of the projectile was considered elastic-perfectly-plastic with a yield stress of 1350 MPa. C3D8R elements are used to mesh the parts, with an average mesh size of 1 mm. Due to the two planes of symmetry associated with the problem, only a quarter of the projectile-target configuration is discretized. A surface to surface kinematic contact algorithm, with a frictional behaviour (friction coefficient of 0.2), is used to describe the contact between the target and the projectile. The projectile is given an initial axial velocity, corresponding to the value obtained experimentally. The stress fields are determined in a cylindrical coordinates system centered on the impact point. The radial and hoop stress fields induced in a Hexoloy SA target at 1, 2 and 3 μs after the EOI impact at 182 m/s, are presented in Figure 4.9.

Table 4.2. Material elasto-plastic properties considered for FE calculations

	Material	Density (g/cm^3)	E (GPa)	ν
Projectile	Steel [194]	7.8	200	0.3
Ceramic target	Hexoloy SA [163]	3.15	430	0.14
	Hexoloy SA-CP*	3.11	390	0.12
	Forceram*	2.77	232	0.14
	Improved Forceram*	2.82	246	0.14**

* data provided by Saint-Gobain Research Provence
** data not provided, taken similar to the Forceram material

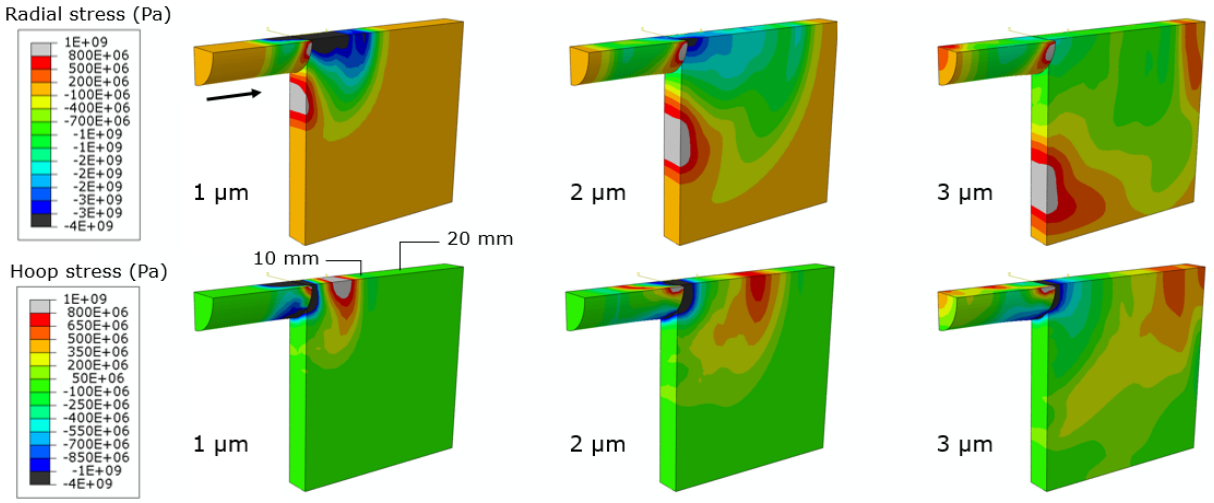

Figure 4.8. Radial and hoop stresses generated in an Hexoloy SA target impacted at 182 m/s in a EOI configuration, from elastic numerical simulations

These simulations demonstrate that the damage patterns obtained experimentally result mainly from the presence of hoop tensile stresses localised along the loading axis, following the compressive wave during the first microseconds. Once the compression wave is reflected at the free surface of the tile, a combination of radial and hoop tensile stresses increase the fragmentation. Therefore, to evaluate the

tensile strain rate reached during the nucleation of radial cracks, the hoop stress profile of elements on the loading axis was plotted as a function of time. Two different distances from the impact point (10 and 20 mm) were considered to evaluate the local stress and strain rates level ($\dot{\sigma} = E\dot{\epsilon}$), as shown in Figure 4.8. By assuming that during the fragmentation process the stress rate is constant (not influenced by the crack trigger), the slope of the curve corresponding to the tensile loading provides an estimation of the stress/strain rate. It is observed that the hoop strain-rate decreases with the distance to the impact point. Indeed, the strain-rate at 10 mm (9060 s^{-1}) is higher than the strain-rate at 20 mm (2560 s^{-1}). Strain rate estimations from elastic simulations are summarized in Table 4.3 for all tests conducted in a sarcophagus configuration. The margin of error on the strain rate was calculated from the gap of slope value depending on the time range considered for the linear regression. The lack of mechanical data (Poisson ratio) for RBBC materials limited their numerical simulation. It can be notice that elastic properties, different for each material, influence the level of strain-rate generated in the material upon impact. Thus, for the same impact velocity of 182 m/s, strain-rate levels reached in the Forceram ceramic (10140-2910 s^{-1}) are about 1.12-1.14 times higher compared to the Hexoloy SA (9060-2560 s^{-1}), regardless of the distance to the impact point. In addition, for the Forceram material impacted at 123 and 182 m/s, it can be noticed that a higher impact velocity generated higher strain rate levels in the target. Thus, for an increase of about 60 m/s, the strain rate level was multiplied by about 1.43 and 1.46 at a distance of 10 mm (from 7060 to 10140 s^{-1}) and 20 mm (from 1990 to 2907 s^{-1}) from the impact point, respectively.

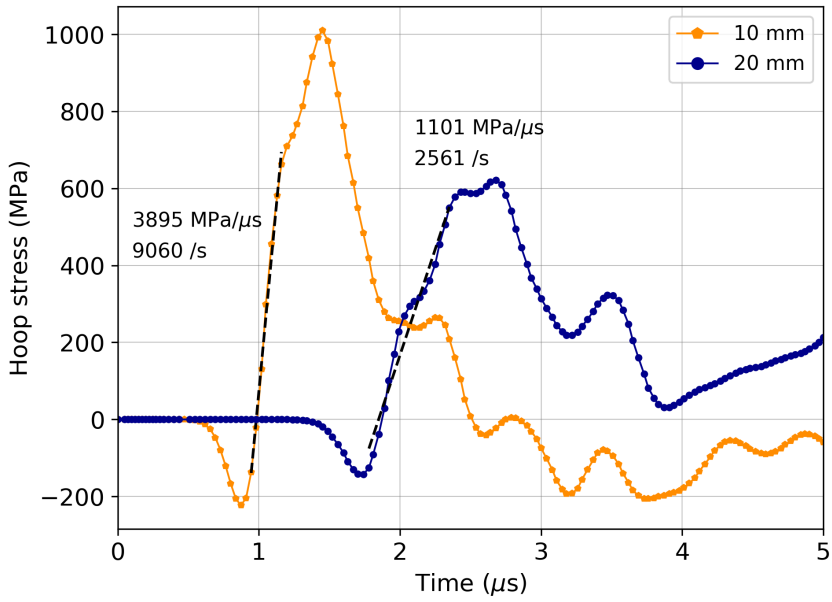

Figure 4.9. Estimation of the strain rate in Hexoloy SA (EOI 182 m/s), at a distance of 10 and 20 mm from the impact point (on the loading axis), from the profiles of the hoop stress as function of time

Table 4.3. Cracking density obtained from EOI impact and corresponding strain rate estimated from numerical simulations. Two distances to the impact point are considered: 10 and 20 mm

Material	Velocity	Cracking density (mm^{-3})		Numerical strain rate (s^{-1})	
		10 mm	20 mm	10 mm	20 mm
Hexoloy SA (1)	182.1	20.3 ± 3.2	2.5 ± 1.3	9060 ± 100	2561 ± 350
Forceram (5)	122.9	0.4 ± 0.2	0.3 ± 0.1	7060 ± 100	1990 ± 400
Forceram (7)	182.3	2.2 ± 0.7	0.6 ± 0.4	10140 ± 100	2907 ± 400
RB2 (4)	184.8	5.5 ± 2.6	0.3 ± 0.1	-	-
RB3 (1)	183.7	1.8 ± 1.2	1.1 ± 0.4	-	-

Determination of the cracking density from micro-tomography analysis

In order to quantify the fragmentation intensity in a given area of the fragmented target and be able to link this value to the strain rate previously evaluated, a sarcophagus configuration was adopted for the EOI test. Therefore, a second series of EOI tests were performed in polycarbonate sarcophagus, as described in section 4.1.1. Post-mortem sarcophagus were analysed via micro-CT tomography. A 3D-segmentation algorithm, applied to the reconstructed 3D-images provided further information on the 3D fragmentation patterns. Based on the local measurement of a Hessian gradient, the Python packages SPAM [176] provided a clear detection of cracks. For this step, a threshold value for the Hessian filter had to be chosen. From this, the fragments could be individually-labelled using the ITK watershed tool [173]. The most suitable value was determined by visually comparing the original 3D-image and the image with fragments identified as individual labels, to verify the proper segmentation of fragments. Due to the calculation cost of this Hessian filter, the size of the 3D-images (20 μm/pixel) had to be reduced by half for this post-processing, increasing the spatial resolution of the post-processed images to 40 μm/pixel. For Forceram grades, the presence of large pores (especially in the median plane) disrupted the Hessian thresholding, so an additional post-processing was necessary to fix the over-segmentation of fragments. An example of fragments identification from the 3D image post-processing is presented in Figure 4.10 for the Hexoloy SA (a) and Forceram (b) materials. Slices extracted from 3D reconstructed images and the corresponding fragment labels are presented via in-plane and cross section views.

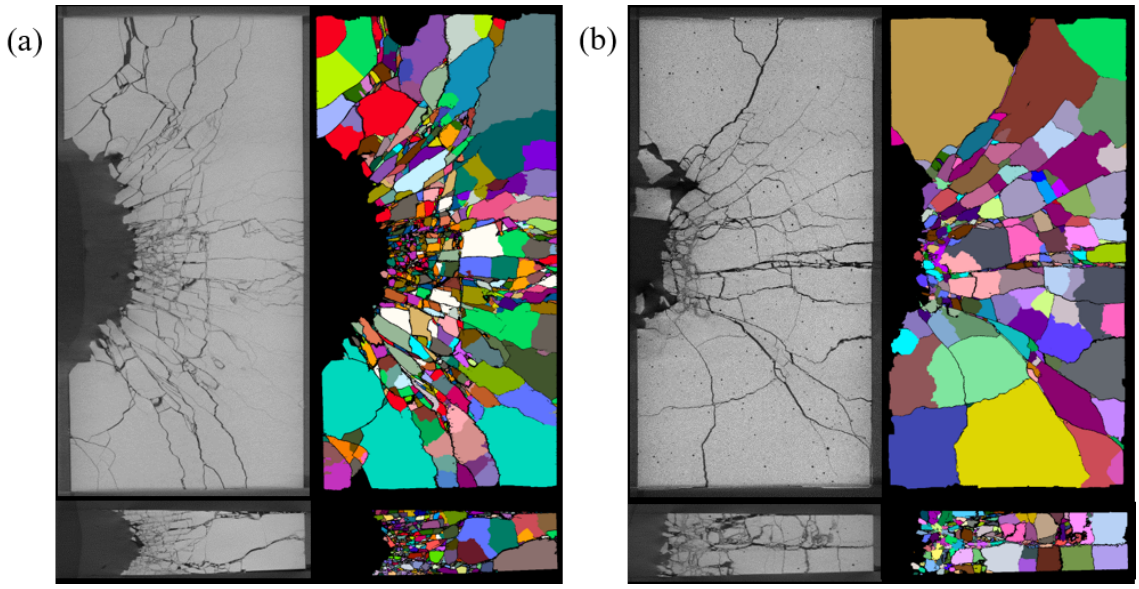

Figure 4.10. In-plane and cross-section slices of 3D-images and fragments identification of the materials (a) Hexoloy SA (1) and (b) and Forceram (7), impacted in an EOI configuration at 182 m/s

Thanks to this tomographic analysis, the cracking density in a given area of the post-mortem ceramic could be estimated. This information cannot be obtained from the random recovery of fragments after impact, but it requires from the fragments to stay close to their initial position. As introduced in section 2.2.1, to do so, it is possible to use a metallic casing and recover a single piece, containing the fragmented ceramic, after a resin infiltration. To evaluate the cracking density generated during their Normal impact tests, Forquin et al. used this technique of sarcophagus/resin and performed a surface mirror-polishing of the infiltrated sample [76]. From this, they could manually quantify the crack density on the rear face of the tile (2D), in a given area, by measuring the average distance between radial cracks. In the present study, the combination of a sarcophagus configuration in polycarbonate and micro-tomography analyses could be used for the crack quantification in the bulk sample (3D). Radial and orthoradial cracks, even if hardly opened, could be identified by micro-tomography. However, the spatial resolution of the scan (20 μm/px), in part limited by the dimensions of the sarcophagus, limit the quantification of the smallest

micro-cracks. For this reason, the cracking density estimation is a lower value for the quantification.

The tomography technique provided a visualisation of fragmentation patterns through the thickness of the post-mortem sample. Thus, the level of fragmentation was found to be stronger in the median plane of the Forceram material, than outside of this area. This observation could be explained by a stronger collapse of porosity under the compressive wave in this area, initially presenting a higher porous volume. In addition, most fragments in the Mescall zone were ejected from the sarcophagus upon impact, so the crack density could not be estimated in this area. The ejection of fragments under the projectile was found to be less pronounced for the Forceram compared to the dense Hexoloy SA and RBBC ceramics. In order to link the measured of crack density to the local strain rate, determined from elasto-plastic numerical simulations (in the previous section), areas close to the loading axis and mainly subject to hoop tensile loading were considered. An angle of $\alpha = 20°$ from the impact point centered on the loading axis is chosen, based on the stress field obtained from numerical simulations. From this, the cracking density is calculated with the following expression:

$$\lambda_{crack} = \left(\frac{N_{cracks}}{\alpha R} \right)^3 \tag{4.1}$$

where N_{cracks} corresponds to the number of cracks at a distance R to the impact point and α is expressed in radian. For the quantification of the cracking density, the number of cracks intersecting a circular arc at a radius R from the impact point was manually counted. This method to determine the cracking density is illustrated in Figure 4.11 (a). Due to the small area analysed for this counting (angle 20°), the cracking density quantification was done on 5 slices of the 3D-image, taken a equal distances through the tile thickness. These five results gave a margin of error on the quantification of the cracking density. Concerning the Forceram material, the quantification was not accurate in the median plane, where cracks were not radially oriented and too numerous to be properly quantified. Cracking densities obtained following this method are summarized in Table 4.3. The cracking density is plotted as a function of the strain rate in Figure 4.11 (b). It can be noticed that for all the tests, a reduction of the strain rate, moving away from the impact point, leads to a decrease of the cracking density. The overall fragmentation of the Hexoloy SA is more intense than the Forceram, in accordance with their fragment size distribution. From Figure 4.11 (b), the material Hexoloy SA presents a cracking density which is more sensitive to the loading rate than the Forceram.

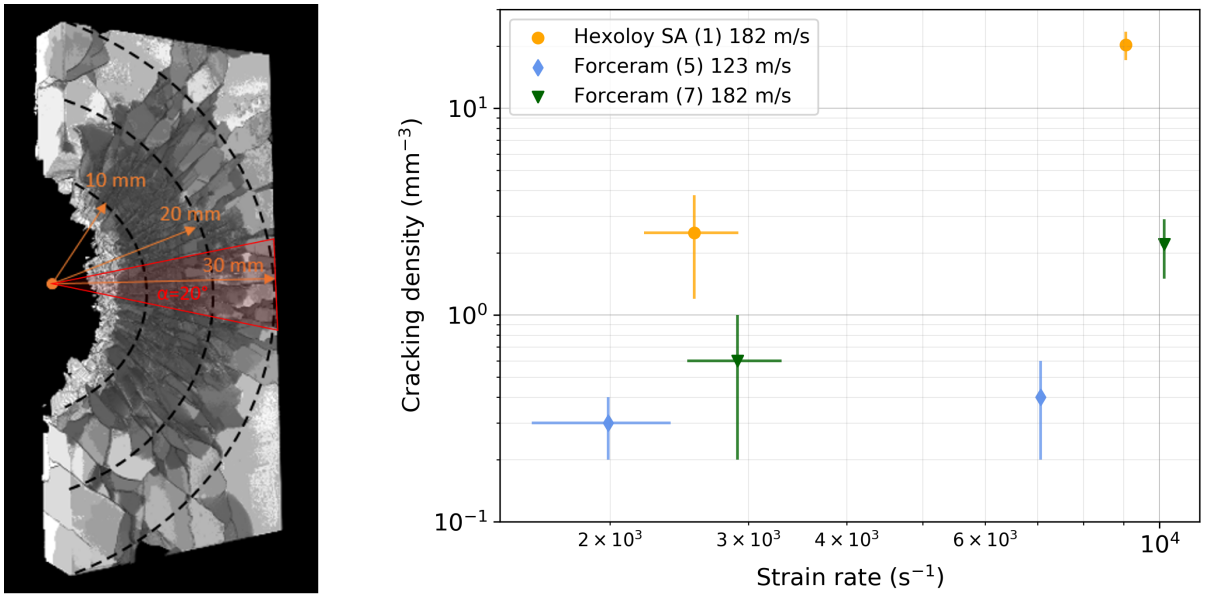

Figure 4.11. Representation of the distance to the impact point on a 3D fragmented tile reconstructed from tomography scan and zone of cracking quantification. Cracking density as a function of the strain rate (determined from numerical simulations)

4.2 Fragmentation generated by a Normal impact test

4.2.1 Experimental configuration: sarcophagus and resin infiltration

In Normal impact tests, the ceramic sample (50 x 50 x 7 mm^3) is impacted by the same cylindrical projectile used for EOI tests, but the loading axis is perpendicular to the ceramic tile. It was demonstrated in previous works that the failure mechanisms activated in EOI and Normal impact configurations are similar [194]. In the Normal impact configuration, previously introduced in section 2.2.3, the ceramic is confined between a 1 mm thick steel front layer having a high elastic strength of about 850 MPa and a backing in 6 mm thick aluminum alloy. This *sandwich* target is placed in a metallic casing. The configuration details are reproduced similarly to the experiments performed by Zinzsner et al., introduced in Chapter 2, but with ceramic tiles slightly smaller (compared to 60 x 60 x 8 mm^3) [194]. A schematic of the Normal impact configuration is given in Figure 4.12. The confinement of the ceramic sample in a metallic casing ensured its intense fragmentation, while keeping all the fragments close to their initial position. A gap of 0.1 mm between the ceramic rear face and the aluminum backing was imposed by sticking small pieces of tape at the corner of the ceramic tile. Zinszner showed from numerical simulation that this gap, limiting the total wave reflection at the rear face of the ceramic, provides a more intense and homogeneous cracking density along the loading axis [93].

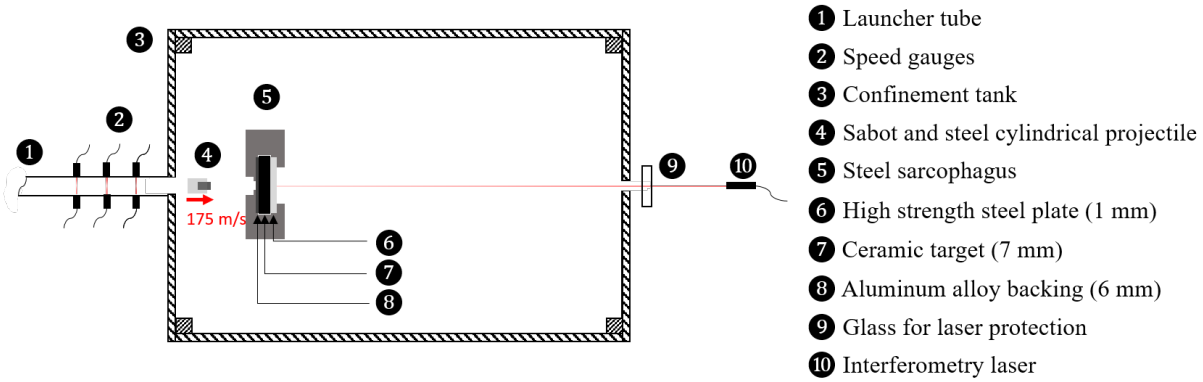

Figure 4.12. Top view of the Normal impact test configuration

Once impacted at a nominal velocity of 180 m/s by the cylindrical projectile, the front face of the sarcophagus was removed, keeping the fragmented ceramic in the sarcophagus. The confinement system is presented in Figure 4.13 (a) after removing the front metallic casing and the 1 mm thick steel front layer. The fragmented media (separated to the casing thanks to the plastic layer) has been infiltrated with a hyper-fluid resin under vacuum, as shown in Figure 4.13 (b). The one-piece fragmented ceramic was then removed from the casing for further analyses via micro-CT tomography. The list of tests performed in the Normal configuration and corresponding characteristics are summarized in Table 4.4.

Table 4.4. List of Normal impact tests and characteristics

Material	Aluminum backing	Impact velocity (m/s)
Hexoloy SA (2)	6 mm	178.5
Hexoloy SA-CP (2)	6 mm	172.3
Forceram (2)	4 mm	104.0
Forceram (1)	6 mm	174.6
Improved Forceram (2)	6 mm	181.4
RBBC RB2 (2)	6 mm	181.4
RBBC RB3 (3)	6 mm	181.4

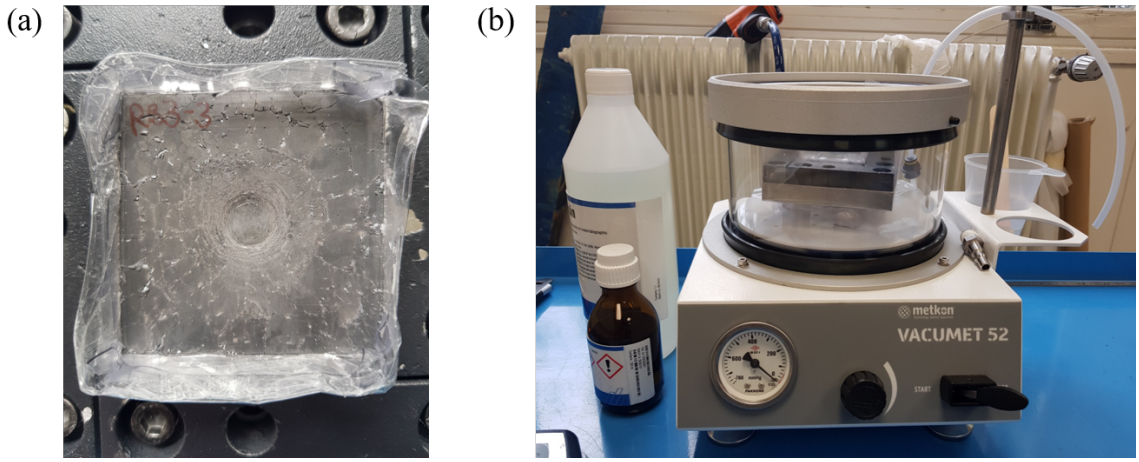

Figure 4.13. (a) Fragmented ceramic from Normal impact, after removing the front metallic casing (sample RBBC RB3 (3)). (b) Setup for the resin infiltration under vacuum

4.2.2 Quantification of the fragmentation from micro-tomography analysis

Post-mortem infiltrated ceramics were scanned via X-ray tomography, with a spatial resolution of 30 μm/pixel for all the samples. Similarly to EOI tests, the trajectory of cracks could be detected by an appropriate selection of a threshold value for a Hessian filter, applied to the 3D images reconstructed from the tomographic scans. From this cracks detection, the fragments could be individually-labelled using the ITK watershed tool [173]. Patterns of fragmentation after Normal impact are visible on the 3D image slices presented in Figures 4.14, 4.15 and 4.16 for Hexoloy, Forceram and RBBC grades of materials, respectively. Front face, rear face and cross section images highlight the variability of fragmentation patterns through the tile thickness. Corresponding segmented images are shown to illustrate the accuracy of the post-processing algorithm used to identify the fragments. The spatial resolution of 30 μm/pixel was sufficient to properly distinguish radial and orthoradial cracks, even if hardly opened. However, fragments in the Mescall zone could not clearly be identified because of the ceramic intense comminution and compaction under the projectile nose.

For all materials, the front face presents a relatively low fragmentation mainly due to the Rayleigh waves (circular cracks), whereas the released waves at the backside of the sample lead to a high increase of the cracking density visible on the rear face. Hertzian cone cracks present in the bulk of the tiles can be visualised on cross-section slices of the 3D-image. Same crack patterns were visible on the surface of the samples tested in the EOI test configuration. Hertz cracks initiate just outside the contact zone with the cylindrical projectile, propagate first perpendicularly to the front face and then progress downwards and outwards from the loading axis. The intensively fragmented zone at 15-20 mm from the tile-centre, on the rear face of the ceramic, corresponds to Hertzian conical cracks (conical in the cross-section). In addition, the presence of a median plane, with a different level of porosity, is visible in the cross-section images of the Forceram and Improved Forceram tomographic scans. This porous zone seems to have no clear influence on the cracks propagation close to the impact zone, whereas it seems to affect the trajectory of cracks further from the loading axis. This is visible on the large cracks delimiting the Hertzian cone, which path is deflected by the presence of the median plane in the tile thickness (some crack paths are dragged into this median plane).

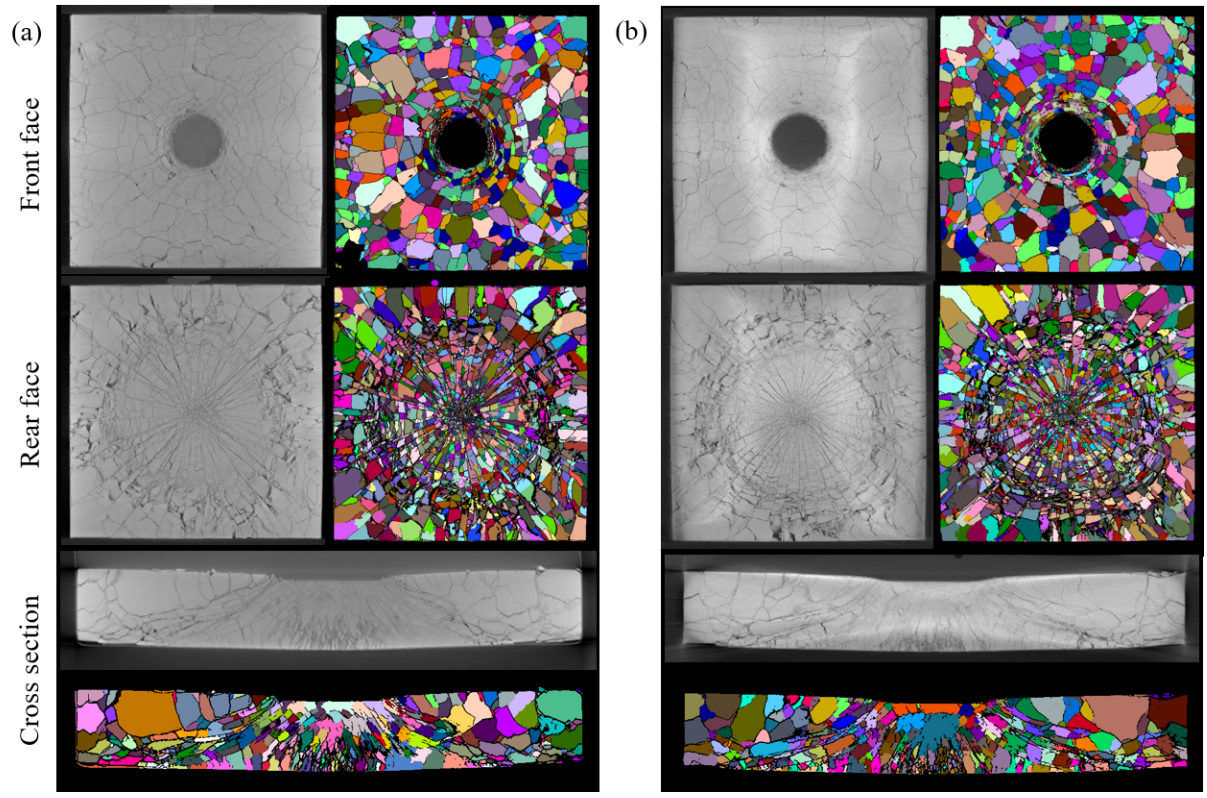

Figure 4.14. Slices extracted from 3D images of post-mortem materials (a) Hexoloy SA (2) and (b) and Hexoloy SA-CP (2), after a Normal impact at about 180 m/s. Fragments identification from post-processing using a 3D segmentation algorithm

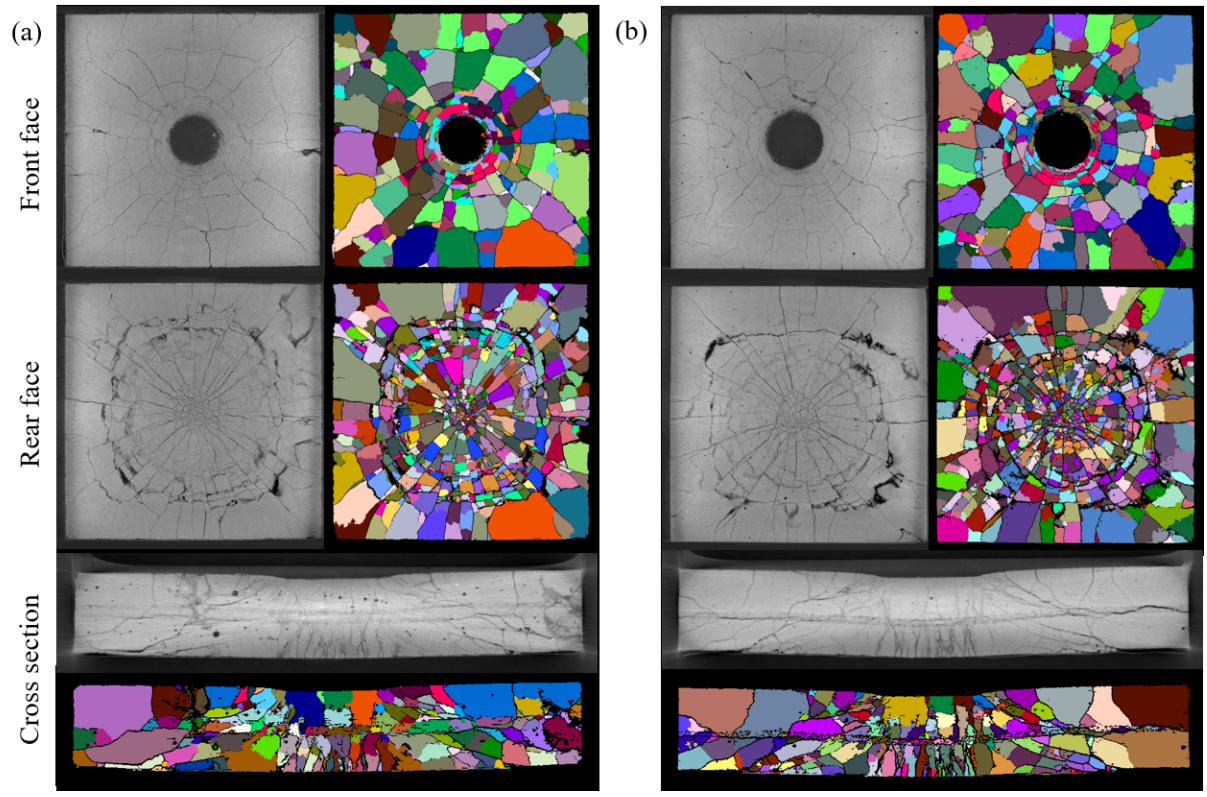

Figure 4.15. Slices extracted from 3D images of post-mortem materials (a) Forceram (1) and (b) Improved Forceram (2), after a Normal impact at about 180 m/s. Fragments identification from post-processing using a 3D segmentation algorithm

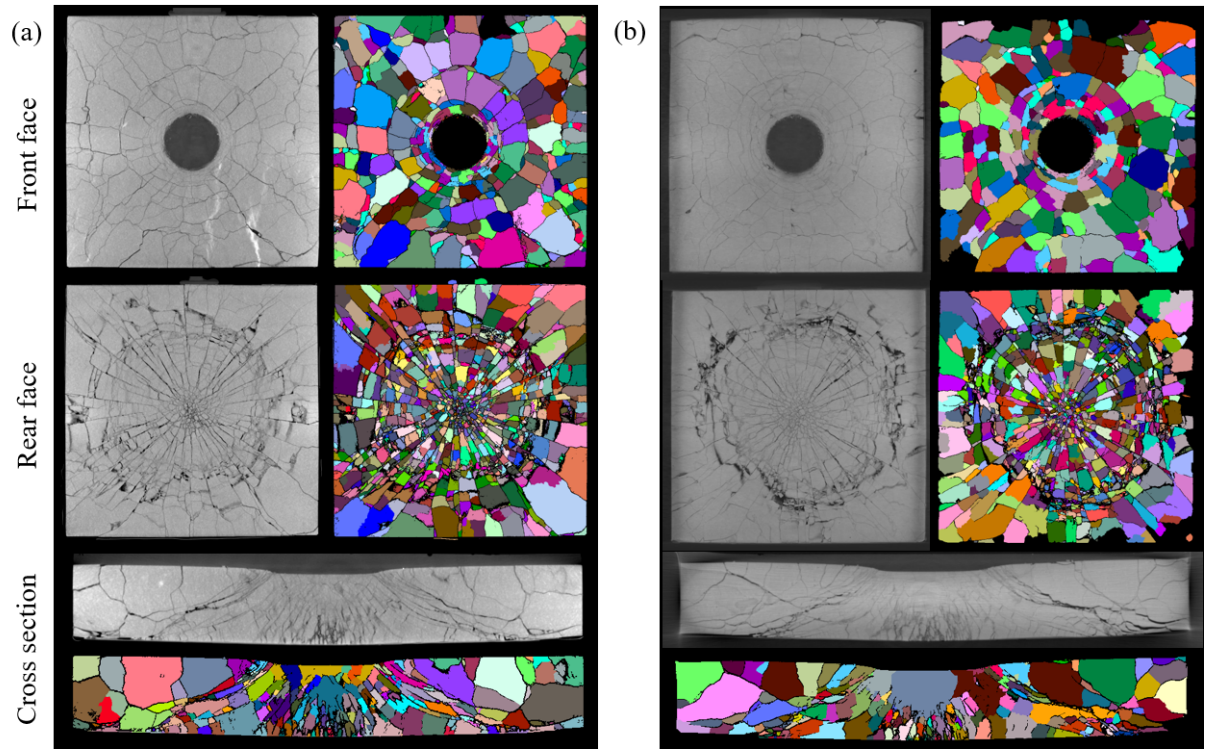

Figure 4.16. Slices extracted from 3D images and fragments identification of post-mortem materials (a) RBBC RB2 (2) and (b) RB3 (3), after a Normal impact at about 180 m/s

From these segmented 3D-images of the post-mortem samples, the size of fragments can be approximated to the equivalent diameter of a sphere of the same volume. With this approach on two SiC materials (EOI test), Forquin and Ando showed that a cumulative fragment size distributions can be obtained from the tomography segmentation, applied to the 3D-reconstructed image, and that resulting distributions are comparable to distribution obtained from classical sieve analyses (introduced in Chapter 2 section 2.2.1) [103]. Therefore, cumulative fragment size distributions obtained from tomographic post-processing on all the studied materials are shown in Figure 4.17. The ranking of materials, in terms of fragments size distribution, is in accordance with EOI tests. Indeed, Hexoloy grades present the most intense fragmentation with no remaining fragments larger than 7 mm. Slightly larger fragments were detected for the Hexoloy SA-CP, compared to the Hexoloy SA, with about 5 wt. % more fragments larger than 5 mm. Coarse fragments remained intact for the porous Forceram grades after Normal impact. Large fragments of about 8-12 mm correspond to about 80 and 90 % of the mass of Forceram and Improved Forceram tiles, respectively. The tendency for a more intense fragmentation of the Improved Forceram, compared to the Forceram, was firstly observed for EOI tests and seems to be confirmed by the Normal impact configuration. Loading the material in the axis of the median plane (EOI), or perpendicularly (Normal impact), did not consequently change both material fragmentation behaviours. As observed for EOI tests, the fragmentation of RBBC material is intermediate. However, the RBBC RB2 fragmentation seems to be a slightly less intense than for the RB3 grade of RBBC, and therefore more similar to the level of fragmentation observed in the Improved Forceram material. Comparisons made between individual material with the same type of microstructure must be taken with care, as fragment size distribution curves are sensitive to the post-processing. Moreover, it can be noticed that the overall fragmentation of ceramics in the EOI configuration is more intense than in the Normal configuration. This can be explained by the faster radial decrease of the loading in the Normal than the EOI impact configuration, as the EOI test is closer to a 2D impact configuration.

Finally, this comparison of fragmentation properties, between the studied materials, is made for the same loading condition (nature of the impactor and impact velocity). However, it has been shown from

the EOI numerical simulation conducted in the previous section that the loading rate generated in a material upon impact depend on the ceramic material properties. For this reason, the goal of the next section is to be able to compared fragmentation properties of different materials, but with respect to the level of loading rate generated in the target.

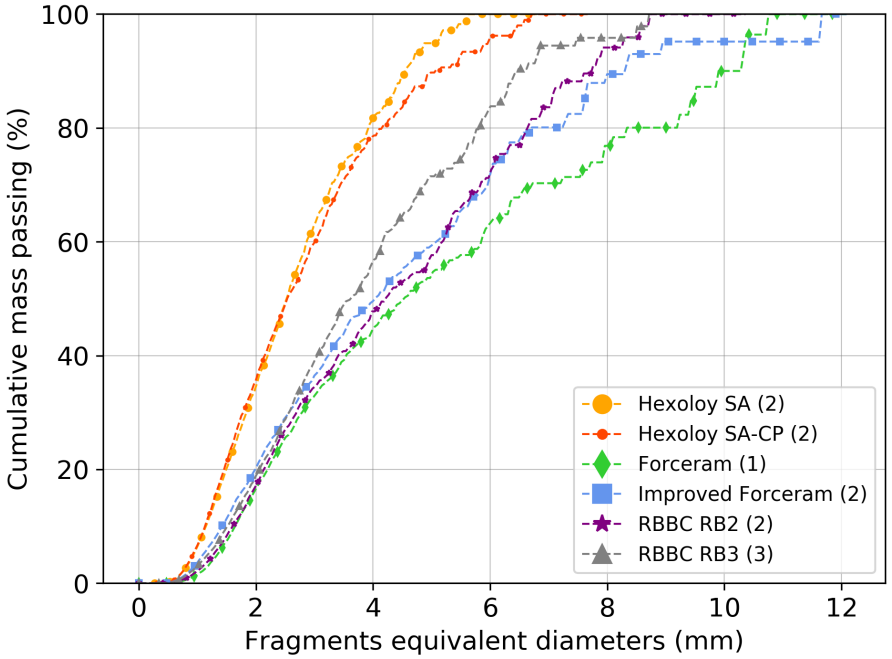

Figure 4.17. Fragment size distributions of all the materials after Normal impact from tomography scans post-processing using SPAM

4.2.3 Strain rate and crack density estimation at a given distance from the loading axis

Determination of the strain rate from elastic numerical simulations

Elastic numerical simulations were used to determine the origin of fragmentation under Normal impact. In this configuration the cylindrical projectile is given an initial axial velocity and impact a 1 mm thick steel front-plate, placed on the front face of the ceramic target. Elastic properties of the projectile and target were taken similarly to the EOI configuration. The 1 mm thick steel front cover-layer has the same elasto-plastic properties as the steel projectile, except a lower elastic limit of 850 MPa. C3D8R elements are used to mesh the parts, with an average mesh size of 1 mm. Due to the two planes of symmetry associated with the problem, only a quarter of the projectile-target-cover configuration is discretized. A surface to surface kinematic contact algorithm, with a frictional behaviour (friction coefficient of 0.2), is used to describe the contact between the projectile/cover-layer and the cover-layer/target parts. Radial and hoop stress fields, generated in a Hexoloy SA target, at 1, 3 and 4 μs after the EOI impact at 178.5 m/s, are presented in Figure 4.18. The Normal impact induces radial and hoop compressive stresses beneath the projectile and generates a tensile state on the rear face of the ceramic. Contrary to radial stresses, the field of hoop tensile stresses spreads radially, therefore being the main cause of radial cracks nucleation upon impact. In addition, the radial tensile stress visible on the front face of the ceramic corresponds to the Rayleigh waves, that would explain the circular cracks obtained experimentally.

As mentioned in the previous section for EOI tests, in order to estimate the rate of deformation responsible for radial crack initiation, care was taken to consider only areas where the fragmentation is due to hoop tensile stresses and not a combination of radial and hoop tensile stresses. Moreover, a local over-fragmentation, resulting from the presence of spall failure, was observed experimentally. Indeed, the

superposition of compressive and waves reflected on the tile edges lead to a tensile loading from which cracks nucleate on defects. In the elastic numerical simulations, only the first loading is considered and no coupling is implemented between the prior and future damage, thus, this type of fragmentation is not captured. Therefore, using elastic numerical simulations only allows an accurate evaluation of the strain rate to failure in a zone at a distance of 5-15 mm from the tile-centre. The tensile strain rate responsible for fragmentation (1-2 μs after impact) was estimated from hoop stress profiles at 7, 10 and 13 mm from the loading axis for the Hexoloy grades and 7, 10 mm for the Forceram grades. An example of hoop stress profile is presented in Figure 4.19 for Hexoloy SA impacted at 178.6 m/s in a Normal impact configuration. Strain rates estimations are summarized in Table 4.3. Similarly to EOI tests, the strain-rate level decreases for an increased distance to the impact point and the estimated strain rate levels differ between materials, due to their different elastic properties.

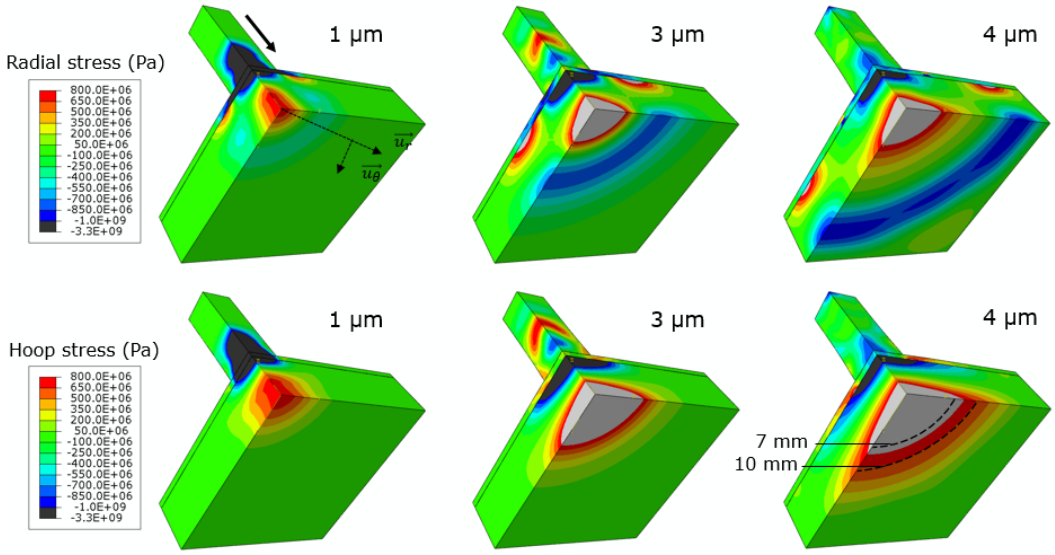

Figure 4.18. Radial and hoop stresses generated in an Hexoloy SA target impacted at 178.5 m/s in a Normal impact configuration, from elastic numerical simulations

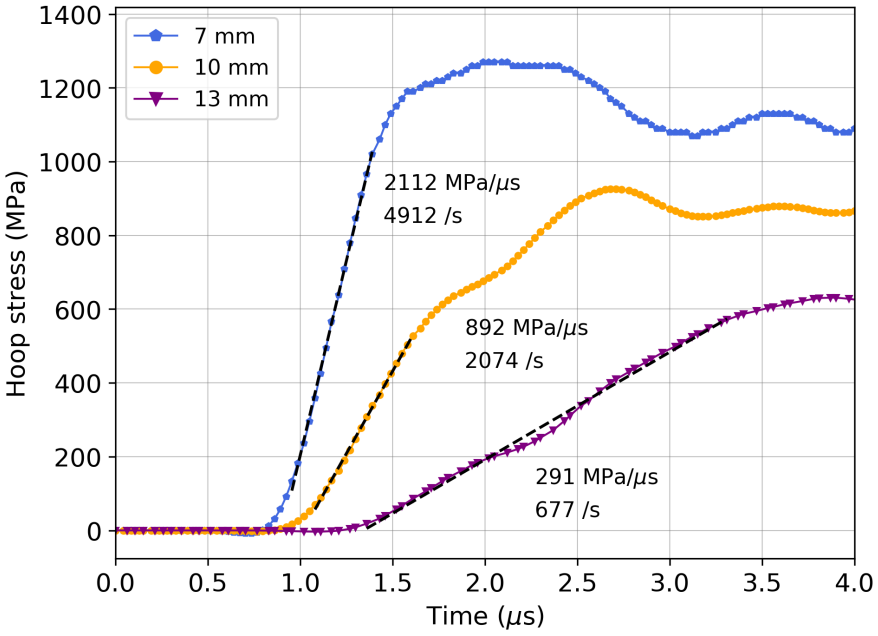

Figure 4.19. Profile of hoop stresses on the rear face of Hexoloy SA after a Normal impact at 178.5 m/s, at a distance of 7, 10 and 13 mm from the loading axis, and estimation of the strain rate

Table 4.5. Cracking density, obtained from manual counting, on the rear face of targets after a Normal impact and corresponding strain rate estimation from numerical simulations. Three distances to the impact point are considered: 7, 10 and 13 mm

Material	Velocity	Cracking density (mm^{-3})			Numerical strain rate (s^{-1})		
		7 mm	10 mm	13 mm	7 mm	10 mm	13 mm
Hexoloy SA (2)	178.5	12.1	3.24	1.67	4830 ± 160	1660 ± 330	668 ± 10
Hexoloy SA-CP (2)	172.3	6.72	4.67	3.25	4940 ± 200	1700 ± 370	683 ± 10
Forceram (2)	104.0	0.287	0.258	-	2800 ± 260	1450 ± 220	-
Forceram (1)	174.6	0.871	0.787	-	5790 ± 130	2060 ± 380	-
Impr. Forceram (2)	181.4	1.96	0.787	-	5970 ± 120	2060 ± 450	-
RBBC RB2 (2)	181.4	2.54	1.77	-	-	-	-
RBBC RB3 (2)	181.4	2.18	1.11	-	-	-	-
RBBC RB3 (3)	181.4	5.16	2.06	-	-	-	-

Determination of the cracking density from micro-tomography analysis

3D images, reconstructed from tomography scans, were used to extract the cracking density at a given distance from the loading axis. As shown from numerical simulations, near the loading axis, both stress fields (radial and hoop) generate a tensile load on the rear side of the ceramic. This is visible on the tomographic images presenting a high density of cracks with no preferential orientation in the rear face centre, Figure 4.20 (a) and (b). At a distance of about 5 to 15 mm from the loading axis, cracks are mainly radial cracks corresponding to hoop tensile stresses. Further ($>$ 15 mm) from the loading axis on the rear face, cracks delimiting the Hertzian cone and spall cracks from released waves (spall) lead to a high increase of circumferential cracks. Therefore, as mentionned before, the most interesting area to study, in order to link the cracking density to the corresponding strain rate at failure, is the circular area between 5 and 15 mm from the loading axis on the rear face of the ceramic. For a Normal impact test, the cracking density is calculated from the following expression:

$$\lambda_{crack} = \left(\frac{N_{cracks}}{2\pi R} \right)^3 \tag{4.2}$$

The cracking density was calculated on the slice of the 3D image, at the rear face of the fragmented tile. A manual counting of the cracks N_{cracks} that intersect a circle of a given radius R centred on the loading axis provided a quantification of the cracking density with equation (4.2). An example of manual determination of the number of cracks at a distance of 10 mm from the loading axis is presented on Figure 4.20 for the samples Hexoloy SA-CP (2) and Forceram (1). The obtained cracking densities at 7, 10 and 13 mm from the loading axis are summarized in Table 4.5 with the corresponding strain-rate levels, estimated from elastic numerical simulations (hoop tensile stress). The value obtained for the Hexoloy SA at 10 mm (3.24 cracks/mm^3) can be compared to the value measured by Forquin et al., on the same material from a manual counting of cracks on the mirror polished rear-surface of the infiltrated sample (0.94 cracks/mm^3) [76]. In their configuration of Normal impact at 175 m/s, the tile was thicker 60 x 60 x 8 mm^3 and the cracking density was measured at 11 mm from the loading axis. These differences possibly explain the slightly lower value obtained compared to the present study. Both types of RBBC materials present very similar cracking densities, with a relatively good repeatability for materials RB3 for which two samples were tested in the same configuration.

Obtained cracking densities are plotted as functions of the corresponding loading rate for a range of loading rates from 600 s^{-1} to 10^4 s^{-1} on Figure 4.21. Results of EOI tests are shown on this same graph for comparison. It can be noticed that same levels of loading rates were generated in EOI and Normal impact configurations. Results obtained for both configurations are in good agreement. All materials present an increase of the cracking density with the strain rate. The Forceram material displays a lowest cracking density compared to the other materials, over the full range of loading rates. The Improved

Forceram shows a higher cracking density than the Forceram. Both Hexoloy grades present a very intense fragmentation compared to Forceram grades. It is interesting to notice that the cracking density, in both Hexoloy grades, is not similarly sensitive to the loading rate. Indeed, the Hexoloy SA exhibits a greater increase of cracking density with the loading rate. Therefore, the relative level of cracking densities between both material is reversed above a threshold value of 3.10^3 s^{-1}. Below this value, the material Hexoloy SA-CP presents a higher cracking density than the Hexoloy SA, whereas above this threshold, the dense Hexoloy SA material shows a more intense fragmentation. A goal of the modelling work, developed in Chapter 6 on Hexoloy grades, is to better understand this type of fragmentation behaviour. In this section, the focus was on the fragmentation generated upon impact in a ceramic target, according to its microstructural properties and the loading rate. In the next part, the residual strength of the fragmented ceramic to a perforating impact is studied.

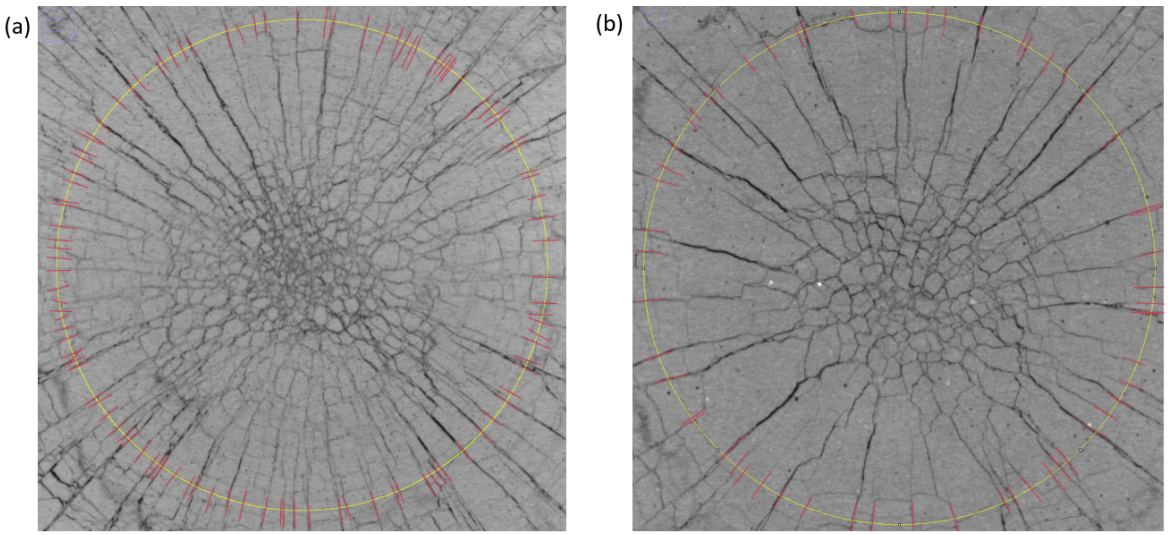

Figure 4.20. Determination of the crack number, at a distance of 10 mm from the loading axis, for the calculation of the cracking density. Rear slice of the 3D image for (a) Hexoloy SA-CP (2) and (b) Forceram (1), showing very different radial crack densities. 105 and 58 cracks detected, respectively

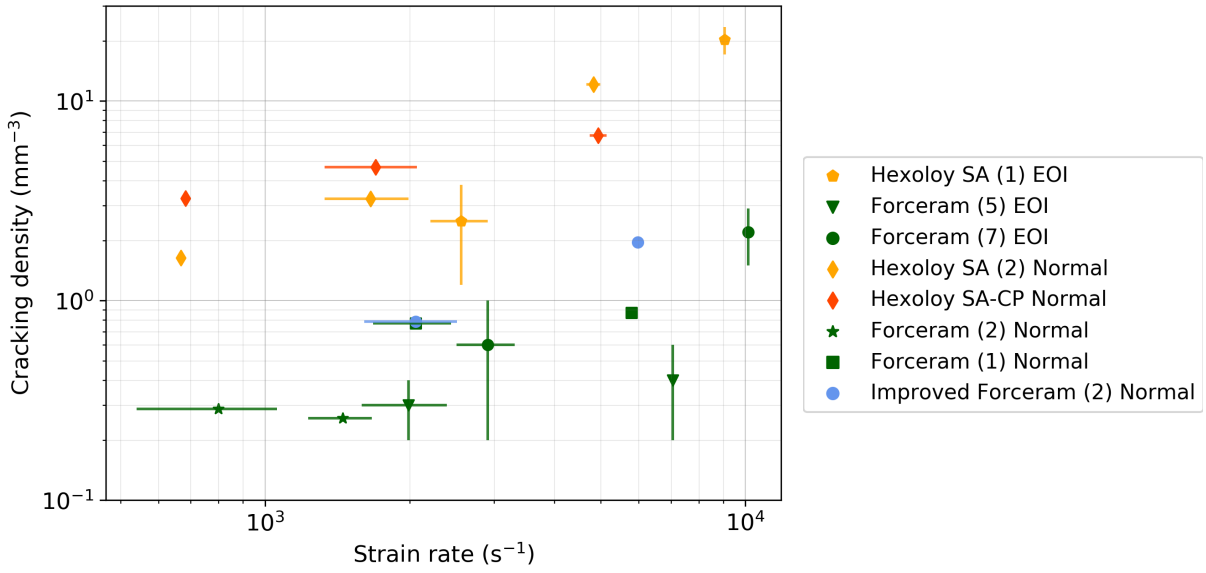

Figure 4.21. Cracking density, obtained from EOI and Normal impact tests, as a function of the strain rate, determined from numerical simulations

4.3 Residual strength of the pre-fragmented ceramic via a Tandem impact

4.3.1 Experimental configuration: two consecutive impacts

In order to predict the interaction between a projectile and a ceramic target, it is necessary to take into account the behaviour of the fragmented media and its resistance to perforation. This residual strength was evaluated using a test often called Tandem test, developed by Forquin and Zinszner [140] [194] and introduced in Chapter 2. This test consists in performing a second shot at the same velocity, but with a perforating projectile, on the ceramic tile already pre-fragmented from a Normal impact. Indeed, as the *sandwich configuration* and the metallic casing, used during the Normal impact, maintain the pre-fragmented tile in position, a second shoot can be performed on the pre-fragmented tile once the 1 mm thick front steel-layer removed. The perforating projectile had a conical head with a top angle of 90° and the same weight as the cylindrical projectile previously used (length 18.3 mm). A schematic of the Tandem test configuration is given in Figure 4.22. The interaction between the fragmented media and the projectile was recorded via the ultra-high-speed camera. The camera and flashlight set up is shown in Figure 4.23 (a). A picture of a pre-fragmented tile in the open sarcophagus is presented in Figure 4.23 (b). The free surface velocity at the rear face of the aluminum alloy backing was recorded via interferometry during the perforating shoot. This signal was first used to trigger the camera, but also used as a valuable information to evaluate the residual strength of the pre-fragmented ceramic. In order to prevent the sabot from passing in front of the camera field of view and hitting the pre-fragmented ceramic, a perforated plate placed at the exit of the launcher tube was used as a stop-sabot. The list of Tandem tests is given in Table 4.6.

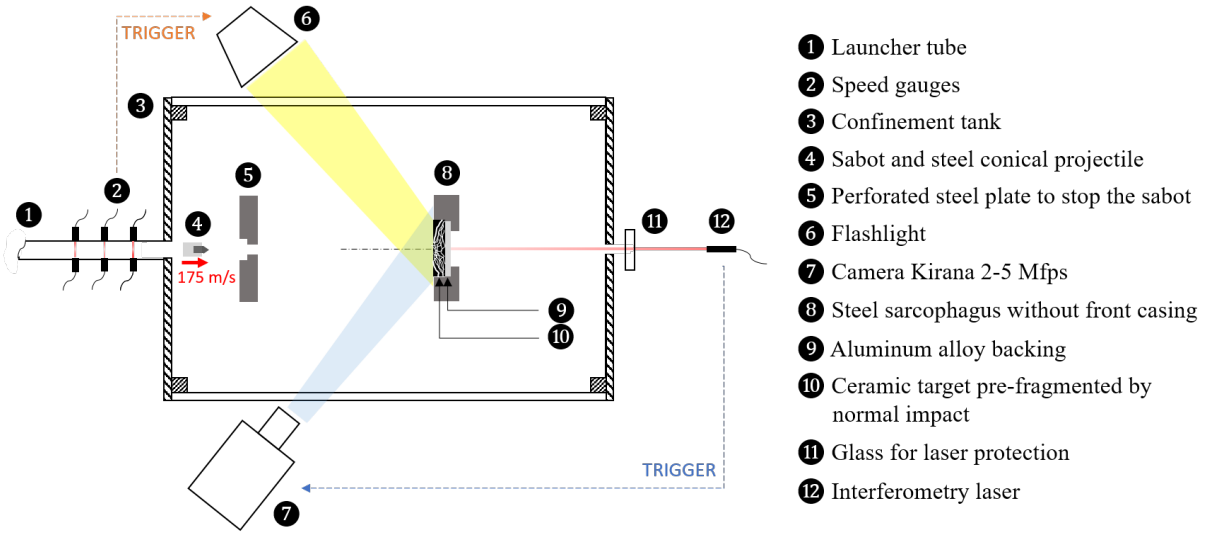

Figure 4.22. Top view of the Tandem impact test configuration

Table 4.6. List of Tandem impact tests and characteristics

Material	Normal velocity (cylindrical proj.)	Tandem velocity (conical proj.)	Camera frame rate	Backing velocity recording
Hexoloy SA (3)	184.2	178.2	2	✓
Hexoloy SA-CP (1)	180.9	178.2	2	-
Hexoloy SA-CP (2)	172.3	178.5	5	✓
Forceram (1)	178.2	178.2	2	-
Forceram (2)	172.3	178.5	5	✓
Improved Forceram (1)	175.1	178.2	2	-
RBBC RB2 (1)	175.1	184.2	2	✓
RBBC RB3 (1)	177.7	178.2	2	✓

(a) 

(b) 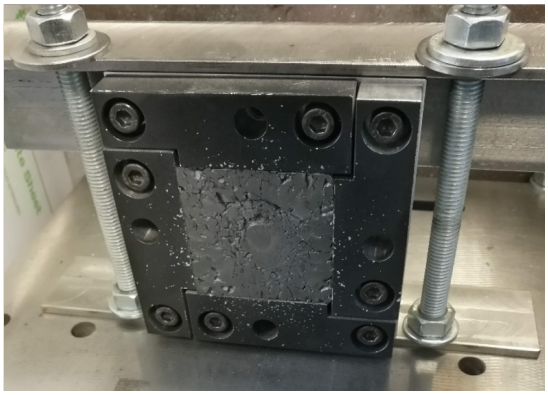

Figure 4.23. (a) Picture of the Tandem set up with recording and light devices. (b) View of pre-fragmented ceramic in the open sarcophagus before the perforating impact

4.3.2 Visualisation via ultra-high speed camera

Sequences of images of the Tandem perforating impact are presented for one tested sample of each type of materials in Figures 4.24, 4.25 and 4.26 (Hexoloy SA-CP, Forceram and RBBC RB2). The visualisation via ultra-high speed camera shows that, for some few tests, the projectile impacted the pre-fragmented ceramic with a slight tilt. This is probably due to the positioning of the stop sabot at the exit end of the launching tube, as no tilt was observed for the EOI tests. However, a small tilt is not expected to have a major effect on the results due to the conical shape of the projectile nose, which can offset a small tilt from the impact direction, whereas for EOI tests, a tilt on the cylindrical projectile would consequently change the loading of the sample, by reducing the strain rate generated in the ceramic sample. In addition, on some images a shadow of the projectile is visible. Also called as *ghosting*, it corresponds to the temporary overlap of subsequent frames. This effect is well known of ultra-high speed imaging, as it is frequent when an object is subject to significant translation (projectile here). It can be seen from Figures 4.24, 4.25 and 4.26 that during the first microseconds after impact, only fragments in the immediate vicinity of the impact point are ejected in the form of powder. Once stopped in its trajectory by the ceramic/aluminum-backing system, the projectile starts to rotate.

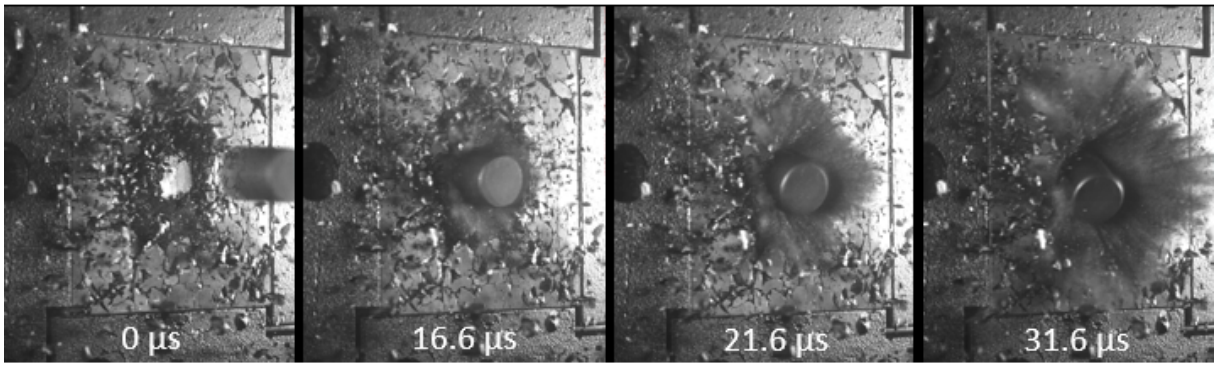

Figure 4.24. Sequence of images captured during the perforating Tandem impact on the pre-fragmented ceramic Hexoloy SA-CP (2), 5 Mps

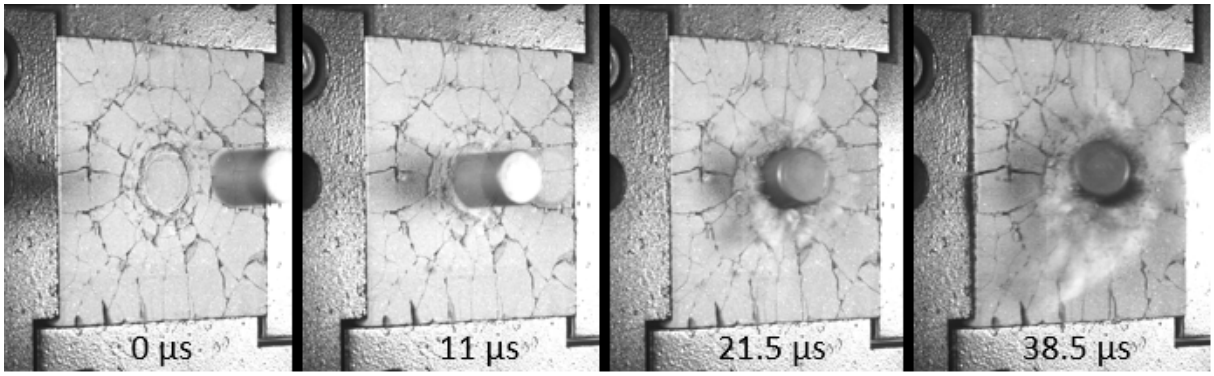

Figure 4.25. Sequence of images captured during the perforating Tandem impact on the pre-fragmented ceramic Forceram (1), 2 Mfps

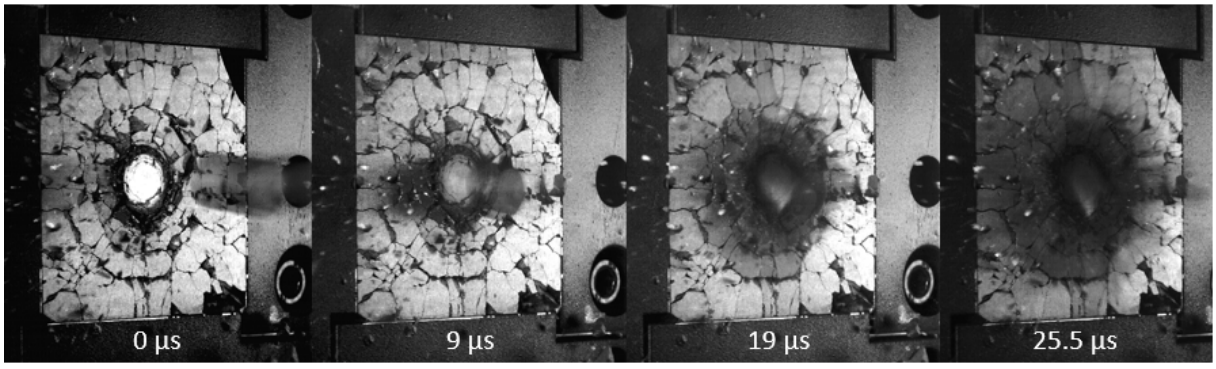

Figure 4.26. Sequence of images captured during the perforating Tandem impact on the pre-fragmented ceramic RBBC RB2 (1), 2 Mfps

4.3.3 Effect of the perforating impact on the fragment size distribution from sieve analysis

Similar sieve analyses than EOI tests, via the Dynamic Image Analysis instrument, were conducted on the fragments collected after Tandem impact. The resulting cumulative fragment size distributions are plotted in Figure 4.27. It can be noticed that the ranking of materials is consistent with previous results obtained from EOI and Normal impacts. Two tests were performed on the Hexoloy SA-CP material (samples Hexoloy SA-CP (1) and (2)) in the same configuration. The good overlap of both sieve curves confirms the high reproducibility of post-processing and the deterministic nature of the ceramic dynamic fragmentation. Two samples of Forceram (samples Forceram (1) and (2)) were also tested in the same configuration but did not show the same repeatability, with a small difference of about 5 points for the cumulative size distribution of fragments sizing from 4 to 8 mm. Such a difference could be attributed to the loading conditions (projectile tilted or slightly off-centre) or to the heterogeneity of the microstructure.

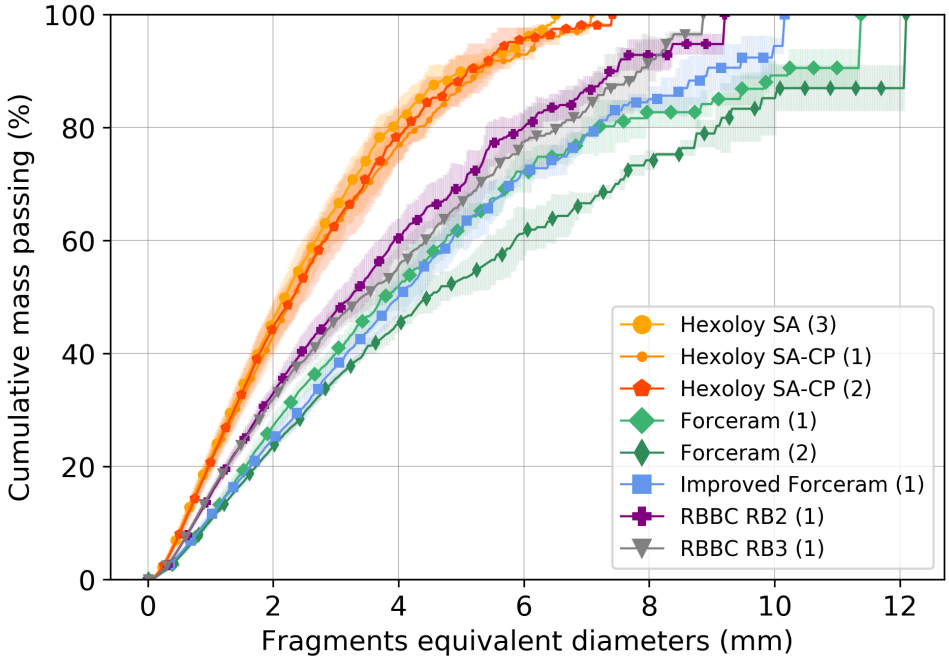

Figure 4.27. Fragment size distributions of all the ceramics from Dynamic Image Analysis, after Tandem impact at about 180 m/s. The only difference compared to fragmented size distribution resulting from normal impact tests concern the small fragments ($\sim$ 2 mm)

When comparing the fragment size distributions resulting from Normal (Figure 4.17) and Tandem impacts (Figure 4.27), the main difference concerns small fragments. For instance, the second perforating impact increased the mass proportion of fragments smaller than 2 mm of 10 points (from 35 to 45 %) for both Hexoloy grades, compared to a single Normal impact. The same observation can be made for the Forceram grades even though the fragment size reduction, due to the perforating impact, is less pronounced. Indeed, for the Forceram, fragments smaller than 2 mm correspond to about 18 % after the Normal impact and increase up to 25 % after the Tandem impact (7 points). Large fragments do not seem to be affected by this second impact. For instance, the mass proportion of fragments smaller than 4 mm of the Hexoloy and Forceram types of material remained around 80 % and 45-50 % after the second perforating impact, respectively. The exact same behaviour is observed for both RBBC materials with a mass proportion increase of about 12 points for fragments smaller than 2 mm. Therefore, the second perforating impact has only a low and local effect on the further fragmentation of the pre-fragmented ceramic tile. So, in principle, the residual strength of the pre-fragmented media detected from the velocity of the backing rear face should mainly correspond to the residual strength of the powder

comminuted just beneath the cylindrical projectile punching. It has to be noticed that the gap in small particles quantification between Normal and Tandem impact, respectively obtained from tomography post-processing and sieve analyses, can be partially due to the fact that committed fragmented beneath the projectile are not properly captured via tomography post-processing (limited crack opening in this area and spatial resolution of 30 μm). A second possible explanation is that fractured grains in Normal impact are completely separated upon the Tandem impact, therefore creating smaller fragments.

4.3.4 Residual strength of the pre-fragmented ceramic from rear face velocity profile

The ability to defeat an incoming projectile is directly related to the ceramic ability to absorb the projectile kinetics energy and reduce the impacting mass by eroding the projectile. Tandem tests allowed comparing the residual strength of pre-fragmented ceramics, through the evaluation of the load transfer to the backing plate during the perforation impact. The velocity of the aluminum backing was recorded via laser interferometry for some of the Tandem tests, as detailed in Table 4.6. Resulting velocity profiles are presented in Figure 4.28 for all the materials (except Improved Forceram). The clear jump of speed for the pre-fragmented Forceram ceramic, compared to other materials, is related to the loading bearing capacity of the fragmented media. As a complementary information, the Forceram material was found to present a lower backing deformation (420 μm) compared to the Hexoloy SA material (658 μm). Such results suggest that the pre-fragmented Forceram ceramic displayed greater resistance to perforation than the dense materials (RBBC and Hexoloy grades). Even by presenting the highest level of residual strength (most efficiency to dissipate the projectile kinetics energy), the Forceram sample (2) remains the material having the overall largest fragment size after two successive impacts in Figure 4.27. The greater residual strength of the pre-fragmented Forceram ceramic could be explained by the presence of relatively coarse fragments or/and the presence of hard large SiC grains ($\sim$ 100-150 μm) under the impactor nose. It was observed that the 1 mm thick steel plate used as front layer during the Normal impact, presented a very different surface aspect on its backside in direct contact with the ceramic, according to the ceramic material. When in contact to Hexoloy and RBBC grades, the high-strength steel under the projectile punch was smooth, whereas it was eroded with some embedded ceramic fragments and/or grains when in contact to the Forceram material. This observation underlines a higher abrasiveness of the Forceram large fragments compared to the small fragments of Hexoloy SA. This result substantiates the hypothesis, found in the literature, that a material subject to a thin fragmentation under impact presents lower resistance to the projectile penetration, whereas a coarse fragmentation provides more potential to erode the projectile and limit the penetration of the projectile [195].

In order to draw clear conclusions from these results, further testing would be necessary, with a repeatability study and considering the effect of different levels of ceramic pre-fragmentation on its residual strength. Nevertheless, this underlines that the pre-damaged crack network is a crucial information to be taken into account in models considering materials failure, as it seems to influence the projectile penetration in the fragmented media and might even dominate the microstructural features when it comes to projectile penetration. The velocity profile obtained from the backing rear face can be used as a way to calibrate numerical simulations and determine parameters via inverse method describing the behaviour of the fragmented ceramic [93] [144]. Moreover, the ability of an armour system to withstand multiple successive impacts is very complicated to assess as this property relies on the ceramic and backing association and the quality of the system integration (front layer, ceramic, confinement, etc.) [133]. The main interest of the present test is that it allows accessing the inherent ability of a fragmented ceramic to resist to an impact loading, independently of the system assembly.

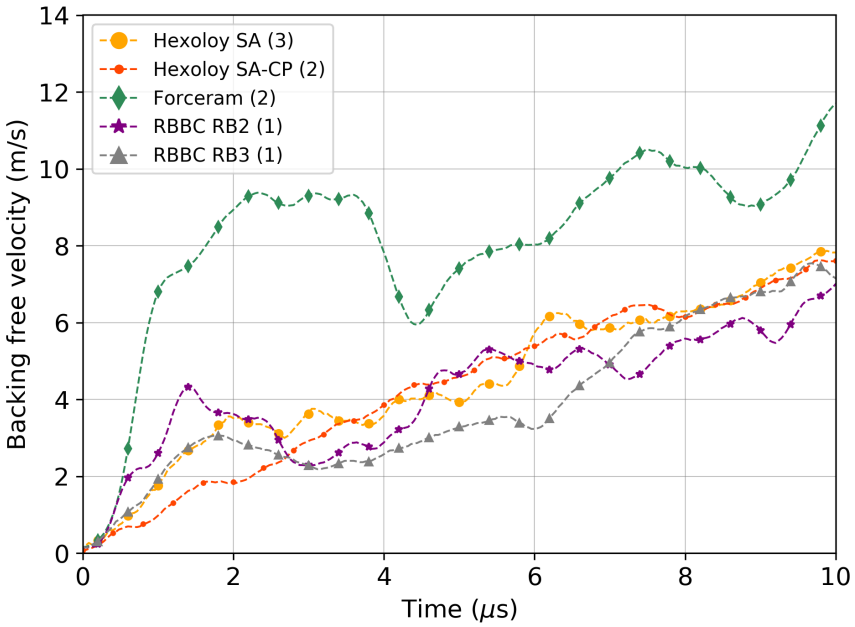

Figure 4.28. Velocity profile of the backing rear face during a Tandem impact

Conclusion of the chapter

Six grades of ceramics were tested in three impact configurations in order to identify the effect of the microstructural features on their fragmentation behaviour and residual strength of the fragmented media. Dynamic testing configurations allowed intermediate strain-rates (6.10^2-10^4 s^{-1}) to be generated in ceramic targets. The edge-on impact test provides a visualisation of the failure kinetics and therefore a possible comparison of the chronology of damage initiation and propagation between each material. The Normal impact configuration provided a fragmentation more similar to a ballistic impact as it has the same loading direction (for anisotropic materials) and generates a 3D-like expansion. EOI and Normal impact tests were performed in open and sarcophagus configurations for further study of fragmentation patterns. The main results obtained in this chapter are summarized as follows:

- the fragmentation behaviour of the studied ceramics is deterministic, in terms of damage chronology, crack patterns and particle size distribution. This was confirmed by ultra-high speed imaging and the analysis of fragment size distributions. EOI and Normal impacts tests allowed an evaluation of the damage severity induced in each ceramic upon dynamic impact. No clear difference in terms of fragmentation chronology could be observed between the Hexoloy grades and RBBC grades, whereas the higher level of porosity (9-13 vol. %) in the Forceram materials had an effect on the failure mechanisms. While the dense ceramics underwent a high fragmentation only few microseconds after impact, typical of brittle materials under dynamic tensile loading, the fragmentation of Forceram grades was delayed and the cracks density remained moderated. One hypothesis that could explain such a difference is a collapse of porosity in Forceram grades under the compressive wave, prior to the tensile loading. This bulk compaction could delay and attenuate the fragmentation process, therefore leading to the conservation of large fragments after impact. Another possible explanation is the high ability for the Forceram meso-structure (interconnected pores, porosity gradient, binder phase and large SiC grains) to limit the propagation of cracks.

- Hexoloy grades presented the most intense fragmentation, followed by RBBC ceramics and finally Forceram grades. This ranking, in terms of cumulative fragment size distributions, was found to be similar for all the three tests (EOI, Normal impact and Tandem impact). In addition, no clear distinction could be made between the two materials of the same family from fragment size distributions. Except for the Improved Forceram, presenting a slightly more intense fragmentation

than the Forceram material.

- In these testing configurations, the fragmentation properties were compared for the same impact configuration. However, elastic numerical simulations showed that the loading rate generated upon impact in the ceramic depends on its elastic properties. Therefore, to have a more accurate comparison of the fragmentation properties between materials, the fragmentation properties were evaluated through the determination of a cracking density and the corresponding loading rate at failure. To do so, tests in sarcophagus configurations were conducted. Tomography analysis of the fragmented ceramics in sarcophagus configurations (polycarbonate casing or fragmented ceramic infiltrated with a resin) is demonstrated to be a relevant tool to investigate the crack network (patterns) generated upon impact and quantify a global and local fragmentation intensity (overall fragment size distribution and local cracking density). The only limit is the scan spatial resolution for the detection of very small fragments (< 200 μm) and crack with limited openings, located close to the impact point. The cracking density could be quantified in specific areas of the tomography slices of the target (distance to the impact point). In parallel, elastic numerical simulations provided an estimation of the loading rate responsible for failure (hoop tensile stresses) in the corresponding areas. Such a study provides a more relevant comparison of the materials fragmentation properties and their sensitivity to the loading rate, over a range of 6.10^3 to 10^4 s^{-1}.

- A comparison of the cracking density, with respect to the loading rate, between the materials confirmed the lower fragmentation of the Forceram material. In comparison, the Improved Forceram material present a more intense fragmentation. This approach underlined the more intense fragmentation of Hexoloy grades compared to Forceram grades, on all the range of considered loading rates. An interesting point, was that the two Hexoloy grades did not show the same sensitivity to the loading rate. The Hexoloy SA material presented a more sensitive cracking density to the strain rate, compared to the Hexoloy SA-CP. Therefore, the Hexoloy SA-CP material, containing size-controlled large pores (about 2 vol. %, 40-100 μm), lead to a higher cracking density below a strain rate of 3.10^3 s^{-1}, but it was found to present a lower fragmentation above this threshold value. Such a result indicates that the presence of the large size-controlled pores might have influenced the fragmentation properties of the material, and that this behaviour is sensitive to the loading rate. The mechanisms responsible for such a behaviour will be studied in the modelling work in Chapter 6.

- Altogether, these experiments generate valuable qualitative (crack network) and quantitative data (cracking density) to be used for the validation of a fragmentation modelling in Chapter 6. Elasto-plastic numerical simulations of the EOI and Normal impact tests allowed an estimation of the strain rate level (from hoop tensile stress) reached in the cracked zones, to be related to the locally generated crack density. The quantitative analysis conducted in the present work, by using a ultra-high speed camera to record the damage kinetics and tomography to evaluate the local fragmentation intensity, are essential tools to support the development and validation of modelling and large-scale impact simulations.

- The Tandem impact testing configuration was used to gain insight on the ability of the pre-fragmented ceramic to limit the penetration of a perforating projectile. The pre-damaged Forceram material was found to present a highest residual strength to the penetration of a perforating projectile. Such a result suggests that the size (and/or morphology) of fragments, generated upon impact below the projectile, drives the ability of the fragmented media to resist the further penetration of a projectile. Thus, the coarser fragments generated in the Forceram material compared to the other materials, whatever the loading rate in the studied range 6.10^3 to 10^4 s^{-1}, were more suitable to limit a projectile penetration. This result underlines the importance of integrating the fragmented ceramic behaviour into numerical calculations, as it might have an influence on the complete armour system ability to withstand the penetration of a single and multiple projectile impacts.

Concerning the analysis of the fragmentation patterns, further tomography scans of smaller zones extracted from the infiltrated fragmented-ceramic could be interesting to visualize micro-cracks and their possible interactions with microstructural features, such as large grains, binder-phases and pores. In addition, concerning Forceram grades such a zoom-in analysis could provide further confirmation of the porosity collapse mechanism (eventually in the median plane) and the presence of remaining large fragments or SiC grains underneath the projectile nose. As for Tandem impact tests, performing a second impact on ceramics presenting different levels of pre-damage would be interesting to further understand the effect of the crack network density on the residual strength of the pre-fragmented media. Such a study could help to better understand if the ability of the fragmented media to limit a projectile penetration is mainly due to the size and morphology of the fragments (flow behaviour, re-arrangement, abrasiveness) or also to the fragments material properties, such as hardness. Furthermore, the backing response to a second impact during the Tandem test corresponds to a quantitative information which can be compared to numerical simulations to integrate the behaviour of pre-damaged ceramics. In the end, a thorough understanding of these failure mechanisms in relation to the ceramic microstructural features should allow a more representative calibration of models to move toward an optimized design of new generation of advanced ceramic materials.

In the present chapter, several tests were used to observe the chronology of fragmentation, and evaluate its severity from a measurement of the fragment size distribution or crack density. However, these dynamic techniques do not provide any quantification of the material tensile strength, according to the loading rate (which was variable in different areas of the sample). The next chapter focuses on developing an experimental technique to quantify the material tensile strength at a controlled loading rate.

5 | Dynamic spall strength at controlled strain rate

Contents

The performance of ceramic-based armour systems relies in part on the ceramic tensile strength, which is consequently lower than its compressive resistance. As presented in Chapter 2, the ceramic tensile behaviour highly depends on the loading rate and the microstructural features. However, most of the experimental studies on the tensile strength of ceramic material in the literature completely neglect these two input parameters. Except the high-pulsed power generator (Electric Generator of Intense Pressures, called GEPI) equipment which provides a smooth and quasi-isentropic loading in the sample [129], no experimental technique provides a controlled loading rate in the failure zone under tensile dynamic test. With this objective, the Brittle CODEX Chair has been launched and developed at the Laboratoire 3SR. This research program aims at investigating the strain-rate sensitivity of brittle materials in order to improve their modelling at high loading rates [28]. As part of this project, an experimental technique based on the plate-impact technique was developed to measure the tensile strength of ceramic materials at a controlled loading rate.

The main issue of the classical plate-impact technique for the determination of tensile strength is the discontinuous change in pressure. The planar shock wave leads to uncontrolled loading-rates. As mentioned in section 2.2.2, the rising and falling edges of the compressive wave generated upon impact must be adapted to avoid any pressure discontinuity. The wave diagrams presented in Figure 5.1 show the stress state in a specimen with a linear elastic material response, according to the shape of the applied compressive wave to the target. The vertical axis corresponds to the free surface of the impacted specimen (x=0). The incident compression wave and reflected tensile waves are coloured in blue and red, respectively, and the orange area shows the stress state in the target ($x \leq 0$) resulting from the overlap of both waves. First of all, Figure 5.1 (a) shows how a compression wave with sharp rising and falling edges causes a stress jump from the compression state to the tension state at a given position ($x_{spall} = -\lambda/2$)

in the material. Same discontinuities are obtained with a smooth rising edge and sharp falling edge or a smooth falling ramp but sharp rising edge, respectively in Figures 5.1 (b) and (c). In addition, in both cases (Figures 5.1 (b) and (c)), the spall stress is suddenly reached in a single location of abscissa x_{spall}. In order to completely avoid any jump of stress, both rising and falling edges of the wave need to be smoothed. Furthermore, having a triangular-shaped compressive wave with the same rising and falling edges (Figure 5.1 (d)) can provide a constant stress-rate and homogeneous stress field in the material *spall area*. Therefore, a constant and controlled strain rate can be reached in the material by mastering the rising and falling edges of the compressive pulse. In addition, the expected stress-rate in the spall area corresponds to the sum of stress-rates of the incident compression wave (falling edge) and the reflected tensile wave (rising edge):

$$\dot{\sigma}_{spall} = \dot{\sigma}_{falling-incident} + \dot{\sigma}_{rising-reflected} \tag{5.1}$$

For this reason, the main goal of the present study is to design a plate-impact experiment in which the compressive wave transferred to the ceramic upon impact is shaped as a triangular pulse in order to impose the desired loading rate to the tested material.

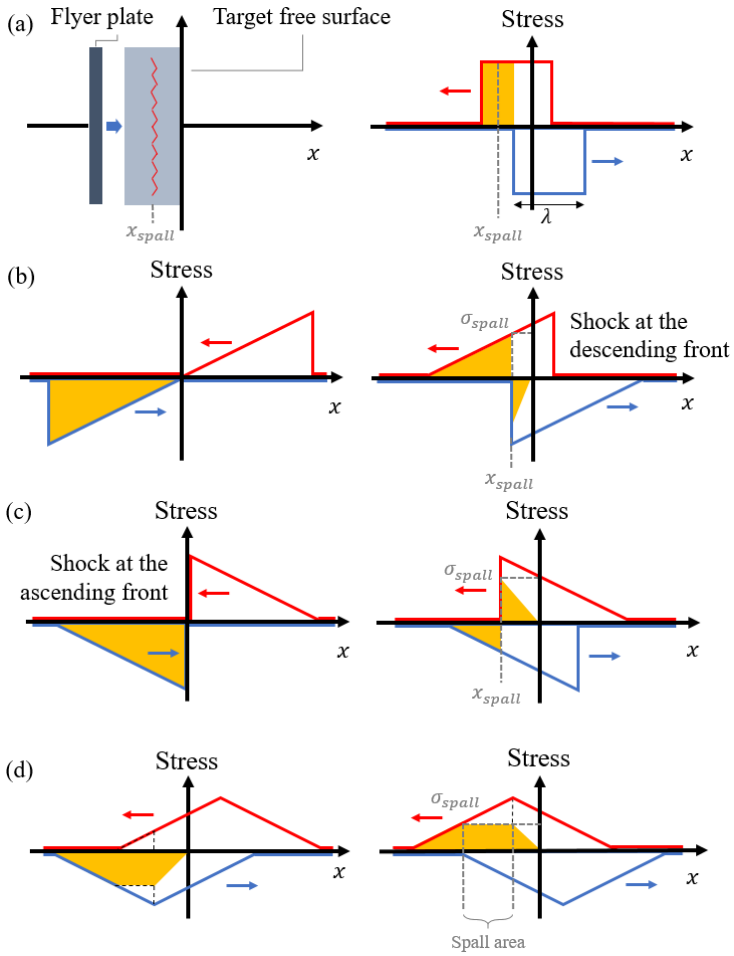

Figure 5.1. a) Plate-impact configuration and corresponding wave diagram with a rectangular compressive wave. (b) Wave diagram for a compressive wave with a smoothed rising edge and sharp descending edge. (c) Wave diagram for a compressive wave with a sharp rising edge and smoothed descending edge. (d) Wave diagram with isosceles triangular pulse-shaped incident wave

In order to transfer such a pulse wave to the target, a high-pulsed power generator (GEPI) equipment can be used [129]. However, this technique currently presents the main drawbacks of having a rising time limited by the electrodes size (needs of large electrodes to reach low magnetic pressure), requiring an adaptation of the set up to reach different loading rates and being relatively expensive. In the present study, a way to overcome these limitations is investigated by adapting the planar impact experiment

to achieve a constant strain rate deformation as well as uniform tensile stress state in the spall area [196]. As the works found in the literature always include a complex flyer-geometry and expensive manufacturing processes, the present work focuses on an easy surface design of a metallic flyer plate, with an homogeneous composition, to reach a controlled strain rate in the ceramic sample [197]. For the development of this shockless plate-impact technique, the Hexoloy SA was chosen as the reference target material because data obtained from GEPI tests on this material were available for comparison in the literature [85]. Numerical simulations were used as a way to evaluate the required wavy-shaped geometry of the flyer plate and estimate the strain rate level reached in the spall region. Experimental tests were performed using the gas gun of 3SR Laboratoire based in Grenoble (France) to verify the proper design of flyer plates. Finally, the spall strengths experimentally obtained for given strain rates are compared to results from GEPI tests found in the literature on the same Hexoloy SA SiC ceramic [85].

5.1 Elastic simulations of shockless plate-impact on a half-period of the wavy flyer plate

5.1.1 Discretized geometry and boundary conditions

In the present work, in order to minimise the initial shock rise and generate a pulse-shaped wave upon impact, the outer surface of the metallic flyer plate was customized. Based on previous studies [123], the front face of the flyer plate was wavy-shaped to smooth the rising and falling edges of the compressive pulse. By using a Lagrangian $x-t$ diagram, it is possible to determine the relation between the flyer and target plate thicknesses to obtain a spalling in the median plane of the target :

$$\frac{3L_t}{2C_t} = \frac{2L_p}{C_p} + \frac{L_t}{2C_t} \tag{5.2}$$

where L and C are respectively the thickness and longitudinal wave speed of the target (t) and projectile (p). Thus, for a flyer plate in aluminum ($C_p \approx 6000$ m/s) and a 7 mm thick ceramic target ($C_t \approx 12000$ m/s), the projectile needs to be about 2 mm thick. In order to have a linear rising edge, a *cosine-shape* is given to the front profile of the flyer plate, with a half-period and height, respectively noted P and H. The radius R is defined according to the following equation :

$$R^2 = \left(\frac{P}{2}\right)^2 + \left(R - \frac{H}{2}\right)^2 \tag{5.3}$$

First, elasto-plastic numerical simulations were run with the explicit transient dynamic FE method, using the Abaqus/Explicit software. The goal of these preliminary simulations is to evaluate the loading conditions (flyer geometry, flyer material properties and impact velocity) allowing the spalling to happen in the ceramic at a controlled strain rate. C3D8R elements (eight-node hexahedral reduced integration elements) are used to mesh the parts, with an average mesh size of 0.05 mm for the buffer and target. The effect of the flyer mesh size was tested with an average size of 0.05, 0.1 and 0.2 mm. Due to the symmetry and periodicity associated with the problem, only half a period of the wavy flyer plate is discretized, the corresponding part is shown in Figure 5.2 (a). Four geometries for the flyer plate were studied, having a flat rear face and a wavy-shaped front profile with a height H and half-period P of 0.125-0.25 mm and 0.5-1 mm, respectively, as shown in Figure 5.2 (b). The simulated geometries represent a portion of the target in the Y-Z plane with the X-axis being the axis of impact. The normal displacement is set to zero on all nodes of the top/bottom ($u_y = 0$) surfaces of the model (given in Figure 5.2 (a)) due to the periodicity of the geometry. The Z-axis displacement is set to zero on all the nodes ($u_z = 0$) to traduce the plane strain state for any point located far enough from the target edge and centre. Only one finite element (with a thickness of 1/10 of the period) is considered in the thickness (plane-strain conditions). A surface to surface contact algorithm with only *hard* normal contact behaviour is used to describe the contact between each component (striker/buffer and buffer/target). The flyer plate is given an initial axial velocity, ranged from 200 to 450 m/s. The influence of the projectile behaviour on the generated pulse in the ceramic is studies in the next section. The mechanical

behaviour of the buffer materials is considered to be elastic and perfectly plastic, as detailed in Table 5.1. Moreover, as the goal is to evaluate the loading rate generated in the ceramic target before its failure, its behaviour is considered elastic, as detailed in the last-mentioned Table 5.1.

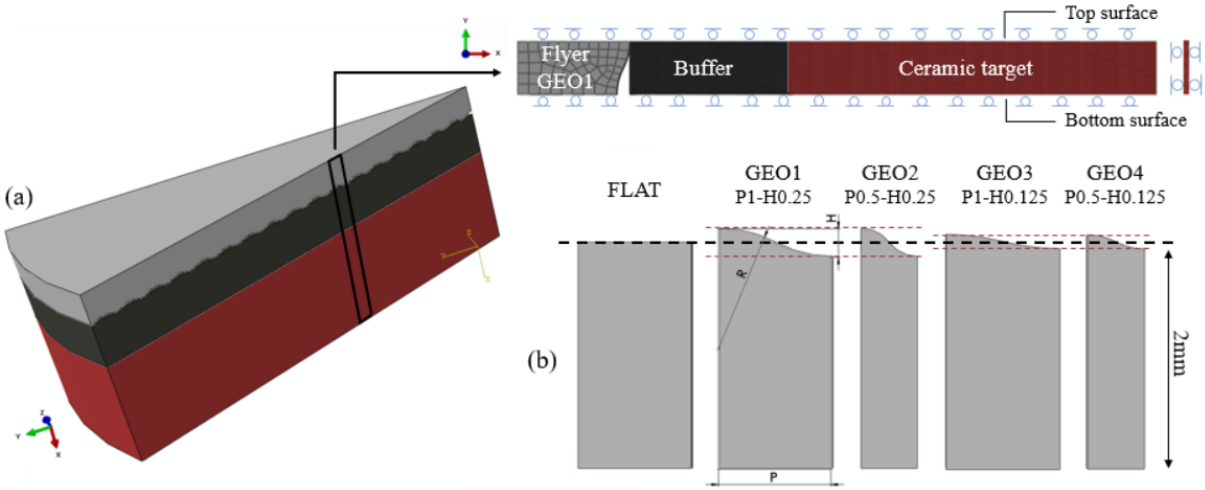

Figure 5.2. (a) Slice of the 3D plate-impact configuration and corresponding geometry considering only a single half-period of the wavy flyer plate for the numerical simulations. (b) Sketches of the flat and the four 'cosine-shaped' flyer geometries

Table 5.1. Material elasto-plastic properties considered for the FE calculation

	Material	Thickness (mm)	Density (g/cm^3)	Elastic properties		Plastic yield strength	
				E (GPa)	ν	σ_y (MPa)	ϵ_p
Flyer	Aluminum 7075	2	2.81	71.7	0.33	450	0
Buffer	Steel	3	7.80	200	0.3	1000	0
Target	Hexoloy SA®	7	3.15	430	0.14	12000 14000	0 0.01

5.1.2 Effect of the flyer behaviour on the compressive stress pulse

As no mechanical characterisation was performed on the flyer plate material in the present study, the effect of the flyer behaviour on the compressive stress pulse was studied via numerical simulations. The influence of the flyer plate material properties is presented for the configuration of a flyer geometry GEO3 with an impact velocity of 350 m/s. Five different sets of material parameters were considered for the aluminum alloy 7075 to evaluate the effect of the elastic limit, strain hardening behavior, density and Young's properties. All the material properties are detailed in Table 5.2.

The average axial stress at the buffer/target interface predicted by considering different material properties of the flyer plate are presented in Figure 5.3. It can be noticed that the density (sets of parameters number 2 and 4 in Table 5.2), elastic limit (sets 1 and 2), strain hardening behavior (sets 2 and 3) do not have a high influence on the compressive pulse shape. However, increasing the flyer elastic properties (sets 4 and 5) was found to slightly change the compressive pulse shape, as it led to a small increase of the average axial stress magnitude. As a conclusion, the behaviour of the flyer plate does not highly influence the shape of the compressive pulse-loading transferred to the ceramic upon the impact of a *wavy-machined* flyer. Therefore, the flyer metallic part is assumed to have a purely elasto-plastic behaviour subsequently, with the set of parameters (1). This assumption is compared to the experimental data in section 5.3.1.

Table 5.2. Sets of material parameters of 7075 aluminium alloy considered for numerical simulations

behaviour	Description	Notations (units)	Sets of numerical values				
			1	2	3	4	5
	Density	ρ (g/cm^3)	2.81	2.81	2.81	2.71	2.71
Elastic	Young's modulus	E (GPa)	71.7	71.7	71.7	71.7	64
	Poisson's ratio	ν	0.33	0.33	0.33	0.33	0.31
Plastic isotropic	Ultimate strength	R_m (MPa)	450	567	567	567	567
	Yield stress	R_p 0.2 (MPa)	-	-	620	-	-
	Elongation	A% (%)	-	-	11	-	-

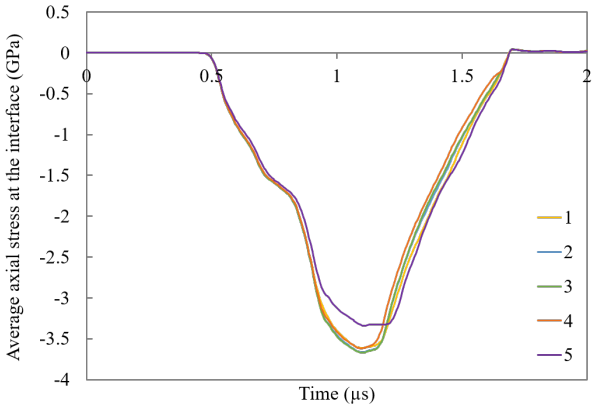

Figure 5.3. Effect of the flyer behaviour on the shape of the compressive pulse transferred to the ceramic upon plate-impacts, GEO3 350 m/s, from numerical simulations. The sets of numerical parameters for the aluminum alloy (1-5) are given in Table 5.2

5.1.3 Pulse-shaped compressive loading

The effect of the flyer profile on the pulse-wave transferred to the target upon impact was explored through numerical simulations. The average axial stress at the buffer/target interface, induced by the different flyer geometries impacting the target at 350 m/s, are compared in Figure 5.4 (a). These results confirm that, unlike the flat striker, the wavy geometries generate a compressive wave with smooth rising and falling edges and therefore ensure a shockless impact. The slope of the falling edge is supposed to be mainly linked to the plastic behaviour of the aluminum flyer plate, as it is also present for the flat geometry. Increasing the height of the 'cosine-shape' increases the rising time of the compressive wave (0.65 μs for GEO3-4 and 1-1.2 μs for GEO1-2). Varying the impact velocity gives direct control on the magnitude of the average axial stress and on the rising edge of the compressive wave, as shown in Figure 5.4 (b). In addition, a stress level higher than 500-600 MPa needs to be reached in the SiC ceramic to ensure its spall failure, as it is the estimated dynamic tensile strength of Hexoloy SA at 10^4 s^{-1} [85]. Therefore, a combination of flyer-geometry/impact-velocity needs to be found to provide a quasi-triangular pulse. Thus, velocities of about 350-450 m/s were found to be more appropriate for flyer geometries 3 and 4, whereas lower velocities 150-250 m/s are more suitable for geometries 1 and 2.

As presented in Figure 5.5 (a) for flyer GEO3 at 350 m/s, the mesh size of flyer plate (0.05, 0.1 and 0.2 mm) has no effect on the pulse profile. Thus, the choice was made to use a mesh size of 0.2 mm. A 1 mm thick steel buffer with a high elastic limit was found to be thick enough to homogenise and smooth the stress transferred to the ceramic target, as shown in Figure 5.5 (b). The buffer thickness has no clear effect on the shape of pulse, so a buffer of thickness 3 mm was used for all the tests. Moreover, the stress profile in the target at different axial positions is given in Figure 5.6 (a) for the same impact configuration (GEO3 at 350 m/s). The slope of the compressive wave remains relatively similar in a zone near the target centre (elements 3-5), whereas closer to the target front and rear surfaces the pulse is flattened.

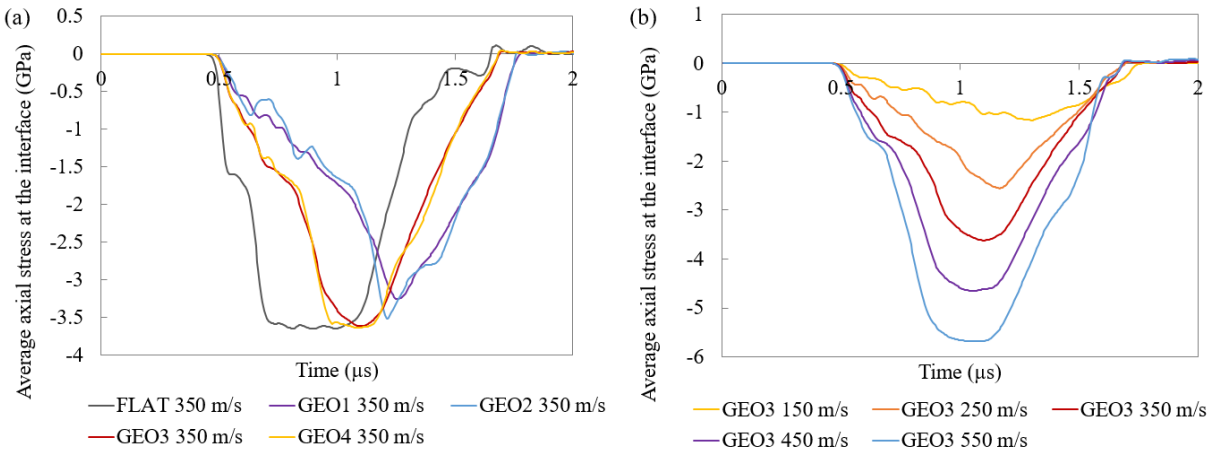

Figure 5.4. Effect of the flyer geometry (a) and impact velocity (b) on the shape of the compressive pulse transferred to the ceramic upon plate-impacts, from numerical simulations

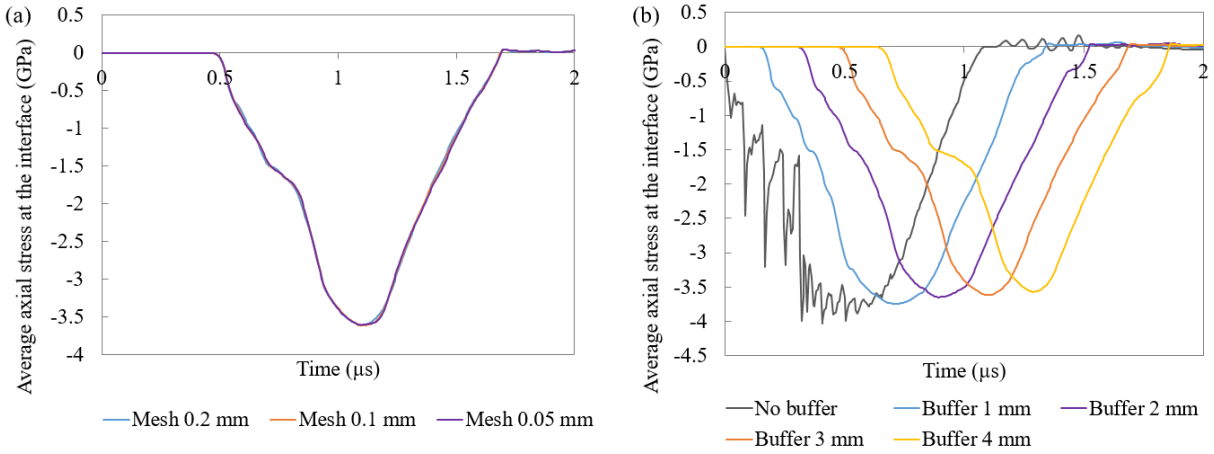

Figure 5.5. Effect of the flyer mesh size (a) and buffer thickness (b) on the shape of the compressive pulse transferred to the ceramic, from numerical simulations considering the GEO3 flyer plate impacting the target at 350 m/s

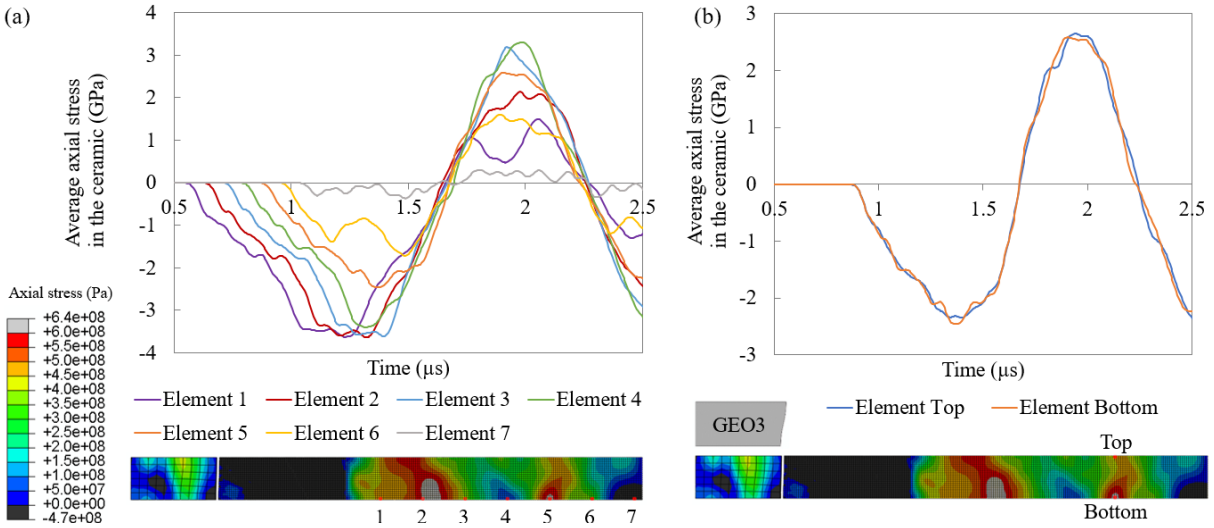

Figure 5.6. Axial stress predicted by numerical simulations considering the GEO3 flyer plate impacting the target at 350 m/s and assuming an elastic behaviour for the ceramic. (a) Axial stress along the impact direction. (b) Axial stress in two elements located on the top and bottom sides in the ceramic

It can be noticed that the loading rate slightly depends on the position of the considered plane, thus, the position of the failure spall plane in the ceramic needs to be properly identified to have an accurate estimation of the strain rate level. A very good homogeneity of stress is shown in Figure 5.6 (b) for two elements located at the same axial position but on the top and bottom edges, which means that, in the spall area, the stress and strain-rate can be assumed to be homogeneous along the radial axis (Y-axis) despite the wavy profile of the flyer plate. These results provided confidence in the ability for the four designs to generate a controlled loading rate in the spall region of the target when launched at the proper velocities. Therefore, experiments were performed using this type of flyer plates and considering impact velocities ranged from 200 to 450 m/s. The nominal configurations chosen to determine the effect of the cosine-shape (H and P) and the impact velocity on the reached strain rate are presented in Table 5.3.

Table 5.3. Selected nominal configurations for the shockless plate-impact experiments

Flyer geometry	Profile period (mm)	Profile height (mm)	Nominal impact velocities (m/s)		
GEO1	1	0.5	350	-	-
GEO2	0.5	0.5	-	250	200
GEO3	1	0.125	350	-	-
GEO4	0.5	0.125	350	450	450

5.2 Experimental configuration

5.2.1 Testing configuration and target instrumentation

Gas gun system

The dynamic testing facility used for the plate-impact tests is a 12 meter-long single stage gas gun installed in 3SR Laboratoire (Figure 5.8 (a)). The major components are a pressure vessel, a poppet valve, a 6-meter long gun barrel with multiple calibres and a ballistic chamber of 12 m^3, in which the target is placed. For this study, experiments were performed using a 80 mm calibre and a striker mass (sabot and flyer plate) of about 400 g, accelerated to an impact speed ranged from 200 to 450 m/s. To reach such impact velocities, compressed helium is used and the vessel pressure is set in the range 6-34 bars, according to the required velocity. In order to prevent the formation of a shock wave in front of the projectile due to the presence of encapsulated air [198], the ballistic chamber is vacuumed down to 17-25 mbar. The projectile is placed on a polycarbonate (PC) sabot, adjusted to the barrel diameter, Figure 5.8 (b). The software Cesar, from Thiot Ingenierie company, was used to evaluate the gas pressure to be imposed in the pressure vessel to reach the required impact velocity. Input data were the projectile (sabot and flyer plate) weight and the type of compressed gas used. Two optical barriers placed at the barrel exit end provided an accurate measure of the projectile velocity at the time of impact. The tests showed that the velocities obtained were within $\pm$ 3 % of the targeted velocities.

Flyer and target configurations

Discs of Aluminum alloy 7075 were used as projectile materials for the plate-impact tests. The nominal diameter of the flyer plates is 70 mm. In order to reach a shockless impact, the classically flat flyer plate used for planar impact is wavy-machined, based on Forquin and Zinzsner study [123]. They explained that the contact force at the striker/buffer interface increases continuously during the rising time, until the gap between both contact surfaces vanishes. For this reason, the time interval before the full contact may be approximated as the height of wavy-surface (H) divided by the impact velocity of the striker. The choice of flyer plates design was also conditioned by the ability to produce complex shapes at small scales and at a reasonable cost by chip-forming process. X-tomography analyses were conducted to control the geometry of the machined flyer plates, in particular the flatness and parallelism of the wavy faces (spatial

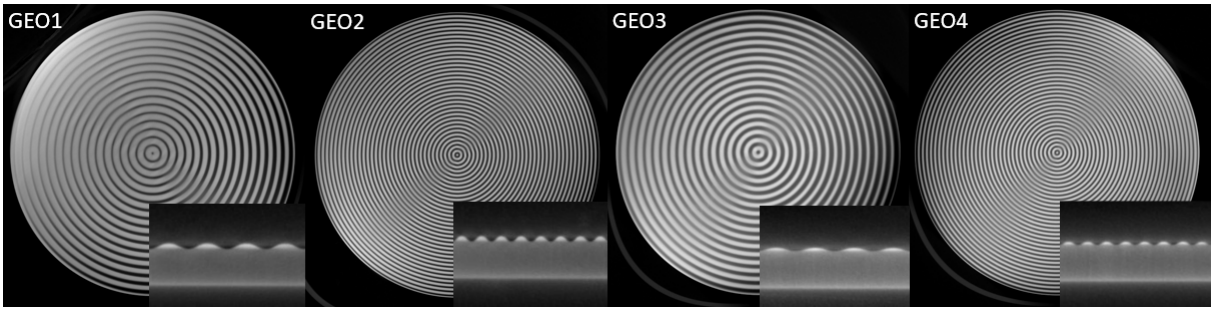

Figure 5.7. Images of the four flyer-plate geometries, extracted from tomography scans with a spatial resolution of 45 μm/px (top and cross sections)

resolution of 45 μm/px). Images of the front face and cross section are shown in Figure 5.7.

The shockless plate-impact testing configuration was developed using the dense Hexoloy SA material as a ceramic target. The nominal size of the rectangular ceramic tiles used for the spall experiments is 50 x 50 mm^2, with a thickness of 7 mm. During samples preparation, a special attention was paid on both faces flatness and parallelism, allowing only a maximum gap of 0.01 mm. No further surface polishing was required for the tests. A disc 70 mm in diameter, made of a steel with a high elastic limit (about 1000 MPa), was used as a buffer plate. According to the numerical simulations of section 5.1.3, a 3 mm thick steel cylinder was used as a buffer plate. Glued to the front face of the target plate, this buffer aims at smoothing the stress heterogeneity transferred to the target material upon impact. A tolerance of 0.02 mm was given to the manufacturer for the flatness and parallelism of both faces of the buffer plate.

The aluminum striker is placed in a polycarbonate (PC) sabot, adjusted to the barrel diameter, as shown in Figure 5.8 (b). The ceramic target is mounted on an aluminum disc attached to the launcher tube exit, Figure 5.9 (c). The aluminum support has a circular opening in its centre to allow some measurements on the ceramic backface during the dynamic test. The buffer material is stuck to the ceramic front face using an Araldite AY103-1 glue (60 wt.%) combined to a HY951 hardener. A foam layer is placed between the ceramic and its support in order to ensure a full impedance mismatch. In order to prevent any tilt at the projectile/buffer interface during the collision, the target had to be placed perpendicular to the barrel axis. To provide an accurate angular adjustment, the target support is oriented using three nylon screws coupled to Belleville washers. A visible laser, aligned to the barrel, is placed at the entrance of the gas gun and reflects on the buffer surface using a mirror. By playing on the nylon screws, the target was correctly oriented by matching the laser source and its reflection, thus a maximum angular misalignment of 1 mrad was tolerated.

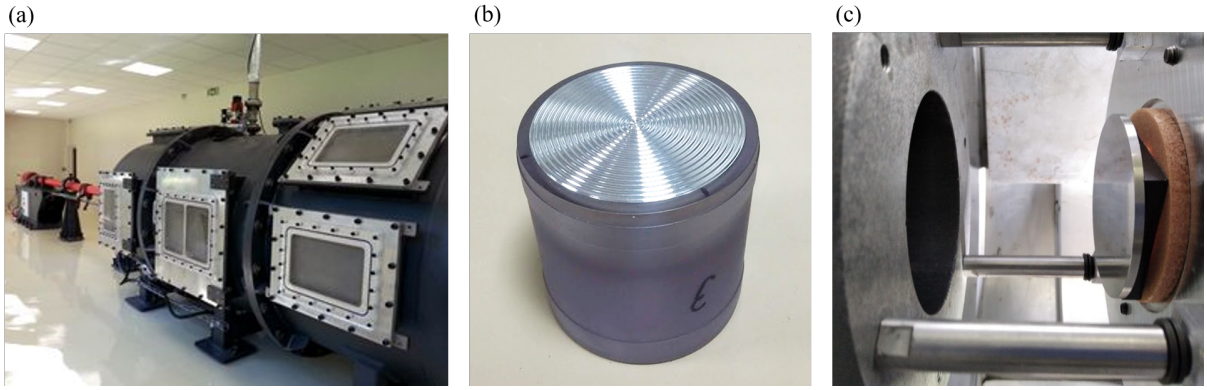

Figure 5.8. (a) Multi-caliber Gas gun installed in 3SR Laboratoire. (b) Wavy-machined flyer plate mounted on a PC sabot. (c) Front side of the target system (buffer + ceramic + support) at the launcher tube exit.

5.2.2 Interferometry system and signal post-processing

A Photon Doppler Velocimetry (PDV) system is used as the principal diagnostic system for the impact tests [199]. An erbium-doped fibre laser from Keopsys is used as a reference source light (wavelength $\lambda = 1550$ nm and power 100 mW) and lights the ceramic backface thought a 8 mm diameter focused optical fibre probe (Oz Optics). This instrumentation is shown in Figure 5.9 (b). Forquin and Zinszner demonstrated from axisymmetric and plane-strain calculations that the same response is obtained in terms of axial stress and particle velocity for various radial positions sufficiently far from the centre with respect to the wave period ($> 2P$) and from the edges to avoid lateral released waves [123]. In this range of radial positions, a plane-strain configuration can be considered. Based on these results, an offset distance of 5 mm in the radial direction was imposed between the laser pointer and the target centre to avoid any measurement error due to the flyer concentric geometry. The tiles were large enough to prevent any edge release waves from interfering with the measurement of the longitudinal wave over the time needed. The light reflected from the measured moving surface, called Doppler-shifted light, is collected by the fibre probe and sent to a home-made detector (provided by CEA Gramat). From the interference between the reflected and reference signals, having different frequencies, the detector generates a signal (in V) which can be recorded on a high-bandwidth oscilloscope (Tektronix DPO 7254 and Keysight DSOS254A). The resulting fringe pattern is directly proportional to the free-surface velocity. As the observed surface moves toward the probe that launches the laser light and collects the shifted return light, the Doppler-shifted frequency is greater than the original laser frequency.

In order to collect a good quality signal, the probe had to be placed perpendicular to the reflecting surface at an initial distance of 20 mm (focal length) [200]. To do so, before any impact test, a function generator is connected to the optical laser and to an oscilloscope to check the shape of the signal, linked to the sample surface quality and probe/surface relative positions. The electronic device was set to generate a sinusoidal waveform with an amplitude of 1-5 V and a frequency of 1-2 kHz. For any adjustments, the optical fibre is placed in an adjustable PMMA support fixed on the aluminum target support. This preliminary step allows a proper positioning of the optical probe with respect to the moving surface (orientation and distance) to capture the best signal possible.

In addition, in all the tests, the velocity of the buffer backside was also measured by using a second optical fibre. To do so, the ceramic target was translated perpendicular to the impact axis. This configuration with two lasers, recording simultaneously the free-velocity of the buffer and the target, provides the loading pulse transferred to the ceramic for each test. The adequate position of both probes, to prevent any boundary effect from interfering with the signal, was determined via numerical simulations. A drawing represents the target configuration when two optical fibres are simultaneously used (Figures 5.9 (a) and (b)). Thus, the pulse loading induced in the ceramic target could be properly determined and directly implemented in the numerical simulations. This point is further detailed in section 5.3.1.

The digitizer was triggered using an optical photodiode. Data were recorded at a sample rate of 10 GS/s (100 ps/pt). The signal was post-processed using a sliding Fourier transform method of analysis. The analysis code used is the application WAVE (WAves data processing for photonic doppler VElocimetry) developed by CEA DAM Gramat, DEA, STEX and LRME. The window size was auto-adapted to respect four times a period of the signal, with an upper bound fixed at 25 ns. In this way, by recording the beat frequency over time, a complete velocity history of the free surface is obtained. Theses post-processing parameters were not found to influence the results.

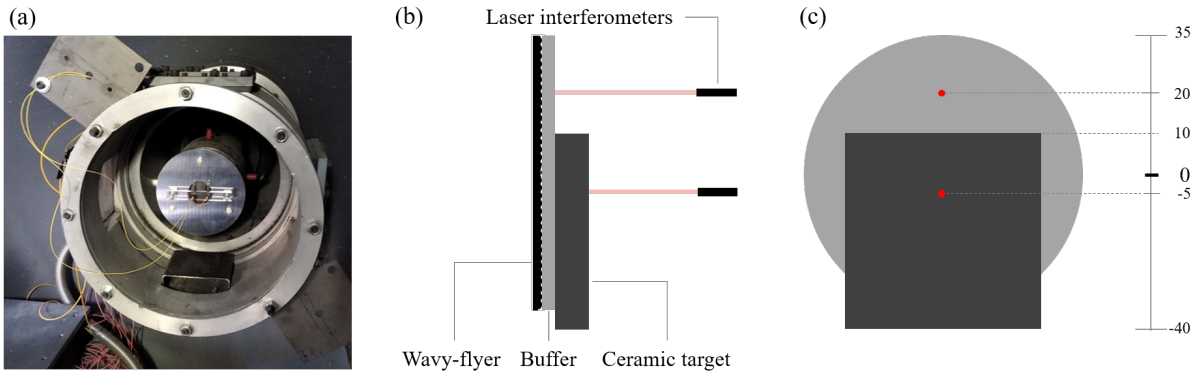

Figure 5.9. (a) Instrumented rear face of the ceramic target. Schematic showing the 2 laser-probes set-up, used to measure simultaneously the loading pulse and the ceramic free-surface velocity. Cross view (a) and back view (b)

5.3 Experimental validation of the flyers design and main spalling results on Hexoloy SA

5.3.1 Validation of the generated pulse from shockless plate-impact tests

The buffer free-surface velocity profile, obtained from the interferometry post-processing, can be converted in a stress transmitted to the ceramic (assuming a perfectly elastic behaviour for the buffer), according to the following equation:

$$\sigma_{transmitted} = \frac{\rho_t C_t * \rho_b C_b}{\rho_t C_t + \rho_b C_b} * v_b \tag{5.4}$$

with $\rho_b C_b$ the acoustic impedance of the buffer and v_b the buffer free-surface velocity. The obtained stress-time profile was smoothed (using a sliding mean value) and extrapolated (prolonged linearly after the rebound) in view of introducing these data in the numerical simulation. The pulse, experimentally obtained in the configuration GEO3 353 m/s, is compared to pulse predicted by numerical simulation in Figure 5.10. The numerical pulse was obtained in two different ways. The first one consisted in measuring the average of the axial stress (converted to positive) of each mesh element of the target in direct contact with the buffer and the second one consisted in converting the buffer free-surface velocity profile to a transmitted stress to the ceramic (using equation (5.4)). The very good agreement between both curves demonstrates the rightness of using the buffer free-surface velocity to deduce the stress loading transmitted to the ceramic. This verification is important because in the next section the buffer free-surface velocity profile, obtained experimentally, was converted into a stress loading. This obtained stress loading was used as an input for numerical simulations, in order to estimate the strain rate in the spall plane (detailed in section 5.3.2). In addition, the good match between experimental and numerical pulses demonstrates the reliability of using a simplified elasto-plastic constitutive model for the aluminum alloy to simulate the deformation of the flyer plate. Moreover, the good match between the numerical stress pulse at the interface buffer/target and the pulse resulting from the buffer free-surface velocity profile converted into a mean axial stress applied to the ceramic validates the following numerical approach to estimate the strain rate (detailed in the next section).

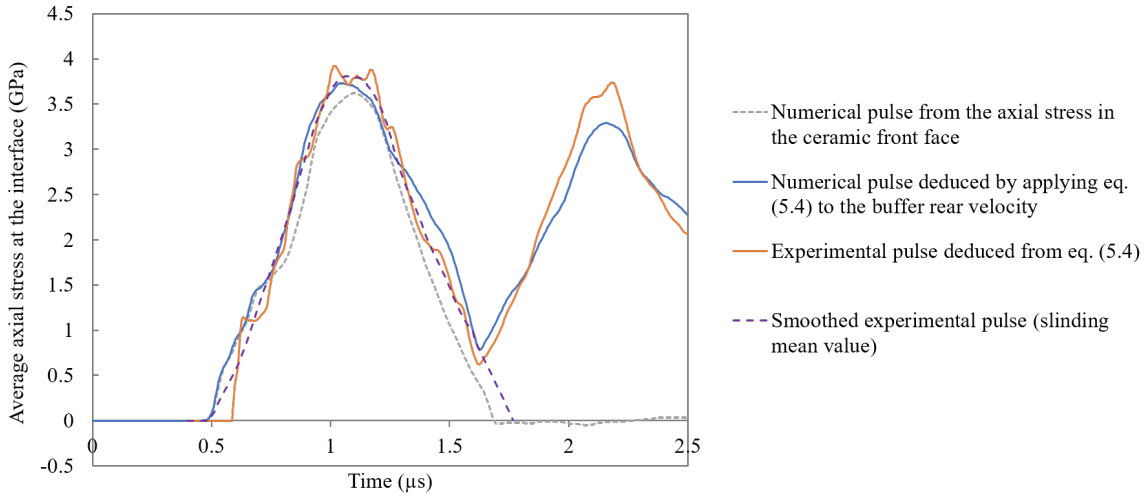

Figure 5.10. Comparison of the stress pulse transmitted to the ceramic from experiment and numerical predictions based on an elasto-plastic simulations, for the configuration GEO3 353 m/s. The smoothed experimental pulse is used as an input to evaluate the strain rate

All the tests performed on Hexoloy SA are summarized in Table 5.4 and the corresponding loading pulse determined experimentally are presented in Figure 5.11 (a). The experimental ceramic free-surface velocity profiles are plot in Figure 5.11 (b) and the spall strength estimated from the pullback velocities are detailed in Table 5.4. The test with the flyer GEO4 at 450 m/s was performed twice to assess the very good repeatability. It can be confirmed that the plate-impact test was pulse-shaped thanks to the use of wavy-machined flyer plates which generate a tailored pulse loading with a various rising time, from 0.65 to 1.2 μs depending on the flyer geometry/impact velocity combination. Moreover, tests performed with the flyer geometries GEO3 and GEO4 (same cosine height) at the same velocity, provide the exact same loading pulse. Therefore, the cosine-period seems to have no influence on the generated pulse. However, the cosine height and impact velocity have a direct effect on the generated compressive wave. Tests with the geometries GEO1 and GEO2 (H = 0.25 mm) at relatively high velocity (360-258 m/s) show a longer rising time compared to GEO3 and GEO4 (H = 0.125 mm, 350 m/s). In addition, at the end of the rising edge $GEO1_{360}$ and $GEO2_{258}$ show a slight stiffening of the rising slope for the buffer and ceramic velocity profiles. Such a behavior results from the fact that at these velocities, the flyer wavy-pattern (having a height of 0.25 mm) was completely flattened before the beginning of the unloading, so the smooth ramp loading started to stiffen before the ceramic failure. Therefore, the impact velocity needs to be kept relatively low for wavy patterns having a high height in order to keep a rising edge linear.

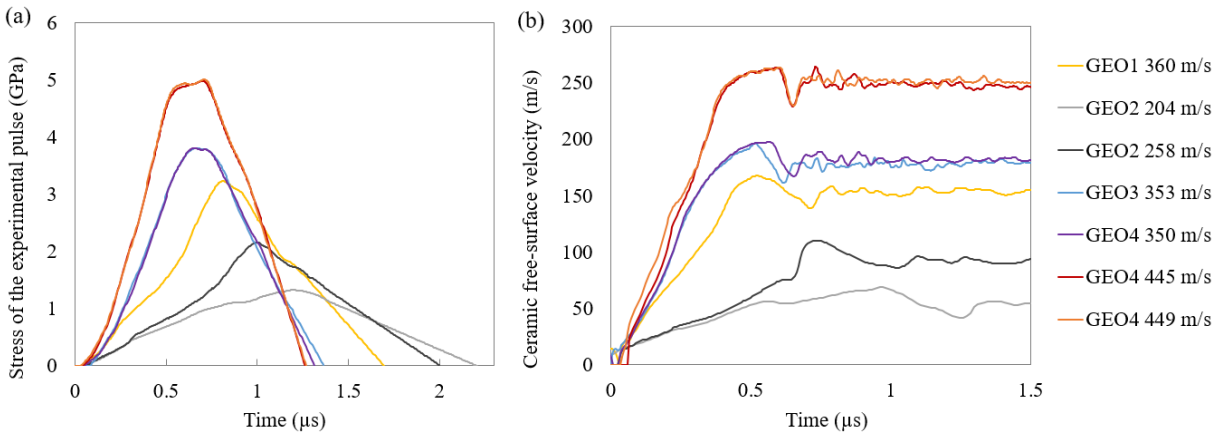

Figure 5.11. (a) Experimental velocity profile at the buffer free-surface converted into a stress pulse transferred to the ceramic and (b) experimental free-velocity profile at ceramic free-surface for all the shockless plate-impact tests performed

As in most of the studies presented in the literature the spall strength of the ceramic is studied with respect to the maximal compression stress reached in the sample, also referred to as *impact stress*, this value is reported in Table 5.4 for all the tests. This maximal pulse stress σ_{max} was estimated from the maximal velocity V_{max} reached by the target free-surface, according to the following equation:

$$\sigma_{max} = \frac{1}{2}\rho_t C_t V_{max} \tag{5.5}$$

Moreover, the maximal axial stress reached in the ceramic target during the impact was estimated from the elasto-plastic numerical simulations. It can be noticed that the test with GEO2 at 204 m/s did not provide a high enough stress level in the target (about 230 MPa) to cause its failure. Therefore, the pullback velocity could not be attributed to a spall failure of the ceramic.

5.3.2 Strain rate estimation at the spall location from elasto-plastic numerical simulations

The strain rate in the failure zone is estimated from elasto-plastic numerical simulations. In order to have a reliable estimation according to the experimental conditions, instead of considering a numerical simulation of the impact between the striker and the target using a half-period of the wavy flyer plate simulations (as in Figures 5.2 and 5.6), the pulse loading obtained experimentally (Figure 5.11 (a)) was directly implemented in the simulation as the input pressure applied to the ceramic target. The spall plane responsible for the measured pullback velocity is assumed to be the plane for which:

- the level of tensile stress reaches the experimental spall strength
- the failure information takes the minimal amount of time to reach the rear face of the ceramic (knowing the longitudinal wave speed of the ceramic material).

Thus, the spall region responsible for the measured pullback can be identified, as shown in Figure 5.12 (a). Then, the strain rate was considered to be the value of axial strain time-derivative in the identified spall plane. In Figure 5.12 (b) the axial stress (S11) and strain rate (LE11 derivative) are plot for the configuration with the flyer geometry GEO3 with an impact velocity of 353 m/s. It can be noticed that the strain rate is relatively constant during the tensile loading. The margin of error of the strain rate estimation was estimated to about $\pm$ 1000 s^{-1}, due to the uncertainty on the exact position of the spall failure.

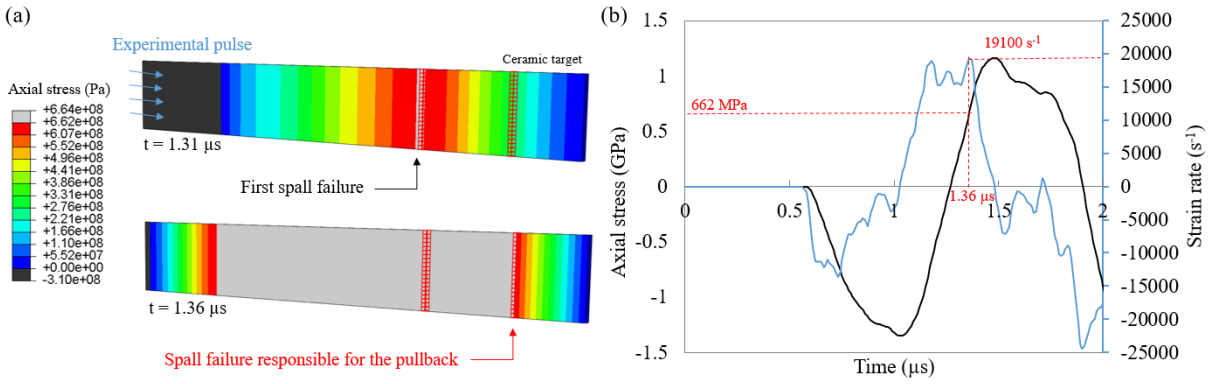

Figure 5.12. (a) Identification of the damaged zone responsible for the pullback velocity from elastic numerical simulations. (b) Estimation of the strain rate in the failure area, σ_{spall} = 662 MPa and $\dot{\epsilon}$ = 19100 s^{-1}

5.3.3 Comparison with results from the literature, obtained from GEPI tests

Spall strength results of the present work are compared to the results obtained via the GEPI technique on the same material Hexoloy SA [85] in Figure 5.13 and Table 5.4. The impact stresses for the GEPI tests, given in Table 5.4, could be estimated by using the velocity profiles provided by Zinszner et al. in their experimental work [85]. In addition, they adopted the same methodology as the one described in section 5.3.2, which combines experimental results and numerical simulations, to evaluate the strain rate during their shockless tests. The only difference is that they used the Denoual-Forquin-Hild (DFH) micro-mechanical model, instead of an elasto-plastic model, to describe the ceramic behaviour [78] [77]. Finally, the range of strain rates reached in the present study via the shockless plate impact is comparable to the range of the GEPI experiments (10^4-10^5 s^{-1}). Results are in excellent agreement between both techniques. A clear increase of the ceramic spall strength with an increase of the strain rate can be observed.

Table 5.4. List of shockless tests conducted via plate-impacts and GEPI techniques on Hexoloy SA

Experimental technique	Flyer geometry	Impact speed (m/s)	Pulse rising time (μs)	Max. pulse stress (GPa)	Max. reached stress (GPa)*	Strain rate (s^{-1})	Spall strength (MPa)
Pulse-shaped plate-impact	GEO1	360	0.8	1.62	0.915	13200	550
	GEO2	204	1.2	1.30	0.230	-	(501)
	GEO2	258	1.0	1.08	0.456	1600	451
	GEO3	353	0.7	1.91	1.162	19100	662
	GEO4	350	0.7	1.91	1.197	12600	573
	GEO4	445	0.65	2.49	1.183	21600	653
	GEO4	449	0.65	2.51	0.910	21200	644
GEPI technique [85]	-	-	0.5	0.76	-	7500	450
	-	-	0.45	2.84	-	17000	608
	-	-	0.35	5.97	-	25000	665

*From elasto-plastic numerical simulations

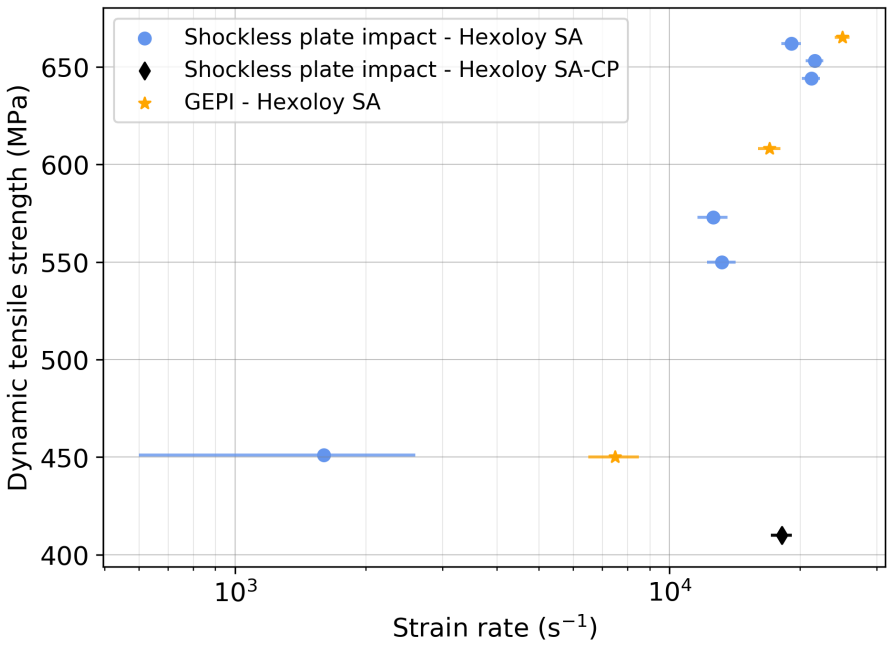

Figure 5.13. Comparison of the shockless plate-impact and GEPI results [85] for the strain rate sensitivity of Hexoloy SA spall strength

An additional test was conducted on the material Hexoloy SA-CP, in the exact same conditions as one of the tests performed on Hexoloy SA, using the flyer plate of geometry GEO3 with an impact velocity of 353 m/s. The free-velocities obtained from laser interferometry at the rear face of buffers, during both tests, are presented in Figure 5.14 (a) (not smoothed). The time scale was adapted to have a same time origin. First, this perfect superposition of the plots confirms the very good reproductibility of loading conditions, for a given flyer geometry and impact velocity. Then, it is a verification that the same compressive pulse was transferred to both materials. The corresponding ceramic free-velocity profiles are plotted in Figure 5.14 (b). The same loading conditions provided similar free-velocity profiles during the first 0.5 μs for both ceramics. After that, the Hexoloy SA-CP material presents a sharper drop of velocity, reflecting a slightly higher loading rate at failure (linked to the elastic properties of the material) than the Hexoloy SA. A spall strength value of 410 MPa was obtained for Hexoloy SA-CP, and the corresponding controlled strain rate was estimated to 18150 $\pm$ 1000 s^{-1} from numerical simulations. This result is compared to spall strength values obtained for Hexoloy SA (608 MPa at 17000 $\pm$ 1000 s^{-1} from GEPI tests and 662 MPa at 19100 $\pm$ 1000 s^{-1}) in Figure 5.13. From this, the presence of relatively large size-controlled pores seems to decrease the ceramic spall strength, at strain-rates of about 17000-19000 s^{-1}.

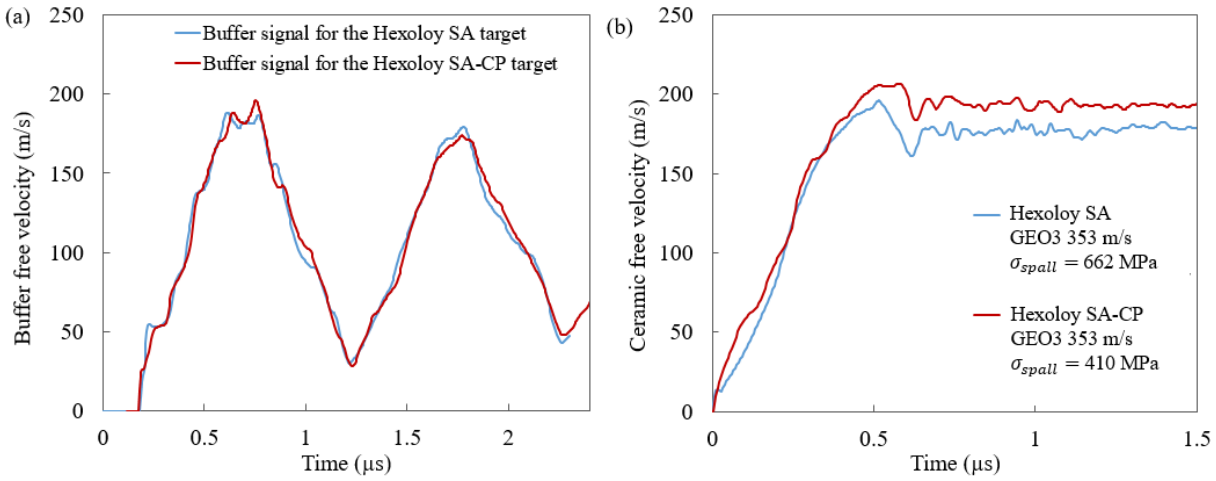

Figure 5.14. Experimental free-velocity profile at the buffer (a) and ceramic (b) free-surfaces, for shockless plate-impact tests performed on Hexoloy SA and Hexoloy SA-CP in the same conditions (GEO3 353 m/s)

The overall method followed in the present chapter to evaluate a ceramic spall-strength sensitivity to strain rate is summarized in Figure 5.15. This diagram highlights the main steps and corresponding tools, from the design of each experimental configuration by numerical simulations to the data processing of plate-impact experiments. The step of experimental processing consists in characterizing the ceramic spall strength from the measurement of its free-surface velocity upon impact, and estimating the corresponding strain-rate from a numerical simulation where the compression loading pulse is obtained from the buffer free-surface velocity, measured experimentally. Finally this methodology makes possible to ensure an adapted and constant strain rate in the failure zone and to characterize the strain-rate sensitivity of the ceramic tensile strength.

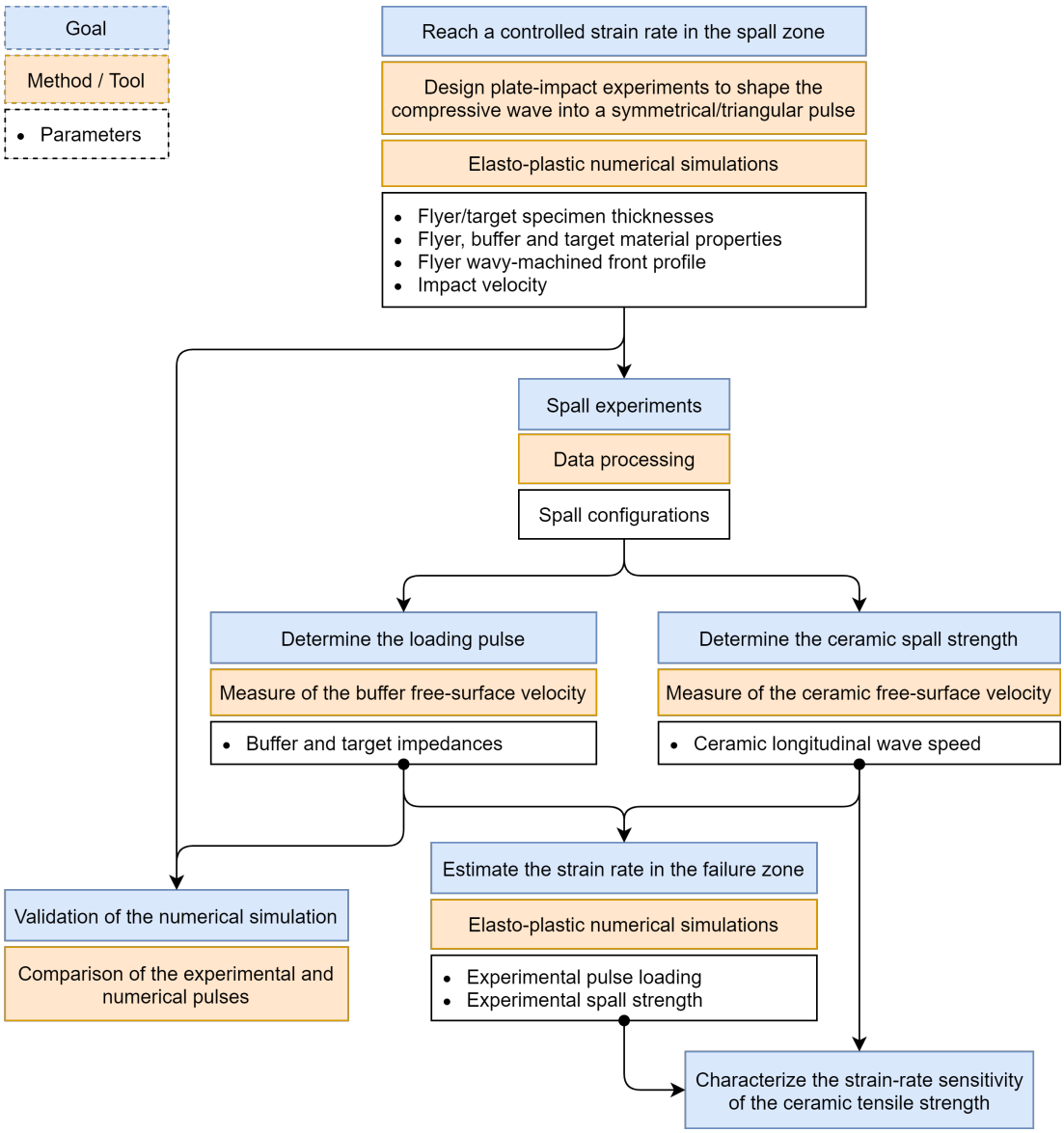

Figure 5.15. Diagram summarizing the approach to determine the strain rate sensitivity of ceramic spall strength via shockless plate impact with a wavy-machined flyer-plate

5.4 Conclusion of the chapter

The aim of the present chapter was to design and perform dynamic spalling tests on ceramic samples at a given strain rate. To do so, the classic planar impact configuration had to be modified, by considering wavy-machined flyer plates, in order to avoid any jump of axial stress and instead maintain a well-controlled loading rate in the specimen failure region. Four geometries of flyer plates were numerically designed by elasto-plastic simulations to control the shape of the loading pulse, according to the flyer geometry, material properties and impact velocity. The preliminary tests performed on a SiC ceramic gave confidence in the ability to use an aluminum wavy-machined flyer-plate to generate a tailored pulse wave in the target upon a gas gun test. In addition, the experimental results confirmed that no stress jump was transferred to the ceramic and thanks to the interferometry instrumentation, the spall strength of the SiC ceramic was determined at almost constant strain-rate. The strain rate reached in the ceramic tensile failure location was evaluated through elasto-plastic numerical simulations for each configuration using the loading pulse and spall strength obtained from the shockless experiments. Finally, the ceramic spall strength sensitivity to strain rate could be demonstrated for strain-rates ranged from 10^4 to 10^5 s^{-1}. The obtained results are in excellent agreement with a previous study using the GEPI

technique based on pulsed current. In addition, this quantification of the material strength at a controlled loading rate will be used as a valuable data to be compared to the modelling prediction in the next chapter.

The subsequent work involves designing other flyer plates to reach a larger range of controlled strain rates (10^5-10^6 s^{-1}). Providing more experimental data for the material Hexoloy SA-CP is an ongoing work. Moreover, as initiated by Zinszner and Forquin, such a technique can be extended to the study of the compressive strength sensitivity to loading rate [123]. By this way, a better insight should be given to the development of an accurate modelling of the behaviour of armour ceramics, by taking into account their ultimate strength sensitivity to strain rate.

6 Modelling of the fragmentation process in Hexoloy materials based on X-ray micro-tomography

Contents

The dynamic fragmentation tests conducted in Chapter 4 showed the development of a large network of radial micro-cracks only few micro-seconds (about 3 μs) after impact in Hexoloy grades. This multiple fragmentation highly depends on the microstructural features because cracks are triggered on pre-existing flaws when subject to tensile stresses. In the present chapter, the goal is to model this fragmentation process, based on a true description of the flaws responsible for failure. To this end, the work is focused on both Hexoloy grades. They present a relatively ideal microstructure for modelling thanks to their uniform microstructure (small SiC grains) and homogeneously distributed pores, acting as main critical flaws.

The Denoual-Forquin-Hild (DFH) micro-mechanical model, introduced in section 2.3.2, is considered to predict the fragmentation behaviour of ceramic materials under tensile loading. This damage model presents the main advantages of including the mechanisms of cracks initiation, propagation and interaction observed in brittle materials. The first section of this chapter focuses on the closed-form solutions of this micro-mechanical. Microstructural parameters are introduced through an explicit law of critical defects and through parameters related to crack propagation. Two different laws of critical defects are implemented in the model to be compared. The first one consists in using a statistical description of the critical flaw population following a Weibull law. As mentioned in section 2.1.2, such a description presents the main limitation of characterizing only defects causing failure under a quasi-static loading (bending tests). Therefore, when such a flaw distribution is considered in the

modelling, the assumption is made that the defects responsible for a dynamic failure are the same as the defects causing fracture under a quasi-static loading. Such a description might not be adapted to materials presenting multi-modal flaw populations, such as the Hexoloy SA-CP. In order to have a more comprehensive description of the materials flaw distribution, the micro-tomography technique is used through two different approached, called Continuous and Discrete approached. In section 3.2.2, this non-destructive technique has been demonstrated to be a relevant way to describe the complete flaw population of both Hexoloy grades. In the Continuous approach, this result is used to identify a continuous function describing the density of critical defects to be implemented in the DFH model. In the Discrete approach, tensile simulations, in which the phenomenology of the DFH damage model is implemented, are conducted on a numerical volume containing pores, extracted from X-ray tomography (exact position). From both approaches, the main effort is concentrated on understanding how the critical flaw population (considered Weibullian or deduced from tomographic data) influences the dynamic fragmentation process. To do so, the predictions of the DFH model based on both flaw descriptions are compared and discussed for a large range of strain rates, in terms of fragmentation intensity and ultimate strength. This work, based on two complementary approaches (Continuous and Discrete) to evaluate the behaviour of brittle materials according to the loading rate led to a paper submitted for publication [201].

Finally, experimental results on the fragmentation and spall strength sensitivity to the loading rate, respectively presented in Chapters 4 and 5, are compared to predictions of the DFH model. These experimental results are expected to bring a validation of the approach and determine which critical flaw description is the most relevant to describe the fragmentation behaviour of both Hexoloy materials over a large range of strain rates.

6.1 Closed-form solution of the DFH model in the case of a multiple-fragmentation and Weibull flaw distribution

6.1.1 Expressions of the ultimate strength and cracking density

The phenomenology of the DFH model has been introduced in section 2.3.2. This model accounts for mechanisms of crack initiation on critical defects, their propagation normal to the loading direction at a constant velocity (kC) and their interaction, through the concept of obscuration volumes. As a reminder, in the case of a multiple-fragmentation at high strain rates, the following expression is given in the DFH model for the probability of a point M in the loaded volume to be obscurated at a time T:

$$P_o(T) = 1 - \underbrace{exp\left(-Z\int_{t=0}^{t_z}\frac{d\lambda_t(t)}{dt}dt\right)}_{Single\ fragmentation} * \underbrace{exp\left(-\int_{t=t_z}^{T}\frac{d\lambda_{flaw}(\sigma(t))}{dt}Z_0(T-t)dt\right)}_{Multiple\ fragmentation} \tag{6.1}$$

where $\lambda_{flaw}(\sigma(T))$ is the density of critical defects, which can be described by a Weibull power law λ^W_{flaw} or any continuous function. The microstructural parameters considered in the DFH model are an explicit law of critical defects λ_{flaw} and parameters related to crack propagation (S, kC).

During the fragmentation process, the material sees its strength evolving as some cracks are triggered. Once a crack is nucleated from a critical defect, its surrounding zone (obscuration zone) is considered fully damaged, with no residual strength. So, the damage at a time T is equal to 0 for an intact volume and equal to 1 when the whole volume is obscurated. Thus, the damage variable can be assimilated to the probability of obscuration previously expressed in equation (2.18):

$$D(T) \equiv P_o(T) \tag{6.2}$$

From this, the residual strength of the loaded volume, called macroscopic stress Σ, depends on the

proportions of already damaged zones and the applied microscopic stress σ, as follows:

$$\Sigma(T) = (1 - D(T))\sigma(T) \tag{6.3}$$

In addition, the strength Σ_u corresponds to the maximal strength that the material can withstand before breaking, called ultimate strength. For brittle materials, this strength is close to the yield point (reached for a damage of about 0.1). It is determined from the maximal value of the macroscopic stress, reached for an ultimate time t_u:

$$\frac{d\Sigma}{dt}(t_u) = 0 \tag{6.4}$$

A crack can only be initiated on critical flaws which were not obscurated by the prior activation of a neighbouring critical defect. Therefore, the crack density λ_{crack} evolution in time relies on the undamaged portion of the material and the evolution of critical defects $\lambda_{flaw}(\sigma(t))$ as the stress keeps increasing in the loaded volume:

$$\frac{d\lambda_{crack}}{dt} = (1 - D(t))\frac{d\lambda_{flaw}(\sigma(t))}{dt} \tag{6.5}$$

The crack density observed in post-mortem samples, recovered from fragmentation tests, corresponds to the crack density when the time tends toward infinite or the damage variable towards 1.

6.1.2 DFH modelling based on a Weibull flaw distribution

If flaws causing failure under dynamic loading are assumed to be flaws responsible for fracture during bending tests, a Weibullian flaw density $\lambda^W_{flaw}(\sigma(t))$, given in equation (2.4), can be considered to describe the density of critical defects. In this case, the damage variable of a volume loaded at a constant stress rate $\dot{\sigma}$, given by the analytical solution of the DFH model (equation 6.2), can be calculated as:

$$D(T) \equiv 1 - \exp\left(-\frac{m!n!}{(m+n)!}\left(\frac{T}{t_c}\right)^{m+n}\right) \tag{6.6}$$

where n is the space dimension, m is the Weibull modulus and t_c is the characteristic time for the whole fragmentation process to end, meaning the time for which all the volume is obscurated, and is given by [78]:

$$t_c = \underbrace{\left(\sigma_0 \lambda_0^{-\frac{1}{m}}\right)^{\frac{m}{m+n}}}_{cracks\ initiation} \quad \underbrace{(\dot{\sigma})^{-\frac{m}{m+n}}}_{loading\ rate} \quad \underbrace{\left(S^{\frac{1}{n}} kC\right)^{-\frac{n}{m+n}}}_{cracks\ propagation} \tag{6.7}$$

Each term of this characteristic time for the fragmentation process are related to the crack initiation, crack propagation and loading rate. From the power expressions of each term (with $n = 3$ and $m \sim 15$), it is possible to notice that the fragmentation process is significantly less sensitive to the crack propagation parameters than to the crack initiation parameters and loading rate. So, keeping a factor $k = 0.38$ for the crack velocity attenuation is expected to have only a limited effect on the model predictions. The characteristic density of flaws $\lambda_c = \lambda_{flaw}(\sigma_c)$, associated to a characteristic stress $\sigma_c = \dot{\sigma} t_c$, can be written as:

$$\lambda_c = \left(\sigma_0 \lambda_0^{-\frac{1}{m}}\right)^{\frac{mn}{m+n}} (\dot{\sigma})^{\frac{mn}{m+n}} \left(S^{\frac{1}{n}} kC\right)^{-\frac{mn}{m+n}} \tag{6.8}$$

From the equation (6.5), the following expression is obtained for the final cracking density based on a Weibullian critical flaw description:

$$\frac{\lambda_{crack}}{\lambda_c}(\sigma \gg \sigma_c) = \left(\frac{(m+n)!}{m!n!}\right)^{\frac{m}{m+n}} \Gamma\left(1 + \frac{m}{m+n}\right) \tag{6.9}$$

where Γ is the incomplete gamma function. Finally, the expression of the ultimate strength given in equation (6.4) and the corresponding ultimate time can be expressed as:

$$\Sigma_u = \sigma_c \left(\frac{1}{e}\frac{(m+n-1)!}{m!n!}\right)^{\frac{1}{m+n}} \quad \text{with} \quad t_u = t_c \left(\frac{(m+n-1)!}{m!n!}\right)^{\frac{1}{m+n}} \tag{6.10}$$

In the following work, these analytical solutions of the DFH model, considering a Weibull flaw distribution for the critical defects, will be referred as the Weibull-based method.

6.1.3 DFH modelling extended to a continuous flaw distribution

In the case, the density of critical defects is not simplified by a Weibullian distribution but is a continuous function, the damage evolution in time (equation (6.2)) can be expressed using the time-evolution expression of an obscured volume given in equation (2.16):

$$\ln(1 - D(T)) = -\int_0^T \frac{d\lambda_{flaw}(\sigma(T))}{dt} S(kC(T-t))^n dt \tag{6.11}$$

In the case of any continuous function for the density of critical flaws, the time derivation of equation (6.11) gives:

$$\frac{1}{1-D(T)}\frac{dD(T)}{dt} = nS(kC)^n \int_0^T \frac{d\lambda_{flaw}(\sigma(T))}{dt}(T-t)^{n-1} dt \tag{6.12}$$

Therefore, in three dimensions ($n = 3$), the damage evolution law can be expressed by the following differential form [78]:

$$\frac{d^2}{dt^2}\left(\frac{1}{1-D}\frac{dD}{dt}\right) = 6S(kC)^3 \lambda_{flaw}(\sigma(t)) \tag{6.13}$$

From this description of the damage evolution and a continuous expression to describe the materials critical flaw distribution, the ultimate strength and cracking density expressed in equations (6.3) and (6.5), respectively, can be calculated. In the next section, it is proposed to identify this continuous function from CT micro-tomography analysis. This approach, based on the implementation of a continuous function extracted from X-ray tomography, will be referred to as the Continuous method [201].

6.2 Predictions of strength and fragmentation sensitivity to strain rate, with the Weibull and the Continuous methods

Predictions from the DFH model rely on the description of the flaw population responsible for failure. It has been shown that the Weibull distribution of flaws, deduced from a series of quasi-static bending tests, can be considered as a first approximation. In this section, the goal is to compare this approach to the case where the distribution of defects is directly extracted from X-ray tomographic analyses. This new approach is suspected to be more adapted to materials presenting multiple flaw populations, which are not properly described by quasi-static bending tests. To challenge the Weibull-based approach, the predictions in terms of dynamic strength and final crack density over a large range of strain-rates, are compared to the one obtained from the Continuous approach based on micro-tomography and discussed for both Hexoloy materials.

6.2.1 Identification of the cumulative critical-flaws density as a function of the applied stress from X-ray tomography

The Weibull description of the density of critical flaws relies on quasi-static bending tests. As described in section 2.1.2, this technique is not adapted to the description of materials containing several flaw populations, for which bending tests at multiple scales would be required. Instead of being limited by the size of the bending tests to have access to the different populations of defects, the idea in the present work consists in extracting them from X-ray tomography. Indeed, it has been demonstrated in Chapter 3 that the density of defects can be captured via this technique. As introduced in section 2.1.1, the Linear Elastic Fracture Mechanics can be used to express the macroscopic critical stress required to trigger any defect in the material, knowing its size and geometry:

$$\sigma_c = \frac{K_{IC}}{Y\sqrt{\pi a}} \tag{6.14}$$

As a reminder, Y is a dimensionless correction factor, related to the geometry of the crack ($Y = 1$ for a straight crack of length $2a$ in 2D plane stress conditions, and $Y = 2/\pi$ for an internal circular flaw of radius a) [52]. This relationship between the strength and flaw size, relies on the assumption that the

flaws are independents and do not interact [53]. Therefore, this approach consists in extending the theory of the *weakest-link-hypothesis* to all the flaws detected by tomography, knowing that, according to the loading rate, they could all be the weakest flaw of a sub-volume. From equation (6.14), the density of pores identified by tomography (Figure 3.11) is converted into a cumulative density of critical defects, expressed as a function of each pore critical stress of activation $\lambda^T_{flaw}(\sigma_c)$:

$$\lambda^T_{flaw}(\sigma_c) = \lambda^T_{flaw}(D_{eq}(\sigma_c, K_{IC}, Y)) \qquad \text{with} \qquad D_{eq} = \frac{2}{\pi}\left(\frac{K_{IC}}{Y\sigma_c}\right)^2 \tag{6.15}$$

Resulting plots are presented in Figure 6.1 for Hexoloy SA and Hexoloy SA-CP. Changing the value of Y leads to an horizontal translation of the curve. In order to calibrate this shape factor Y, the Weibull law provided by the bending tests was superimposed to the density of critical defects obtained from the large-volume tomography scans (pixel-size 3 μm), as shown in Figures 6.1 (1.a) and (2.a). The best value for the Y parameter was considered to be the value for which both curves (Weibull law and tomography) overlap at the average flexural stress obtained during bending tests. This condition was satisfied for a Y factor of 1.2 and 0.85 for the Hexoloy SA and Hexoloy SA-CP, respectively. It has to be kept in mind that considering a unique shape factor to describe all the flaws (even if they belong to different flaw populations) is a simplification that might reduce the accuracy of the description.

First, it can be noticed in Figure 6.1 (1.b) that the overall flaw population of the material Hexoloy SA presents a good fit between the Weibull and tomography-based flaw descriptions. So, the use of a Weibullian distribution for the homogeneous small sintering defects seems to be acceptable for this material. As for the porous Hexoloy, the slope of the Weibull law is slightly lower than the slope of the tomography curve for the largest defects (lowest critical stresses 280-360 MPa) in Figure 6.1 (2.a). This can be explained by two main reasons. First, during the bending tests, the critical stress considered corresponds to the maximal failure stress. However, this value might not perfectly match the stress field surrounding the defect causing fracture. In the case of the Hexoloy SA-CP, the presence of large and well dispersed pores increases the scatter on the position of the sites of crack nucleation, possibly relatively far from the maximal stress. The second reason, which is more general, is that the quality of stress field is often neglected in bending tests (possible torsion fields, surface defects), which leads to a greater dispersion of results (lower m value) [202] [203]. The tomography technique overcomes these limitations of the bending test configuration when applied to heterogeneous materials or materials presenting multiple flaw populations. As for the rest of the plot in Figure 6.1 (2.b), the tomography description consequently deviates from the Weibull behaviour at higher strengths. The flaw density extracted from tomography presents a plateau between 400 and 700 MPa which is consistent with the quasi-absence of porosity of size 20-40 μm in the material (Figure 3.11). It is clearly visible that the Weibull law is not adequate to provide a full description of the flaw population of the Hexoloy SA-CP material. This is due to the fact that the small pores ($\leq$ 60 μm) were not activated during the QS bending tests, so the bi-modal flaw population cannot be simplified to a single Weibull law.

After calibrating the Y factor, a continuous function depending on the critical stress can be identified to fit the flaw density obtained from X-ray tomography, as shown in Figures 6.1 (1.b) and (2.b). This interpolation function Λ was determined in logarithm scale:

$$\log(\lambda^T_{flaw}) = \Lambda(X) \quad \text{with} \quad X = \log(\sigma_c) \tag{6.16}$$

This continuous function was defined as the smooth junction of three (Hexoloy SA, $i \in \{0;1;2\}$) or four (Hexoloy SA-CP, $i \in \{0;1;2;3\}$) affine functions f_i, as follows:

$$\Lambda(X) = \begin{cases} f_0(X) & \text{for } X \leq X_{t_0} \\ \dfrac{f_i(X) f_{i+1}(X)}{\left(f_i(X)^{q_i} + f_{i+1}(X)^{q_i}\right)^{\frac{1}{q_i}}} & \text{for } X_i \leq X \leq X_{i+1} \\ f_n(X) & \text{for } X \geq X_n \end{cases} \tag{6.17}$$

$$\text{with} \quad f_i(X) = a_i(X - X_i) + Y_i \tag{6.18}$$

The q_i coefficients determine how sharp the change of slope is between two affine functions f_i and f_{i+1}. The function coefficients providing the best fit of the cumulative flaw density function are given in Table 6.1. They were identified for a given value of the shape factor Y and for λ_{flaw}^{T} and σ_c expressed in $1/m^3$ and Pa, respectively. The main interest of this continuous function is that it can be explicitly implemented in the DFH model to account for the critical flaw population, instead of using an idealised Weibull-based approach.

Table 6.1. Coefficients of the continuous function identified to fit the density of critical flaws extracted from X-ray tomography

Hexoloy SA (Y=1.2)	$X_0 = 6.26$	$Y_0 = 0.5$	$a_0 = 12$	q_0 = -2
	$X_1 = 6.27$	$Y_1 = 0.8$	$a_1 = 110$	$q_1 = 3$
	$X_2 = 6.5$	$Y_2 = 4.1$	$a_2 = 12.7$	
Hexoloy SA-CP (Y=0.85)	$X_0 = 5.77$	$Y_0 = 1.47$	$a_0 = 27$	$q_0 = 5$
	$X_1 = 6.45$	$Y_1 = 4.85$	$a_1 = 0$	q_1 = -7
	$X_2 = 6.9$	$Y_2 = 8$	$a_2 = 13$	$q_2 = 40$
	$X_3 = 7.1$	$Y_3 = 10.1$	$a_3 = 8.5$	

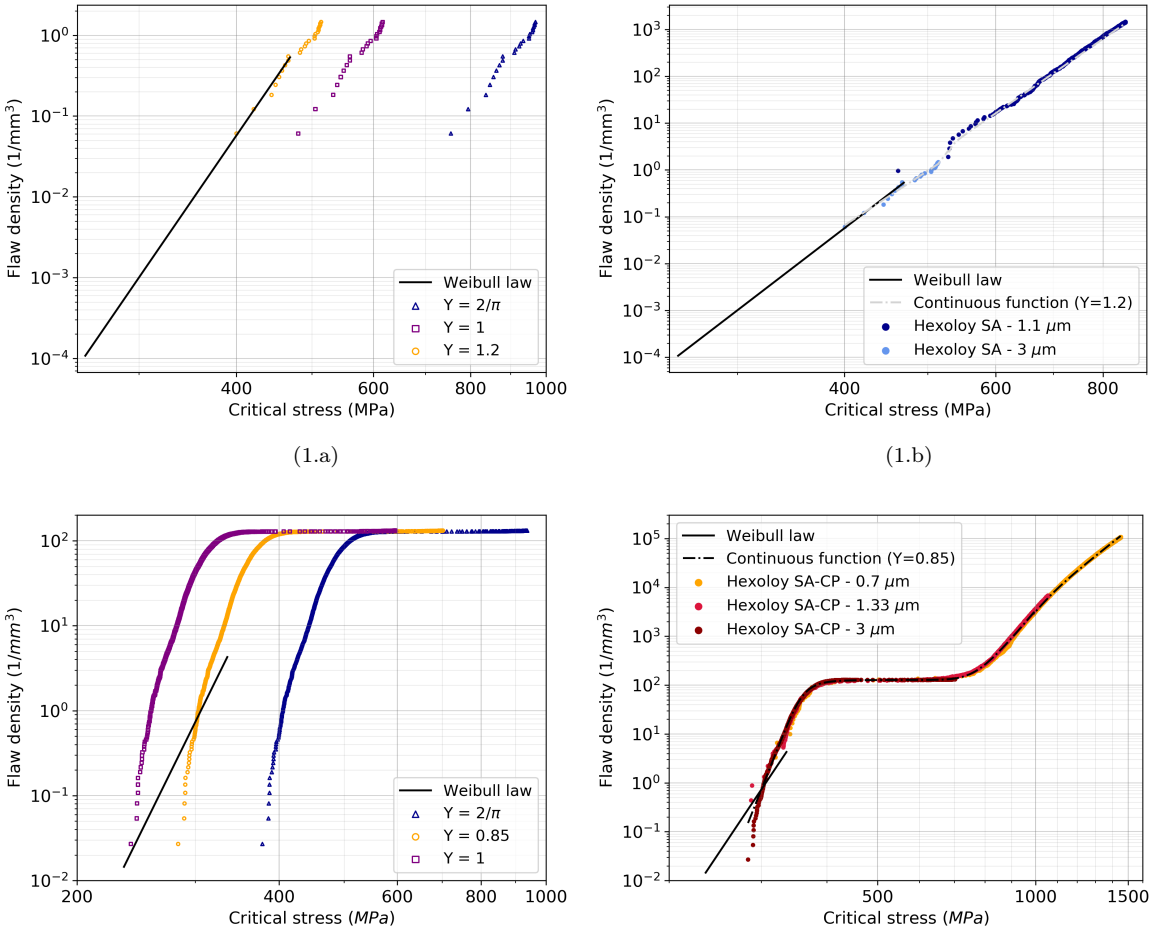

Figure 6.1. Cumulative flaw densities as a function of the critical stresses of the defects, for three values of shape factors Y (a) (scans 3 μm/pixel). Y values of 1.2 and 0.85 provided the best fit with the Weibull law at the average bending strength, for the Hexoloy SA (1) and Hexoloy SA-CP (2), respectively. Continuous function identified for the selected Y values (b), from equation (6.17)

6.2.2 Comparison of ultimate strength and cracking density sensitivity to strain rate

The Weibull flaw distribution can be a relevant approximation at low strain rate, as the flaw population triggered in quasi-static conditions is relatively well described by the bending tests. In this section, a larger range of strain rates is explored. The predictions of the DFH model, in terms of cracking density and ultimate strength, are computed for both flaw descriptions. For a Weibullian flaw distribution, equations (6.10) and (6.9) were used to compute the ultimate strength and cracking density, respectively, at different levels of constant strain rates. Considering the flaw distribution identified from X-ray tomography, the continuous function was first implemented in equation (6.13) in order to determine the damage variable from double integration with respect to time. From this, the cracking density could be calculated from equation (6.5) and the ultimate strength from equations (6.3) and (6.4), for a given loading rate. The material parameters used in the DFH modelling are given for the Hexoloy SA and Hexoloy SA-CP in Table 6.2. The resulting predictions, in terms of ultimate strength and cracking density are presented in Figure 6.2 for a range of strain rates ($\dot{\epsilon} = \dot{\sigma}/E$) between 10^2 and 10^6 s^{-1}.

Table 6.2. Material parameters used in the DFH model for the Hexoloy SA and Hexoloy SA-CP ceramics

		Hexoloy SA	Hexoloy SA-CP
Mechanical parameters	Density ρ (kg/m^3)	3150	3110
	Young's modulus E (GPa)	430 [163]	390*
	Poisson ratio ν	0.14*	0.12*
	Fracture toughness K_{IC} (MPa.$\sqrt{m}$)	3.0 [40]	2.9*
Weibull parameters	Weibull modulus m	14.05**	16.04*
	Average bending stress σ_w (MPa)	406**	300*
	Effective volume V_{eff} (mm^3)	4.53**	0.836*
Obscuration volume parameters	Shape factor S	3.74	3.74
	Crack velocity ratio k	0.38	0.38
	Longitudinal wave speed C (m/s)	11680	11200

* data provided by Saint-Gobain Research Provence
** data provided by Saint-Gobain Research North America (NRDC)

First, it can be noticed from Figures 6.2 (1.a) and (1.b) that the fragmentation behaviour of both materials is highly strain-rate dependant. An increase of the loading rate leads to an increase of the tensile strength of the material and to an intensification of its fragmentation (number of triggered cracks). This result is in accordance with the transition from single to multiple fragmentation observed in brittle materials [58]. For the Hexoloy SA material, the Weibull-based (dashed line) and Continuous approaches (continuous line) give almost identical results. This confirms that the Weibull approach, yet only based on quasi-static data, is able to give accurate predictions over a large range of strain rates (including dynamic) for this material. For the Hexoloy SA-CP material, it is interesting to notice that both laws of critical defects lead to predictions relatively close for strain rates up to 10^4 s^{-1}, Figures 6.2 (1.a) and (2.a). This shows that, for both materials, the Weibull approximation seems to be actually relevant, not only for very low strain rates (QS), but also for intermediate strain rates ($\leq 10^4$ s^{-1}). Nevertheless, at high or very high strain rates the Weibull-based and Continuous predictions drastically diverge for the Hexoloy SA-CP ceramic. Indeed, the Weibull method highly under-estimates the resistance of the material (Figure 6.2 (2.a)), whereas the Continuous method predicts a sharp increase of the ultimate strength for loading rates higher than 2.10^4 s^{-1}.

As a reminder, the cracking density corresponds to the density of activated flaws. It means that it does not take into account the critical flaws from which no crack could be initiated because of the stress relaxation induced by the crack propagation of a neighbouring critical flaw. What is interesting is that

for strain rates in the range 8.10^3 - 4.10^4 s^{-1} in Figure 6.2 (2.b), the crack density of the porous Hexoloy reaches a plateau at about 100 cracks/mm^3. This matches the plateau in the flaw distribution detected from tomography (Figure 6.1 (2.b)). This means that the loading rate is not high enough to trigger the relatively small pores and in this range of loading rates, the volume is fully damaged by the growth of obscuration zones spreading from the activation of the large spherical pores. As no pores of sizes between 20 - 40 μm are available to be activated in the material, the cracking density presents a plateau for a relatively large range of strain rates 8.10^3 - 4.10^4 s^{-1}. At higher strain rates ($\leq 4.10^4$ s^{-1}), the growth velocity of the obscuration zones from the large pores is no longer sufficient to prevent the triggering of smaller flaws, so the cracking density increase again. Finally, the growth of obscuration zones from large flaws prevented the initiation of numerous micro-cracks in the material for loading rates between 8.10^3 and 4.10^4 s^{-1}. In order to highlight this kinetic effect, a complementary approach, named the Discrete method [201], also based on tomography data, was developed and is described in the next section.

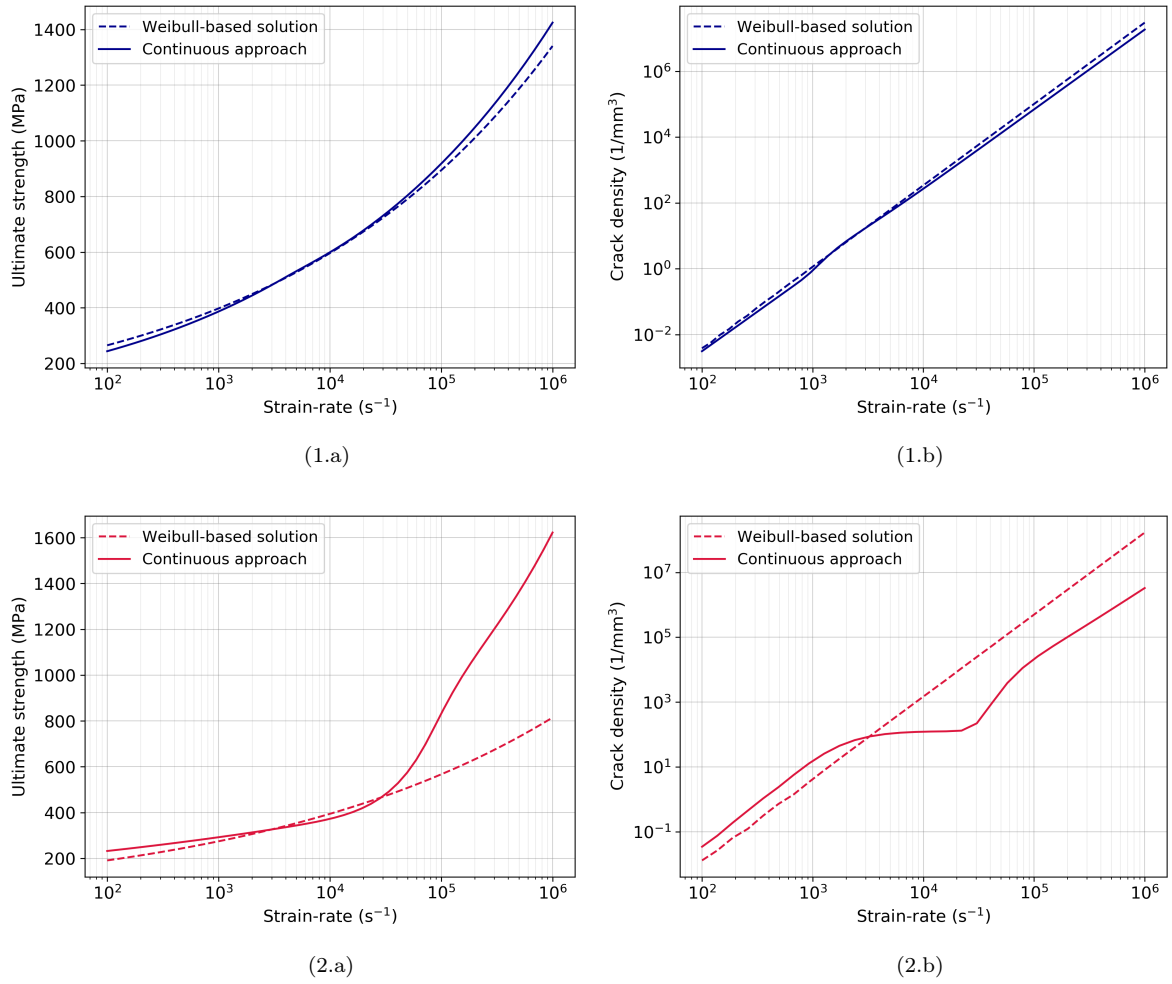

Figure 6.2. Predictions of the ultimate strength (a) and final cracking density (b) evolution according to the strain rate for the Hexoloy SA (1) and Hexoloy SA-CP (2) materials. A Weibullian flaw population and a flaw description based on the continuous function identified from micro-tomographic data are considered

When comparing the two Hexoloy grades in Figure 6.3, the dense Hexoloy SA ceramic presents a higher resistance than the Hexoloy SA-CP material up to a strain rate of about 1.5×10^5 s^{-1}. This is consistent with the fact that, at least at low and intermediate strain rates, the introduction of large pores decreased the tensile strength of the material. The more intense fragmentation of the Hexoloy SA-CP in this range of loading rates, shown in Figure 6.3 (b), is also in line with the overall presence of a larger number of pores compared with the Hexoloy SA (flaw densities in Figure 6.1). The presence of a plateau for the crack density of the Hexoloy SA-CP considerably reduces the number of cracks compared to the

Hexoloy SA. Thus, for strain rates higher than 7.10^3 s^{-1}, the Hexoloy SA-CP finally presents a lower cracking density than the Hexoloy SA, reaching about ten times less cracks at 2.10^4 s^{-1}, despite its overall greater amount of pores.

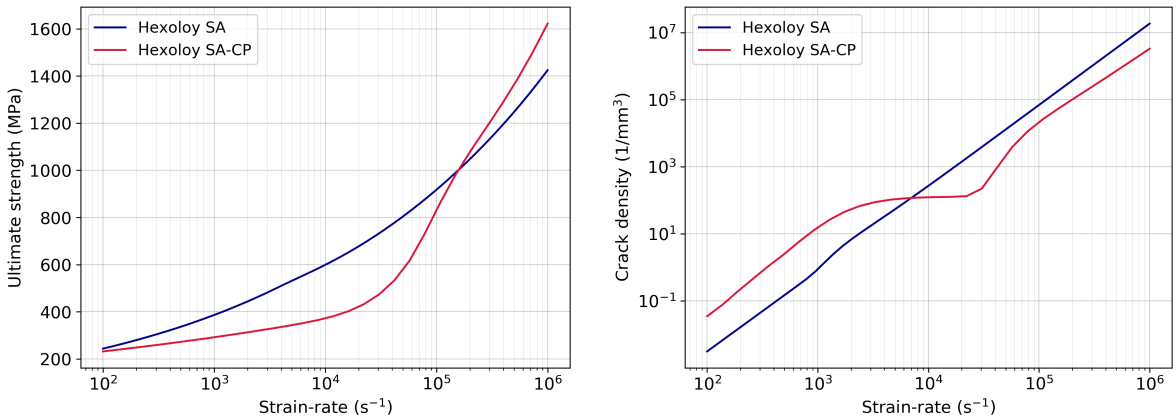

Figure 6.3. Comparison of the ultimate strength (a) and cracking density (b) predicted by the DFH model based on the Continuous approach, for Hexoloy SA and Hexoloy SA-CP

6.2.3 Kinetic effect on the fragmentation process, the Discrete method

Methodology for the Discrete simulations

The goal of this complementary study is to better understand the discrete fragmentation process and to identify which population of pores is triggered according to the loading rate. To do so, simulations of a tensile test on a volume containing discrete flaws were computed for different loading rates. To implement the true population of defects of both Hexoloy grades in calculations, the X-ray tomography technique is used. Micro-tomography was used to capture the position (centre of mass) and size (equivalent diameter) of each pore in a scanned volume (crop into a cubic shape). On the basis of this information, the cubic numerical volume is created, containing all the centre of mass of the pores detected by tomography at their exact positions. The numerical cube is discredited in 100*100*100 cubic elements. A triggering time, corresponding to a stress of activation, is assigned to each flaw according to its size, using equation (6.14) with the Y factor calibrated for the Continuous approach. A Python-based algorithm was developed to apply a uniform tensile loading, increasing linearly with time, on this numerical volume and to study the fragmentation process with respect to the applied loading rate. All the fragmentation phenomenology described in section 2.3.2 was implemented in the algorithm. Once the applied stress, which is gradually incremented (time increment of 0.1 ns), exceeds the critical stress of a defect present in the volume, the defect is activated unless it was previously obscurated by the prior activation of a neighbouring defect. Obscuration volumes grow around the triggered pores (centered on its centre of mass) at a constant velocity, proportional to the 1D-wave speed. In order to have an obscuration volume equivalent to a shape factor of $S = 3.74$, the parameter k initially equal to 0.38 was adapted to keep an expression $S(kC)^3$ constant between the approaches. When the spreading obscuration zone reaches a new element of the mesh volume, the damage variable of this element is set to 1. Finally, the total damage corresponds to the number of damaged elements (containing an obscured zone), divided by the total number of elements:

$$D_{tot} = \frac{N_{damaged\ elements}}{N_{total\ elements}} \tag{6.19}$$

The simulation stops once this damage variable reaches a value of 0.999. The final cracking density λ^{∞}_{crack} is defined by the number of triggered pores N^{∞}_{crack}, reached at the end of the simulation (T_{max}), divided by the total volume of the cube V_{tot}:

$$\lambda^{\infty}_{crack} = \frac{N^{\infty}_{crack}}{V_{tot}} \tag{6.20}$$

The strength $\Sigma(T)$ at a time T is deduced from the damage variable D_{tot} and applied stress, according to equation (6.3). Finally, the ultimate strength Σ_u is the maximal value reached for a time t_u, according to the condition given in equation (6.3).

The simulation was run for strain rates values ranged from 10^2 to 10^6 s^{-1}. The material (ρ, E, K_{IC}) and DFH ($S(kC)^3$) input parameters used for the Discrete simulations are the same as the one used for the Weibull-based and Continuous approaches, presented in Table 6.2. Concerning the parameters specific to the tomography scan and numerical discretization, they are detailed in Table 6.3 and were defined to reach a fine resolution of the damage growth. The main outputs of the Discrete simulations are detailed in Table 6.4 for some strain-rates values. The number of triggered defects N^u_{crack} and the size of the largest undamaged pore (not triggered or obscurated) L^u_{max} at the time the ultimate strength is reached are given. In the same way, the number of triggered defects N^∞_{crack} and the size of the largest undamaged pore L^∞_{max} at the time the whole cube is fully damaged ($D_{tot} > 0.999$) are given in Table 6.3. These output data provide information on the strain rate value for which the transition between a single fragmentation (N^∞_{crack}=1) and multiple fragmentation occurs, according to the considered volume. Moreover, it allows for all the pores detected from micro-tomography (size cut-off $D_{eq} < 5$ px) to know if they are triggered or obscurated (L^∞_{max}= ∅), according to the loading rate.

Table 6.3. Input parameters for the Discrete simulations

		Hexoloy SA	Hexoloy SA-CP
Tomography scan parameters	Scan spatial resolution (μm/pixel)	1.1	1.33
	Shape factor Y	1.2	0.85
Discretizing parameters	Total cubic volume (mm^3)	0.88	1.4
	Number of elements	100 x 100 x 100	100 x 100 x 100
	Time increment (ns)	0.1	0.1

Table 6.4. Main outputs of the Discrete simulations for the determination of the ultimate strength and final crack density

	Strain-rates	Ultimate strength (until Σ_{max})			Final cracking density (until D_{max})		
	(s^{-1})	N^u_{crack}	L^u_{max} (μm)	Σ_u (MPa)	N^∞_{crack}	L^∞_{max}	λ^∞_{crack} (mm^{-3})
Hexoloy SA	100	1	12.9	462	1	12.9	1.5
	1000	1	12.9	467	2	11.2	2.9
	10000	14	8.9	599	226	∅	333
	100000	918	∅	945	918	∅	1351
	1000000	927	∅	3484	927	∅	1364
Hexoloy SA-CP	100	1	89.4	288	2	80.6	0.72
	1000	3	78.2	299	47	51.5	16.9
	10000	251	46.7	380	282	13.9	102
	100000	7321	7.3	860	12411	∅	4468
	1000000	14306	∅	2471	14306	∅	5151

Comparison of the Discrete and Continuous approaches

Predictions given by the Discrete approach for the ultimate strength and final crack density are graphically compared to predictions obtained from the Weibull-based and Continuous methods in Figure 6.4. On the one hand, it can be noticed that the Continuous and Discrete methods, both based on the real flaws detected by tomography analysis, give the same results for intermediate loading rates. This first result confirms that the continuous function properly describes the flaw population detected by tomography. Then, this similarity means that the exact position of defects (Discrete simulations) does not change

the fragmentation behaviour as it leads to similar predictions as the Continuous approach, for which the pores are assumed to be randomly distributed in the volume. It suggests that defects in both materials are homogeneously (randomly) distributed in the volume.

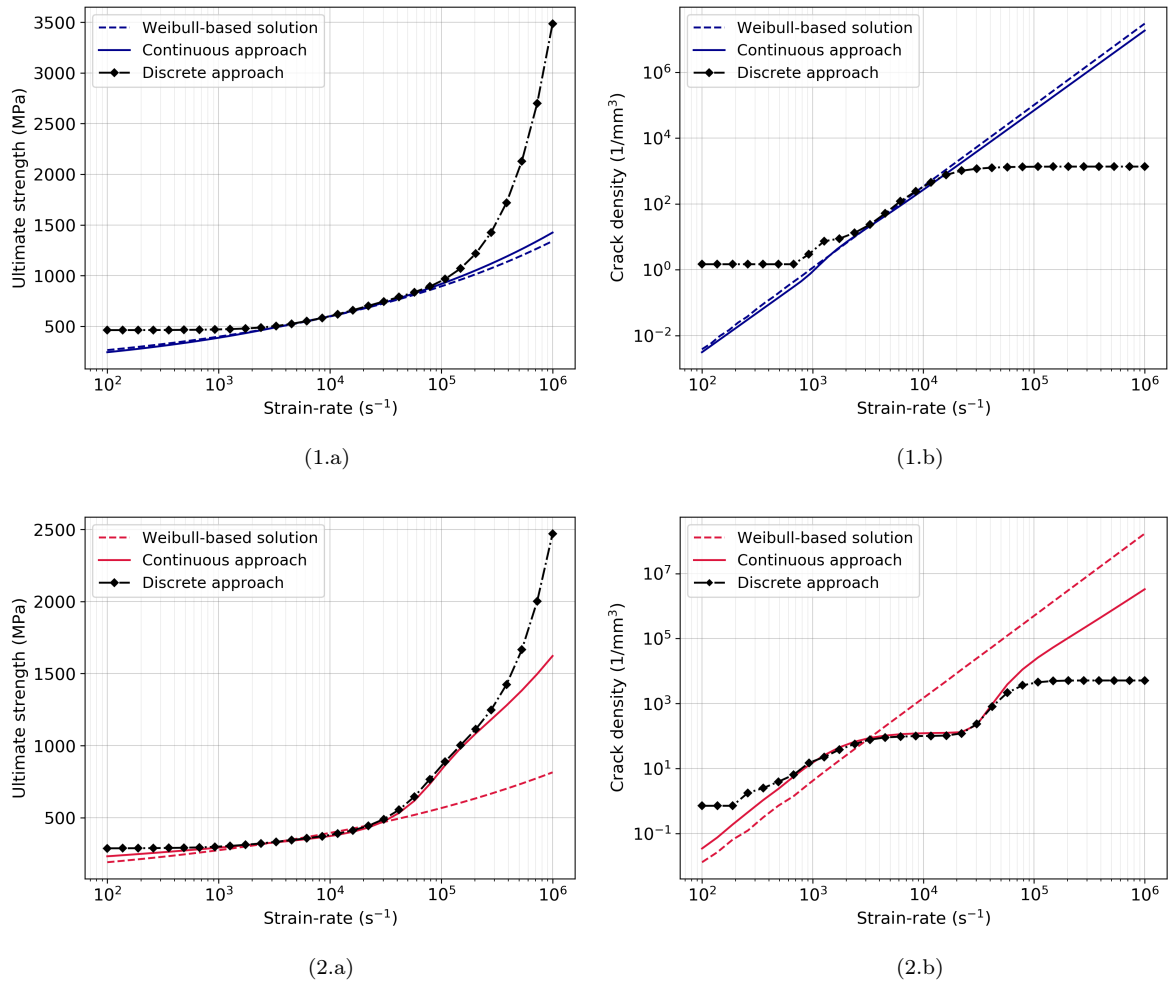

Figure 6.4. Comparison of the prediction of the Weibull, Continuous and Discrete approaches, in terms of ultimate strength (a) and cracking density (b), for Hexoloy SA (1) and Hexoloy SA-CP (2)

On the other hand, the Discrete and Continuous approached diverge at low and high strain rates. First, the Discrete method presents a plateau at strain rates lower than about 7.10^2 and 2.10^3 s^{-1} for Hexoloy SA and Hexoloy SA-CP, respectively. This means that the Discrete method predicts a single fragmentation process in the considered cubic volume, resulting in a unique crack. The ultimate strength value of this plateau corresponds to the critical stress of the largest flaw in the scanned volume (462 MPa for the Hexoloy SA and 288 MPa for the Hexoloy SA-CP). So, the position of this plateau actually depends on the scanned volume, and the biggest flaw that it includes. For both materials, the considered volume was large enough to capture pores responsible for quasi-static failure, as levels of strengths reached at the plateau are close to the average bending strengths (406 and 300 MPa). This single fragmentation process is not captured in the Continuous method, which does not involve the size of the considered volume. At very high strain rates, above 4.10^4 for the Hexoloy SA and 10^5 for the Hexoloy SA-CP, the Discrete method presents another plateau for the final crack density in Figures 6.4 (1.b) and (2.b). This plateau is due to the limited spatial resolution of tomography scans. As pores with a diameter lower than 5 pixels (cut-off value) could not be accurately identified, at a certain high strain rate all detected pores are either activated or obscurated, but no smaller pores are available to be triggered. This absence of small pores leads to a plateau for the final crack density and an artificial increase of the material strength in Figures 6.4 (1.a) and (2.a). Conversely, very small

pores are extrapolated by the fit of the continuous unbounded function in the Continuous approach. Results of the Discrete approach depend on the spatial resolution and size of the considered scan. In Figure 6.5, predictions given by the Discrete approach are compared for three different scans made on Hexoloy SA-CP (spatial resolution of 0.7, 1.33 and 3 μ). A relatively high voxel size provides more accurate predictions at low and intermediate strain rates, whereas the lowest voxel size leads to better predictions for high strain rates. These results show the most appropriate spatial resolution, needed for the tomography analysis, according the range of loading rates of interest for the application. In order to better understand how the presence of an intermediate plateau on the range 8.10^3-5.10^4 s^{-1}, for the Hexoloy SA-CP material, correlates a sharp increase of the material strength, the fragmentation kinetic is studied in the next section.

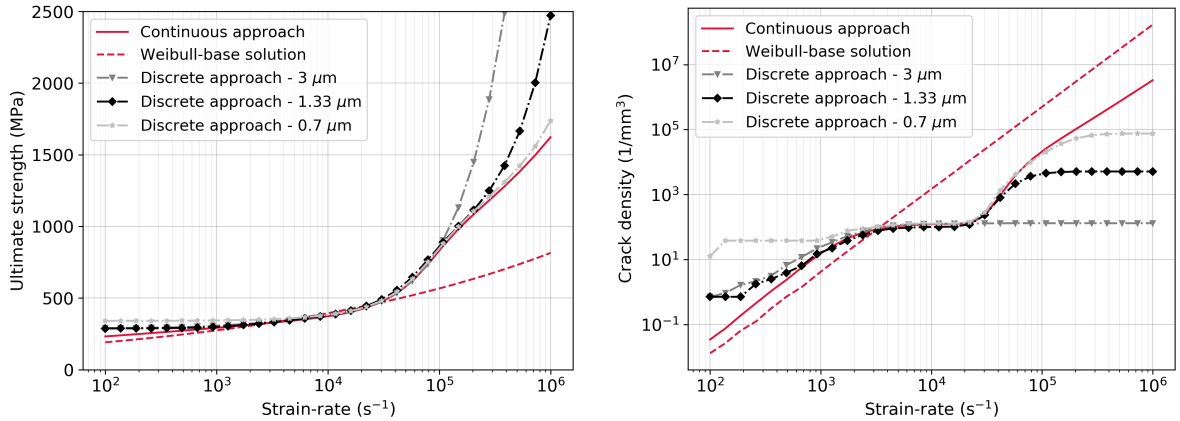

Figure 6.5. Effect of the scan spatial resolution on the results of the Discrete simulations for the Hexoloy SA-CP (voxel size of 0.7, 1.33 and 3 μm)

Correlation between the distribution of pre-existing defects and the fragmentation kinetic

Families of pores triggered at a given loading rate can be identified from this Discrete approach. In Figures 6.6 (1.a) and (2.a), the histograms present the critical stresses of the triggered defects, for three different strain-rates. Activated pores, responsible for the calculation of the ultimate strength (at T_u) and final crack density (at T_{max}), are distinguished. It is noticeable that for the Hexoloy SA-CP, at low and intermediate loading rates ($< 2.10^4$ s^{-1}), the triggered pores are only the largest ones (spherical size-controlled pores) with a critical stress lower the 500 MPa, whereas at higher loading rates, the second population of smaller pores (sintering defects) is initiated. To better understand which flaws population is triggered according to the applied strain-rate, the evolution of the crack density is plotted for three different loading rates as a function of the microscopic stress of the activated pores in Figures 6.6 (1.b) and (2.b). Contrary to the Hexoloy SA material for which the crack density keeps increasing as the loading rate is increased, for the Hexoloy SA-CP, the crack density presents a plateau around 100 cracks/mm^3. This plateau results from the quasi-absence of pores of size 20-40 μm in the material (plateau in the input flaw distribution in Figure 3.11). Only large pores are triggered at low strain-rates, therefore leading to a low ultimate strength. For intermediate strain rates, from about 1.10^4 to 5.10^4 s^{-1}, a clear increase of the microscopic stress of the activated pores is obtained while maintaining a quasi-constant amount of cracks. This means that the whole volume is only damaged by the obscuration zones spreading from the large pores. Finally, for strain rates above 5.10^4 s^{-1}, the growth of obscuration volumes around triggered cracks becomes too slow compared to the loading rate, so a high amount of small cracks are simultaneously nucleated out of these damaged volumes, resulting in a sharp increase of the final crack density. This limited amount of micro-cracks plays a role on the kinetics of the damage variable, therefore resulting in a great increase of the material strength.

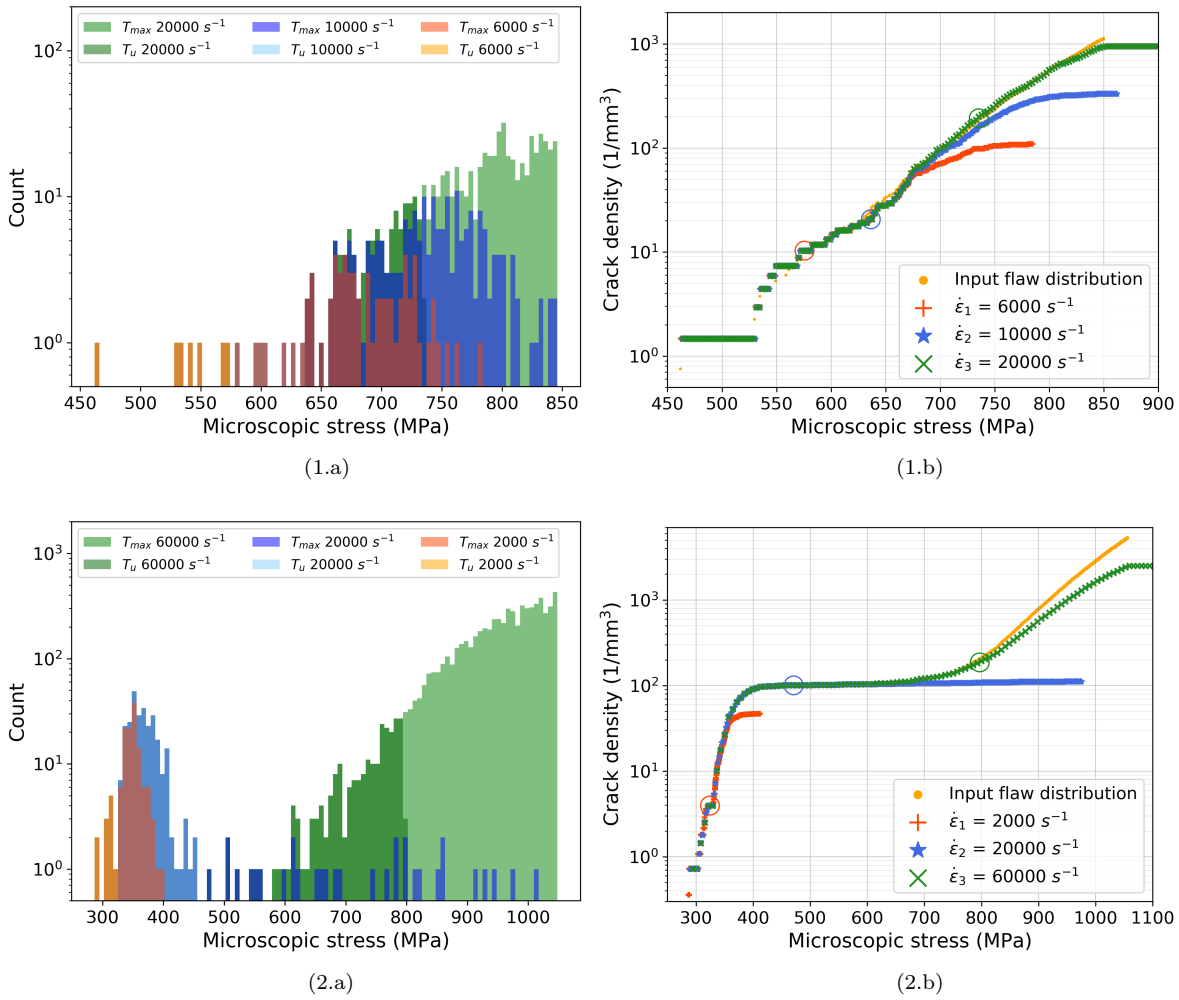

Figure 6.6. Results of discrete numerical simulations for Hexoloy SA (1) and Hexoloy SA-CP (2). (a) Overlapped histograms of the critical stresses of each activated pore for three levels of strain rates. (b) Evolution of the crack density as a function of the microscopic stress for three levels of strain rates. The crack density level corresponding to the time at which the ultimate strength is reached is circled for each loading rate

These results are consistent with the numerical observations of Zhou et al. (2005) from one-dimensional fragmentation analysis of a ceramic bar under uniform tensile loading, over a large range of strain rates (10 - 5.10^6 s^{-1}) [151]. They considered defects equally and randomly spaced along the bar and incorporated elastic wave propagation and a cohesive failure process. From this, they highlighted the presence of three regimes where the fragmentation process is respectively driven by the largest defect ($<$ 250 s^{-1}, quasi-static regime), the defect population (250 - 25000 s^{-1}, according to the defects spacing) and the kinetic process ($>$ 25000 s^{-1}). Moreover, from their qualitative predictions, they introduced the fact that a heterogeneous material should present a more strain-rate dependent behaviour than an homogeneous material. This is confirmed in the present work by comparing the homogeneous (Weibullian flaw distribution) Hexoloy SA material and the heterogeneous Hexoloy SA-CP material (size-controlled large pores). The Hexoloy SA-CP material exhibits a high rate-hardened strength (Figure 6.3). The comprehensive modelling methodology developed in this chapter brought further insight on the correlation between the material pre-existing flaws and its 3D fragmentation process, over a large range of strain rates. Thus, instead of considering an idealized defect distribution, as proposed by Denoual and Hild [78] and Forquin and Hild [77], a more realistic flaw distribution extracted from X-ray tomography analysis can be directly implemented in the fragmentation modelling [201].

6.3 Validation of the modelling based on tomography by comparison with experimental results

The goal of this section is to bring elements of validation to this fragmentation modelling, based on the defect description via X-ray tomography analyses and the DFH model, for the Hexoloy grades. To do so, the predictions given by the DFH model with the Continuous approach, are compared to experimental data obtained from dynamic fragmentation tests (Chapter 4) and shockless spalling tests (Chapter 5).

6.3.1 Comparison of the fragmentation patterns from experiments and numerical simulations, with the Weibull and Continuous methods

Finite Element Modelling using Abaqus was used in order to compare the crack network experimentally obtained during the EOI and Normal impacts tests, presented in Chapter 4, and the fragmentation patterns predicted by the DFH model. A FORTRAN-based user subroutine was used to include the constitutive behaviour of the ceramic material, according to the DFH model. In this way, the critical flaw density could be explicitly implemented in the simulations to describe the ceramic tensile damage behaviour. Both Weibull-based and continuous flaw densities were implemented for their resulting fragmentation patterns to be compared to crack patterns obtained experimentally.

Implementation of the DFH model for the numerical simulations

Numerical simulations of the EOI and Normal impact tests were performed on the finite-element code Abaqus/Explicit. Simulation parameters (mechanical behaviour of the projectile, discretized geometries, interactions, mesh and boundary conditions) were kept identical to elastic simulations conducted in section 4.1.4 (Table 4.2), except for the ceramic material. The DFH model was implemented in the finite element code, using a user subroutine VUMAT, to describe the failure behaviour of the ceramic target. The main interest of the Continuous method is that the function interpolated from tomography analyses could be directly implemented in the finite element code (to replace the Weibull power law). The VUMAT was modified to compute the damage variable and increment of cracking density according to equations (6.13) and (6.5), using the continuous function of critical defects given in Table 6.1. Such simulations give access to the damage variables, macroscopic stresses and densities of cracks along the three directions. To compare the fields of cracks with experimental results, direct attention was on the cracking density along the maximum principal stress direction. The proper functioning of the VUMAT was checked by conducting initial tests on a single-element model with a traction loading. For several given strain rates, the maximal stress reached in the loading direction and the crack density obtained in a single element were compared to the ultimate strength and final crack density computed in the analytical modelling (previous section Figure 6.3).

Comparison of the fragmentation chronology and patterns for EOI test

EOI tests were numerically simulated with the modified VUMAT. Final fields of cracking density, obtained 2.5, 4 and 5 μs after impact, are shown in Figures 6.7 and 6.8 for the Hexoloy SA and Hexoloy SA-CP materials, respectively. Fragmentation patterns obtained from the Weibull-based approach (a) and the Continuous approach (b), at the same impact velocity of 175 m/s, are compared. The crack density variable is expressed in a log scale, meaning that a value of 9 on the scale bar corresponds to 10^9 cracks/m^3, so 1 crack/mm^3. The cracking density evolution in time is relatively similar for both input flaw distributions, with the rapid development of cracks along the loading axis, followed by some spalling cracks at the rear edge of the target due to tensile stresses induced by the released waves from the free surface, and the final propagation of some cracks (damage corridors) in the rest of the tile at about 5 μs after impact. As expected, the Weibull-based and Continuous approaches give almost the same results for the Hexoloy SA material, which flaw population is almost Weibullian. The only noticeable difference for the Hexoloy SA is a more intense fragmentation close to the projectile and along the loading

axis with the Continuous approach. For the Hexoloy SA-CP material, the overall fragmentation is more intense than the Hexoloy SA, except far from the projectile, where some relatively large zones remained poorly fragmented at the end of the fragmentation process (5 μs). The Continuous approach predicts a less intense fragmentation close to the impact point ($<$ 15 mm) along the loading axis with about 10^2 cracks/mm^3, whereas the Weibull-based approach reaches about 10 times more cracks. It can be noticed that the cracking density is more homogeneous in this area with the Continuous approach.

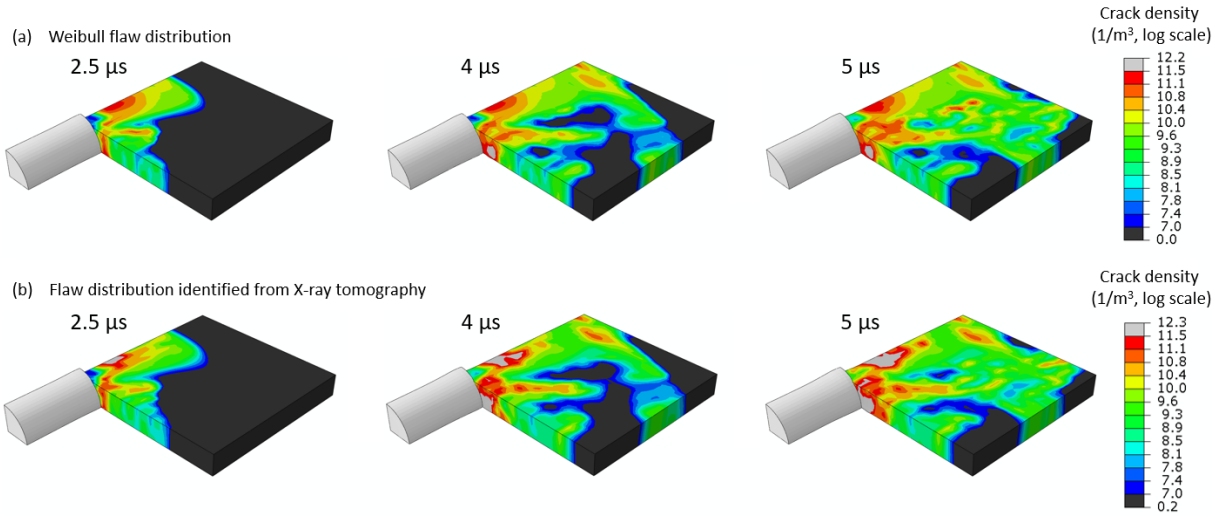

Figure 6.7. Crack density obtained from DFH numerical simulations of EOI tests (175 m/s) with the Weibullian (a) and Continuous (b) flaw densities as an input, for the Hexoloy SA material

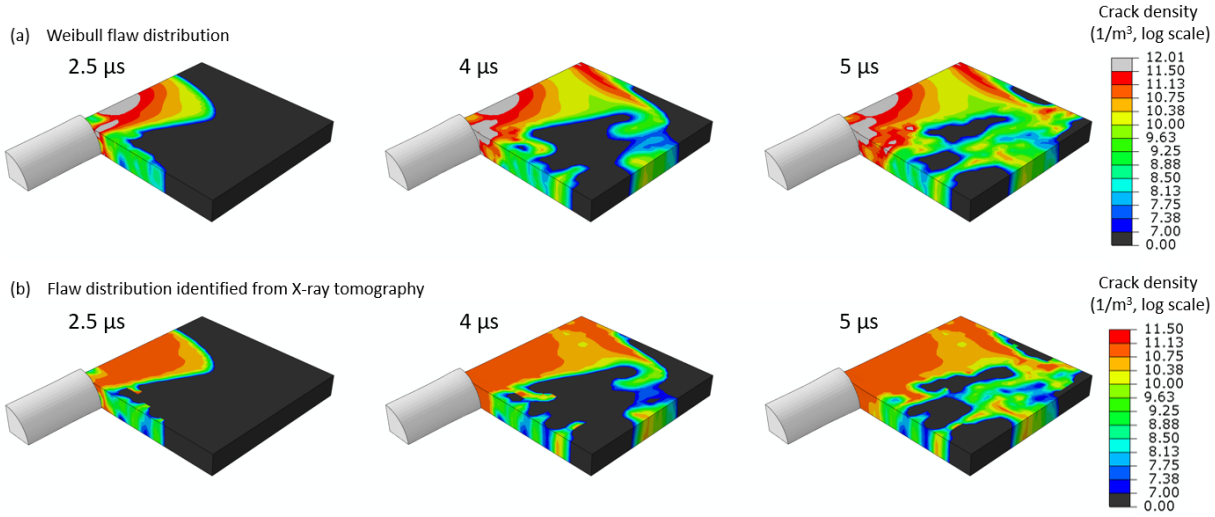

Figure 6.8. Crack density obtained from DFH numerical simulations of EOI tests (175 m/s) with an input Weibullian (a) and Continuous (b) flaw densities, for the Hexoloy SA-CP material

Cracking density patters obtained from numerical predictions are qualitatively compared to the crack-network capture by ultra-high speed imaging 12 μs after EOI tests (Chapter 4) in Figures 6.9 and 6.10. For this comparison, the numerical impact velocity is taken equal to the projectile velocity obtained experimentally. The comparison with the numerical simulation and high speed images is limited to a zone relatively far from the impact points as close to the projectile nose, the fragments tilt led to a loss of light reflection (no information on the crack density). Finally, no clear differences can be seen for the Hexoloy SA because the flaw density are very similar for both Weibull-base and Continuous approaches, resulting in similar numerical cracking densities. On the other hand, for the Hexoloy SA-CP, fragmentation patterns obtained from the Continuous approach seem to be more accurate than the one from the Weibull-based approach, with respect to the experimental patterns. Indeed, the cracking density

along the loading axis is more homogeneous with the Continuous solution, which visually seems to be closer to the experimental fragmentation.

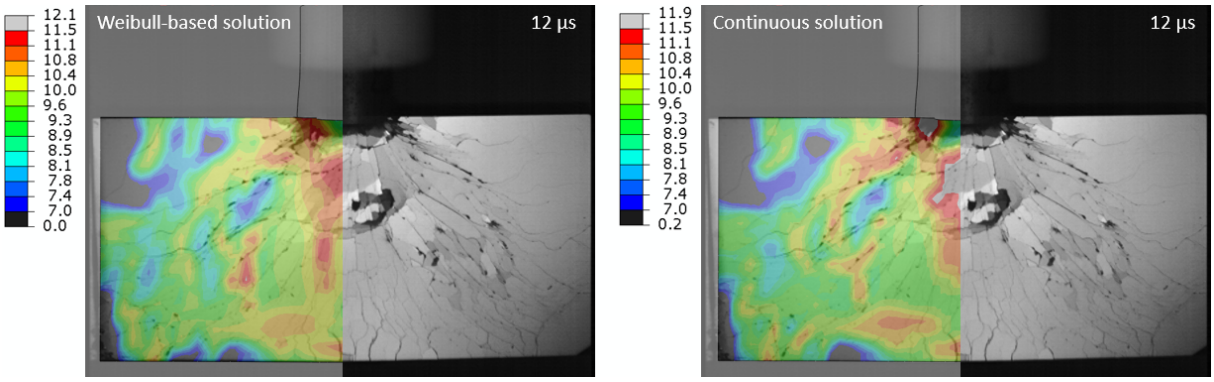

Figure 6.9. Comparison of the crack density in a Hexoloy SA target impacted in an EOI configuration (181 m/s) between experimental results (ultra-high speed imaging, 12 μs) and numerical predictions. Flaw density considered for the numerical simulations is Weibullian (a) and Continuous (b)

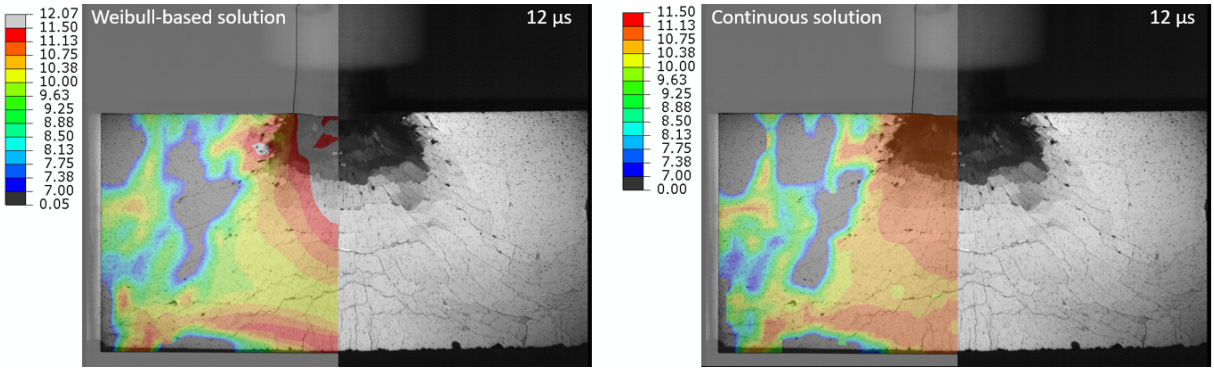

Figure 6.10. Comparison of the crack density of an Hexoloy SA-CP target impacted in an EOI configuration (184.5 m/s) between experimental results (ultra-high speed imaging, 12 μs) and numerical predictions. Flaw densities considered for the numerical simulations are Weibullian (a) and Continuous (b)

Comparison of the fragmentation patterns for Normal impact tests

In the same way, the development of the crack network over time (4, 6 and 10 μs) after a Normal impact (175 m/s) is compared for numerical simulation with the DFH model, considering the Weibull (a) and Continuous approaches (b) in Figures 6.11 and 6.12, using numerical simulations. The main observations made for EOI tests (between both materials and both input flaw distributions) are globally the same for the Normal impact configuration. The chronology of fragmentation from both approaches on the Hexoloy SA are not leading to major differences. Concerning the Hexoloy SA-CP materials, the field of cracking density on the rear face of the ceramic is more homogeneous and less intense. Indeed, the cracking density below the projectile and on the rear face of the ceramic is of about 10^2 cracks/mm^3 with the continuous approach, whereas it reaches about 4.10^3 cracks/mm^3 for the Weibull-based description of the flaw population.

Numerical predictions with both flaw distributions are compared to the crack patterns on a tomography slice of the rear face of the fragmented tile recovered from Normal impact test (sarcophagus and resin infiltration, section 4.2.1). Comparisons are presented in Figures 6.13 and 6.14. For the Hexoloy SA-CP, it can be noticed that the Continuous approach (b) predicts a more compatible field of cracking density compared to the experimental quantification, in terms of homogeneity (under-estimated due to the limitation of crack detection).

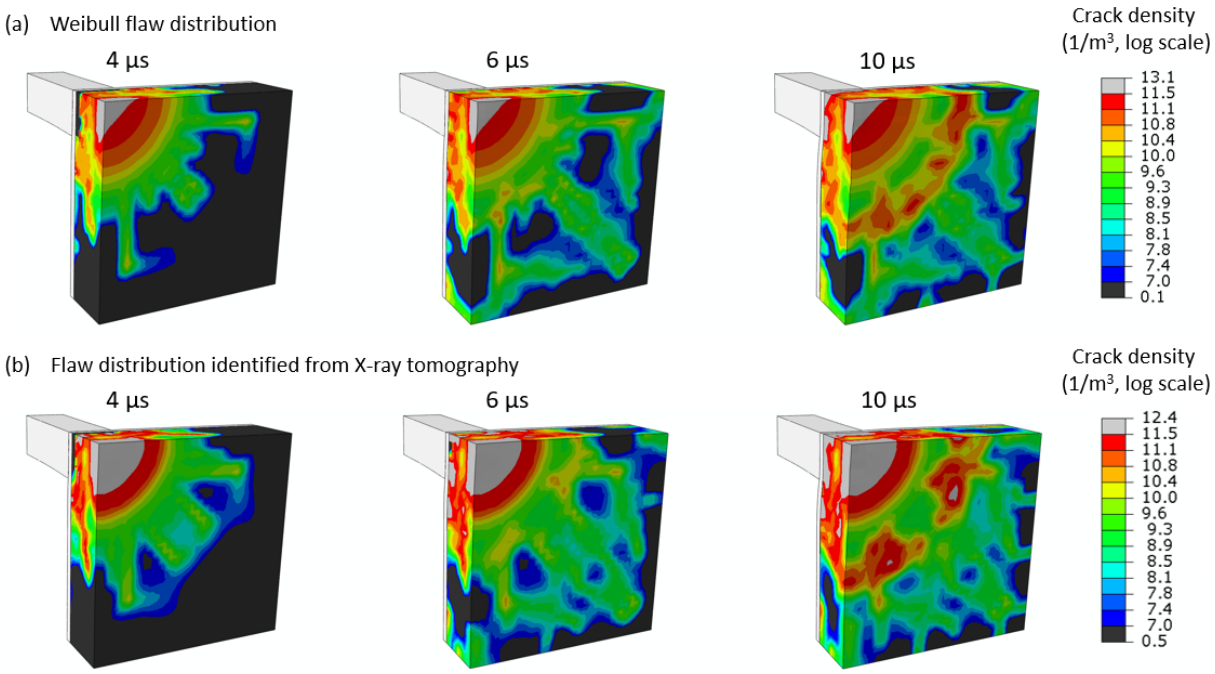

Figure 6.11. Evolution of the crack density on the backside of an Hexoloy SA target after a Normal impact (175 m/s), obtained from DFH numerical simulations. A Weibullian (a) and Continuous (b) flaw densities were considered as an input of the modelling

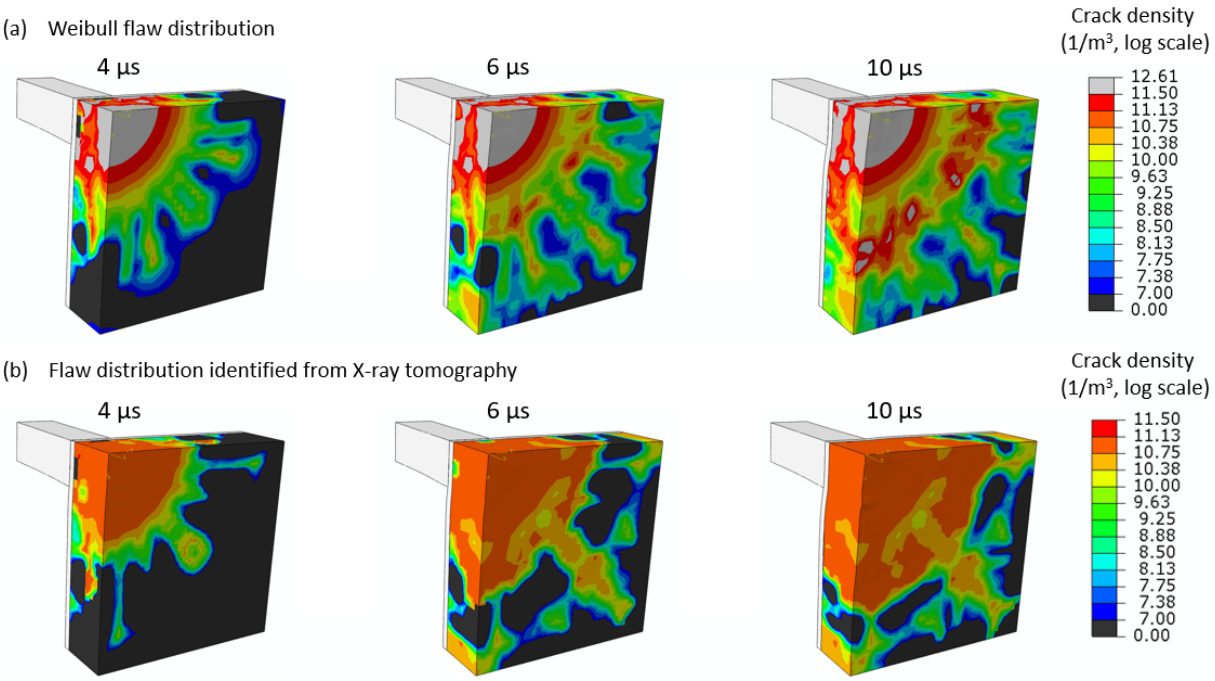

Figure 6.12. Evolution of the crack density on the backside of an Hexoloy SA-CP target after a Normal impact (175 m/s), obtained from DFH numerical simulations. A Weibullian (a) and Continuous (b) flaw densities were considered as an input of the modelling

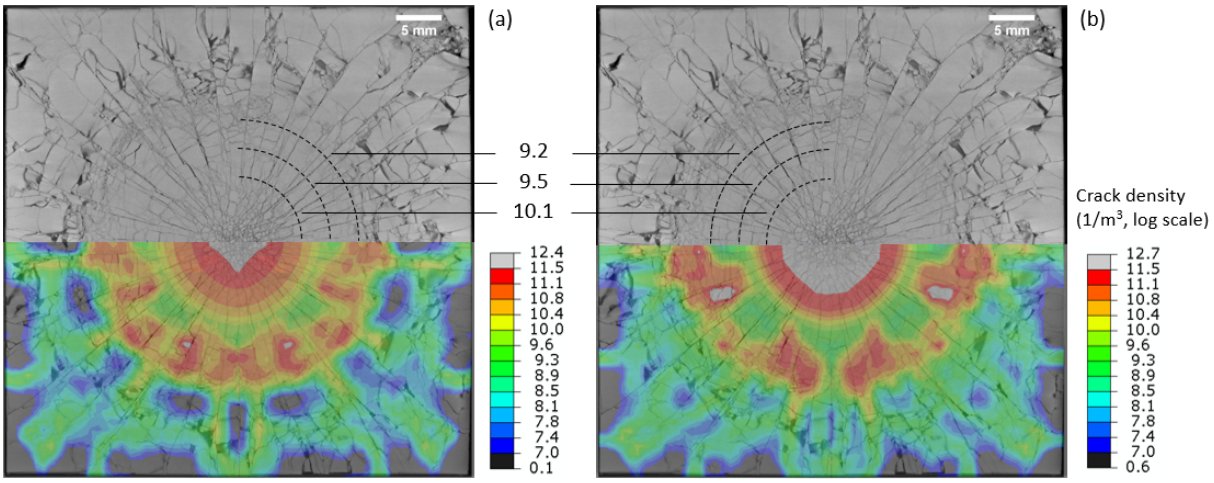

Figure 6.13. Comparison of the fragmentation patterns obtained experimentally (tomography scan) and from numerical simulations on the rear face of an Hexoloy SA target impacted in a Normal impact configuration (178.5 m/s). The flaw density considered for the numerical simulations is Weibullian (a) and Continuous (b)

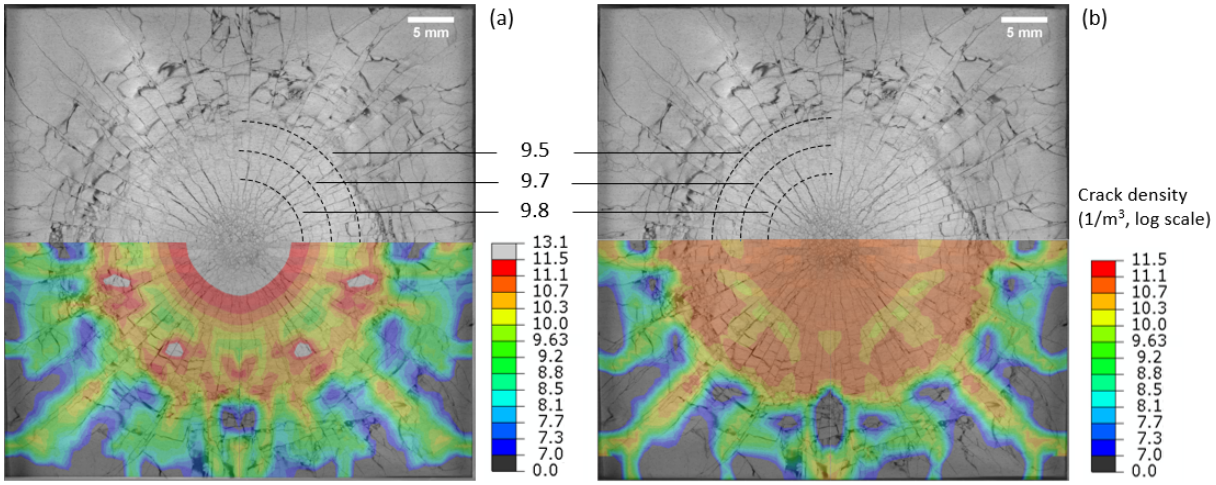

Figure 6.14. Comparison of the fragmentation patterns obtained experimentally (tomography scan) and from numerical simulations on the rear face of an Hexoloy SA-CP target impacted in a Normal impact configuration (172.3 m/s). The flaw density considered for the numerical simulations is Weibullian (a) and Continuous (b)

6.3.2 Comparison of the cracking density sensitivity to strain rate, obtained from the DFH model and fragmentation tests

In Chapter 4, the final crack density was quantified in certain zones of the post-mortem samples recovered from EOI (polycarbonate sarcophagus) and Normal impact (metallic sarcophagus and resin infiltration) tests. Tomography analyses on both post-mortem samples provided experimental data on the cracking density sensitivity to the loading rate. The different zones which were considered for the crack quantification are summarized as follows:

- Edge-on-impact: at a distance of 10 and 20 mm from the impact point, with an angle of 20° on both sides of the loading axis and averaged on five slices through the tile thickness
- Normal impact: on the ceramic rear-face at a distance of 7, 10 and 13 mm from the impact point

The strain rate responsible for the nucleation of radial cracks in these zones was evaluated from elastic numerical simulations (hoop tensile stresses). Thus, EOI and Normal impact fragmentation tests provided experimental data, given in Tables 4.3 and 4.5 respectively, for strain rates in the range 6.10^2-10^4 s^{-1}. These results are compared to the DFH modelling predictions in Figure 6.15 (a) and (b) for Hexoloy SA and Hexoloy SA-CP.

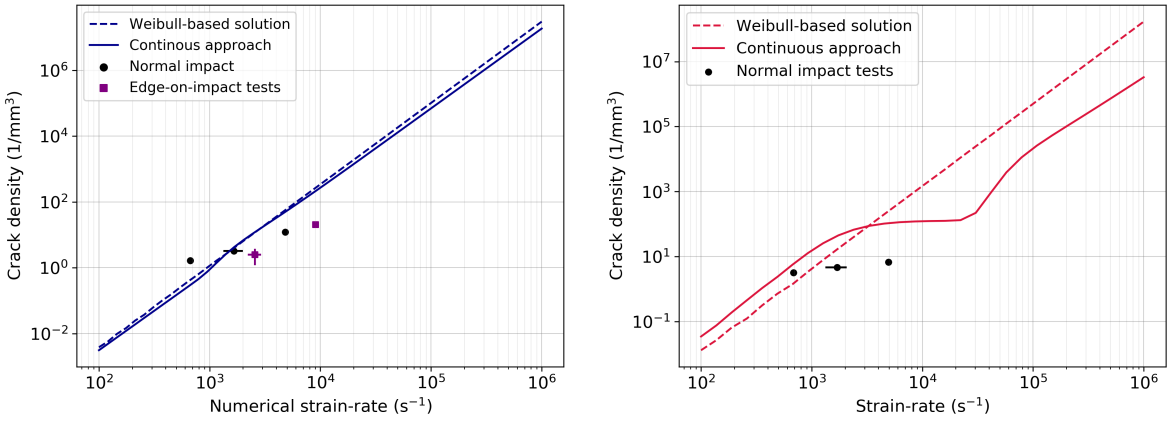

Figure 6.15. Comparison of the DFH predictions, via the Weibull and Continuous approaches, to the cracking densities experimentally obtained from EOI and Normal impacts, for the Hexoloy SA (a) and Hexoloy SA-CP (b)

It can be noticed that the predictions of the Continuous approach are relatively close to the experimental points obtained from EOI and Normal impact. Nevertheless, the experimental quantification tends to under-estimate the amount of cracks. This gap can be explained by the fact that some micro-cracks have limited crack opening and could not be detected for the spatial resolutions of the X-ray tomography scans. Even if the quantification is not exact, it seems that the slope of the sensitivity to the loading rate is not far from the predictions. From theses cracking density quantification, it is not possible to clearly determine between the Weibull-based and Continuous approaches which is the most relevant approach to model the fragmentation behaviour of both materials.

From the fragmentation tests, the Hexoloy SA-CP material was found to present a less sensitive cracking density to the strain rate, compared to the Hexoloy SA. Thus, the Hexoloy SA-CP material had a higher cracking density below a strain rate of 3.10^3 s^{-1}, and a lower fragmentation above this threshold value compared to the Hexoloy SA. It is interesting to notice that the same behaviour was observed in the modelling work. Indeed, predictions of the Continuous approach, compared in Figure 6.3 for both Hexoloy grades, showed that the cracking density of the Hexoloy SA-CP is also less sensitive to the loading rate compared to the Hexoloy SA, and both curves intersect for a threshold value of about 7.10^3 s^{-1}, which is in the same order of magnitude.

6.3.3 Comparison of ultimate strength sensitivity to strain rate, obtained from the DFH model and shockless spalling tests

Concerning the ultimate strength, the DFH model predictions are compared to the material tensile strength determined from the shockless spalling tests developed in Chapter 5. The shockless plate-impacts were designed to maintain a controlled and constant loading rate in the failure zone in order to be able to correlate the dynamic tensile strength to the strain rate. Thus, these experiments allowed reaching controlled strain rates ranged from 10^3 to 2.10^4 s^{-1}, depending on the front-profile of the wavy-machined flyer plate and the impact velocity. The comparison between the modelling and experimental results is presented in Figure 6.16 (a) and (b) for Hexoloy SA and Hexoloy SA-CP, respectively. The DFH modelling predictions, in terms of ultimate strength, are in line with the experimental results for both materials. However, the strain rates reached during the tests correspond to an interval where the Weibull-based and Continuous approaches give similar predictions. It would be interesting to reach higher loading rates (of about 10^5 s^{-1} to obtained a clear experimental validation of the necessity to use the Continuous approach, based on X-ray tomography, to properly model the fragmentation behaviour of the Hexoloy SA-CP material, instead of the Weibull-based solution.

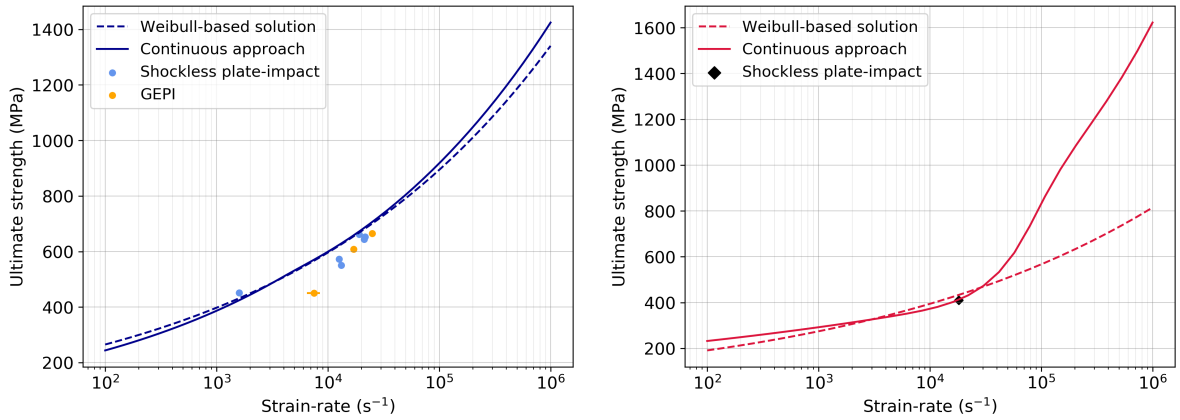

Figure 6.16. Comparison of the strength predictions of the DFH model, via the Weibull-based and Continuous approaches, to the spall strength experimentally obtained from shockless plate-impacts and GEPI tests [85], for the Hexoloy SA (a) and Hexoloy SA-CP (b)

Conclusion of the chapter

Under a dynamic loading, ceramic materials, undergoes an intense dynamic fragmentation due to the lack of plastic deformation. Microstructural defects (such as porosity, embedded impurities or sintering defect at the grain boundaries) prove to be the source of crack nucleation under tensile loading. Therefore, a proper description of the flaw population causing failure is essential to describe the fragmentation process and accurately model ceramic behaviour under dynamic solicitations. In the present chapter, ceramics Hexoloy SA and Hexoloy SA-CP were studied. Both materials present the same dense microstructure with fine grains, but with different pores distributions, homogeneously distributed in the material bulk. Contrary to Hexoloy SA, large size-controlled pores (about 2 vol.% in the range 40-100 μm) are present in Hexoloy SA-CP. From their microstructural analysis in Chapter 6, it was demonstrated that the pores can be considered as the main defects responsible for failure. The common approach to model the behaviour of ceramic materials consists in considering a Weibull distribution of the flaws causing failure, in the form of a power law of the maximal principal stress (Weibull modulus as the power). However, this approach is expected to be unsuitable for the study over a large range of strain rates in the case of materials presenting multiple flaw populations not properly characterized by quasi-static bending tests.

In order to bring insight on the limitation of the Weibull flaw description, the real population of defects of both Hexoloy grades was extracted via CT micro-tomography. Contrary to the Weibull approach, such a description is not restricted to the largest defects triggered under quasi-static loading (volume effect), but provides a more accurate description of the whole flaws distribution. By explicitly implementing this flaw description in the Denoual-Forquin-Hild (DFH) damage model (continuous function), a better understanding of the ceramic fragmentation and strain rate sensitive behaviour is given. The main results of this Chapter can be summarized as follows:

- An accurate description of the material pore population is made possible by micro-tomography analyses conducted with a proper spatial resolution (ideally several scans at different scales). By combining this result to the Linear Fracture Mechanics, a density of critical defects can be identified as a continuous function of the stress applied to the loaded volume. This approach only needs to be calibrated by the determination of the Y shape factor, traducing the geometry of the pre-existing cracks in the materials. To do so, the results of quasi-static bending tests were used.

- This continuous law can be explicitly implemented in the DFH model to compute the damage variable and density of cracks, based on the obscuration mechanism. At low strain rate, the weakest-link theory drives the strength of the whole material, therefore being stochastic (depends on the largest defect included in the volume). For the Hexoloy SA material, this Weibull-based approach was found to correctly describe the material behaviour over the complete range of strain rates considered (10^2-10^6 s^{-1}). For the Hexoloy SA-CP material, the Weibull-based and Continuous approaches provided almost the same predictions in terms of ultimate strength and crack density at low and intermediate stain-rates ($< 2.10^4$ s^{-1}). But at high loading rates, this material presented a sharp increase of ultimate strength, which was not captured by the Weibull-based solution.

- A Discrete modelling was developed to perform tensile simulations on numerical volumes extracted from micro-tomography (real pore positions and equivalent sizes). This approach provided information on the valuable effect of the size-controlled fuse flaw in the porous Hexoloy on the cracking density sensitivity to strain rate. Depending on the loading rate, a competition between the spreading of the obscuration zones and the initiation of new flaw drives the material strength. Such a kinetic-dependant crack nucleation on pre-existing flaws explains the high rate-hardening strength, which is characteristic of brittle materials but magnified for the Hexoloy SA-CP.

- Fragmentation tests (EOI and Normal impacts) and shockless spalling developed in the previous chapters were used as valuable tools to validate the DFH modelling though a numerical-computation versus experiments confrontation. The good match between the predictions and the experimental results, both in terms of ultimate strength and cracking density, are encouraging. It can be noticed that the cracking density is difficult to properly quantify, and often leads to an under-estimation compared to the predictions.

- For both Hexoloy materials, in order to clearly confirm the interest of adopting a method based on X-ray tomography instead of a Weibull-based approach, further experiments would be required to reach higher strain rates (about 10^5 s^{-1}), for which both approaches fairly diverge.

Some assumptions were made in constructing the DFH damage model. The main goal of the present work was to suppress the hypothesis of a Weibull flaw distribution from the DFH modelling, as it was regarded as the most critical assumption (especially for materials with multi-flaw populations). This was successfully done by considering a more realistic description of the flaw distribution using micro-tomography. This micro-mechanical model presents some remaining assumptions. The main assumptions are listed bellow in order of importance and possible ways to strip away from them are introduced as some interesting prospects:

- The microstructure of porous ceramics is highly complex, as it includes highly *irregular* pores and micro-cracks of diverse shapes and orientations [204]. For example, the large spherical pores in

the Hexoloy SA-CP material presents some consequent ramifications. Despite this high complexity, some simplifications are required to develop a micro-mechanical modelling. So, the pore critical length is assimilated to its equivalent diameter (diameter of a sphere of the same volume) and is corrected by a unique shape factor to account for its severity for failure. Such a simplification can be questioned as for different flaw populations, different shape factors should arise [69]. One solution to verify if this assumption is relevant, or to correct it, could be to use the spalling experiments to calibrate the shape factor Y for small pores, through an inverse approach. If different Y parameters are required, compared to the bending test, this would expand or retract the plots according to the loading rate axis.

- The effect of weak inclusions (not detected by tomography) on the fragmentation process is neglected, whereas this type of defects could affect the material strength. Such a simplification is based on the fact that the fragmentation is nucleated on the largest and most critical defects, which were found to be the pores for both Hexoloy grades, containing some well embedded B_4C grains and small carbon inclusions.

- The obscuration zones are linked to the elastic wave but are supposed to be not influenced by the porosity. Moreover, the material in the obscuration zones is considered as fully damaged, with no remaining strength. Such an assumption was questioned by Levy and Molinari [145]. Indeed, if the matrix presents some residual cohesion, such an hypothesis can lose its reliability. This could be the case for heterogeneous microstructures such as some concrete materials for which the number of cracks is very small compared to the characteristic size of heterogeneities (REV). However, this assumption is acceptable for the SiC ceramics considered in the present modelling work, as they present almost no residual cohesion due to their highly homogeneous brittle microstructure with very small grain sizes.

- The crack velocity is supposed to be proportional to the Rayleigh waves speed, with a coefficient k=0.38. It has been mentioned before that this parameter has only a little effect on the predictions. Nevertheless, several authors obtained higher values for ceramic materials [205] [94], so this constant could therefore simply be an increase in the present modelling work. An increase of this parameter is expected to slightly reduce the strength of the material, because obscuration zones will grow more rapidly. Crack velocity could also be expressed as a function of the applied stress, as it is the case in the damage model of Hazell and Iremonger (1997) [206].

- A uniform distribution of the defects is supposed in the Continuous approach. Such an assumption was verified for Hexoloy grades by comparing the predictions with the one obtained from the Discrete simulations (including the real pore positions). However, the Continuous approach would not be suitable for some materials like Forceram grades, which present a bulk heterogeneity of porosity. In order to model the fragmentation behaviour of a material with pores gradients (flaw clusters due to the manufacturing process, gradient of fuse flaw intentionally generated or not, etc.), the Discrete approach would be more adapted.

- The present modelling, as it is, is not adapted to heterogeneous materials, as the meso-structure is not considered. For more complex microstructures (large grain sizes, interconnected pores, different phases, etc.) additional mechanisms, more realistic of the material physics, should be introduced (stress concentration at the grains boundaries, pore collapse, ductility of a binder phase, etc.). So far, the effect of the meso-structure is indirectly taken into account through the experimental determination of the static fracture toughness (ability of the microstructure to resist the crack propagation). In the present modelling, this critical stress intensity factor is considered to be a constant intrinsic property of the material (athermal and independent of loading rate). This simplification can fairly be questioned. Indeed, some authors demonstrated higher values for K_{IC} under dynamic solicitations compared to static loading [207] [208] [209]. With some experimental data, incorporating a rate dependency of critical stress intensity factor (crack growth rate) in the DFH model could be considered.

- In the same way, no distinction was made between static and dynamic crack initiation stress intensity factors, but micro-inertial factors could be introduced for the trigger of a new crack [210].

Ultimately, this study paved the way for a microstructural design to control fragmentation properties for a given range of strain rates. Many studies focus on ways to make advanced ceramics as pure and dense as possible to limit such an intense fragmentation from developing on residual microstructural flaws. The present work shows that with a good understanding of how pre-existing defects influence the fragmentation process, it becomes possible to control them in order to steer the fragmentation properties according to the considered loading rate.

Conclusion and perspectives

Main conclusions

The last decades have witnessed a marked increase of lightweight ceramic-based armour protections. In a bilayer bulletproof system, the ceramic is used as a hard front face to break and erode the projectile, whereas a ductile backing dissipates the residual energy. Reducing the weight of armour solutions, while reaching improved ballistic performance, is a continuous challenge. But to do so, it is necessary to **understand the involved failure mechanisms and their link with material properties**. The present work focused on the ceramic part and its intrinsic behaviour towards dynamic loading. Preliminary ballistic tests (ballistic limit velocity of perforation) on the studied ceramic materials showed that changing the ceramic microstructure (mainly pore size distribution) can lead to an improvement of the ballistic performance. Such a result motivated the present work to better understand the link between the microstructural properties of a ceramic armour and its dynamic behaviour, according to the loading rate.

During a ballistic event, the ceramic undergoes three main loading conditions: confined compression, fragmentation under tensile loading and fragments flow/rearrangement during the projectile penetration. The ceramic fragmentation is directly related to the nucleation of micro-cracks on the microstructural defects under dynamic tensile loading. Moreover, the ability of a ceramic armour to defeat a projectile (erosion and further penetration) is supposed to be correlated to the behaviour of the fragmented ceramic. For this reason, it has been chosen to mainly **concentrate on the fragmentation behaviour of ceramic materials under tensile loading**, its link with the ceramic microstructural properties and its sensitivity to the loading rate on the range 10^2-10^6 s^{-1}. To do so, six ceramic materials, presenting different microstructural features, were investigated in this project. Two of them correspond to commercial ceramics of Saint-Gobain (Hexoloy SA® and Forceram®) and two others are deviated grades with a different pore size distribution (Hexoloy SA-CP and Improved Forceram). The two last materials were specifically developed during this PhD thesis (RBBC materials called RB2 and RB3).

The first step, presented in Chapter 3, consisted in analysing the **microstructural features** of each material, via scanning electron microscopy and X-ray tomography techniques. The focus was on the **identification of defects** (voids, inclusions and heterogeneities). The development of adapted post-processing techniques, applied to 3D images reconstructed from X-ray tomographic analyses, provided key information on the microstructural properties of each material. Finally, these materials can be paired to form three families of materials of the same type, in terms of manufacturing process and resulting microstructures. The first pair of materials, named Hexoloy grades (Hexoloy SA® and Hexoloy SA-CP), are dense silicon carbides presenting a relatively homogeneous microstructure, with small and uniform grain sizes of the same composition (SiC). They present some few defects such as pores (voids, sintering defects at the grain boundaries) and residual sintering aids. Between both materials, the only changing microstructural parameter is the size distribution of porosity. The Hexoloy SA material presents some few sintering pores, classical from solid-state sintered SiC materials. The Hexoloy SA-CP material also presents these sintering pores, in a slightly greater extent compared to the Hexoloy SA. The main difference is that the Hexoloy SA-CP material contains a size Controlled Porosity. Indeed, some large (40-100 μm) spherical pores, controlled in size and volume proportion (about 2 %) are homogeneously distributed in Hexoloy SA-CP bulk material. The second pair of materials, called

Forceram grades (Forceram® and Improved Forceram), present an apparent meso-structure with large SiC grains (50-150 μm) and a matrix of a ceramic binder-phase. A porous network (9-13 %) is present in the two materials and only differs in terms of volume proportion and local distribution. The last pair of materials studied are Reaction Bonded Boron Carbide (RBBC) materials. One specificity of this type of metal-ceramic composite is the almost absence of pores, filled by the infiltration of a metallic phase during the firing process. The main difference between the two materials of this RBBC type (RB2 and RB3) is the size distribution of B_4C and β-SiC grains.

Under a tensile dynamic loading, ceramic materials, undergo an intense dynamic fragmentation due to the lack of plastic deformation. It has been demonstrated in previous studies that this fragmentation results from the tensile state generated by the impulse waves propagating around the projectile nose upon impact. In order to study the fragmentation behaviour of all the studied materials, in Chapter 4, two dynamic tests were conducted. First, the **Edge-on-impact** (EOI) configuration consists in impacting the ceramic tile on its edge with a rigid projectile (cylindrical, 180 m/s). Such a configuration, combined to the use of an ultra-high-speed camera (operated at 2-5 Mfps in the present work), provided a visualisation of the fragmentation process, usually not-visible in a classical impact as it develops in the material bulk. Ultra-high-speed imaging and an analysis of fragment size distributions showed that the **fragmentation behaviour is deterministic**, in terms of damage chronology, crack patterns and fragment size distribution. Furthermore, it highlighted a clear **correlation between the microstructural and fragmentation properties**. Indeed, materials of the same family presented almost the same fragmentation properties. Interestingly, both Forceram materials presented a different behaviour compared to the other materials. The dense ceramics showed an intense fragmentation, developing only in 3-4 μs after impact, whereas in the Forceram materials the fragmentation process was delayed (about 10 μs) and attenuated. A sieve analysis of the recovered fragments showed that Hexoloy grades presented the most intense fragmentation, Forceram grades resulted in a moderated fragmentation with some large remaining fragments, and RBBC materials had an intermediate level of fragmentation. A possible explanation of the lower fragmentation of the Forceram grades could be that a collapse of porosity occurs under the compression wave, prior to the tensile loading. This crushing of the porous network in Forceram grades could be responsible for some energy dissipation, preventing the intense fragmentation from developing. Test performed at a lower velocity (100 m/s), for these materials, showed that an increase of the impact velocity from 100 to 180 m/s had almost no-influence on the fragmentation intensity. This result is a further argument in favour of a possible damage under the compressive wave generated upon impact.

Additional EOI tests were conducted on ceramic tiles confined in a polycarbonate sarcophagus in order to maintain fragments close to their initial position. Such a casing combined the transparency and resistance required to capture the fragmentation growth, from high-speed imaging, and to perform **post-mortem analyses on the fragmented tile, via X-ray tomography examination**. The 3D-image reconstructed from tomography was post-processed to observe the crack network, generated upon impact, in the volume of the post-mortem sample. An originality of the present analysis was to use micro-tomography to evaluate the cracking density in a given zone of the target (along the loading axis, at 10-20 mm from the impact point) and determine the corresponding loading rate from elastic numerical simulations (hoop tensile stresses). The strain rate level generated upon impact was found to depend on the elastic properties of the material and to decrease with an increase of the distance to the impact point. Thus, comparing the materials fragmentation properties for a given loading rate, instead of the impact velocity, is a more relevant approach. The first results showed a **sensitivity of the cracking density to the loading rate**, on a range of about 2.10^3-10^4 s^{-1} according to the material.

The second fragmentation test conducted is a **Normal impact**. In this configuration, the ceramic tile is placed between a hard steel cover-layer and an aluminium alloy backing. This *sandwich* target is confined in a metallic casing to limit the movement of fragments and their ejection upon impact. Once

the ceramic impacted (cylindrical projectile, 180 m/s), the front cover-layer was removed to infiltrate the post-mortem fragmented sample with a resin. The recovered fragmented tile was analysed via X-ray tomography analysis. A segmentation post-processing on the 3D-image was performed to identify the different fragments. From this analysis, the fragment size distribution could be computed and compared to the distribution obtained from EOI tests. Both tests lead to the same ranking of the materials, in terms of fragmentation intensity. In addition, the cracking density could be evaluated on the ceramic rear face, where an intense fragmentation is caused by the presence of hoop tensile stresses. Similarly, to the EOI tests, this cracking density was correlated to the local strain rate, estimated from elastic numerical simulations. This test provided additional experimental data for the **sensitivity of the cracking density to the tensile loading rate** (hoop stress), on a range of about 6.10^2-6.10^3 s^{-1}, according to the material and distance to the loading axis.

A complementary dynamic test, called **Tandem impact**, was conducted on a pre-fragmented ceramic to evaluate its resistance to a projectile perforation. Contrary to what is found in the literature a special attention was paid to generate a ceramic pre-damaging (fragments shape), which is close to a damaged ceramic from a ballistic event (not ceramic powders). To do so, the pre-damaging was generated in the ceramic tile via a Normal dynamic impact. After this first impact, the front steel cover-layer is removed from the fragmented ceramic front face and a second impact, with a perforating projectile, is performed on the fragmented media. This two-step testing configuration aims at decomposing the different stages of a ballistic impact into a first step of ceramic damaging, below the projectile nose, and a second step of penetration of the projectile in the fragmented media (fragment flow, rearrangement). The interaction between the pre-damaged ceramic and the projectile was recorded via ultra-high-speed imaging. A laser pointing at the rear face of the aluminium backing recorded the interaction between the projectile and the fragmented ceramic. From this test, it was observed that the pre-fragmented Forceram material presented the higher residual strength to the projectile penetration. This result shows that a coarser fragmentation should result in a greater **ability for the fragmented media to limit the penetration of an upcoming projectile**. In addition, this result underlines the importance of integrating the behaviour of the fragmented ceramic into numerical calculations, as it might have an influence on the complete armour system ability to withstand the penetration of a single and multiple projectile impacts. A sieve analysis of the recovered fragments showed the same ranking of the different types of materials compared to EOI and Normal impact. For all the materials, a small decrease of the overall fragment size, compared to a normal impact, could possibly be explained by the further breakage of partially cracked fragments. Finally, EOI and Normal impact dynamic tests provided valuable information on the tensile fragmentation chronology, intensity and sensitivity to strain rate. Tandem impact tests highlighted the necessity to study the behaviour of the fragmented media. Nevertheless, these tests did not provide a quantification of the material strength when subjected to a dynamic tensile loading, according to the loading rate.

In Chapter 5, the goal was to **evaluate the intrinsic dynamic tensile strength of ceramic materials and its sensitivity to strain rate**. This work was performed in the framework of the Brittle CODEX Chair, which aims at investigating the strain-rate sensitivity of brittle materials in order to improve their modelling at high loading rates. The planar impact technique is the most commonly used experimental technique to characterise ceramic materials at high strain rates. This testing configuration consists in impacting the studied specimen with a thin and flat flyer-plate in order to generate a shock loading, with an intensity high enough to cause its failure. For spall strength determination, the compressive waves generated upon impact between the flyer-plate and target (propagating in opposite directions) are reflected at the free surfaces and their overlap generates a tensile state, which can cause a spall failure. However, a classical plate-impact configuration leads to a discontinuous change in pressure and un-controlled loading rates. A lack of experimental techniques via plate-impact was found in the literature to evaluate the spall strength of ceramic material at a controlled loading rate. For this reason, an innovative experimental solution had to be developed in the present work. In order to reach a controlled and homogeneous loading rate in the failure zone, the

classical plate-impact technique was adapted using a wavy-shaped metallic flyer-plate. Such a flyer-plate geometry was designed via elastic numerical simulations to transfer a triangular compressive pulse to the ceramic target. This loading condition provided a **shockless impact**, leading to a constant and more homogeneous strain rate in the failure zone. The wavy cosine-profile of the flyer-plate (height and period) and the impact velocity could be adapted to generate different levels of **controlled loading rates** in the spall area. Thus, four geometries of stricker plate were tested with velocities between 200-450 m/s according to the flyer design, to obtain different strain rates. This technique was designed for the material Hexoloy SA. The strain rate in the spall zone was evaluated from a hybrid approach combining elasto-plastic numerical simulations and experimental tests. From this, the spall strength sensitivity to the strain rate was experimentally evaluated for strain-rates between 10^3 and 2.10^4 s^{-1}. Finally, this approach was validated by comparing the results to data available in the literature for the same Hexoloy SA material, and obtained from the GEPI technique, based on pulsed current.

In order to better understand the sensitivity to the loading rate of the tensile strength and fragmentation state of ceramic materials under dynamic tensile loading, a **modelling work**, presented in Chapter 6, was developed. For the development of this modelling approach, the focus was on both Hexoloy materials due to their relatively simple microstructure, homogeneity (one phase SiC and small grains) and with pores as main defects. The **Denoual-Forquin-Hild (DFH) damage model** was used to evaluate the strength and cracking density generated in both ceramic materials under tensile loading and over a large range of strain rates (10^2-10^6 s^{-1}). This micro-mechanical model presents the main advantages of considering the distribution of flaws and physic-based mechanisms to model cracks nucleation from defects, their propagation and their interaction (obscuration mechanism). The distribution of flaws is explicitly implemented in this model. The common approach consists in using quasi-static tests to identify the defects responsible for failure (Weibull approach) and assuming that the same ones are causing failure at high loading rates. Such hypothesis was questioned in the present work. An innovative approach was proposed to use a **real flaws (pores) distribution, extracted from X-ray tomography analyses** on both Hexoloy materials, to be implemented in the model. This approach presents the key benefit of capturing the material complete flaw-population, whereas the conventional way, based on the Weibull approach, is limited to the description of the largest defects, causing failure under quasi-static loading.

Two different approaches, based on X-ray tomography, were used to incorporate the real population of defects into the DFH model, called the **Continuous and Discrete approaches**. The Continuous approach consists in using the density of flaws, identified via tomography, and the Linear Fracture Mechanics to determine a continuous function representative of the density of critical stress of activation of each pore. The only calibration required for this approach is the evaluation a Y factor, traducing the shape of the defect. This parameter was determined by using the Weibull law obtained from bending tests. The main advantage of this Continuous approach is that the continuous function, identified to describe the density of critical defects, can be directly implemented in a finite element calculation to perform numerical simulation of dynamic tests. In the Discrete approach, numerical tensile tests are performed on a cubic numerical volume, containing pores detected via X-ray tomography at their exact position (real pore positions and equivalent sizes). The time at which a crack can nucleate from a pore is directly correlated to the size of the defect and the loading rate. The phenomenology of crack initiation, propagation and interaction of the DFH model was implemented in the Discrete approach. The main advantage of this approach is that the spatial distribution of defects is considered, whereas in the Continuous approach flaws are assumed to be homogeneously distributed in the volume. In addition, the Discrete approach gives access to the kinetics of the damage and the defects involved in the fragmentation process, according to the loading rate. Both Continuous and Discrete approached provide similar predictions, with a strain-rate dependant fragmentation behaviour of both materials. An increase of the loading rate leads to an increase of the tensile strength of the material and to an intensification of its fragmentation (number of nucleated cracks). Both approaches only diverge for low

($< 10^3$ s^{-1}) and high strain rates ($> 10^4$-10^5 s^{-1}). This is explained by the fact the Discrete approach is limited by the size of the analysed volume at low strain rates (a single fragmentation driven by the most critical defect) and the scan spatial resolution at high strain rate, respectively. Indeed, at high strain rates, the accuracy of the Discrete approach depends on the size of the smallest defects captured though the micro-tomography analysis, whereas in the Continuous approach the density of critical defects is extrapolated beyond the smallest size of defects by the continuous function.

For the Hexoloy SA material, the Weibull-based (i.e. based on Weibull distribution of flaws) and Continuous approaches gave the same predictions, in terms of ultimate strength and crack density, over the complete range of strain rates considered (10^2-10^6 s^{-1}). For the Hexoloy SA-CP material, the Weibull-based and Continuous approaches provided almost the same predictions at low and intermediate stain-rates ($< 2.10^4$ s^{-1}). But at high loading rates, this material presented a sharp increase of ultimate strength, which was not captured by the Weibull-based solution. This is due to the fact the Weibull-based solution only relies on a description of the critical defects from quasi-static tests, corresponding to the large size-controlled spherical pores. Therefore, this approach is not adapted for the description of the fragmentation behaviour of this material at strain rates above about 2.10^3 s^{-1}, which involves the nucleation of cracks on smaller pores, not described by the bending tests. Finally, both approaches based on micro-tomography, provided information on the **valuable effect of the size-controlled fuse flaws** in the porous Hexoloy, with a near absence of pores of size 20-40 μm, on the cracking density sensitivity to strain rate. Depending on the loading rate, a competition between the spreading of the obscuration zones and the initiation of new flaw drives the material strength. Such a kinetic-dependant crack nucleation on pre-existing flaws explains the high rate-hardening strength, which is characteristic of brittle materials, but is magnified for the Hexoloy SA-CP. The high strain-rate hardening strength of the material Hexoloy SA-CP and its limited fragmentation at high strain rates are arguments that could, at least partially, justify the higher ballistic performance, compared to the material Hexoloy SA®.

The DFH model was implemented in a **finite element code** to simulate EOI and Normal impact tests. Both flaw distributions, Weibullian and Continuous, were considered. Their predictions, in terms of fields of cracking density, were compared to the damage patterns obtained experimentally. The Continuous approach provided a more accurate estimation of the cracking density close to the impact point, which was lower than from the Weibull approach. Such a behaviour is consistent with the modelling predictions at relatively high strain rates (10^4 s^{-1}). Finally, the experimental data obtained in the Chapters 4 and 5, for the fragmentation intensity and shockless spall strength sensitivity to the loading rate were used to validate the modelling work developed in Chapter 6, via a **numerical-computation versus experiments confrontation**. The good match between the predictions and the experimental results, both in terms of ultimate strength and cracking density, are very encouraging.

Perspectives

A first perspective concerns the experimental work developed in this PhD thesis. To validate results obtained from the Tandem impact configuration, it would be interesting to perform additional tests on a given ceramic material, but for different levels of pre-damage. Such an approach could clarify the respective contributions of the fragments size/morphology and the material properties in the ability of the fragmented media to erode the projectile and limit its penetration.

Concerning the loading rate sensitivity of ceramic fragmentation and strength, it would be key to adapt or develop testing configurations to reach a higher range of controlled loading rates (10^4-10^6 s^{-1}). This would bring valuable experimental data to validate modelling works. For instance, this would enable a validation of the interest/necessity to consider a flaw population based on X-ray tomography, instead of a Weibull distribution, to accurately model the behaviour of ceramics under tensile loading at high strain

rates. To do so, the geometry of the wavy-shaped flyer plate, used in the shockless plate impact test, could be adapted and a sarcophagus configuration could be designed to recover the post-mortem specimen.

The present work brought insight on the role played by pore defects on the fragmentation behaviour of ceramic materials under dynamic tensile loading. From this, a natural prospect consists in using these elements of understanding to move toward a design of the material microstructure, according to the desired fragmentation properties. Within this framework, the Continuous and Discrete approaches are complementary tools to focus on homogeneous size-controlled population of defects or non-homogeneous distribution of defects in the bulk material.

Some examples, in the present work, showed that armour materials can present complex microstructural features such as a porous network, an heterogeneous meso-structure, multi-phases or even an absence of pores. For such materials, a transposition of the global modelling strategy developed here (tomography analysis, fragmentation tests, spalling tests, numerical simulations, etc.) could be possible, but not trivial. It would require to identify the mechanisms driving the material behaviour at the meso-scale.

Finally, with the goal to develop numerical models able to predict the dynamic or ballistic behaviour of ceramics, the present study of the tensile and fragmentation properties of the material has to be competed with a characterisation of its behaviour under confined compression. For instance, this would involve the determination of the material elastic limit under uniaxial deformation (HEL).

List of Tables

Bibliography

[1] W. Gooch. Overview of the development of ceramic armor technology: Past, present and in the future. In *30th International Conference on Advanced Ceramics and Composites, Cocoa Beach, Fl*, pages 22–27, 2006.

[2] E. Lewis and D.J. Carr. Personal armor. In *Lightweight Ballistic Composites*, pages 217–229. Elsevier, 2016.

[3] S. Hayun. Reaction-bonded boron carbide for lightweight armor: the interrelationship between processing, microstructure, and mechanical properties. *American Ceramic Society Bulletin*, 96(6):20–6, 2017.

[4] K. Taylor and R. Palicka. Dense carbide composite bodies and method of making same, March 12 1974. US Patent 3,796,564.

[5] P.R.S. Reddy, S.G. Savio, and V. Madhu. Ceramic composite armour for ballistic protection. *Handbook of Advanced Ceramics and Composites: Defense, Security, Aerospace and Energy Applications*, pages 357–402, 2020.

[6] J. Mescall. Materials issues in computer simulations of penetration mechanics. In *Computational Aspects of Penetration Mechanics*, pages 47–62. Springer, 1983.

[7] J.C. LaSalvia and J.W. McCauley. Inelastic deformation mechanisms and damage in structural ceramics subjected to high-velocity impact. *International journal of applied ceramic technology*, 7(5):595–605, 2010.

[8] J.C. LaSalvia, R.B. Leavy, J.R. Houskamp, H.T. Miller, D.E. MacKenzie, and J. Campbell. Ballistic impact damage observations in a hot-pressed boron carbide. In *Ceramic Engineering and Science Proceedings*, volume 30, page 45, 2009.

[9] P. Forquin, C. Denoual, C.E. Cottenot, and F. Hild. Experiments and modelling of the compressive behaviour of two sic ceramics. *Mechanics of materials*, 35(10):987–1002, 2003.

[10] H. Deng and S. Nemat-Nasser. Dynamic damage evolution in brittle solids. *Mechanics of materials*, 14(2):83–103, 1992.

[11] R. Danzer, A. Borger, and M. Fellner. Evolution of defects in pressed and sintered electro-ceramic components. In *27th Annual Cocoa Beach Conference on Advanced Ceramics and Composites-B*, volume 270, page 343. John Wiley & Sons, 2009.

[12] D.A. Shockey, A.H. Marchand, S.R. Skaggs, G.E. Cort, M.W. Burkett, and R. Parker. Failure phenomenology of confined ceramic targets and impacting rods. *International Journal of Impact Engineering*, 9(3):263–275, 1990.

[13] M.J. Normandia, J.C. LaSalvia, W.A. Gooch, J.W. McCauley, and A.M. Rajendran. Protecting the future force: ceramics research leads to improved armor performance. *Amptiac Q*, 8(4):21–7, 2004.

[14] KMW. Ceramic materials for light-weight ceramic polymer armor systems.

[15] B.R. Lawn. Indentation of ceramics with spheres: a century after hertz. *Journal of the American Ceramic Society*, 81(8):1977–1994, 1998.

[16] R.L. Woodward, Jr. W.A. Gooch, R.G O'donnell, W.J. Perciballi, B.J. Baxter, and S.D. Pattie. A study of fragmentation in the ballistic impact of ceramics. *International Journal of Impact Engineering*, 15(5):605–618, 1994.

[17] I.G. Crouch. Effects of cladding ceramic and its influence on ballistic. In *28th international symposium on ballistics*, pages 1084–1094, 2014.

[18] A. Krell and E. Strassburger. Order of influences on the ballistic resistance of armor ceramics and single crystals. *Materials Science and Engineering: A*, 597:422–430, 2014.

[19] I.G. Crouch and B. Eu. Ballistic testing methodologies. In *The Science of Armour Materials*, pages 639–673. Elsevier, 2017.

[20] E. Carton and G.H.J.J. Roebroeks. Testing method for ceramic armor and bare ceramic tiles. 09 2016.

[21] Z. Rosenberg, S.J. Bless, Y. Yeshurun, and K. Okajima. A new definition of ballistic efficiency of brittle materials based on the use of thick backing plates. *DGM Informationsgesellschaft mbH, Impact Loading and Dynamic Behavior of Materials.*, 1:491–498, 1988.

[22] P.J. Hazell. Measuring the strength of brittle materials by depth-of-penetration testing. *Advances in Applied Ceramics*, 109(8):504–510, 2010.

[23] D.E. Grady. Local inertial effects in dynamic fragmentation. *Journal of Applied Physics*, 53(1):322–325, 1982.

[24] L.A. Glenn and A. Chudnovsky. Strain-energy effects on dynamic fragmentation. *Journal of Applied Physics*, 59(4):1379–1380, 1986.

[25] G.R. Johnson and T.J. Holmquist. A computational constitutive model for brittle materials subjected to large strains, high strain rates and high pressures. *Shock wave and high-strain-rate phenomena in materials*, pages 1075–1081, 1992.

[26] N.F. Mott. Fragmentation of he shells: a theoretical formula for the distribution of weights of fragments. In *Fragmentation of Rings and Shells*, pages 227–241. Springer, 2006.

[27] F. Hild and D. Marquis. A statistical approach to the rupture of brittle materials. *European journal of mechanics. A. Solids*, 11(6):753–765, 1992.

[28] P. Forquin, M. Blasone, D. Georges, M. Dargaud, D. Saletti, and E. Andò. The brittle's codex chair. In *DYMAT Winter School 2020*, pages 180–185, 2020.

[29] R.W. Rice. Microstructure dependence of mechanical behavior of ceramics. In *Treatise on Materials Science & Technology*, volume 11, pages 199–381. Elsevier, 1977.

[30] R. Danzer, T. Lube, P. Supancic, and R. Damani. Fracture of ceramics. *Advanced engineering materials*, 10(4):275–298, 2008.

[31] M. Bakas, J.W. McCauley, V. Greenhut, D. Niesz, R. Haber, and B. West. Quantitative analysis of inclusion distributions in hot pressed silicon carbide. *International journal of impact engineering*, 50:40–48, 2012.

[32] S.R. Martin. *Experimental Characterization of the Effect of Microstructure on the Dynamic Behavior of SiC*. PhD thesis, Georgia Institute of Technology, 2004.

[33] W. Braue and R.W. Carpenter. Analytical electron microscopy of graphite-rich inclusions in sintered α-silicon carbide. *Journal of materials science*, 25(6):2943–2948, 1990.

[34] T. Lube. *Entwicklung eines Zugversuches zur Zuverlässigkeitsprüfung von keramischen Ventilen*. PhD thesis, Diplomarbeit am Institut für Metallkunde und Werkstoffprüfung, 1993.

[35] R.W. Rice. Pores as fracture origins in ceramics. *Journal of Materials science*, 19(3):895–914, 1984.

[36] J.J. Swab, A.A. Wereszczak, J. Tice, R. Caspe, and R.H. Kraft. Mechanical and thermal properties of advanced ceramics for gun barrel applications. Technical report, Army Research Lab Aberdeen Proving Ground MD Weapons and Materials Research, 2005.

[37] S. Song, Z. Gao, B. Lu, C. Bao, and B. Zheng. Effect of boron carbide on the liquid silicon infiltration and performance enhancement of reaction-bonded silicon carbide composites. *Materials Research Express*, 6(9):095612, 2019.

[38] S. PROCHAZKA and R.M. SCANLAN. Effect of boron and carbon on sintering of SiC. *Journal of the American Ceramic Society*, 58(1-2):72–72, 1975.

[39] H-M. Kim and Y-W. Kim. Low temperature pressureless sintering of silicon carbide ceramics with alumina–yttria–magnesia-calcia. *Journal of the Ceramic Society of Japan*, 127(4):207–214, 2019.

[40] G. Rossiquet. *Carbure de silicium pour application blindage: élaboration et étude du comportement à l'impact*. PhD thesis, Dijon, 2012.

[41] L.S. Sigl and H-J. Kleebe. Core/rim structure of liquid-phase-sintered silicon carbide. *Journal of the American Ceramic Society*, 76(3):773–776, 1993.

[42] S. Sundaram and R.J. Clifton. The influence of a glassy phase on the high strain rate response of a ceramic. *Mechanics of materials*, 29(3-4):233–251, 1998.

[43] A.N. Pick and H. Jones. Sialon bonded silicon carbide material, 2014. Patent WO 2014/096846 Al.

[44] S. Hayun, A. Weizmann, .P. Dariel, and N. Frage. Microstructural evolution during the infiltration of boron carbide with molten silicon. *Journal of the European Ceramic Society*, 30(4):1007–1014, 2010.

[45] J. Seidel, N. Claussen, and J. Rödel. Reliability of alumina ceramics: effect of grain size. *Journal of the European Ceramic Society*, 15(5):395–404, 1995.

[46] A. Zimmermann, M. Hoffman, B.D. Flinn, R.K. Bordiadra, T-J. Chuang, Jr. E.R. Fuller, and J. Rödel. Fracture of alumina with controlled pores. *Journal of the American Ceramic Society*, 81(9):2449–2457, 1998.

[47] R.B. Matthews, W.G. Hutchings, and F. Havelock. A relation between fracture and flaws in reaction-bonded silicon carbide. *J. Can. Ceram. Soc*, 42(1), 1973.

[48] R.W. Rice. Limitations of pore-stress concentrations on the mechanical properties of porous materials. *Journal of Materials Science*, 32(17):4731–4736, 1997.

[49] R.W. Davidge. *Mechanical behaviour of ceramics*. CUP Archive, 1979.

[50] B. Lawn. *Fracture of brittle solids*. Cambridge university press, 1993.

[51] W. Weibull. A statistical theory of strength of materials. *IVB-Handl.*, 1939.

[52] R.A. Sack. Extension of Griffith's theory of rupture to three dimensions. *Proceedings of the Physical Society*, 58(6):729, 1946.

[53] R. Danzer. A general strength distribution function for brittle materials. *Journal of the European Ceramic Society*, 10(6):461–472, 1992.

[54] J. Kovalcik, J. Dusza, T. Lube, J. Kiibler, and R. Danzer. Slow crack growth behavior of the esis silicon nitride reference material. 2002.

[55] L.S. Sigl. Microcrack toughening in brittle materials containing weak and strong interfaces. *Acta materialia*, 44(9):3599–3609, 1996.

[56] P.F. Becher, E.Y. Sun, K.P. Plucknett, K.B. Alexander, C-H. Hsueh, H-T. Lin, S.B. Waters, C.G. Westmoreland, E-S. Kang, K. Hirao, et al. Microstructural design of silicon nitride with improved fracture toughness: I, effects of grain shape and size. *Journal of the American Ceramic Society*, 81(11):2821–2830, 1998.

[57] A. de S. Jayatilaka and K. Trustrum. Statistical approach to brittle fracture. *Journal of Materials Science*, 12(7):1426–1430, 1977.

[58] F. Hild, C. Denoual, P. Forquin, and X. Brajer. On the probabilistic–deterministic transition involved in a fragmentation process of brittle materials. *Computers & Structures*, 81(12):1241–1253, 2003.

[59] R. Danzer, P. Supancic, J. Pascual, and T. Lube. Fracture statistics of ceramics–weibull statistics and deviations from weibull statistics. *Engineering Fracture Mechanics*, 74(18):2919–2932, 2007.

[60] K. Trustrum and A. de S. Jayatilaka. On estimating the weibull modulus for a brittle material. *Journal of Materials Science*, 14(5):1080–1084, 1979.

[61] L. Gorjan and M. Ambrožič. Bend strength of alumina ceramics: A comparison of weibull statistics with other statistics based on very large experimental data set. *Journal of the European Ceramic Society*, 32(6):1221–1227, 2012.

[62] S. Grange, P. Forquin, S. Mencacci, and F. Hild. On the dynamic fragmentation of two limestones using edge-on impact tests. *International Journal of Impact Engineering*, 35(9):977–991, 2008.

[63] F. Hild, P. Forquin, and A.R. Cordeiro da Silva. Single and multiple fragmentation of brittle geomaterials. *Revue française de génie civil*, 7(7-8):973–1002, 2003.

[64] B.L. Parsons, M. Lal, F.M. Williams, J.P. Dempsey J.B., Snellen, J. Everard, T. Slade, and J. Wlliams. The influence of beam size on the flexural strength of sea ice, freshwater ice and iceberg ice. *Philosophical Magazine A*, 66(6):1017–1036, 1992.

[65] EN 843-5. Advanced technical ceramics—monolithic ceramics—mechanical tests at room temperature—part 5: Statistical analysis. *EN 843-5*, page 40, 1997.

[66] D.G.S. Davies. The statistical approach to engineering design in ceramics. In *Proceedings of the British Ceramic Society*, volume 22, pages 429–452, 1973.

[67] T.E. Easler, R.C. Bradt, and R.E. Tressler. Concurrent flaw populations in sic. *Journal of the American Ceramic Society*, 64(3):c–53, 1981.

[68] R. Danzer, T. Lube, and P. Supancic. Monte carlo simulations of strength distributions of brittle materials-type of distribution, specimen and sample size. *Zeitschrift fur Metallkunde*, 92(7):773–783, 2001.

[69] H. Peterlik. Relationship of strength and defects of ceramic materials and their treatment by weibull theory. *Journal of the Ceramic Society of Japan*, 109(1272):S121–S126, 2001.

[70] H. Peterlik and D. Loidl. Bimodal strength distributions and flaw populations of ceramics and fibres. *Engineering Fracture Mechanics*, 68(3):253–261, 2001.

[71] K. Goda and H. Fukunaga. The evaluation of the strength distribution of silicon carbide and alumina fibres by a multi-modal weibull distribution. *Journal of Materials Science*, 21(12):4475–4480, 1986.

[72] R. Danzer. Some notes on the correlation between fracture and defect statistics: are weibull statistics valid for very small specimens? *Journal of the European Ceramic Society*, 26(15):3043–3049, 2006.

[73] K.T. Ramesh, J.D. Hogan, J. Kimberley, and A. Stickle. A review of mechanisms and models for dynamic failure, strength, and fragmentation. *Planetary and Space Science*, 107:10–23, 2015.

[74] R.N. Katz and W.A. Brantley. Fractography of high boron ceramics subjected to ballistic loading. In *Ceramics in Severe Environments*, pages 271–282. Springer, 1971.

[75] M.A. Meyers. *Dynamic behavior of materials*. John Wiley & sons, 1994.

[76] P. Forquin, G. Rossiquet, J.L. Zinszner, and B. Erzar. Microstructure influence on the fragmentation properties of dense silicon carbides under impact. *Mechanics of Materials*, 123:59–76, 2018.

[77] P. Forquin and F. Hild. A probabilistic damage model of the dynamic fragmentation process in brittle materials. In *Advances in applied mechanics*, volume 44, pages 1–72. Elsevier, 2010.

[78] C. Denoual and F. Hild. A damage model for the dynamic fragmentation of brittle solids. *Computer methods in applied mechanics and engineering*, 183(3-4):247–258, 2000.

[79] H. Schuler, C. Mayrhofer, and K. Thoma. Spall experiments for the measurement of the tensile strength and fracture energy of concrete at high strain rates. *International Journal of Impact Engineering*, 32(10):1635–1650, 2006.

[80] P. Forquin and B. Erzar. Dynamic fragmentation process in concrete under impact and spalling tests. *International Journal of Fracture*, 163(1-2):193–215, 2010.

[81] B. Erzar and P. Forquin. An experimental method to determine the tensile strength of concrete at high rates of strain. *Experimental Mechanics*, 50(7):941–955, 2010.

[82] P. Forquin and B. Lukić. On the processing of spalling experiments. part i: identification of the dynamic tensile strength of concrete. *Journal of Dynamic Behavior of Materials*, 4(1):34–55, 2018.

[83] D.P. Dandekar and P.T. Bartkowski. Tensile strengths of silicon carbide (SiC) under shock loading. Technical report, Army Research Lab Aberdeen proving ground MD, 2001.

[84] J.L. Zinszner, B. Erzar, P. Forquin, and E. Buzaud. Dynamic fragmentation of an alumina ceramic subjected to shockless spalling: an experimental and numerical study. *Journal of the Mechanics and Physics of Solids*, 85:112–127, 2015.

[85] J.L. Zinszner, B. Erzar, and P. Forquin. Strain rate sensitivity of the tensile strength of two silicon carbides: Experimental evidence and micromechanical modelling. *Philosophical Transactions of The Royal Society A Mathematical Physical and Engineering Sciences*, 375:20160167, 01 2017.

[86] B. Erzar and E. Buzaud. Shockless spalling damage of alumina ceramic. *The European Physical Journal Special Topics*, 206(1):71–77, 2012.

[87] B. Erzar and P. Forquin. Analysis and modelling of the cohesion strength of concrete at high strain-rates. *International Journal of Solids and Structures*, 51(14):2559–2574, 2014.

[88] J. Weerheijm and P. Forquin. Response mechanisms of concrete under impulsive tensile loading. In *Understanding the Tensile Properties of Concrete*, pages 181–217. Elsevier, 2013.

[89] I.G. Crouch. Body armour–new materials, new systems. *Defence Technology*, 15(3):241–253, 2019.

[90] A. Healey, J. Cotton, S. Maclachlan, P. Smith, and J. Yeomans. Understanding the ballistic event: methodology and initial observations. *Journal of Materials Science*, 52(6):3074–3085, 2017.

[91] K.T. Ramesh. High rates and impact experiments. *Handbook of experimental solid mechanics*, 933, 2008.

[92] N. Bourne, J. Millett, and I. Pickup. Delayed failure in shocked silicon carbide. *Journal of Applied Physics*, 81(9):6019–6023, 1997.

[93] J.L. Zinszner. *Identification des paramètres matériau gouvernant les performances de céramiques à blindage*. PhD thesis, Université de Lorraine, 2014.

[94] E. Strassburger and H. Senf. Experimental investigations of wave and fracture phenomena in impacted ceramics and glasses. Technical report, Fraunhofer-Inst Fuer Kurzzeitdynamik-Ernst-Mach-Inst Weil Am Rhein (Germany), 1995.

[95] P. RIOU, C. DENOUAL, and C.E. COTTENOT. Visualization of the damage evolution in impacted silicon carbide ceramics. *International journal of impact engineering*, 21(4):225–235, 1998.

[96] E. Strassburger, H. Senf, C. Denoual, P. Riou, and C. Cottenot. An experimental approach to validate damage evolution laws for brittle materials. *Le Journal de Physique IV*, 7(C3):C3–909, 1997.

[97] C. Denoual and F. Hild. Dynamic fragmentation of brittle solids: a multi-scale model. *European Journal of Mechanics-A/Solids*, 21(1):105–120, 2002.

[98] P. Forquin and F. Hild. Dynamic fragmentation of an ultrahigh-strength concrete during edge-on impact tests. *Journal of engineering mechanics*, 134(4):302–315, 2008.

[99] J.W. McCauley, E. Strassburger, P. Patel, B. Paliwal, and K.T. Ramesh. Experimental observations on dynamic response of selected transparent armor materials. *Experimental Mechanics*, 53(1):3–29, 2013.

[100] N.D. Parab, Z. Guo, M. Hudspeth, B. Claus, B.H. Lim, T. Sun, X. Xiao, K. Fezzaa, and W.W. Chen. In situ observation of fracture processes in high-strength concretes and limestone using high-speed x-ray phase-contrast imaging. *Philosophical Transactions of the Royal Society A: Mathematical, Physical and Engineering Sciences*, 375(2085):20160178, 2017.

[101] P. Forquin, B. Lukić, Y. Duplan, D. Saletti, D. Eakins, and A. Rack. Investigation of the dynamic fragmentation process in ceramics by using ultra-high speed x-ray imaging with synchrotron radiation. In *32nd International Congress on High-Speed Imaging and Photonics*, volume 11051, page 110510Q. International Society for Optics and Photonics, 2019.

[102] X.F. Li, H.B. Li, Q.B. Zhang, J.L. Jiang, and J. Zhao. Dynamic fragmentation of rock material: characteristic size, fragment distribution and pulverization law. *Engineering Fracture Mechanics*, 199:739–759, 2018.

[103] P. Forquin and E. Andò. Application of microtomography and image analysis to the quantification of fragmentation in ceramics after impact loading. *Philosophical Transactions of the Royal Society A: Mathematical, Physical and Engineering Sciences*, 375(2085):20160166, 2017.

[104] J.D. Hogan, L. Farbaniec, D. Mallick, V. Domnich, K. Kuwelkar, T. Sano, J.W. McCauley, and K.T. Ramesh. Fragmentation of an advanced ceramic under ballistic impact: mechanisms and microstructure. *International journal of impact engineering*, 102:47–54, 2017.

[105] C. Denoual. *Approche probabiliste du comportement à l'impact du carbure de silicium: application aux blindages moyens*. PhD thesis, 1998.

[106] P. Forquin, L. Tran, P.F. Louvigné, L. Rota, and F.Hild. Effect of aluminum reinforcement on the dynamic fragmentation of SiC ceramics. *International journal of impact engineering*, 28(10):1061–1076, 2003.

[107] J.M. Wells and R.M. Brannon. Advances in x-ray computed tomography diagnostics of ballistic impact damage. *Metallurgical and Materials Transactions A*, 38(12):2943–2949, 2007.

[108] B.G. Compton, E.A. Gamble, and F.W. Zok. Failure initiation during impact of metal spheres onto ceramic targets. *International Journal of Impact Engineering*, 55:11–23, 2013.

[109] D. Grady. Dynamic fragmentation of solids. *Shock wave science and technology reference library*, 3:169–276, 2009.

[110] D.E. Lambert and C.A. Ross. Strain rate effects on dynamic fracture and strength. *International Journal of Impact Engineering*, 24(10):985–998, 2000.

[111] F. Gálvez, J. Rodriguez, and V. Sánchez. Tensile strength measurements of ceramic materials at high rates of strain. *Le Journal de Physique IV*, 7(C3):C3–151, 1997.

[112] K.T. Ramesh. High rates and impact experiments. *Handbook of experimental solid mechanics*, 933:929–960, 2008.

[113] P. Forquin, W. Riedel, and J. Weerheijm. Dynamic test devices for analyzing the tensile properties of concrete. In *Understanding the Tensile Properties of Concrete*, pages 137–181e. Elsevier, 2013.

[114] P. Forquin. Brittle materials at high-loading rates: an open area of research. *Philosophical transactions. Series A, Mathematical, physical, and engineering sciences*, 375(2085), 2017.

[115] J. Pelleg. Deformation in ceramics. In *Mechanical Properties of Ceramics*, pages 281–350. Springer, 2014.

[116] V. Paris, N. Frage, M.P. Dariel, and E. Zaretsky. The spall strength of silicon carbide and boron carbide ceramics processed by spark plasma sintering. *International journal of impact engineering*, 37(11):1092–1099, 2010.

[117] T. Antoun, D. Curran, S. Razorenov, L. Seaman, G.I. Kanel, and A. Utkin. Spall fracture. *Spall Fracture: Shock Wave and High Pressure Phenomena. Springer-Verlag New York, Inc.*, 01 2003.

[118] S.A. Novikov, I.I Divnov, and A.G. Ivanov. Investigation of the fracture of steel, aluminum and copper during explosive loading. *Fiz Metallov Metalloved*, 21(4):608–615, 1966.

[119] P. Bartkowski and D.P. Dandekar. Spall strengths of sintered and hot pressed silicon carbide. In *AIP Conference Proceedings*, volume 370, pages 535–538. American Institute of Physics, 1996.

[120] D.P. Dandekar and P.T. Bartkowski. Spall strengths of silicon carbides under shock loading. *Fundamental Issues and Applications of Shock-Wave and High Strain-Rate Phenomena*, pages 71–77, 2001.

[121] D.E. Grady. Dynamic properties of ceramic materials. Technical report, Sandia National Labs., Albuquerque, NM (United States), 1995.

[122] D.E. Grady. The spall strength of condensed matter. *Journal of the Mechanics and Physics of Solids*, 36(3):353–384, 1988.

[123] P. Forquin and J.L. Zinszner. A pulse-shaping technique to investigate the behaviour of brittle materials subjected to plate-impact tests. *Philosophical Transactions of the Royal Society A: Mathematical, Physical and Engineering Sciences*, 375(2085):20160333, 12 2016.

[124] B.M. LaLone and Y.M. Gupta. Elastic limit of x-cut quartz under shockless and shock wave compression: Loading rate dependence. *Journal of Applied Physics*, 106(5):053526, 2009.

[125] S. Yep, J. Belof, D. Orlikowski, and J. Nguyen. Fabrication and application of high impedance graded density impactors in light gas gun experiments. *The Review of scientific instruments*, 84:103909, 10 2013.

[126] L.P. Martin, J.R. Patterson, D. Orlikowski, and J.H. Nguyen. Application of tape-cast graded impedance impactors for light-gas gun experiments. *Journal of Applied Physics*, 102(2):023507, 2007.

[127] A.C. Hall, C.C. Battaile, E.B. Webb, J.L. Wise, D.A. Urrea, J.F. McCloskey, T.J. Roemer, and D.E. Beatty. Graded-density thermal spray coatings for light gas gun flyer plates. Technical report, Sandia National Lab.(SNL-NM), Albuquerque, NM (United States), 2008.

[128] M. Cotton, D. Chapman, R. Winter, E. Harris, and D. Eakins. Tailored ramp wave generation in gas gun experiments. In *EPJ Web of Conferences*, volume 94, page 01065. EDP Sciences, 2015.

[129] J.P. Davis, C. Deeney, M.D. Knudson, R.W. Lemke, T.D. Pointon, and D.E. Bliss. Magnetically driven isentropic compression to multimegabar pressures using shaped current pulses on the z accelerator. *Physics of Plasmas*, 12(5):056310, 2005.

[130] B. Erzar and E. Buzaud. Shockless spalling damage of alumina ceramic. *The European Physical Journal Special Topics*, 206, 05 2012.

[131] F. Zucchiniand C. Chauvin, T. d'Almeida, F. Lassalle, A. Morell, and A. Loyen. Dynamical compression studies at CEA Gramat on going experimental and numerical work. *ESRF - Dynamic compression studies with X-rays Workshop*, 2015.

[132] D.R. Curran, L. Seaman, T. Cooper, and D.A. Shockey. Micromechanical model for comminution and granular flow of brittle material under high strain rate application to penetration of ceramic targets. *International Journal of Impact Engineering*, 13(1):53–83, 1993.

[133] D.B. Rahbek and B.B. Johnsen. Dynamic behaviour of ceramic armour systems. 2015.

[134] M.B. Cil, R.C. Hurley, and L. Graham-Brady. A rate-dependent constitutive model for brittle granular materials based on breakage mechanics. *Journal of the American Ceramic Society*, 102(9):5524–5534, 2019.

[135] G.J. Appleby-Thomas, D.C. Wood, A. Hameed, J. Painter, and B. Fitzmaurice. On the effects of powder morphology on the post-comminution ballistic strength of ceramics. *International Journal of Impact Engineering*, 100:46–55, 2017.

[136] I. Horsfall, M.R. Edwards, and M.J. Hallas. Ballistic and physical properties of highly fractured alumina. *Advances in Applied Ceramics*, 109(8):498–503, 2010.

[137] H. Nanda, G.J. Appleby-Thomas, D.C. Wood, and P.J. Hazell. Ballistic behaviour of explosively shattered alumina and silicon carbide targets. *Advances in Applied Ceramics*, 110(5):287–292, 2011.

[138] Jr C.E. Anderson, S. Chocron, and T. Behner. A constitutive model for in situ comminuted silicon carbide. *Journal of the American Ceramic Society*, 92(6):1280–1286, 2009.

[139] D.C. Drucker and W. Prager. Soil mechanics and plastic analysis or limit design. *Quarterly of applied mathematics*, 10(2):157–165, 1952.

[140] P. Forquin. Compréhension des mécanismes de résistance à l'impact de matériaux á base de céramique. *Contrat de recherche Saint-Gobain CREE*, 2011.

[141] J.L. Zinszner, P. Forquin, and G. Rossiquet. Design of an experimental configuration for studying the dynamic fragmentation of ceramics under impact. *The European Physical Journal Special Topics*, 206(1):107–115, 2012.

[142] A.M. Rajendran and D.J. Grove. Modeling the shock response of silicon carbide, boron carbide and titanium diboride. *International Journal of Impact Engineering*, 18(6):611–631, 1996.

[143] G.R. Johnson and T.J. Holmquist. An improved computational constitutive model for brittle materials. In *AIP conference proceedings*, volume 309, pages 981–984. American Institute of Physics, 1994.

[144] Y. Duplan and P. Forquin. Investigation of the multiple-fragmentation process and post-fragmentation behaviour of dense and nacre-like alumina ceramics by means of tandem impact experiments and tomographic analysis. *International Journal of Impact Engineering*, 2021. (submitted for publication).

[145] S. Levy and J.F. Molinari. Dynamic fragmentation of ceramics, signature of defects and scaling of fragment sizes. *Journal of the Mechanics and Physics of Solids*, 58(1):12–26, 2010.

[146] C. Dascalu. Dynamic damage law with fragmentation length: strain-rate sensitivity of the tensile response. *Journal of Dynamic Behavior of Materials*, pages 1–5, 2020.

[147] N.F. Mott and E.H. Linfoot. A theory of fragmentation. *Ministry of Supply*, AC3348, 1943.

[148] D. Grady. *Fragmentation of rings and shells: the legacy of NF Mott*. Springer Science & Business Media, 2007.

[149] V.B. Shenoy and K-S. Kim. Disorder effects in dynamic fragmentation of brittle materials. *Journal of the Mechanics and Physics of Solids*, 51(11-12):2023–2035, 2003.

[150] F. Zhou, J.F. Molinari, and K.T. Ramesh. Analysis of the brittle fragmentation of an expanding ring. *Computational Materials Science*, 37(1-2):74–85, 2006.

[151] F. Zhou, J.F. Molinari, and K.T. Ramesh. A cohesive model based fragmentation analysis: effects of strain rate and initial defects distribution. *International Journal of Solids and Structures*, 42(18-19):5181–5207, 2005.

[152] M.F. Kanninen. *Advanced fracture mechanics*. Oxford University Press, 1985.

[153] D. Broek. Practical problems. In *Elementary engineering fracture mechanics*, pages 347–376. Springer, 1982.

[154] Y. Duplan, B. Lukić, and P. Forquin. Comparison of two processing techniques to characterise the dynamic crack velocity in armour ceramic based on digital image correlation. In *Conference DYMAT Winter School, Les Houches (France)*, 2020.

[155] C. Denoual, G. Barbier, and F. Hild. A probabilistic approach for fragmentation of brittle materials under dynamic loading. *Academie des Sciences Paris Comptes Rendus Serie B Sciences Physiques*, 325(12):685–691, 1997.

[156] P. Forquin. *Endommagement et fissuration de matériaux fragiles sous impact balistique: rôle de la microstructure*. LMT-Cachan, 2006.

[157] H.D. Espinosa and P.D. Zavattieri. A grain level model for the study of failure initiation and evolution in polycrystalline brittle materials. part i: Theory and numerical implementation. *Mechanics of Materials*, 35(3-6):333–364, 2003.

[158] O. Stamati, E. Roubin, E. Andò, and Y. Malecot. Phase segmentation of concrete x-ray tomographic images at meso-scale: Validation with neutron tomography. *Cement and Concrete Composites*, 88:8–16, 2018.

[159] G.T. Camacho and M. Ortiz. Computational modelling of impact damage in brittle materials. *International Journal of solids and structures*, 33(20-22):2899–2938, 1996.

[160] X.P. Xu and A. Needleman. Numerical simulations of dynamic interfacial crack growth allowing for crack growth away from the bond line. *International Journal of Fracture*, 74(3):253–275, 1996.

[161] P.D. Zavattieri, P.V. Raghuram, and H.D. Espinosa. A computational model of ceramic microstructures subjected to multi-axial dynamic loading. *Journal of the Mechanics and Physics of Solids*, 49(1):27–68, 2001.

[162] K.L. More, Jr. C.H. Carter, J. Bentley, W.H. Wadlin, L. Lavanier, and R.F. Davis. Occurrence and distribution of boron-containing phases in sintered a-silicon carbide. *Journal of the American Ceramic Society*, 69(9):695–698, 1986.

[163] Saint-Gobain Performance Ceramics and Refractories. Technical Data Hexoloy SA Silicon Carbide. https://www.ceramicsrefractories.saint-gobain.com/products/hexoloy-sic-materials/grades/sa.

[164] Website Saint-Gobain. https://www.ceramicsrefractories.saint-gobain.com/hexoloy/why-use-hexoloy-sic-material.

[165] Saint-Gobain. Material Data Sheet - Forceram. https://www.ceramicsrefractories.saint-gobain.com/sites/imdf.hpr.com/files/hpr-forceram-ds-en.pdf.

[166] T.K. Roy, C. Subramanian, and A.K. Suri. Pressureless sintering of boron carbide. *Ceramics international*, 32(3):227–233, 2006.

[167] R. Angers and M. Beauvy. Hot-pressing of boron carbide. *Ceramics international*, 10(2):49–55, 1984.

[168] S. Hayun, N. Frage, and M.P. Dariel. The morphology of ceramic phases in BxC–SiC–Si infiltrated composites. *Journal of solid state chemistry*, 179(9):2875–2879, 2006.

[169] D.D. Nesmelov and S.N. Perevislov. Reaction sintered materials based on boron carbide and silicon carbide. *Glass and Ceramics*, 71(9-10):313–319, 2015.

[170] M. Dargaud, J. Brulin, M. Graveleau, J. Sant, and P. Forquin. Reaction-bonded boron carbide armor material: An investigation of the microstructure effect on the ballistic limit velocity V_{50}. In *LWAG 2019 (Light-Weight Armour for Defence & Security)*, 2019.

[171] V. Ischenko, Y.S. Jang, M. Kormann, P. Greil, N. Popovska, C. Zollfrank, and J. Woltersdorf. The effect of sic substrate microstructure and impurities on the phase formation in carbide-derived carbon. *Carbon*, 49(4):1189–1198, 2011.

[172] G. Magnani, G. Beltrami, G.L. Minoccari, and L. Pilotti. Pressureless sintering and properties of αSiC–B4C composite. *Journal of the European Ceramic Society*, 21(5):633–638, 2001.

[173] R. Beare and G. Lehmann. The watershed transform in ITK-discussion and new developments. *The Insight Journal*, 1:1–24, 2006.

[174] G.A.R. Gualda and M. Rivers. Quantitative 3d petrography using x-ray tomography: Application to bishop tuff pumice clasts. *Journal of Volcanology and Geothermal Research*, 154(1-2):48–62, 2006.

[175] S. Tammas-Williams, H. Zhao, F. Léonard, F. Derguti, I. Todd, and P.B. Prangnell. Xct analysis of the influence of melt strategies on defect population in ti–6al–4v components manufactured by selective electron beam melting. *Materials Characterization*, 102:47–61, 2015.

[176] O. Stamati, E. Andò, E. Roubin, R. Cailletaud, M. Wiebicke, G. Pinzon, C. Couture, R.C. Hurley, R. Caulk, D. Caillerie, et al. spam: Software for practical analysis of materials. *Journal of Open Source Software*, 5(51):2286, 2020.

[177] I.G. Crouch, M. Kesharaju, and R. Nagarajah. Characterisation, significance and detection of manufacturing defects in reaction sintered silicon carbide armour materials. *Ceramics International*, 41(9):11581–11591, 2015.

[178] E. Medvedovski. Ballistic performance of armour ceramics: Influence of design and structure. part 1. *Ceramics International*, 36:2103–2115, 09 2010.

[179] P. Barick, D.C. Jana, and N. Thiyagarajan. Effect of particle size on the mechanical properties of reaction bonded boron carbide ceramics. *Ceramics International*, 39(1):763–770, 2013.

[180] S. Hayun, M.P. Dariel, N. Frage, and E. Zaretsky. The high-strain-rate dynamic response of boron carbide-based composites: The effect of microstructure. *Acta materialia*, 58(5):1721–1731, 2010.

[181] W.J. Moberlychan, J.J. Cao, and L.C. De Jonghe. The roles of amorphous grain boundaries and the β–α transformation in toughening sic. *Acta materialia*, 46(5):1625–1635, 1998.

[182] Y. Zhou, D. Ni, Y. Kan, P. He, S. Dong, and X. Zhang. Microstructure and mechanical properties of reaction bonded b_4c-sic composites: The effect of polycarbosilane addition. *Ceramics International*, 43(8):5887–5895, 2017.

[183] S.G. Savio, A.S. Rao, P.R.S. Reddy, and Y. Madhu. Microstructure and ballistic performance of hot pressed & reaction bonded boron carbides against an armour piercing projectile. *Advances in Applied Ceramics*, 118(5):264–273, 2019.

[184] C. Kaufmann, D. Cronin, M. Worswick, G. Pageau, and A. Beth. Influence of material properties on the ballistic performance of ceramics for personal body armour. *Shock and Vibration*, 10(1):51–58, 2003.

[185] ASTM C1259-15, Standard Test Method for Dynamic Young's Modulus, Shear Modulus, and Poisson's Ratio for Advanced Ceramics by Impulse Excitation of Vibration. *ASTM International*, 2015.

[186] ASTM C1421-10, Standard Test Methods for Determination of Fracture Toughness of Advanced Ceramics at Ambient Temperature. *ASTM International*, 2010.

[187] M. Mitomo and S. Uenosono. Microstructural development during gas-pressure sintering of α-silicon nitride. *Journal of the American Ceramic Society*, 75(1):103–107, 1992.

[188] P. Chhillar, M.K. Aghajanian, D.D. Marchant, R. Haber, and M. Sennett. The effect of si content on the properties of b4c-sic-si composites. In *31st International Conference on Advanced Ceramics and Composites*, pages 161–167, 2008.

[189] M.K. Aghajanian. Toughness enhanced silicon-containing composite bodies, and methods for making same, February 7 2006. US Patent 6,995,103.

[190] M.K. Aghajanian, A.L. McCormick, B.N. Morgan, and A.F. Liszkiewicz. Boron carbide composite bodies, and methods for making same, 2004. US Patent US7332221B2.

[191] M. Cafri, A. Malka, H. Dilman, M.P. Dariel, and N. Frage. Reaction-bonded boron carbide/magnesium–silicon composites. *International Journal of Applied Ceramic Technology*, 11(2):273–279, 2014.

[192] C. Denoual and C.E. Cottenot et al. Visualization of the damage evolution in impacted silicon carbide ceramics. *International Journal of Impact Engineering*, 21(4):225–235, 1998.

[193] Particle sizer ANALYSETTE 28 ImageSizer. https://www.fritsch-international.com/particle-sizing/dynamic-image-analysis/details/product/particle-sizer-analysette-28-imagesizer/.

[194] J.L. Zinszner, P. Forquin, and G. Rossiquet. Experimental and numerical analysis of the dynamic fragmentation in a SiC ceramic under impact. *International Journal of Impact Engineering*, 76:9–19, 2015.

[195] I. Horsfall and D. Buckley. The effect of through-thickness cracks on the ballistic performance of ceramic armour systems. *International journal of impact engineering*, 18(3):309–318, 1996.

[196] M. Dargaud and P. Forquin. A shockless plate-impact spalling technique, based on wavy-machined flyer-plates, to evaluate the strain-rate sensitivity of ceramic tensile strength. *Journal of Dynamic Behavior of Materials*, 2021. (submitted for publication).

[197] P. Forquin. Procede et dispositif pour mesurer la resistance des materiaux solides par impact de plaques sans choc, October 11 2016. Patent UGA, INPI, N°1000369617.

[198] F. Plassard, J. Mespoulet, and P.L. Héreil. Analysis of a single stage compressed gas launcher behaviour : from breech opening to sabot separation. *8th European LS-DYNA Users Conference, Strasbourg*, 05 2011.

[199] O.T. Strand, D.R. Goosman, C. Martinez, T.L. Whitworth, and W.W. Kuhlow. Compact system for high-speed velocimetry using heterodyne techniques. *Review of Scientific Instruments*, 77:083108–083108, 08 2006.

[200] C. Kettenbeil, M. Mello, M. Bischann, and G. Ravichandran. Heterodyne transverse velocimetry for pressure-shear plate impact experiments. *Journal of Applied Physics*, 123:125902, 03 2018.

[201] P. Forquin, M. Blasone, D. Georges, and M. Dargaud. Continuous and discrete methods based on X-ray computed-tomography to model the fragmentation process in brittle solids over a wide range of strain-rates - application to three brittle materials. *Journal of the Mechanics and Physics of Solids*, page 104412, 2021.

[202] F.I. Baratta, W.T. Matthews, and G.D. Quinn. Errors associated with flexure testing of brittle materials. Technical report, Army Lab Command Watertown MA Material Technology Lab, 1987.

[203] G.D. Quinn and R. Morrell. Design data for engineering ceramics: a review of the flexure test. *Journal of the American Ceramic Society*, 74(9):2037–2066, 1991.

[204] G. Bruno and M. Kachanov. Microstructure–property connections for porous ceramics: The possibilities offered by micromechanics. *Journal of the American Ceramic Society*, 99(12):3829–3852, 2016.

[205] Y. Duplan, P. Forquin, B. Lukić, and D. Saletti. Numerical analysis of a testing technique to investigate the dynamic crack propagation in armour ceramic. In *EPJ Web of Conferences*, volume 183, page 02039. EDP Sciences, 2018.

[206] P.J. Hazell and M.J. Iremonger. Crack softening damage model for ceramic impact and its application within a hydrocode. *Journal of applied physics*, 82(3):1088–1092, 1997.

[207] M. Sakai and R.C. Bradt. Fracture toughness testing of brittle materials. *International Materials Reviews*, 38(2):53–78, 1993.

[208] T. Weerasooriya, P. Moy, D. Casem, M. Cheng, and W. Chen. A four-point bend technique to determine dynamic fracture toughness of ceramics. *Journal of the American Ceramic Society*, 89(3):990–995, 2006.

[209] J. Pittari III, G. Subhash, J. Zheng, V. Halls, and P. Jannotti. The rate-dependent fracture toughness of silicon carbide-and boron carbide-based ceramics. *Journal of the European Ceramic Society*, 35(16):4411–4422, 2015.

[210] J.R. Brockenbrough, S. Suresh, and J. Duffy. An analysis of dynamic fracture in microcracking brittle solids. *Philosophical Magazine A*, 58(4):619–634, 1988.

[211] P. Forquin, Y. Duplan, M. Dargaud, D. Saletti, and J.L. Zinszner. A Review of Experimental Approaches to Analyse Damage Modes and the Ballistic Performances of Armour Ceramics. In *Conference Light-Weight Armour Group for Defence and Security LWAG*, Roubaix, France, 2019.

[212] P. Forquin, M. Blasone, D. Georges, M. Dargaud, and E. Andò. Modelling of the fragmentation process in brittle solids based on x-ray micro-tomography analysis. In *24^{me} Congrès Français de Mécanique*, 2019.

Communications

Scientific journal papers

P. Forquin, M. Blasone, D. Georges, M. Dargaud. Continuous and discrete methods based on X-ray computed-tomography to model the fragmentation process in brittle solids over a wide range of strain-rates - Application to three brittle materials. *Journal of the Mechanics and Physics of Solids* [201]

M. Dargaud and P. Forquin. A shockless plate-impact spalling technique, based on wavy-machined flyer-plates, to evaluate the strain-rate sensitivity of ceramic tensile strength. *Journal of Dynamic Behavior of Materials* (submitted for publication)

M. Dargaud and P. Forquin. Improved modelling of the dynamic behaviour of ceramics from an accurate flaw description via micro-tomography, with experimental validation (in progress)

Conferences

M. Dargaud, J. Brulin, M. Graveleau, J. Sant, and P. Forquin. Reaction-bonded boron carbide armor material: an investigation of the microstructure effect on the ballistic limit velocity V_{50}. *Conference Light-Weight Armour Group for Defense and Security LWAG*, Roubaix, France, 2019 [170]

P. Forquin, Y. Duplan, M. Dargaud, D. Saletti, J.-L. Zinszner. A review of experimental approaches to analyse the damage modes and the ballistic performances of armour ceramics. *Conference Light-Weight Armour Group for Defence and Security LWAG*, Roubaix, France, 2019 [211]

P. Forquin, M. Blasone, D. Georges, M. Dargaud, E. Ando. Modelling of the fragmentation process in brittle solids based on x-ray micro-tomography analysis. *24ème Congrès Français de Mécanique*, Brest, France, 2019 [212]

M. Dargaud and P. Forquin. Effect of porosity on the failure mechanisms induced in SiC brittle materials upon dynamic impact. *Conference DYMAT*, Les Houches, France, 2020.

P. Forquin, M. Blasone, M. Dargaud, D. Georges. Dynamic fragmentation in brittle solids: experimental approaches and modelling. *Conference DYMAT*, Les Houches, France, 2020.

M. Dargaud and P. Forquin. Experimental technique to evaluate the strain-rate sensitivity of ceramic spall strength using shockless plate-impact. *2nd International Conference on Materials Science & Engineering, Mat Science* (virtual), San Francisco, United States, 2020.